VERÖFFENTLICHUNGEN
des Instituts für Geotechnik
der Technischen Universität Bergakademie Freiberg

Herausgeber: H. Konietzky

Heft 2014-2

43. Geomechanik-Kolloquium

Freiberg • 14. November 2014

Freiberg 2014

Veröffentlichungen des Instituts für Geotechnik der TU Bergakademie Freiberg

Herausgeber: Prof. Dr.-Ing. habil. Heinz Konietzky

Anschrift: TU Bergakademie Freiberg
Institut für Geotechnik
Gustav-Zeuner-Straße 1
09596 Freiberg
Telefon: 03731 39-2458
Fax: 03731 39-3638
E-Mail: ifgt@ifgt.tu-freiberg.de
Internet: http://tu-freiberg.de/fakult3/gt/

Herstellung: Druckerei Wagner
Verlag und Werbung GmbH
Printed in Germany

Für den Inhalt ist der Autor allein verantwortlich.

ISSN 1611-1605

Table of contents

Applied rock mechanics in mining and tunnelling

Laboratory and field investigations

Salt mechanics / fracture mechanics

Waste repositories / Geothermal energy

More articles

Applied rock mechanics in mining and tunnelling

The Brenner Base Tunnel – project and status of realisation

Der Brenner Basis Tunnel – Projekt und Stand der Arbeiten

C. Reinhold
Galleria di base del Brennero - Brenner Basistunnel BBT SE

Abstract

The current traffic situation at the Brenner absolutely requires the development of a high-capacity transit connection between Austria and Italy. The Brenner Base Tunnel, a low-gradient railway running below the Brenner Pass, will be such a railway link between Innsbruck (Austria) and Fortezza (Italy). At 64 km, it will be the longest underground railway line in the world once it is finished. The tunnel system consists of two single track tunnels and an exploratory tunnel which is located between and below the main tubes. Beside the two portals Innsbruck and Franzenfeste, the access to the tunnel system is carried out by four additional access tunnels located sidewise. Furthermore, three emergency stations will be built along the tunnel route. Altogether, for the whole tunnel system a total length of more than 200 km tunnels and other cavities are to be excavated. First of all this paper will give an overview of the Brenner Base Tunnel project, presenting some interesting characteristics and details of the project. Geological and geotechnical conditions are explained in detail. Subsequently, the current progress of the works is shown. Finally, an overview of several research projects with geotechnical emphasis which are currently being carried out during the design and construction phases of the Brenner Base Tunnel will be given.

Zusammenfassung

Aufgrund der aktuellen Verkehrssituation am Brenner ist der Ausbau einer leistungsfähigen Transitverbindung zwischen Österreich und Italien zwingend erforderlich. Mit dem Brenner Basistunnel, einer Flachbahn unterhalb des Brenners, wird diese leistungsfähige Eisenbahnverbindung zwischen Innsbruck (Österreich) und Franzenfeste (Italien) geschaffen. Der Tunnel weist eine Länge von 64 km auf, womit die weltweit längste unterirdische Eisenbahnverbindung entsteht. Das Tunnelsystem besteht aus zwei eingleisigen Richtungsröhren und einem mittig unterhalb verlaufenden durchgängigen Erkundungsstollen. Der Zugang zum Tunnelsystem erfolgt neben den beiden Portalen in Innsbruck und Franzensfeste zusätzlich durch vier seitliche Zufahrtstunnel. Des Weiteren werden im Verlauf des Tunnels 3 Nothaltestellen errichtet. Insgesamt sind für das gesamte Tunnelsystem mehr als 200 km Stollen und Tunnel auszubrechen. Der gegenständliche Beitrag gibt zunächst einen Überblick über das Projekt des Brenner Basistunnels. Es werden einige interessante Besonderheiten und Details des Projektes vorgestellt. Die geologisch-geotechnischen Verhältnisse werden ausführlich erläutert. Darauf folgend wird der aktuelle Stand der Arbeiten dargelegt. Abschließend wird ein Überblick über

einige Forschungsprojekte mit geotechnischem Schwerpunkt gegeben, welche derzeit im Zuge von Planung und Bau des Brenner Basistunnels bearbeitet werden.

1 Project

1.1 History

The idea of building a flat rail route under the Brenner dates back to the time before the construction of the existing Brenner railway line (1859-1867). Strong traffic growth after the Second World War intensified the search for ways to build a base tunnel beneath the Brenner. In 1971, the International Union of Railways UIC defined the main European rail axes, which included the Munich-Verona Brenner axis. From the 1980s, development of the Trans-European Networks (TEN) began. In 1992, the Brenner base tunnel was classified as a priority project during the first presentation of the TEN networks. In 2005, the 30 TEN priority projects to be started before 2010 were presented, together with the required construction work. The Brenner Base Tunnel, as part of the TEN-1 Berlin-Palermo axis, was among these projects. The main project planning phases are as follows:

- 1987-1989 feasibility study
- 1999-2002 preliminary project
- 2005-2008 submission and EIA project
- 2009-2009 approval in Austria and Italy
- 18 April 2011, start of main construction phase

Since 21 December 2013, in accordance with EU Regulation 1315/2013, the Brenner Base Tunnel project forms part of the "Scan-Med" Scandinavia-Mediterranean North-South Corridor.

1.2 Current traffic situation at the Brenner:

Approximately 50 million net tonnes of goods currently cross the Brenner annually. This is equivalent to approximately 2 million trucks. This is distributed as around 35 million net tonnes by road and about 14 million net tonnes by rail. Because of the gradients on the existing Brenner railway line, three locomotives are needed for each freight train. Furthermore, owing to the different traction systems in Austria (15 kV 16173 Hz alternating current) and Italy (3 KV direct current), the locomotives have to be changed on the Brenner. In addition, approximately 242 passenger trains use the Brenner railway every day. The capacity limit is 260 trains per day.

1.3 Facts and figures

Figure 1 shows an overview of the tunnel system of the Brenner Base Tunnel. The Brenner Base Tunnel between Innsbruck (Austria) and Franzenfeste (Italy) has a length of 55 km. With the Innsbruck bypass, this will form the world's longest underground rail line, with a total length of approximately 64 km between Tulfes and Franzenfeste. The tunnel is designed as a two-tube system, each with a directional track. A special feature is the continuous exploratory tunnel, which is located centrally below the two main tubes. This will be constructed one section at a time in advance in order to explore the geological and geotechnical conditions. The exploration results flow directly into the planning of the main tunnels. Thus reduces the risk and also enables construction costs and construction times to be optimised. In the operating phase, the exploratory tunnel will be used as a drainage and maintenance tunnel.

The most important characteristics of the Brenner base tunnel are:

- Length: 55 km (Innsbruck-Franzensfeste) + 9 km = 64 km (Tulfes-Franzenfeste)
- 3 emergency stopping points (Innsbruck, St. Jodok and Trens), 4 side access tunnels (Ampass, Ahrental, Wolf and Mauls)
- Tunnel system overall length: approximately 230 km
- Gradient: 5 ‰ - 6.7 ‰
- High point (Austria-Italy border): 795 metres above sea level.
- Maximum overlying strata 1,800 m
- Excavated cross-section, main tubes: approximately 72 m²
- Excavated cross-section, exploratory tunnel: 26-49 m²
- Excavated cross-section, access tunnels: 100-120 m²
- Distances between cross passages: 333 m

1.4 Costs, risks and financing

In line with the ÖGG Directive (2005), the total costs of the Brenner Base Tunnel comprise the base costs B, the portion of costs for risks R, the portion of costs for slipping G and the portion of costs for valorisation V. The Brenner Base Tunnel costs were determined taking account of the risk provisioning of 8,455 million euros. The costs are distributed over approximately 60 % for the structural work, 14 % for equipment, 12 % for management and land and 14 % for risks. The risks involved fall into the three categories of technical risks, approval risks and administrative risks. Risks are currently divided into 45 % for identifiable risks and non-identifiable, non-quantifiable risks are 55 %.

The Brenner Base Tunnel is being co-financed by the European Union to the tune of 50 % for the conduct of studies, planning and construction of the exploratory tunnel. However, the share of the cost being borne by the EU for the construction of the main tunnel tubes is 30 %. The remaining amount will be divided equally between the governments of Austria and Italy.

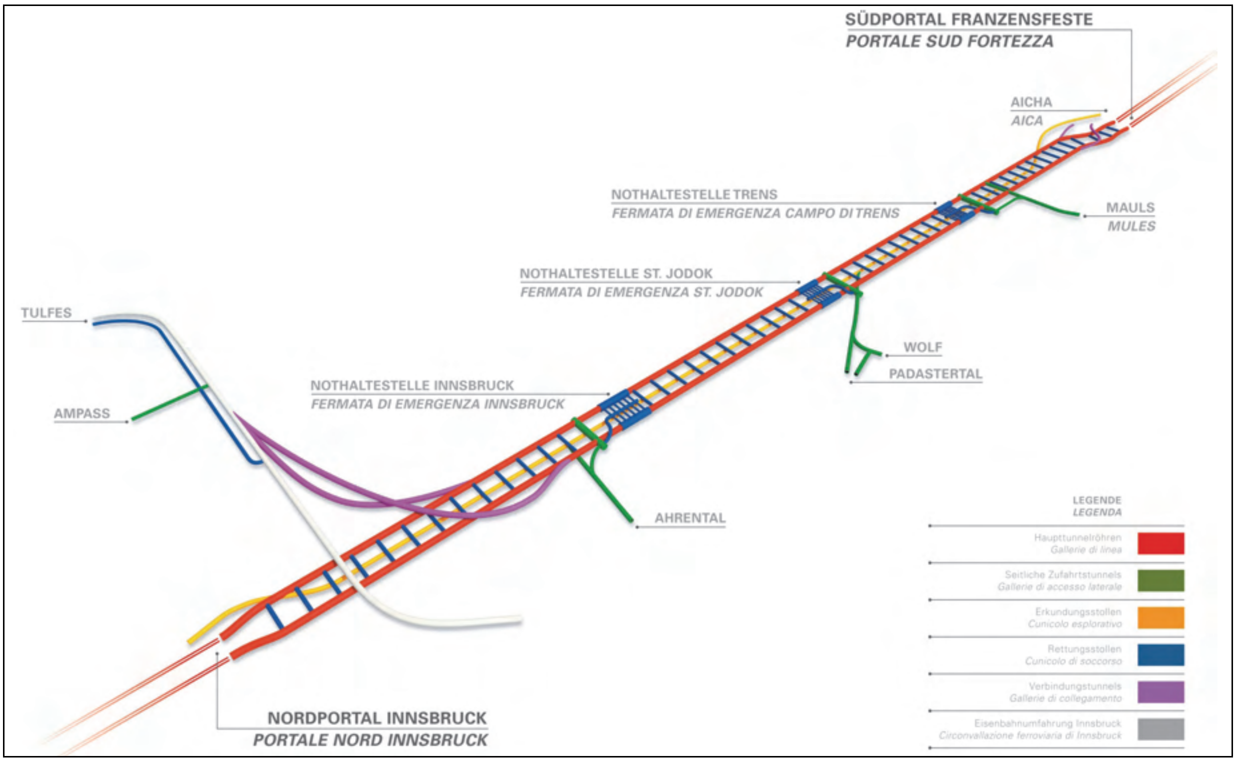

Fig. 1.1: Brenner-Base Tunnel – Site plan

1.5 Excavated material – disposal sites

The total volume of excavated material is approximately 15.5 million cubic metres in the re-compacted state. In order to minimise transportation routes, disposal sites have been placed directly at the portals of the access tunnels and, in the case of the Padastertal landfill, connected by means of a dedicated spoil tunnel. This means that no excavated material is transported via the public transport network.

1.6 Recycling of tunnel excavated material

For the Brenner Base Tunnel, targeted studies in the field of materials technology were conducted for the recycling of excavated material from the tunnel. Three utilization classes were defined for this

Class A) material that is suitable for use as a concrete aggregate

Class B) material that is suitable for use for embankments and backfills

Class C) recyclable material for final disposal in disposal sites

Based on prospection done during the submission phase, the recycling of approximately 25 % of the material excavated from the tunnel was possible. Only class A material was excluded when determining the required the disposal site volume. However, based on more recent materials technology investigations, it can now be assumed that it will be possible to use a significantly higher proportion as filling material and as a concrete aggregate (see Voit, 2013).

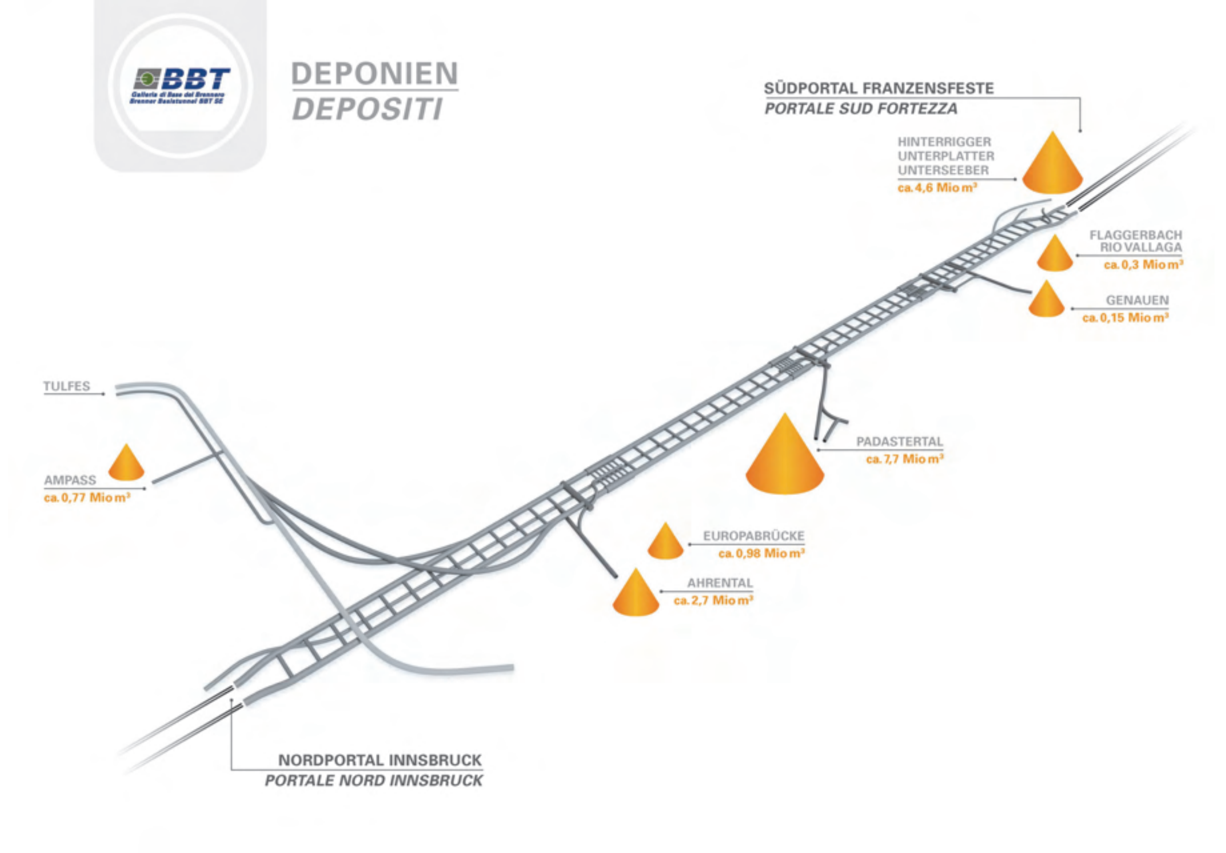

Fig. 1.2: Brenner Base Tunnel – disposal sites

1.7 Design Guide

Following approval of the construction phase, the entire project was subjected to basic optimisation in the course of cross-project design engineering. The aim was to create a uniform technical basis for further planning steps (specifications and detailed design). The main focus was on the following:

- Route planning review and adoption of all optimisation measures
- Incorporation of approval process regulations into the project documents
- Creating uniform normative foundations and technical specifications for tender planning and construction planning
- Developing principles for dimensioning and structural design for a service life of 200 years
- Preparing detailed interface and type plans
- Developing tolerance specifications compatible with surveying and construction methods
- Preparatory measures for rail engineering equipment

Furthermore, the entirety of the route planning for the project was converted from the UTM coordinate system to a project-specific coordinate system (BBT-TM) using a transverse Mercator projection. The average project altitude was defined at an orthometric height of 720 m, which corresponds to an approximate ellipsoidal height of 770 m. This means that track distortion is reduced to less than 2-3 mm per kilometre.

1.8 Geomechanical design team

Given the special nature of the exploratory tunnel at the Brenner Base Tunnel, a special geomechanical planning team was set up at BBT SE. This team, consisting of geologists, hydrogeologists and geotechnical engineers, is continuously analysing the data from the exploratory tunnel and transposing this data into geological and geotechnical design principles for the main tunnel. This guarantees that the BBT benefits from internal knowledge pooling and on-going internal knowledge building.

2 Geology and Geotechnics

2.1 Geology

In geological terms, the Brenner Base Tunnel passes through the central region of the Eastern Alps. The main geological zones and their main tectonic units along the tunnel route from north to south are as follows:

- Innsbruck quartz phyllite (lower austroalpine)
- Upper schist shell with predominantly Bündner schists (Tauern Window/Penninic zone), – partly folded with the lower schist shell
- Lower schist shell and central gneiss cores (Tauern Window/Helvetic zone)
- Upper schist shell with predominantly Bündner schists (Tauern Window/Penninic zone), – partly folded with the lower schist shell
- East alpine crystalline with thin Mauls Triassic
- Mauls tonalite lamella/Periadriatic fault zone
- Brixen granite (Southern Alps)

The relevant lithological units are the following:

- Innsbruck quartz phyllite: A metamorphic, schistose rock, which mineralogically comprises mainly quartz, mica and subordinate feldspar, and other constituents.
- Schist shell shale – Bündner schists for the most part: These are sedimentary and subordinate volcanic deposits in a marine trough, which were subjected to rock metamorphosis during the emergence of the Alps. A wide range of rocks is present, including limestone marble, calcareous slate, phyllite containing limestone and graphitic phyllite. There are also frequent green shale and paragneiss sections.
- Central gneiss: A metamorphic, crystalline rock, which initially sunk to deep levels during the formation of the Alps, was subsequently lifted up, and is now present on the surface. The central gneiss is mostly a pale, granite gneiss, which mainly consists of quartz, feldspar and mica.

- Granite: Modest, crystalline, medium-grained rock of magmatic origin, which is rich in quartz and feldspar and also contains slightly subordinated dark minerals, such as biotite.

Major fault zones:
Some fault zones occur on the route corridor, which are of both regional and supraregional geological significance.
The significant fault zone is the so-called "Periadriatic shear". It separates the Southern Alps from the Eastern Alps and the Southern Limestone Alps from the Austrian Central Alps respectively. The displacement values along this fault zone are estimated to be approximately 100 km. Displacements occurred in both the horizontal and vertical directions. Fault rocks such ultra cataclasite, foliated proto-cataclasite, proto-cataclasite, phyllite slate and black phyllite occur in the immediate vicinity of the fault zone. The overlay thicknesses in the fault zone area are between 400 and 700 m. The tunnel cuts through the fault over a length of approximately 600 m.

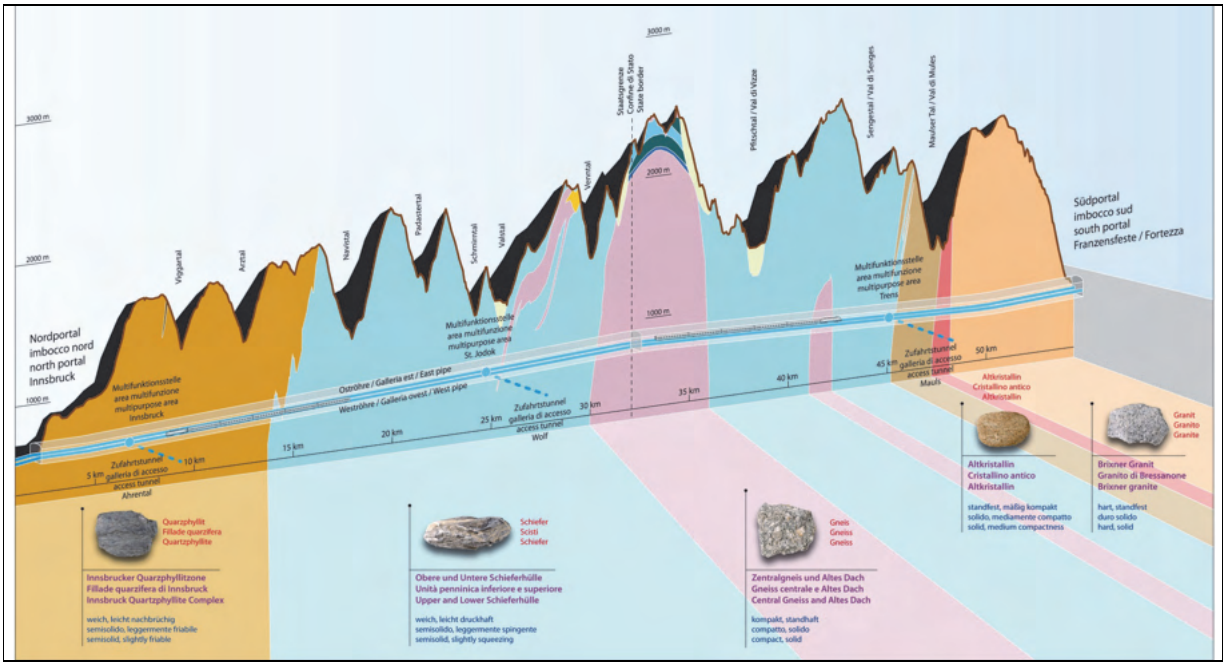

Fig. 2.1: Geological longitudinal section

Fault register:
All fault zones encountered in the exploration tunnel are detected and evaluated by the geomechanical design team by means of a fault register. Among other things, the following data is recorded:

- Location
- Sketch of tunnel face/photo of working face/horizontal section/ sketch perpendicular to the fault axis/schematic sketch of fault zone
- Orientation and stereographic representation of the fault zone
- Fault type and fault system allocation

- Geological description of rocks
- Total thickness of fault zone and distribution of fault rocks within the fault zone
- Water ingress and influence of water ingress on rocks
- Evaluation of geotechnical measuring devices within the fault zone (deformation measurements, etc.)
- Evaluation of the tunnelling data in the fault zone
- Features (e.g. failure of construction, overbreaks, etc.)

The data from the fault register will eventually be used as a basis for preparation of the geological-geotechnical fault zone model for the main tunnel prognosis.

2.2 Geotechnics

Methodology

The geotechnical design procedure is based on a geotechnical guideline, which was developed as part of the guide design phase. The aim in developing the guideline was, among other things, to harmonise geotechnical design between Italy and Austria, in order to be able to apply uniform planning standards as a geotechnical design basis on both territories. To achieve this, all rules, standards, codes and guidelines that were in force in the two countries were initially compared and evaluated for their harmonisation potential. As a result, it was decided to use the ÖGG Directive 2009, which applies in Austria, and the guidelines for the planning, tendering and construction of underground structures (SIG'97), which apply in Italy, as the primary references for the new project-specific guideline (BBT Geomechanical Directive) to be developed. The basic geotechnical planning process in this case comprises the steps as shown in figure 2.2.

Rock characteristics

Extensive laboratory tests were carried out during the initial exploration phases in order to determine rock characteristics. While the exploratory tunnel is being bored, sampling is carried out continuously and the collected samples are analysed in the laboratory. Two types of sampling are performed in the exploratory tunnel. In the "short test series", uniform lithological sampling is carried out every 250 metres. In the "long test series", uniform lithological sampling is carried out either every 1,000 m or whenever a new lithology is encountered. Table 2.1 shows the scope of the two test series. Table 2.2 and the chart in figure 3.3 give an overview of the main geotechnical characteristics of the main lithologies of the Brenner Base Tunnel.

Rock mass

Based on the geological model, homogeneous regions are defined by similar properties in terms of geological structure. A rock mass is defined by a geologically and geotechnically homogenous unit, which has the same or comparable properties. Together with large tectonic units, these also include structural geological units, hydrogeological boundary conditions, the state of stress of the rock, the rock mass / lithological unit and the geotechnical characteristics of the rock, as well as the rock mass and its discontinuities. All the characteristics that are required for the technical tunnel design are assigned to the rock mass.

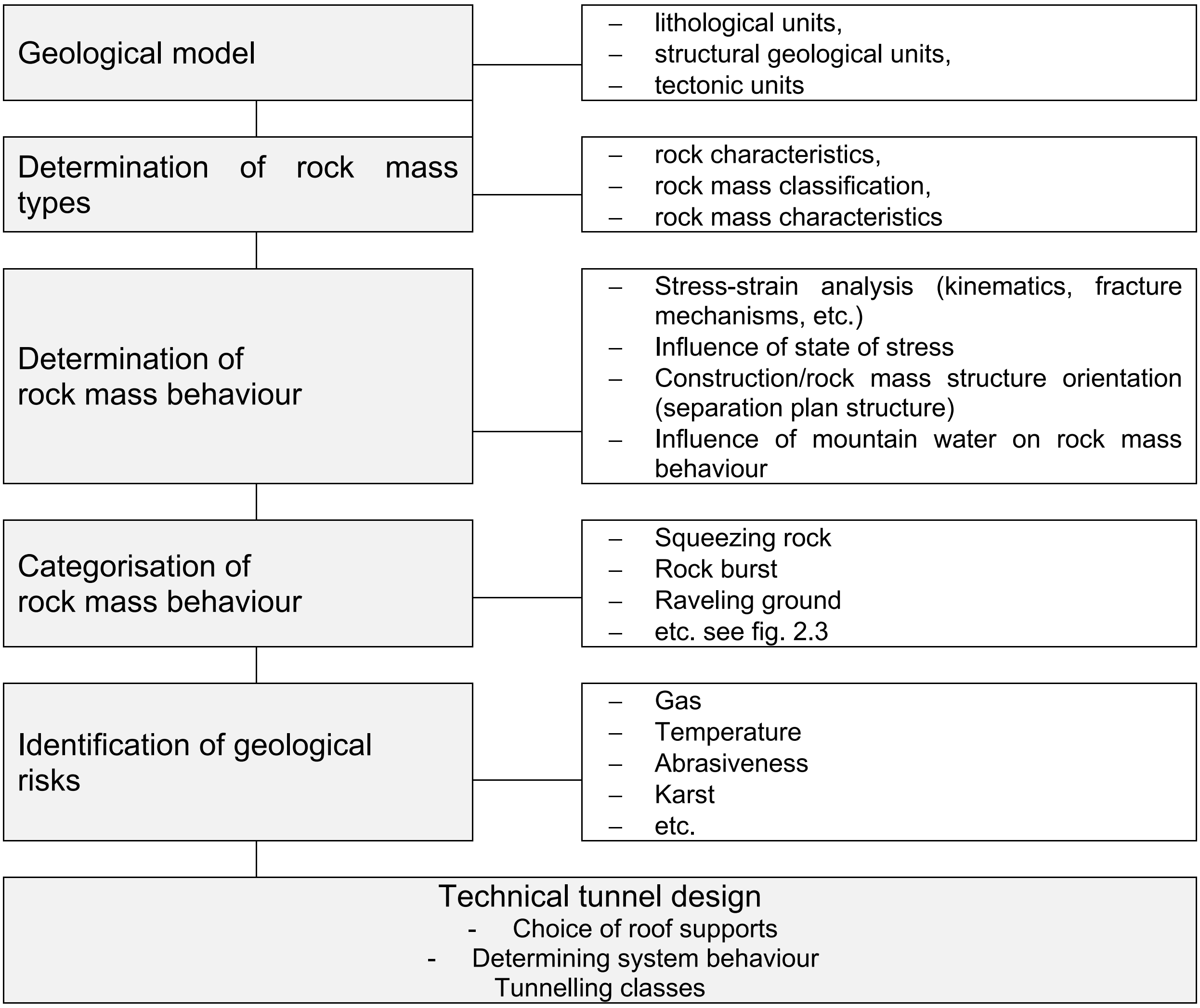

Fig. 2.2: Geotechnical planning process

The basic procedure for determining the rock mass properties can be described as follows:

- Evaluation of the geological model and pre-determination of geotechnically homogeneous areas based on tectonic units, lithological units and the derived geologically homogeneous areas.
- Evaluation of the available laboratory tests in order to determine rock and discontinuity properties.
- Assessment of the available in-situ experiments, e.g. for detecting the deformation modulus of the rock or of the primary stresses.
- Determining rock mass characteristics from the rock characteristics and the in-situ rock mass characteristics (GSI, RMR) using various methods according to current technological standards.
- Evaluation of cavities that have already been created under comparable geological and geotechnical conditions (e.g. evaluation of the tunnelling documentation for the exploratory tunnel).

- Final determination of geotechnically homogeneous areas, allocation of corresponding rock mass and geotechnical characteristics.

A four-part system is used to provide a clear rock mass type designation. This system comprises the tectonic unit, the lithological unit, the structurally geological homogeneous area and the associated structure designation. While the lithological unit describes the rocks, the structurally geological homogeneous area defines the discontinuities. The following example shows this four-part system for rock mass designation:

ZG	Gr	2a	EKS
Central gneiss	Granitic gneiss	Unit with discontinuity distribution nr 2a	Exploratory tunnel
Tectonic unit specifies the geologic main unit	Lithology specifies the main rock type and it's properties	Structural geological unit specifies the discontinuity distribution	specifies the associated structure

For the whole tunnel system, more than 300 rock mass types are relevant. Additionally more than 50 rock mass types for fault zones are to be considered.

Tab. 2.1: Scope of the standard test series in the exploration tunnel

Testing	Short test series		Long test series	
	isotropic	anisotropic	isotropic	anisotropic
Density/porosity/water content	-	-	3	3
Wave propagation speed	-	-	1	1
Uniaxial compression test	5	10	5	10
Triaxial compression tests	1	3	5	5
Splitting tensile test	1	3	3	6
MTT	-	-	1	1
Point load test	3	3	3	3
Shear strength of discontinuities	-	-	3	3
Thin sections	1	1	1	1
Equivalent quartz content	1	1	1	1
Cerchar	1	2	1	4
CLI + DRI	-	-	1	1

Tab. 2.2: Overview of the main geotechnical characteristics of some main lithologies of the Brenner Base Tunnel.

Lithology	Bulk density [kN/m³]	Compressive strength [MPa]	Modulus of elasticity [GPa]	Splitting tensile strength [MPa]	Quartz content [%]	Cerchar CAI [-]
Quartz phyllite	27	36	30	4.7	48	3.0
Calcareous schists	27	60	33	8.5	41	1.4
Graphitic phyllite	27	25	15	3.5	52	2.3
Gneiss	27	124	38	9.9	53	4.8
Granite	26	200	45	10.0	72	4.8

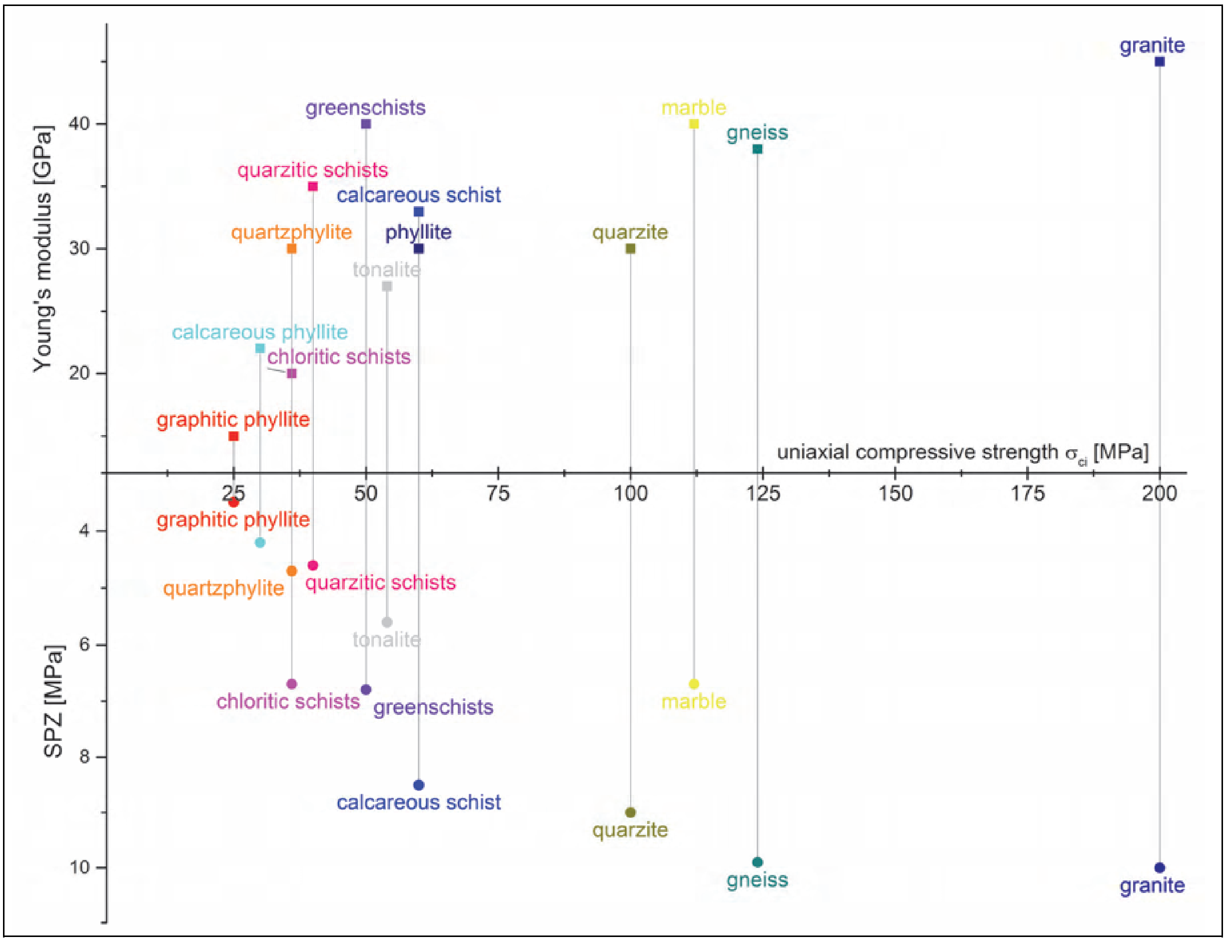

Fig. 2.3: Overview of the geotechnical parameters uniaxial compressive strength, Young's modulus and splitting tensile strength of some main lithologies of the Brenner Base Tunnel

Rock mass behaviour

Using the rock mass types as a starting point, the rock mass behaviour during cavity excavation must be used to determine the technical tunnel design. Potential failure mechanisms and hazard scenarios can then be determined and described. The rock mass behaviour for an unsupported cavity with full-circle mining of the tunnel heading is determined in this process. The following failure scenarios, essentially, apply to the Brenner Base Tunnel:

- small voluminous discontinuity controlled, gravity induced breakout of rock wedges
- breakout of voluminous, discontinuity controlled rock wedges, not only gravity induced, but also by exceeding shear strength of discontinuities
- Stress induced, shallow overstressing / plastication of the rock mass combined with discontinuity and gravity controlled failure
- Stress induced, profoundly overstressing / plastication of the rock mass („squeezing rock“) with large deformations
- Rock burst – rapid release of accumulated strain energy within highly stressed brittle rocks
- Crown failure – over breaks on the crown of the excavation associated with shear failure
- Ravelling ground – ravelling of frictional, poor interlocked soil with low cohesion
- Flowing Ground – ravelling of frictional, poor interlocked soil with high water content
- Swelling Ground

The Brenner Base Tunnel project-specific criteria for determining the rock mass behaviour have been defined for this (see Figure 2.3).

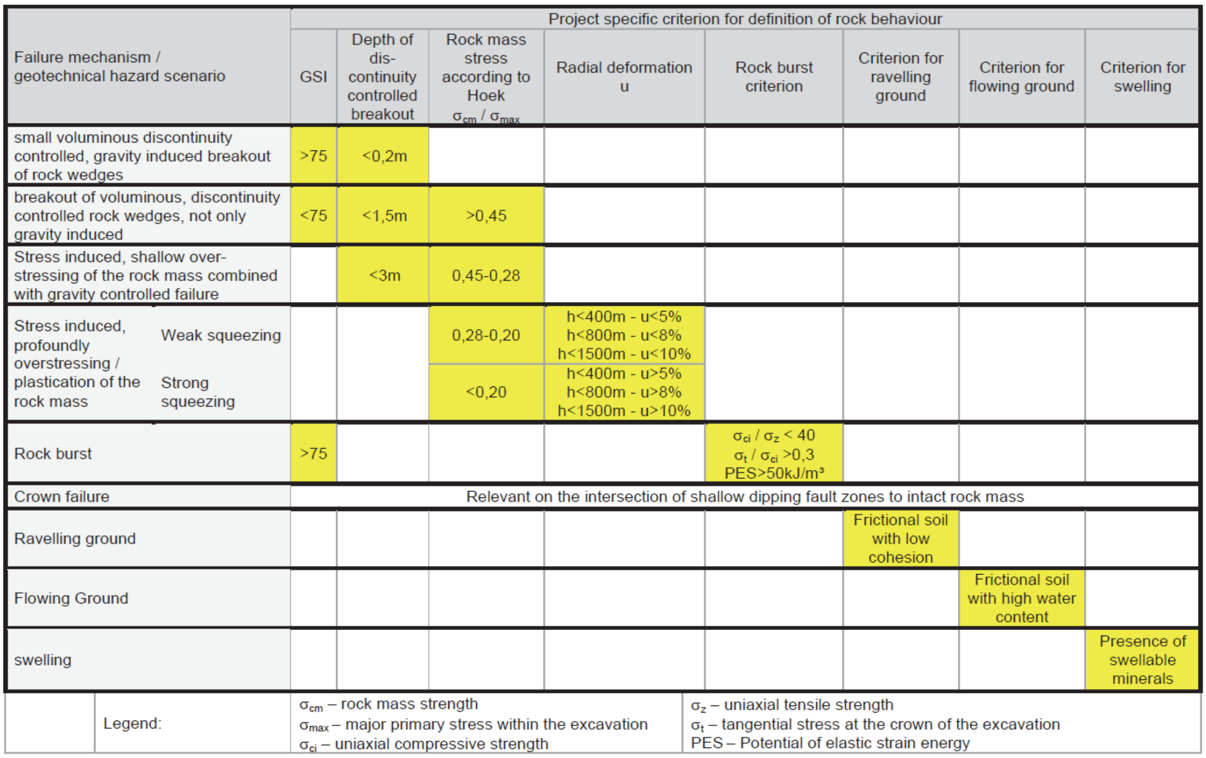

Failure mechanism / geotechnical hazard scenario		Project specific criterion for definition of rock behaviour							
		GSI	Depth of dis-continuity controlled breakout	Rock mass stress according to Hoek $\sigma_{cm} / \sigma_{max}$	Radial deformation u	Rock burst criterion	Criterion for ravelling ground	Criterion for flowing ground	Criterion for swelling
small voluminous discontinuity controlled, gravity induced breakout of rock wedges		>75	<0,2m						
breakout of voluminous, discontinuity controlled rock wedges, not only gravity induced		<75	<1,5m	>0,45					
Stress induced, shallow over-stressing of the rock mass combined with gravity controlled failure			<3m	0,45-0,28					
Stress induced, profoundly overstressing / plastication of the rock mass	Weak squeezing			0,28-0,20	h<400m - u<5% h<800m - u<8% h<1500m - u<10%				
	Strong squeezing			<0,20	h<400m - u>5% h<800m - u>8% h<1500m - u>10%				
Rock burst		>75				$\sigma_{ci} / \sigma_z < 40$ $\sigma_t / \sigma_{ci} > 0,3$ PES>50kJ/m³			
Crown failure		Relevant on the intersection of shallow dipping fault zones to intact rock mass							
Ravelling ground							Frictional soil with low cohesion		
Flowing Ground								Frictional soil with high water content	
swelling									Presence of swellable minerals

Legend:

σ_{cm} – rock mass strength
σ_{max} – major primary stress within the excavation
σ_{ci} – uniaxial compressive strength
σ_z – uniaxial tensile strength
σ_t – tangential stress at the crown of the excavation
PES – Potential of elastic strain energy

Fig. 2.4: project specific criterion for definition of rock mass behaviour

Brief description of the rock mass behaviour in the main units of the Brenner Base Tunnel:

- Innsbruck quartz phyllite (lower austroalpine):

The experience from the exploratory tunnel, 4 km of which has already been tunnelled in Innsbruck quartz phyllite, show rocks with only small-volume outbursts and small deformations. Because of the flat-lying foliation and steep fissured surfaces, the relevant unstable blocks occur in the ridges. With increasing proximity to the Tauern window and increasing overlay, it is to be expected that the rock mass behaviour will change to slightly squeezing rock. Three distinct fault zones have been excavated to date in the exploratory tunnel. All had an orientation that lay between a parallel and an acute angle with the tunnel axis, with steep inclination. In the fault zone areas, the rock mass behaviour can be described as slightly squeezing. An increase in deformation compared to the rock outside the fault zones was clearly measurable. Inside the fault zone areas, the support system was significantly damaged and subsequently had to be renovated.

- Bündner schists/Glockner nappe (Tauern window – Penninic)

The conditions in the Bündner schists area are variable. In addition to calcareous schist and limestone phyllite, areas with increased incidence of black phyllite are also predicted. In the calcareous schist/limestone phyllite areas, breakout of voluminous, discontinuity controlled rock wedges, not only gravity-induced, but also caused by exceeding shear strength of discontinuities to stress-induced, shallow overstressing/plastication of the rock mass combined with discontinuity and gravity controlled failure are expected. Where black phyllite occurs, lightly to heavily squeezing rock is forecast, depending on the black phyllite proportion. Triassic areas with anhydrite and rubblestone are also expected. Swelling rock is accordingly forecast in areas with anhydrite. In areas where the anhydrite is already worn out, non-cohesive and/or flowing rock masses are expected.

- Central gneiss Brenner massif (Tauern window/Helvetic zone)

Solid rock is generally expected in the central gneiss. However, a high potential for rock burst is predicted owing to the high overlying strata. Squeezing rock is only predicted in the Olperer fault

- Mauls tonalite lamella/Periadriatic fault zone

This area is characterized by fault material of varying formations. Ultra cataclasite, foliated proto-cataclasite, proto-cataclasite, phyllite slate and black phyllite in particular were encountered during exploratory boring and excavation of the exploratory tunnel. In conjunction with the high overlying strata of approximately 700 m in this area, the rock mass behaviour in the area can be described as heavily squeezing rock. It has not so far been possible to confirm the strong water inflow that was initially predicted based on the bores during excavation of the exploratory tunnel.

- Brixen granite (Southern Alps)

In the Brixen granite, solid rock formations are projected outside the fault zones. The tunnelling that has already been done in Brixen granite (the Aicha-Mauls exploration tunnel, Mauls access tunnel) confirms this. However, the excavation of the Aicha-Mauls exploratory tunnel has shown that massive fault zones are to be expected, even in the granite. An almost axially parallel fault zone, which had not initially been predicted, was thus encountered during the excavation. Although it is geologically relatively insignificant, this fault caused a complete failure of the support system and jamming of the tunnelling machine. This meant that tunnelling had to be stopped for a 4-month period.

3 State of progress

3.1 Completed work

Innsbruck area:

The tunnelling work on the Innsbruck-Ahrental exploratory tunnels started on 04 December 2009. Since then, about 4 km of exploratory tunnels have been excavated by drilling and blasting in the southbound direction. The 2.4 km long Ahrental access tunnel with a 120 m² excavated cross-section with a 10.5 % gradient was completed in October 2012 with the breakthrough of the Innsbruck-Ahrental exploratory tunnels. Immediately after the portal, the access tunnel passes beneath the A13 Brenner motorway with little overlying ground. The tunnel was driven here beneath running traffic using the pipe roof securing method. The Ahrental disposal site is immediately before the portal of the Ahrental access tunnel. This is being filled continuously with the excavated material from the tunnelling operation in the Innsbruck-Ahrental area.

The Ampass access tunnel, which is 1.4 km long and has an excavated cross-section of 55 m², was completed in June 2013. The portal area of the Ampass access tunnel had to be made to pass under the state road using the cut-and-cover method. The excavated material from the tunnelling operation was dumped at the Ampass South disposal site.

Wolf area:

In the Wolf area, extensive preparatory work was necessary before the actual excavation of the Wolf tunnel could be started. This meant that the Brenner federal road had to be moved in order to make room for the construction site area. An interchange to the Brenner motorway also had to be created in the Plon area. Extensive slope stabilization work, among other things, was required to make this possible. In summer 2010, the Wolf access tunnel was created with the passage under the existing Brenner railway line. A frame structure had to be created under running rail traffic for this purpose. As part of Wolf I construction lot, the Saxener tunnel, which is approximately 1 km long, was excavated to form a link between the Plon motorway junction and the Wolf construction site. The 700-metre-long Padaster tunnel connects the Wolf construction site to the Wolf South access tunnel to the Padaster Valley, and is designed as a supply and spoil tunnel. In the Padaster Valley, among other measures, the drinking water pipe supplying the Steinach community was moved outside the disposal site area in preparation for the Padaster Valley disposal site.

Mauls area:

The initial work on the Aicha-Mauls exploration tunnel was awarded in August 2007 and began in April 2008 with the mechanical boring of the 10.5-kilometre long section. The tunnel was completed with the breakthrough of the machine into the disassembly cavern at the end of the Mauls access tunnel in February 2011.

The construction site area, several deposit areas and noise control measures were initially set up in cramped conditions to the south of the village of Mauls. The 1.8-km-long Mauls access tunnel, with an excavated cross-section of approximately 90 square metres and a gradient of 8.5 % was created by drilling and blasting through the Brixen granite, and was completed in 2009. Furthermore, during the Mauls II construction lot the starting and logistics caverns were excavated for the mechanized tunnelling in the Franzensfeste direction. These caverns have an excavated cross-section of approximately 350 m².

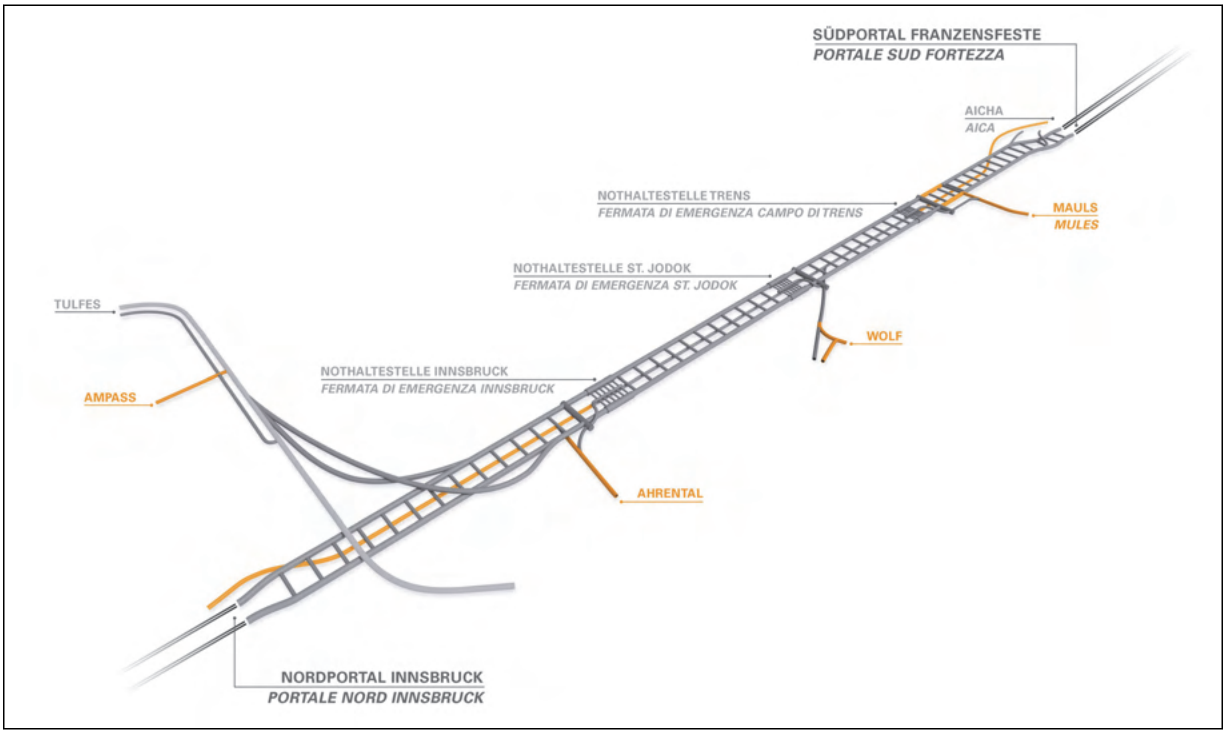

Fig. 3.1: Presently already finished excavations

3.2 Ongoing work

Innsbruck area:

As part of the Tulfes-Pfons construction lot, which is currently in the initial stages, the rescue tunnel is being excavated parallel to the existing Innsbruck bypass tunnel, as are the two connecting tunnels, approximately 15 km of exploration tunnel from Ahrental south to Pfons and the Innsbruck emergency stopping point.
Furthermore, the Patsch ventilation shaft is being constructed in the Patsch area, while the ventilation cavern is being constructed in the Ahrental access tunnel.

Wolf area:

As part of the Wolf II – Padaster Valley construction lot, the 4-km long Wolf South access tunnel, including several cavern constructions for ventilation and spoil removal, is currently being excavated. Furthermore, at present, further preparations are being made for the installation of the Padaster Valley disposal site. This will also comprise a 1,360-metre long diversion tunnel through which the Padasterbach stream will be diverted during construction of the Padaster Valley disposal site, including all barriers and driftwood gratings.

Mules area:
As part of the Mules II construction lot, work is currently being carried out on the excavation through the Periadriatic fault zone in the southern section of the exploratory tunnel. The aim is to complete the excavation of both the exploratory tunnel and the two main tunnels in the Periadriatic fault zone area by early 2015.

Passage under the Isarco/Fortezza area:
Work on the "Isarco underpass" has been functionally tendered and awarded across Europe. The plans for the construction work are currently being drawn up.

3.3 State of progress summary

Of the total of more than 200 km of access tunnels, exploratory tunnels, main tunnels, cross passages and other underground structures to be constructed, approximately 35 km had been excavated by mid-2014.

4 Geotechnical Research as part of planning and construction

The BBT SE also means to create scientific added value with the Brenner Base Tunnel project. New topics are therefore being addressed and the development of new technologies supported as part of the project. Work is being carried out on both internal BBT SE research projects and several other research projects in collaboration with external research partners. The following geotechnical/geomechanical issues, among others, are currently being researched:

Determining fault zone values by back analysis
Determining rock mass characteristics applicable to fault zones as the basis for the tunnel design is often ineffective. More than 33,000 m of exploration drillings were drilled to a depth of 1,500 m for the Brenner Base Tunnel preliminary exploration. Fault zones and their varying configurations were investigated during this process. However, it was almost impossible to determine the geomechanical characteristics applicable to these fault zones. On the one hand, it has proven difficult, or even impossible, to obtain fault material that is suitable for geotechnical laboratory tests. On the other hand, because of the heterogeneity of the faults, only rock mass characteristics that are difficult to actually apply can be derived from the laboratory results (rock characteristics). However, the exploration tunnel being excavated ahead of the main tubes of the Brenner Base Tunnel provides the ideal opportunity for estimating rock mass characteristics by back analysis. The rock mass parameters of the fault zones can be obtained from the back analysis results. These parameters are then incorporated directly into the planning of the main tubes as input parameters. Figure 4.1 gives an overview of the back analysis procedure based on two fault zones. Geological documentation that is almost complete was produced during excavation of the exploratory tunnel. If a fault zone is excavated, a geological model of the fault zone is initially developed based on the geological documentation results (Figure 4.1, top). The geological model includes the fault zone orientation, internal structure (fault rocks), dimensions, etc. In addition, a project-specific classification scheme for fault materials was developed (see Reinhold, Töchterle, 2013). The geological model of the fault zone is then transferred to a geotechnical model in a second step (Figure 4.1, centre). A breakdown into core zone and damage zone is undertaken to the extent possible. The history of the entire tunnelling processes is

also evaluated in this step. This comprises evaluating the temporal sequence of excavation and support installation, as well as evaluating the geotechnical measurements.

ESI-f2088		ESI-f4158	
Geological model based on geological face documentation (sketch perpendicular to the fault axis and horizontal section)			
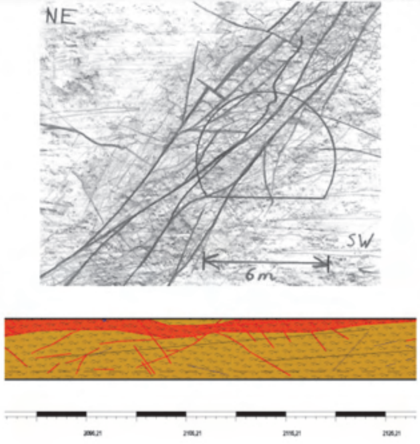		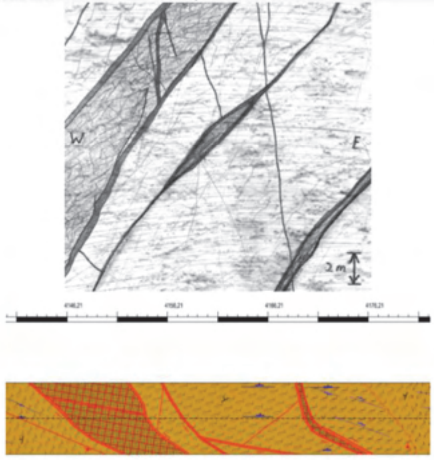	
Composition of the fault zone and thickness			
Core Zone	Damage Zone	Core Zone	Damage Zone
fprc 90%, fg 10%	jrm 70%, fprc 20%, fg 10% (GSI 25-30)	fprc 90%, fg 10%	jrm 80%, fprc 10%, fg 10% (GSI 30-35)
3 m	5,5 m / 5,5 m	5,5 m	10,5 m / 1 m
Geotechnical model			
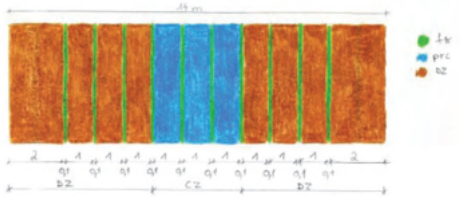		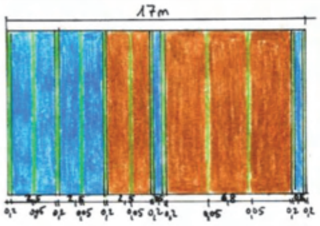	
Overburden: 300 m		Overburden: 690 m	
Calculation model			
2D numerical		3D numerical	
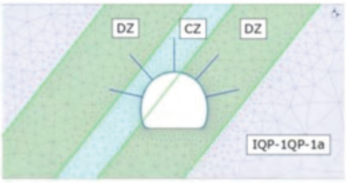		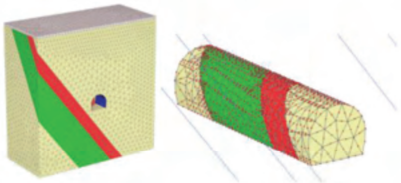	
Calculation results – geomechanical fault zone parameters			
Core Zone	Damage Zone	Core Zone	Damage Zone
E = 400MPa	E = 1000MPa	E = 600MPa	E = 1000MPa
c = 0,15MPa	c = 0,45MPa	c = 0,30MPa	c = 0,50MPa
φ = 25°	φ = 26°	φ = 26°	φ = 28°

Fig. 4.1: Back analysis modelling of fault zones using the example of two fault zones in the Innsbruck-Ahrental exploration tunnel

In the next step, the geotechnical model finally has to be transferred to a suitable calculation model (Figure 4.1, below). Depending on the boundary conditions, various calculation methods (rock mass characteristic curve, 2D numerical, 3D numerical) are applied. An overview of back analysis calculations that have been performed in the Innsbruck-Ahrental exploration tunnel section can be found in Reinhold, Töchterle (2013).

Development of a constitutive law for rock masses in deep tunnels

A key aspect in the use of finite element calculations for rock mechanical purposes is the modelling of the constitutive behaviour of the rock mass. Intact rock shows a complex nonlinear mechanical behaviour which is quite similar to concrete. The well-known constitutive models for rock, like Hoek-Brown or Mohr-Coulomb, exhibit some shortcomings. The development of irreversible deformations in the prepeak regime as well as strain softening in the post peak regime as exhibited in laboratory tests cannot be modelled. Furthermore the degradation of stiffness associated with strain softening is neglected. Although it is well known that deformation properties depend on the hydrostatic pressure, usually linear elastic behaviour is predicted for predominantly hydrostatic compression. These shortcomings have been the motivation for a cooperative research project of the Brenner base Tunnel association BBT-SE and the Unit for Strength of Materials and Structural Analysis of the University of Innsbruck. Within this currently running research project an advanced 3D constitutive model for rock mass will be developed, which allows for reliable numerical simulations of deep tunnel excavations. The developed rock mass model is based on a constitutive model in the framework of continuum mechanics – an isotropic damage plasticity model. This model is based on the combination of linear elasticity, single surface plasticity with nonlinear isotropic hardening, non-associated plastic flow and isotropic damage describing strain hardening. Furthermore hardening is predicted for both shear and hydrostatic loading. The model is calibrated on extensive field investigations conducted during excavation of the exploratory tunnel. Detailed information about the model and the research project is given in Unteregger et. al. (2014).

Detection of pre-deformation ahead of the tunnel face

Pre-deformation is the proportion of rock deformation that appears before the zero measurement of the usual convergence measurements that accompany tunnelling. This consists of both deformation proportions ahead of the tunnel face and non-measurable deformation proportions behind the tunnel face up to the zero measurement of the convergence measurement points. In conventional tunnelling, the convergence measurement points are incorporated after the excavation and initial shoring at a defined distance behind the tunnel face. The zero measurement of this measuring bolt is usually made before the next blasting round. These measuring bolts are used to measure all the deformations that the support system is subjected to during further tunnelling. These deformations consist of two important parts: Firstly, the deformations resulting from immediate further tunnelling produce stress redistribution by longitudinal carrier effect in the axial direction. Secondly, deformations that appear from the excavation of the cross-section in which the measuring point is located owing to delayed development (time-dependent deformation behaviour of the rock). Any analysis of these deformation components is made almost impossible because of fast tunnelling progress. Numerical simulations of deformations are therefore usually made using theoretical approaches. These are often based on the evaluation of three-dimensional numerical calculations. Knowledge of the pre-deformation is of crucial importance in the design of the support system. The later the support system is installed, the greater the deformations that have already subsided and the lower the required resistance of the support system. The detection of deformations is of even greater importance in mechanical tunnelling. Pre-deformation has a significant influence in the machine type selection decision (open machine or shield machine). For shield machines in particular, the proportion of deformations occurring immediately behind the cutter head is of particular importance, since they indicate the risk scenario of the cutter head jamming. Knowledge of the deformations is therefore a decisive factor, which must be evaluated. This applies in particular to the Brenner Base Tunnel construction projects, in which a majority of the tunnels and galleries are to be excavated mechanically.

BLA laboratory correlation

The engineering fracture theories and constitutive equations that are commonly used in geotechnical engineering are usually based on an elastoplastic approach. This means that characteristic values are required for both the elastic component and the plastic component (failure mode) in order to describe the material behaviour of soil and rock. The elastic component and the identification of the relevant parameters specifically are taken into account in the BBT-SE internal project. The elastic parameters can be determined by means of laboratory tests, such as unconfined compression tests or triaxial tests, as well as in-situ tests, such as dilatometer tests. For each of these tests, several evaluation methods exist worldwide. The results show significant differences, depending on the evaluation method used. The difficulty for the geotechnical engineer in the course of geotechnical design now consists of defining the corresponding characteristic values based on the experimental results. The most common evaluation methods for the individual tests are initially compared during the project. The main focus is finally placed on comparing the results, the elastic characteristics from the laboratory and in-situ testing. A variety of laboratory and field tests were conducted as part of the Brenner Base Tunnel exploration. These were fully incorporated into the evaluation. This means that, currently, approximately 70 dilatometer tests at depths of up to 1,000 m, more than 100 uniaxial compression tests and more than 100 triaxial tests have been evaluated and examined for interrelationships. Various correlations between the results of laboratory tests and field tests were found. The first results are expected to be published to experts in 2015.

Evaluation of rock mass parameters without the use of a rock mass classification system

For the geomechanical design of tunnels in rock, knowledge of the mechanical properties of the groundmass as input parameters for static analysis is of crucial importance. As part of the planning approval of the Brenner Base Tunnel, the rock mass was classified using, among other things, the GSI and rock mass parameters determined from the characteristic values obtained from rock core samples using the known Hoek/Brown method. Meanwhile, the exploratory tunnel was driven to several kilometres and the findings from it were geomechanically evaluated. This has shown, in particular, that the rock mass characteristics determined using the GSI method are not applicable and that actual rock mass behaviour with these characteristics cannot be detected. The problems of determining rock mass parameters were then analysed. The known problems that arise in the conversion of rock characteristics via the GSI based on empirical formulas have been discussed and published frequently within the professional world (e. g. Anagnostou, Pimentel 2012). The fact that the proposed method has no scientific basis in particular has been criticised and the accuracy of the method has been called into question. Further problems were also determined during internal investigations, in particular regarding the application of the GSI method in strongly foliated rocks. As part of an internal BBT SE research project, intensive work is currently being carried out on a method in which rock mass characteristics can be determined without using a classification system.

5 References

Anagnostou, G.; Pimentel. E. (2012): Zu den Felsklassifikationen mit Indexwerten im Tunnelbau. Geotechnik 35, pp 83-93

Bergmeister, K. (2011): *Brenner Basistunnel – Der Tunnel kommt.* Tappeinerverlag – Lana

Brandner, R.; Reiter, F.; Töchterle, A. (2008): *Überblick zu den Ergebnissen der geologischen Vorerkundung für den Brenner Basistunnel*. Geo.Alp, Vol. 5, pp 165-174

Burger, U.; Kirsch, A.; Marcher, T.; Reinhold, C. (2013): *Geologisch-geotechnischer Planungsprozess von Tunnelbauten mit Schwerpunkt tiefliegender Tunnel.* In: Beton-Kalender 2014: Unterirdisches Bauen, Grundbau, Eurocode 7, pp 37-62

John, A.; Reiter, F.; Skuk, S.; Venturi, G. (2007): *Geotechnische Aspekte für den Bau des Brenner Basistunnels*. BBT-Symposium; S. 13-23

ÖGG-Richtlinie (2009):*Richtlinie für die geotechnische Planung von Untertagebauten mit zyklischem Vortrieb*. Salzburg

ÖGG-Richtlinie (2005): *Kostenermittlung für Projekte der Verkehrsinfrastruktur unter Berücksichtigung relevanter Projektrisiken*. Salzburg

Töchterle, A. (2011): *Aspects of the geological evolution of the northwestern Tauern Window*. Dissertation University of Innsbruck, 2011

Töchterle, A.; Schierl, H.; Reinhold, C.; (2013): *Ingenieurgeologische Charakterisierung von Störungszonen im Innsbrucker Quarzphyllit.* Extended Abstracts zum Workshop „Characterization of Fault Zones“ der österreichischen Gesellschaft für Geomechanik, 09.10.2013, Salzburg, S. 6-12

Reinhold, C.; Töchterle, A. (2013): *Ermittlung der geomechanischen Kennwerte von Störungszonen im Innsbrucker Quarzphyllit auf Basis der Erkundungsergebnisse beim Brenner Basistunnel.* Veröffentlichungen der 19. Tagung für Ingenieurgeologie und des Forums für junge Ingenieurgeologen, München, 13.-15. März 2013, 20.-24.09.2009, pp 95-100

Unteregger, D.; Hofstetter, G.; Burger, U.; Reinhold, C.; Rieder, A.; Weifner, T. (2014): *Constituive modeling of rock mass in deep tunnels*. Proceedings of Brenner congress 2014, pp 189-194

Voit, K. (2013): *Einsatz und Optimierung von Tunnelausbruchmaterial des Brenner Basistunnels.* Dissertation Universität für Bodenkultur, Wien

TBM Tunneling in Deep Underground Excavation in Hard Rock with Spalling Behavior

TBM Tunnelvortrieb für tiefliegende Auffahrungen im Hartgestein mit Spödbruchcharakter

G. Barla
Politecnico di Torino, Italy

Abstract

It is shown that for an accurate TBM excavation design the complex interaction between rock, tunnel machine and its system components and tunnel support can be analyzed through a 3D finite element model. A 3D simulator recently developed is presented with reference to two rock mass conditions which may characterize deep underground excavation, i.e. squeezing and spalling. In this paper spalling is considered. Two case examples are discussed with reference to the Alpine Base Tunnels: the Lyon-Turin tunnel (between Italy and France) and the Brenner tunnel (between Italy and Austria). Brittle failure in the Ambin Massif (Gneiss and Micaschist) and in the Brixner Granite respectively are analyzed. The results obtained show that the 3D model implemented is effective in reproducing the rock mass response and its interaction with the TBM components and may contribute effectively to TBM excavation design.

Zusammenfassung

Es wird gezeigt, dass für ein korrektes TBM-Design die komplexe Interaktion zwischen Gebirge, TBM mit ihren Systemkomponenten sowie dem Ausbau mittels 3D-Finite-Elemente-Berechnungen analysiert werden kann. Ein kürzlich entwickelter 3D-Simulator wird vorgestellt mit Anwendung auf zwei unterschiedliche Gebirgsbedingungen, die tiefliegende Auffahrungen charakterisieren: drückendes und brechendes Gebirge. In diesem Beitrag wird nur brechendes Gebirge betrachtet. Die Anwendung wird an zwei Projekten der alpinen Basistunnel diskutiert: dem Lyon-Turin-Tunnel (zwischen Italien und Frankreich) sowie dem Brenner-Tunnel (zwischen Italien und Österreich). Sprödbruchverhalten im Ambin-Massiv (Gneis und Glimmerschiefer) und in den Brixener Graniten werden analysiert. Die Resultate zeigen, dass das implementierte 3D-Modell in der Lage ist, das Verhalten des Gebirges und seine Interaktion mit der TBM zu reproduzieren und zu einem effektiven TBM-Design beizutragen.

1 Introduction

Tunnels to be excavated to a depth greater than 1000 m and with lengths in excess of 10 - 15 km, in complex geological, hydrogeological, and geomechanical conditions, represent significant challenges in providing, prior to excavation, reliable geological and hydrogeological models, appropriate understanding of ground behavior (including the rock mass parameters), selection of the excavation/construction method to be adopted, and design and optimization of the tunnel support in short- and long-term conditions. This has been and presently is the case of the deep tunnels constructed to cross the European Alps, with mountains in height up to 4800 meters and a width of about 150-200 km.

The first tunnels (Frejus Railway, Gotthard Railway, Lötschberg, Simplon, Arlberg), constructed in the second half of the 19th century with overburden of 700-2100 m, were located such that tunnel length and overburden were minimized. The Alpine tunnels constructed today cross the mountain belt at the elevation of the main cities and are longer (up to 57 km) and deeper (up to 2500 m) than all tunnels constructed before (Fig.1.1). As the first railway and traffic tunnels could in general be excavated successfully by conventional methods, although with unexpected ground behavior which in cases led to severe delays and cost overruns, the new base tunnels need preferentially be excavated by using TBMs (Tunnel Boring Machines).

One is aware that the use of the TBM in severe ground conditions has not always been successful and negative experiences which resulted in cases in very low rates of advancement and even TBM entrapment are well known (the Yacambu-Quibor tunnel (Hoek and Guevara, 2009) or the Headrace Tunnel of the Gilgel Gibe II Hydroelectric Project (Barla, 2010) can be mentioned). However, the improved technology has permitted impressive development in the last decades, including large diameter TBMs, decreased dependence on ground conditions, new cutting technology and efficient auxiliary processes. Thus, there is no question today that long deep tunnels such as the Alpine Base Tunnels need be excavated by systematic mechanized tunneling.

For the design of mechanized tunneling, the complex interaction between the rock mass, the tunnel machine and its system components, and the tunnel support has to be analyzed in detail and three-dimensional numerical models including all these components are suitable to correctly simulate this interplay. This lecture will describe an advanced 3D model which has been recently developed for the detailed simulation of TBM excavation, with specific problems in mind as in the case of excavation of deep tunnels through rock masses which exhibit either spalling or squeezing behavior (Barla et al., 2011; Zhao et al., 2012).

Following a few preliminary remarks on the latest improvements in TBM technology and the presentation of the main features of a TBM of reference for this lecture, the 3D model is described. Then, a short introduction to the hazard scenarios during tunnel excavation will be given, with a special attention to spalling. Two case examples are finally discussed with reference to the Alpine Base Tunnels: the Lyon-Turin tunnel (between Italy and France) and the Brenner tunnel (between Italy and Austria).

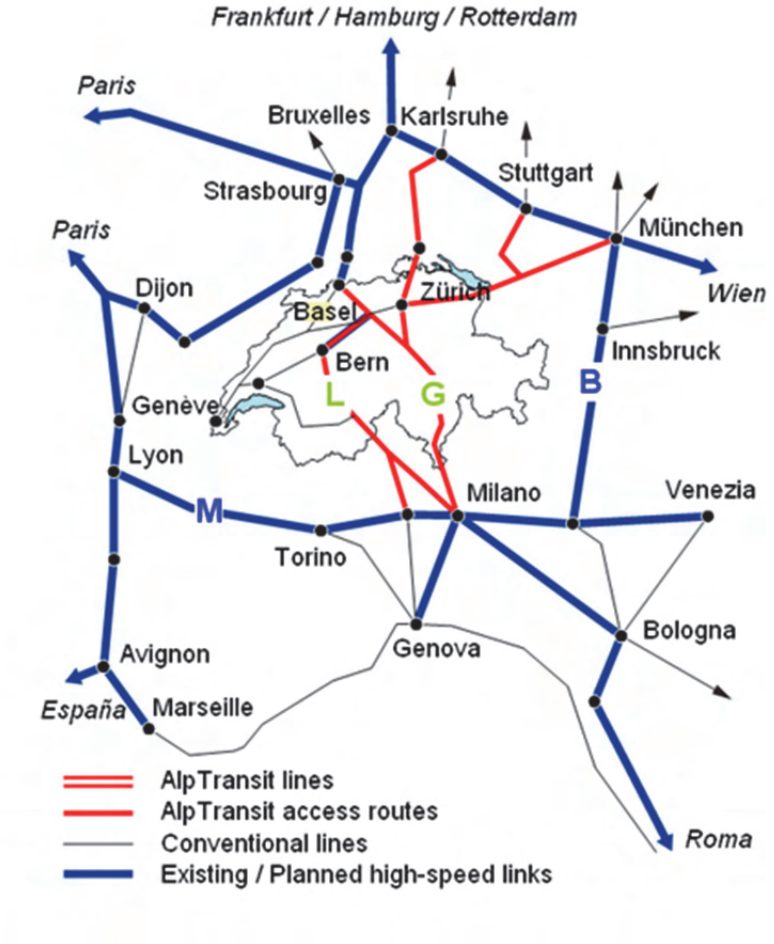

Fig.1.1: AlpTransit Base Tunnels and High-Speed Railway Links under the Alps (L: Lötschberg Base Tunnel, G: Gotthard Base Tunnel, M: Lyon-Turin Base Tunnel, and B: Brenner Base Tunnel).

2 Remarks on TBM tunneling

TBMs can be grouped into three main categories: Gripper TBM (i.e. Open TBM), Single Shield TBM and Double Shield TBM.

The Gripper TBM (Fig. 2.1 a) is suitable for all the rock conditions, provided that a minimum ‘‘stand-up’’ time is available for installing the support behind the cutter head. Over the years, two different clamping systems have been developed, single clamping and double clamping. Sometimes a cutter head shield can also be used to protect the crew from isolated rock falls.

The Double Shield TBM (Fig. 2.1 b), which is the type of machine to be considered for application in this lecture, has come into fairly common use in rock tunnels. It consists of the front shield with a cutter head, main bearing and drive and a gripper shield with clamping unit (gripper plates), tail shield and auxiliary thrust cylinders. Both parts are connected by a section (the telescopic shield) with telescopic thrust cylinders, which operate as the main thrust cylinders.

The basic principle is that the machine is clamped radially to the tunnel wall through the grippers and the excavation and installation of the segmental lining are performed at the same time. Where the rock is weak and it is not possible to clamp radially through the grippers, the necessary thrust forces can either be provided by the telescopic cylinders or by the auxiliary thrust cylinders.

In the first mode with the telescopic cylinders, the auxiliary cylinders only transfer the thrust forces to the segmental lining. In the second mode, which is also called single shield mode, the front and gripper shield form a rigid unit and the auxiliary cylinders produce the necessary forward thrust (Maidl et al, 2008).

The capability of the Double Shield TBM design was clearly demonstrated at the end of the 80s when it was used in the Channel Tunnel. In 2000, the design was completely reviewed and improved with the introduction of the Double Shield Universal (DSU) TBM, in order to cope also with important and rapid developing squeezing phenomena and very unstable tunnel faces as typical for flowing ground conditions.

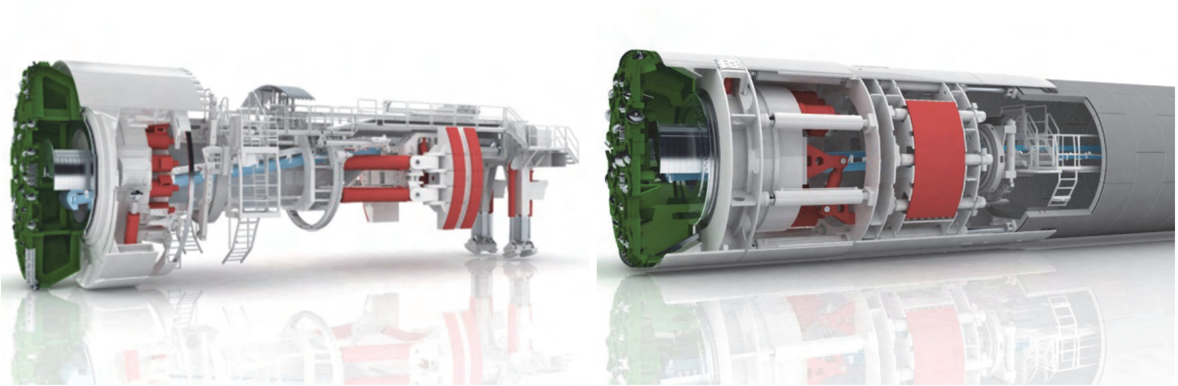

(a) (b)

Fig. 2.1: TBMs: (a) Gripper TBM; (b) Double Shield TBM (from Herrenknecht website: www.herrenknecht.com).

3 Remarks on geological/geomechanical hazards

The major geological/geomechanical hazards encountered during deep tunnel excavation relate to the prediction and behavior of faults at depth, heavy water inflows and high water heads, in heterogeneous fractured or karstified rock masses, stress-induced brittle failures (spalling and rockburst), plastic shear failure and squeezing of weak rocks (mainly fractured schists, phyllites and cataclastic fault rocks), instability of the excavation face and sidewalls, exceptional stress anisotropy, karstification of evaporites and limestones in relation to regional groundwater circulation systems and other hydrogeological problems (Loew et al., 2010).

Brittle failure, which is to be considered in the following, is a typical hazard which is difficult to be anticipated at the design stage and may pose challenging problems during construction, affecting the performance of TBM excavation. In such conditions, considerable uncertainties and many unresolved issues are present so that reliable predictions become very difficult. Nearly a half century ago, mines began to experience a form of rock damage called “spalling” in which apparently intact rock walls fractured into slabs, typically in a symmetrical pattern, parallel to the excavation boundary and to the far-field maximum compressive stress.

These slabs can range in thickness from a few millimeters to tens of centimeters and with large openings can be several square meters in surface area. In unsupported conditions and under anisotropic *in situ* stress field, spall progression results in the formation of a v-shaped notch, regardless of the original opening shape or size that deepens as the tunnel advances until steady-state conditions are reached (Martin, Kaiser and McCreath, 1999).

This failure mode can create a significant safety hazard for workers immediately behind the shield. Gripper problems and machine operations delays can result when a vertically dominant stress leads to substantial wall spalling and overbreak in front of the grippers (Fig. 3.1). The interaction with subtle structure in the rock mass can lead to delayed release of spall damaged ground. In extreme cases, this delayed release can be associated with significant energy release in the form of a rockburst. Spalling and bulking within the TBM shield can even lead to jamming of the shield. Spalling can also happen at the tunnel face, if enhanced with face-parallel foliation.

Rock formations prone to spalling are principally granite, granodiorite, gneiss, quartzite and more foliated metamorphic rocks, but also many weaker rock types such as lightly cemented sandstones, clay shale, mudstones, etc., do often fail in a brittle manner if they have few joints.


(a) (b)

Fig. 3.1: Severe operational issues (gripper pads cannot be seated on the sidewall) associated with overbreak (notch) in the Lötschberg Base Tunnel (Loew et al., 2010).

4 3D Model for simulation of mechanized excavation (TBM)

A completely 3D simulator of mechanized excavation in deep tunnels has been recently developed (Barla et al., 2011; Zhao et al., 2012) by using the finite element method and the midas GTS computer code. This simulator is intended to be more general than previous 3D models and allows one to consider both hard rock and weak rock conditions. The presence of water pressure and consolidation problems are not yet taken into account. The focus is on the mechanical behavior of the rock mass and on the interaction between the rock mass and the TBM and the support components.

Under the assumption of symmetry with reference to a vertical plane through the tunnel axis, the finite element model as developed consists of 8-nodes hexahedron solid elements and considers only half of the entire domain (Fig. 4.1). The *in situ* state of stress is applied as a uniform initial stress without consideration of the free ground surface and of the stress gradient due to the gravity. The three principal stresses can be input independently and this is one of the important advantages of a 3D model.

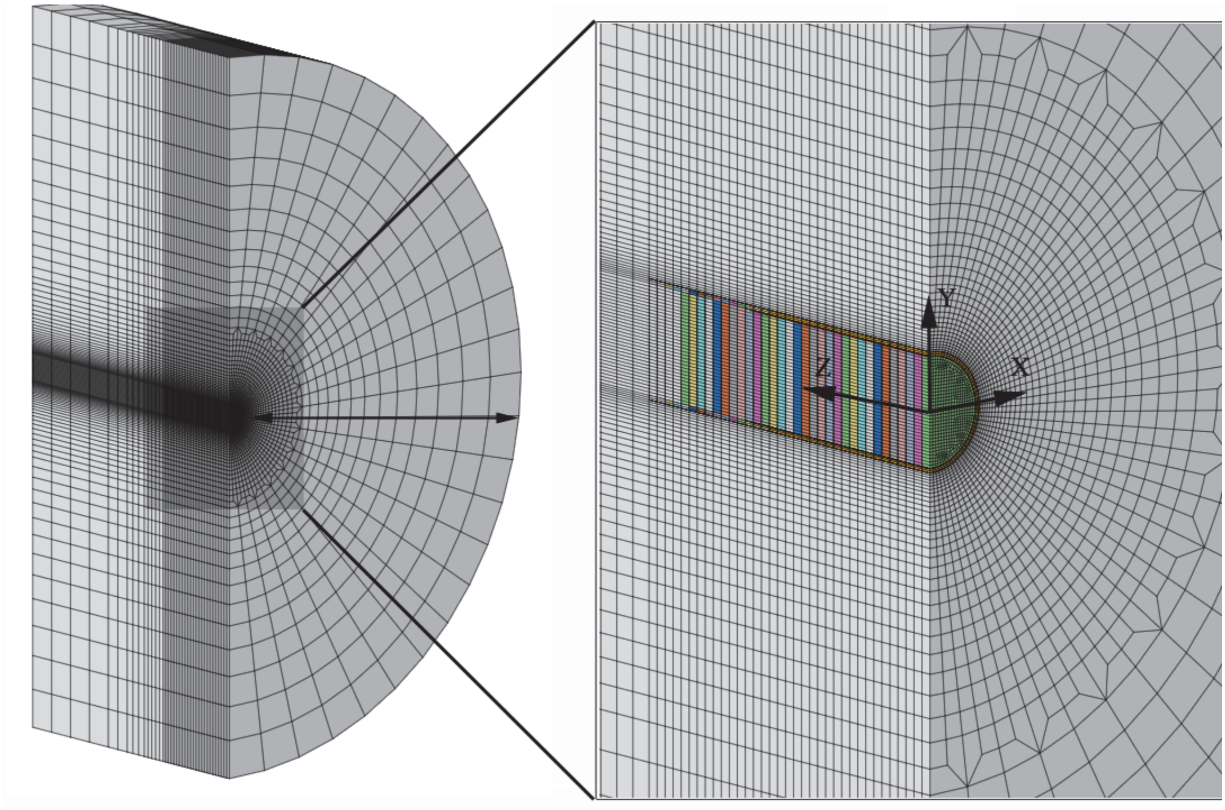

Fig. 4.1: 3D mesh at the initial stage (only rock mass elements are shown) with detail.

4.1 Modeling the main TBM components

The following TBM components are considered in line with the use of the Double Shield TBM:

- *Shields* (front and rear), which are modeled with plate elements applied at the excavation boundary and with the stiffness properties of steel.
- *Cutter head*, which is modeled with plate elements (with the stiffness properties of steel) at the current excavation face and where a pressure is applied.
- *Backfilling*, which is modeled with solid elements; the material filling the gap ranges from pea gravel to cement grout and is given specific properties as desired.

- *Lining*, which is modeled with plate elements (with the stiffness properties of concrete); no joints are introduced and the lining is considered to be continuous.
- *Grippers*, which are modeled with plate elements at the excavation boundary (with the stiffness properties of steel); they are positioned at a certain distance from the face and a given pressure is applied on them.
- *Jack pressure*, which is applied, in the form of an edge pressure, on the last lining ring installed, if the rock is weak, in place of the grippers.

All these components are modeled with a linearly elastic isotropic law. For plate elements, 4-nodes quadrilateral elements are used. The self-weight is applied to all these components.

4.2 Modeling TBM advancement

The model simulates the ongoing TBM excavation by a step-by-step method. This is characterized by the excavation length and construction stages. The excavation length is taken to be equal to 1 m. The construction stages and the total number of steps to be performed depend on the geometry of the excavation, the TBM type, and the rock mass, as:

- the construction length has to be such as to allow for a representative steady state condition to be reached, also considering the boundary effects (the first few meters of the excavation containing these effects are removed from the results);
- the operation modes of the Double Shield TBMs, which are different for hard rock and weak rock.

In hard rock, the only case reported here with some details, the TBM operates using the grippers.The construction stages are defined as follows:

- in the first step, initialization takes place accounting for the *in situ* stress field;
- in the second step, the TBM enters the model (the cutter head elements are activated) and the first slice is excavated;
- in the third step, the first slice of the front shield invert is activated;
- in each step thereafter the TBM progresses into the model;
- in the tenth step, the grippers and the applied pressure become active for the first time. The position of the grippers is changed every 2 m, in order to simulate the re-gripping, with a distance from the face comprised between 6 and 7 m. The re-gripping operation phase (in which the cutter head do not excavate and the clamping of the grippers is released) is not simulated as a stand-alone step but it is associated with the further excavation step;
- in the fifteenth step, the lining is activated as well as backfilling;
- the stages proceed until a steady-state condition is reached.

To illustrate the simulation process, the model for a typical case is shown in Figure 4.2. The shield invert in contact with the rock mass is also shown.

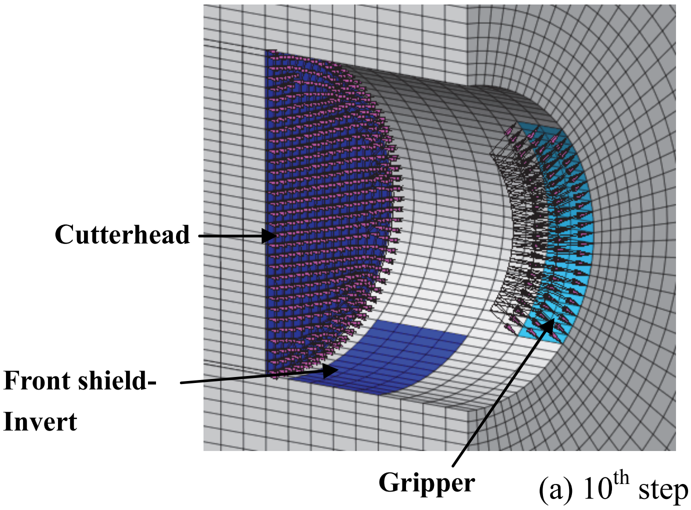

(a) 10th step

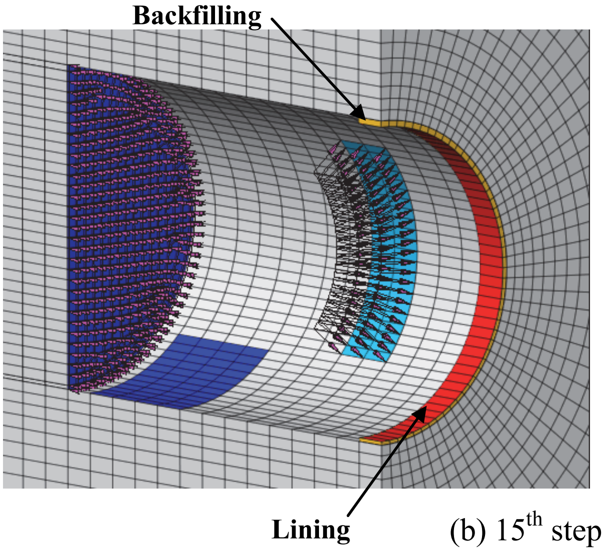

(b) 15th step

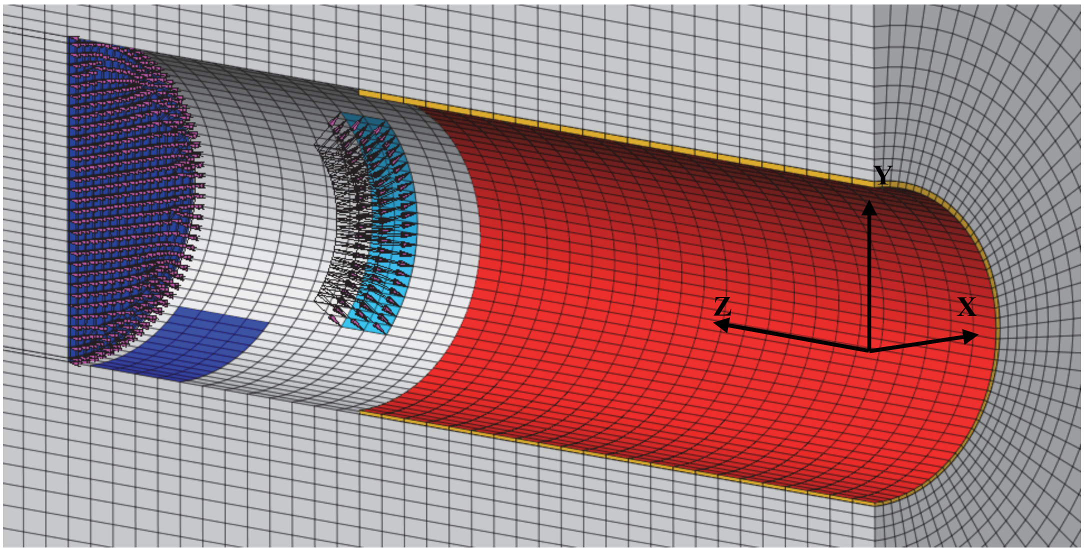

(c) Final step

Fig. 4.2: 3D model in a typical case of TBM excavation in hard rock.

4.3 Rock mass models

The rock mass is considered to be continuous, homogeneous and isotropic. Any constitutive law based on these assumptions for rock masses can be implemented in the model. As already noted, the simulator so far has been developed and tested to deal with the spalling and squeezing phenomena and different constitutive models for reproducing them have been implemented (Barla et al., 2011; Zhao et al., 2012). In view of the case studies illustrated in the following, some details of the model used for spalling are given.

With the assumption that the rock mass is a continuum, the failure zones around the tunnel are simulated by using the criterion developed by Diederichs (2007), which si based on an elastic-perfectly-brittle plastic model. The composite strength envelope for brittle materials (Diederichs, 2010), resulting from studies and observations on the mechanisms leading to spalling, can be implemented in numerical codes through the use of the generalized Hoek-Brown criterion (Fig. 4.3). Peak and residual yield functions are defined by the damage threshold and spalling limit, respectively.

The procedure for determining the input parameters for the generalized Hoek-Brown criterion is the following (Diederichs, 2010):

- Determine the crack initiation threshold *CI* from uniaxial compression tests;
- Set a_{peak} to 0.25;
- Obtain a reliable estimate of tensile strength, *T* (from laboratory tests);
- Calculate the appropriate *s* and *m* from:

$$s_{peak} = (CI/UCS)^{\frac{1}{a_{peak}}} \tag{1}$$

$$m_{peak} = s_{peak}(UCS/|T|) \tag{2}$$

In order to model the transition envelope to high confinement shear (spalling limit), set $a_{res}=0.75$, $s_{res}=0$ or 10^{-6} (for numerical stability) and $m_{res}=5$ to 9.

The equivalent Mohr-Coulomb parameters can also be used and the equivalent cohesion, friction and tensile strength parameters can be varied according to the plastic strain (Cohesion Softening-Friction Hardening approach, CSFH; Diederichs, 2007).

The process of fracturing generates dilation; nevertheless, an accurate reproduction of bulking and of the resulting displacements with continuum models in spalling rock is still an open issue, as actually the process is discontinuous after yield. According to Diederichs (2007), a near-maximum dilation can be used for supported tunnels, while a near zero dilation for unsupported conditions, as there is free fallout of spalls of rock.

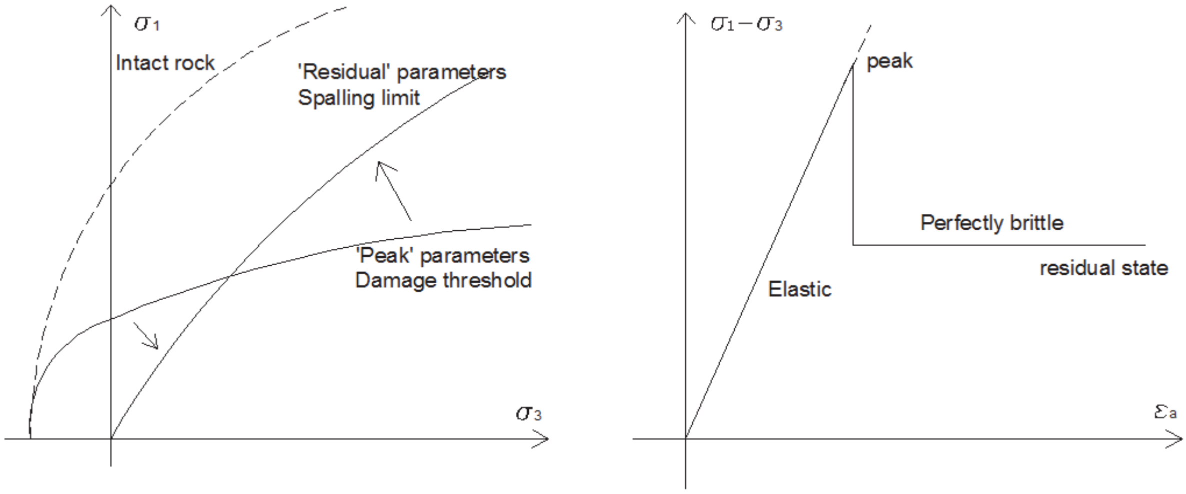

Fig. 4.3: Constitutive law for brittle behaviour: Diederichs (2007) criterion and stress-strain relationship. The intact rock criterion is shown for comparison.

4.4 Interaction between the machine components and the rock mass

The simulation of the interaction problems requires a special attention to the discontinuous behavior at the following interfaces: (i) rock mass-shield and (ii) pea gravel-lining. This behavior involves frictional sliding and the possible closure of the gap between the shield and the rock mass. Zero thickness interface elements are used to represent the frictional shearing mechanism. High normal and shear stiffness values are set and, for plastic slip, a Coulomb friction law with null-cohesion and a value of the skin friction coefficient $\mu=0.3$ is adopted for both the interfaces.

Since the numerical formulation used is based on the small-strain/displacement assumption, the shields are modeled right on the tunnel boundary even if there is a gap in between. In order to simulate the gap between the rock mass and the shields, special interface elements are used in which the elastic stiffness is set to zero, i.e., $K_n=K_s=K_t=0$, so that no stress can transfer from the rock mass elements to the shield elements.

In the case of hard rock, the closure of the entire gap should not occur as convergences are small in the elastic zones. In the localized failure zones due to spalling, dilation is followed by the fallout of rock slabs and it is assumed that the gap is not closed because (i) during the re-gripping operation, the front shield sweeps and displaces the material accumulated and (ii) the crushed material cannot provide a consistent support. Therefore, only the invert of the front shield is significantly in contact with the rock mass, as the gap is really very small.

The load transfer between the rock mass and the lining occurs through a backfilling layer. In particular when tunneling in hard rock, the gap is filled, at the invert, with dry mortar in order to support the ring. Along the remaining surface pea gravel and later cement grout are injected. It is important, in the case of spalling, to correctly fill this gap which could even be bigger due to the stress-induced notches. The backfilling is usually performed at a certain distance behind the shield. Therefore the backfilling is modeled in only one stage. The pea gravel and the lining are activated 2 m behind.

5. Case studies

In order to illustrate the 3D simulator of TBM excavation in brittle rock conditions, the case studies of the Lyon-Turin and Brenner Base Tunnels are briefly considered in the following.

5.1 Lyon-Turin Base Tunnel

The Maddalena exploratory tunnel, along the Lyon-Turin Base Tunnel, is presently being excavated. The 6 m diameter tunnel will cross the “Ambin complex” (Gneiss and Micaschist) and the “Clarea complex” (Micaschist) with a maximum overburden of 2000 m approximately. Fig. 5.1 illustrates the spalling model adopted for the rock mass.

Based on the available hydro-fracture tests the *in situ* state of stress in the rock mass is assumed to be defined by the following components: σ_v (minimum vertical principal stress) = 33.2 MPa; σ_h (maximum horizontal principal stress) = 53.1 MPa. The excavation is assumed to be performed by a Double Shield TBM.

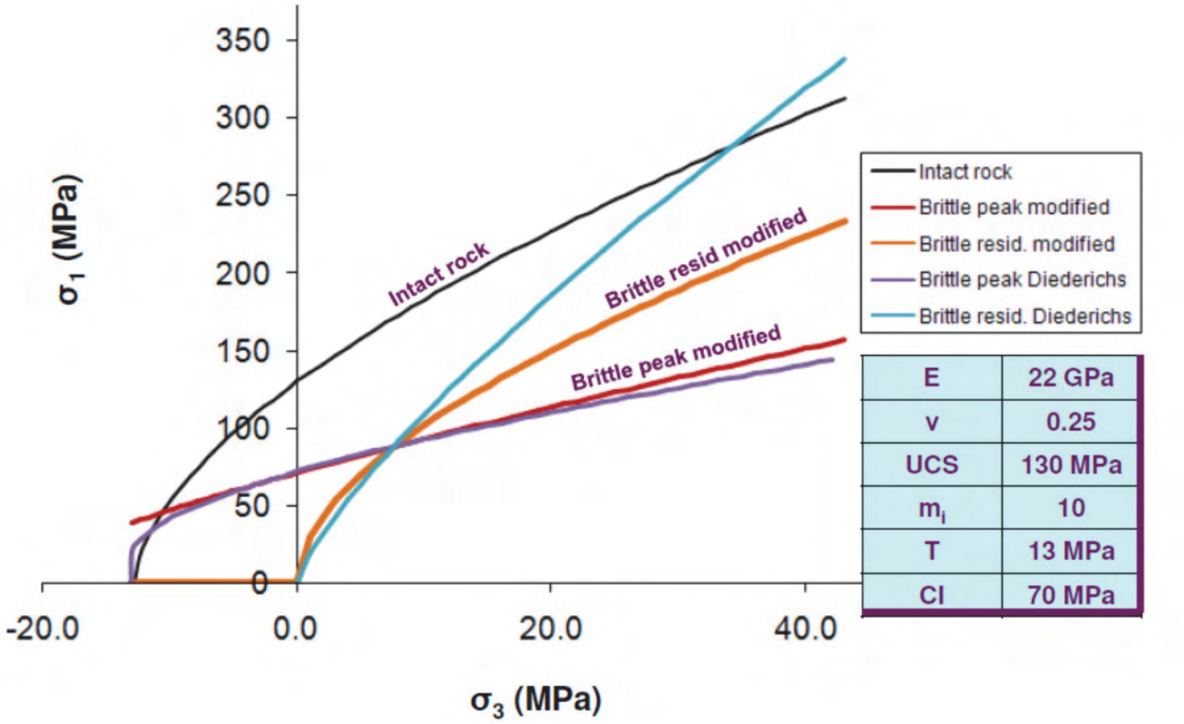

E	22 GPa
v	0.25
UCS	130 MPa
m_i	10
T	13 MPa
CI	70 MPa

Fig. 5.1: Lyon-Turin Base Tunnel, Maddalena exploratory tunnel, rock mass behavior: Diederichs model (based on the generalised Hoek-Brown criterion) and modified model (based on the traditional Hoek-Brown criterion).

Fig. 5.2 shows the 3D spall damage and overbreak prediction along the tunnel axis. The degree of spalling failure and over-break is expressed through the equivalent plastic strain, defined as:

$$\varepsilon_{pl} = \sqrt{\frac{2}{3}\left(\varepsilon_{p1}^{2} + \varepsilon_{p2}^{2} + \varepsilon_{p3}^{2}\right)} \qquad (3)$$

with ε_{p1}, ε_{p2}, ε_{p3} the principal plastic strains.

Fig. 5.2 a gives such a prediction when a steady simulation in unsupported conditions is reached, whereas Fig. 2 b gives the same prediction when the 3D model accounts for the presence of the TBM.

It is shown that the over-break zones exhibit a maximum depth of failure of 0.8 m approximately. Due to the moderate *in situ* stress ratio of 1.6, over-break zones are all around the excavation, although moderate in intensity at the sidewalls. It is seen that the front shield and its self-weight produce a confinement at the invert so that over-break is significantly reduced.

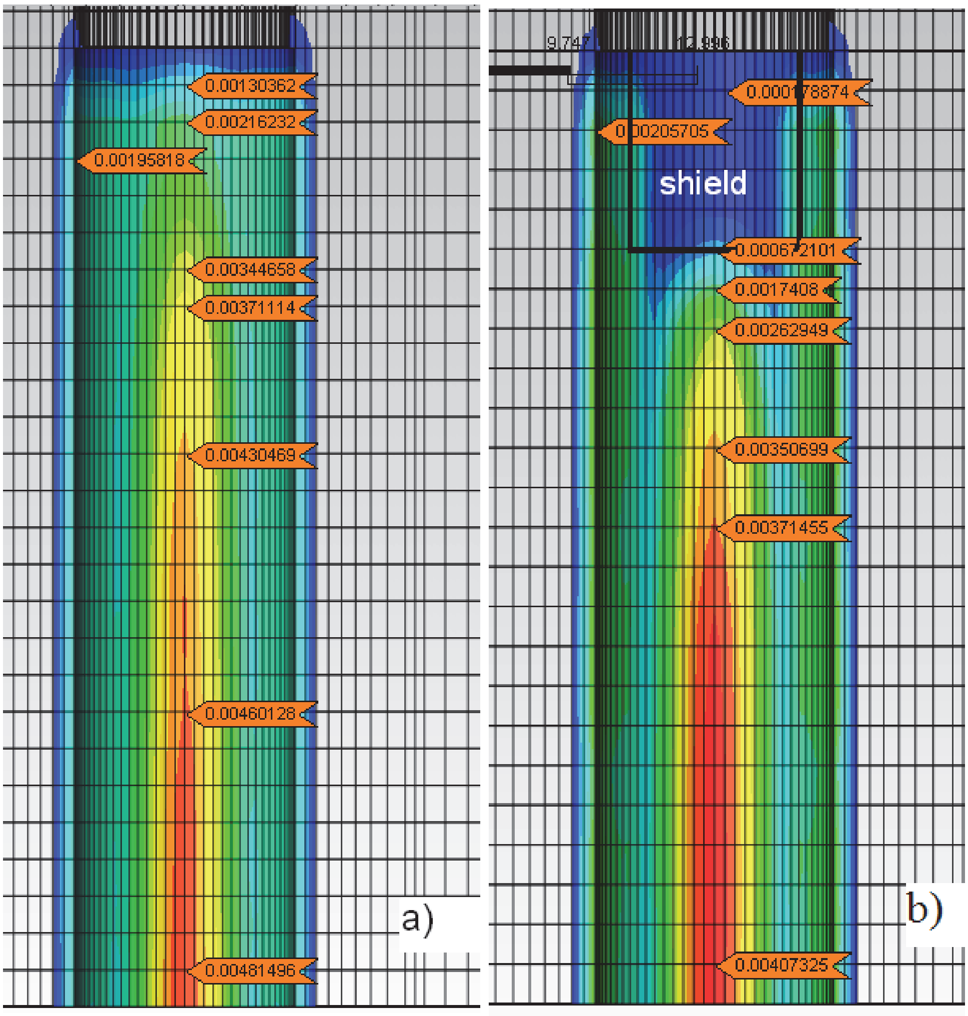

Fig. 5.2: Lyon-Turin Base Tunnel, Maddalena exploratory tunnel, plastic strain contours along the tunnel in a 3D top view: a) in the intrinsic (no TBM interaction) model and b) in the TBM interaction model.

5.2 Brenner Base Tunnel

A section of the Brenner Base Tunnel starting from the Italian Portal in Fortezza is taken as a case study. The 9 m diameter tunnel is to be excavated in the “Brixner granite complex” with a maximum overburden of 1350 m. This granite is medium to coarse grained. Fig. 5.3 illustrates the spalling model adopted.

In order to demonstrate the capability of the 3D model to capture the spalling behavior, the state of stress in the rock mass has been assumed to be characterized by a stress ratio σ_h (horizontal stress) / σ_v (vertical stress) equal to 2, with $\sigma_v = 24$ MPa. It is noted that no data are available in the tunnel to confirm such assumption. The excavation is assumed to be performed by a Double Shield TBM.

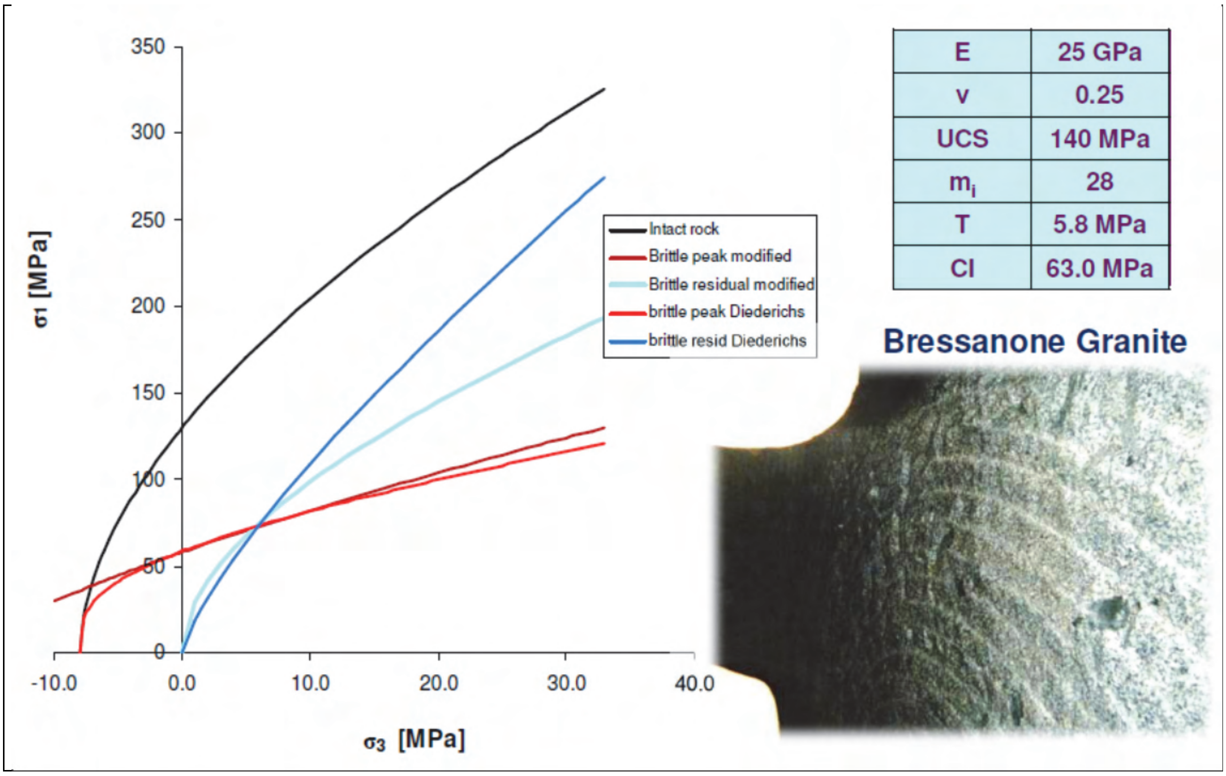

E	25 GPa
v	0.25
UCS	140 MPa
m_i	28
T	5.8 MPa
CI	63.0 MPa

Fig. 5.3: Brenner Base Tunnel, rock mass behavior: Diederichs model (based on the generalised Hoek-Brown criterion) and modified model (based on the traditional Hoek-Brown criterion).

Fig. 5.4 shows the 3D spalling failure and over-break prediction along the tunnel axis. As for the previous case, the degree of spalling failure and over-break is expressed through the equivalent plastic strain given by equation (3). The spalling zones are shown to occur at the invert and at the crown with a maximum depth of approximately 1 m.

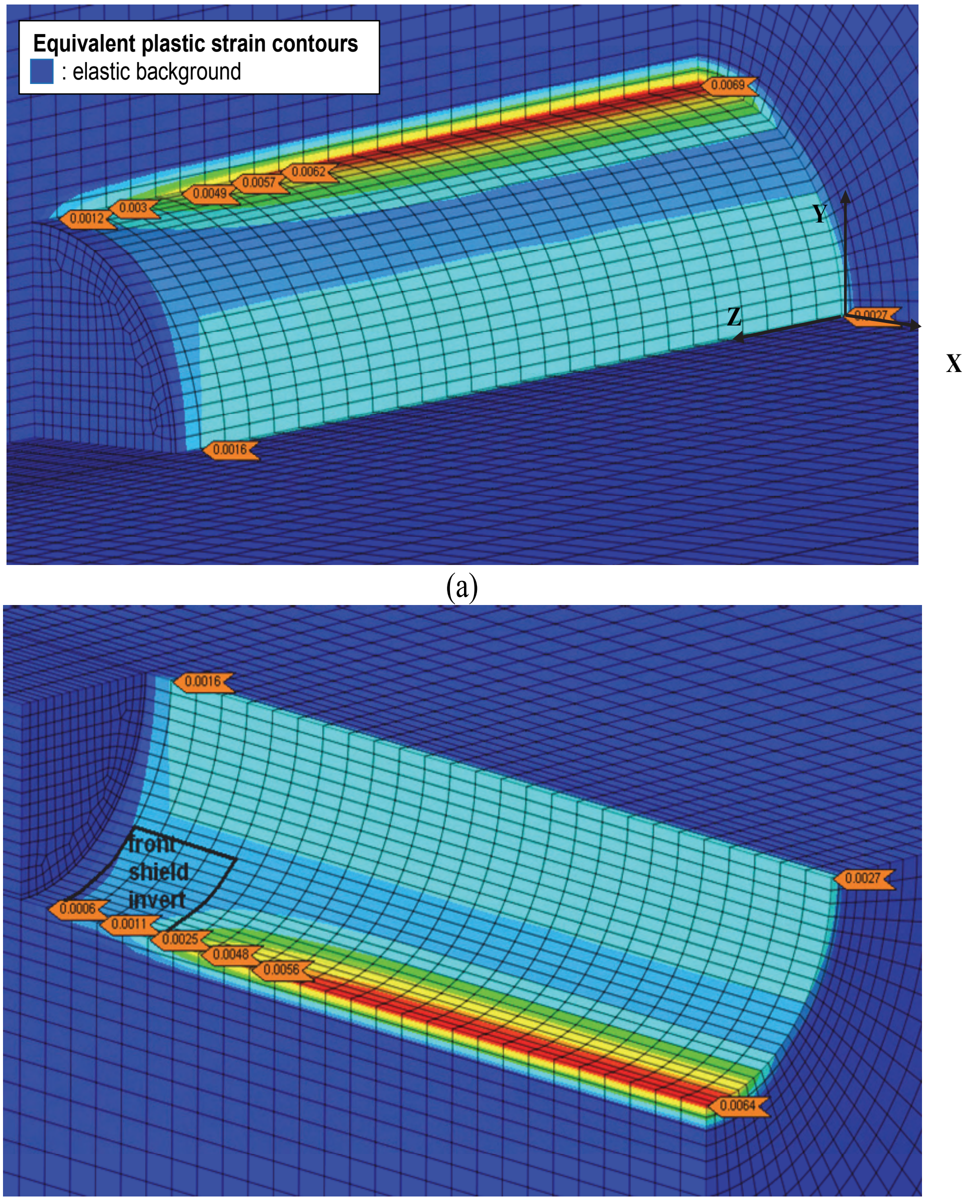

(a)

(b)

Fig. 5.4: Brenner Base Tunnel: plastic strain contours along the tunnel in the TBM interaction model: (a) upper half and (b) lower half.

It is seen that the front shield and its self-weight produce a confinement at the invert, so that the plastic strain at the front shield invert is reduced. The grippers are shown to have very limited influence whereas the support produces only a slight decrease of the failure extent, as it is applied at a certain distance from the face, where most of failure did already occur.

As soon as the front shield is passed and the invert walls are exposed, the plastic strain increases, reaching however a value in steady state conditions which is lower than in the intrinsic case (reduction of 14 %). This means that the crushing and subsequent fallout of rock at the crown and at the invert will take place along the rear shield.

6 Conclusions

With major interest in mechanized tunneling (TBM excavation) and with reference to the Alpine Base Tunnels, the Lyon-Turin tunnel (between Italy and France) and the Brenner tunnel (between Italy and Austria), this lecture has illustrated a 3D finite element model of deep mechanized tunnel excavation in rock masses. This model is intended to simulate the complex interaction between the rock mass, the tunnel machine and its system components, and the tunnel support.

With specific reference to “spalling”, one of the important geological/geomechanical hazards in deep tunnel excavation, two case studies have been briefly illustrated under the assumption that a Double Shield TBM (and the support system) is used for excavation in order to cope with “hard rock conditions” (Gneiss-Micaschist and Granite) where this type of instability is expected to occur.

The results obtained with the numerical simulations show that the newly developed 3D model is highly effective in reproducing both the rock mass response and its interaction with the TBM system components. The 3D nature of TBM excavation has been taken into account by using a non-axisymmetric model for the state of stress in the rock mass, the geometry of the TBM, and the support system.

References

Barla G (2010) Analysis of an extraordinary event of TBM entrapment in squeezing ground conditions. In: No Friction No Tunnelling. Fetschift zum 60. Gebustag von Wulf Schubert, Institut für Felsmechanik und Tunnelbau, Technische Universität Graz. Ed. T. Pilgerstorfer, 66-76.

Barla G, Janutolo M, Zhao K (2011) Open issues in Tunnel Boring Machine excavation of deep tunnels. Keynote Lecture. 14th Australasian Tunnelling Conference. Auckland, New Zealand.

Diederichs M (2007) The 2003 Canadian Geotechnical Colloquium: Mechanistic interpretation and practical application of damage and spalling prediction criteria for deep tunneling, Can Geot J, 44, 1082-1116.

Diederichs M (2010) Brittle spalling, practical limits. Keynote paper, BEFO 2010, Swedish Rock Mechanics Symposium, Sweden.

Hoek E, Guevara R (2009) Overcoming squeezing in the Yacambù-Quibor tunnel, Venezuela. Rock Mech Rock Eng, 42, 389-418.

Loew S, Barla G, Diederichs M (2010) Engineering Geology of Alpine tunnels: past, present and future. Keynote lecture, 11th IAEG Congress, Auckland, New Zealand.

Maidl B, Schmid L, Ritz W, Herrenknecht M (2008) Hard rock Tunnel Boring Machines, Ernst & Sohn, A Wiley Company.

Martin C D, Kaiser P K, Mc Creath D R (1999) Hoek-Brown parameters for predicting the depth of brittle failure around tunnels, Can Geot J, 36, 136-151.

Zhao K, Janutolo M, Barla G. (2012) A completely 3D model for the simulation of mechanized tunnel excavation. Rock Mech Rock Eng, 45 (4), 475-497.

Deformation processes at the area of the closed Idrija Mercury Mine

Deformationsprozesse im Gebiet des stillgelegten Idrija Quecksilberbergbaus

J. Likar, T. Marolt
University of Ljubljana, Faculty of Natural Sciences and Engineering

Abstract

The history of the Mercury production at the Idrija area was extra important for better understanding the wider deformation processes in the rock structure and consequently in the surface above mine. In the past five centuries mine operations have had consequences on the environment, which have directly influenced the deformations developing in the wider exploration area. During the more centuries of mercury ore exploitation, the cross-stope mining method with backfilling from bottom to top was used. This had big influence on the stress-strain field transformation in the surrounding rock masses and backfilling, caused long-term deformation processes that are not finished yet till nowadays. The deformation process has a small time gradient and thus bigger breaks or faster sliding terrain above old mine workings is not expected. The surface displacements are bigger in the area built of Permian-Carboniferous, low-bearing-capacity rock mass, which in the past was destroyed by major tectonic movements in the rock structure in different geological ages. Mine closure works, which included grouting and hardening of destroyed underground areas, as well as filling parts of the mine and backfilling empty spaces (i.e., mine roadways, blind shafts), were finished two years ago. In mean time the hydraulic level of mine water was arise from XI. Level at altitude 65.13 m to IX. Level at altitude 133.09 which caused some additional surface displacement. The efficiency of mine shutdown works is constantly being verified by means of geotechnical, other measurements and observations, and will continue in the future.

Zusammenfassung

Die Geschichte der Quecksilberproduktion im Gebiet Idrija ist sehr bedeutend für das bessere Verständnis der Deformationsprozesse innerhalb des Gebirges und schließlich auch der Erdoberfläche oberhalb des Grubengebäudes. Die letzten 500 Jahre Bergbau haben die Umwelt beeinflusst mit Auswirkungen auf das Deformationsgeschehen im gesamten Erkundungsgebiet. Über die Jahrhunderte des Quecksilberabbaus hinweg wurde die ‚cross-stope‘ Abbaumethode mit Einbringen von Versatz von unten nach oben angewendet. Dieser Prozess hat großen Einfluss auf die Änderungen des Spannungs- und Deformationsfeldes im umgebenden Gestein und im Versatz, die langzeitliche und bis heute andauernde Deformationsprozesse verursachen. Diese Deformationsprozesse sind durch geringe zeitliche Gradienten charakterisiert, so dass größere Verbrüche oder schnelleres Rutschen von Erdmassen an der Erdoberfläche nicht zu erwarten sind. Die Oberflächendeformationen sind größer in den geringer festen geologischen Einheiten

des Perm/Karbon, die durch größere tektonische Bewegungen stark beansprucht wurden. Vor 2 Jahren wurden die Arbeiten zum Schließen der Gruben beendet, die das Verfüllen offener Grubenräume und teilversetzer Bereiche (z. B. Förderstecken, Blindschächte) sowie das Ertüchtigen verbrochener Bereiche mittels Injektionen beinhaltete. In der Zwischenzeit ist das Grundwasser vom Niveau der XI. Sohle (65,13 m) auf das Niveau der IX. Sohle (133,09 m) angestiegen, was zusätzliche Deformationen an der Oberfläche hervorgerufen hat. Die Effizienz der Stillegungsarbeiten wir permanent überwacht mittels geotechnischer und anderer Messungen und Beobachtungen und wird auch in Zukunft andauern.

1 Introduction

The Idrija Mercury Mine has caused extensive deformations in the wider mining area in the last five centuries. The mine closure works were finished, but various observations and measurements in the mine and on the surface above the mine are still active, because the time-dependent deformation processes in the wider area were not finished. The measurements are conducted in the prescribed time intervals twice a year in order to ensure the monitoring of deformation processes.

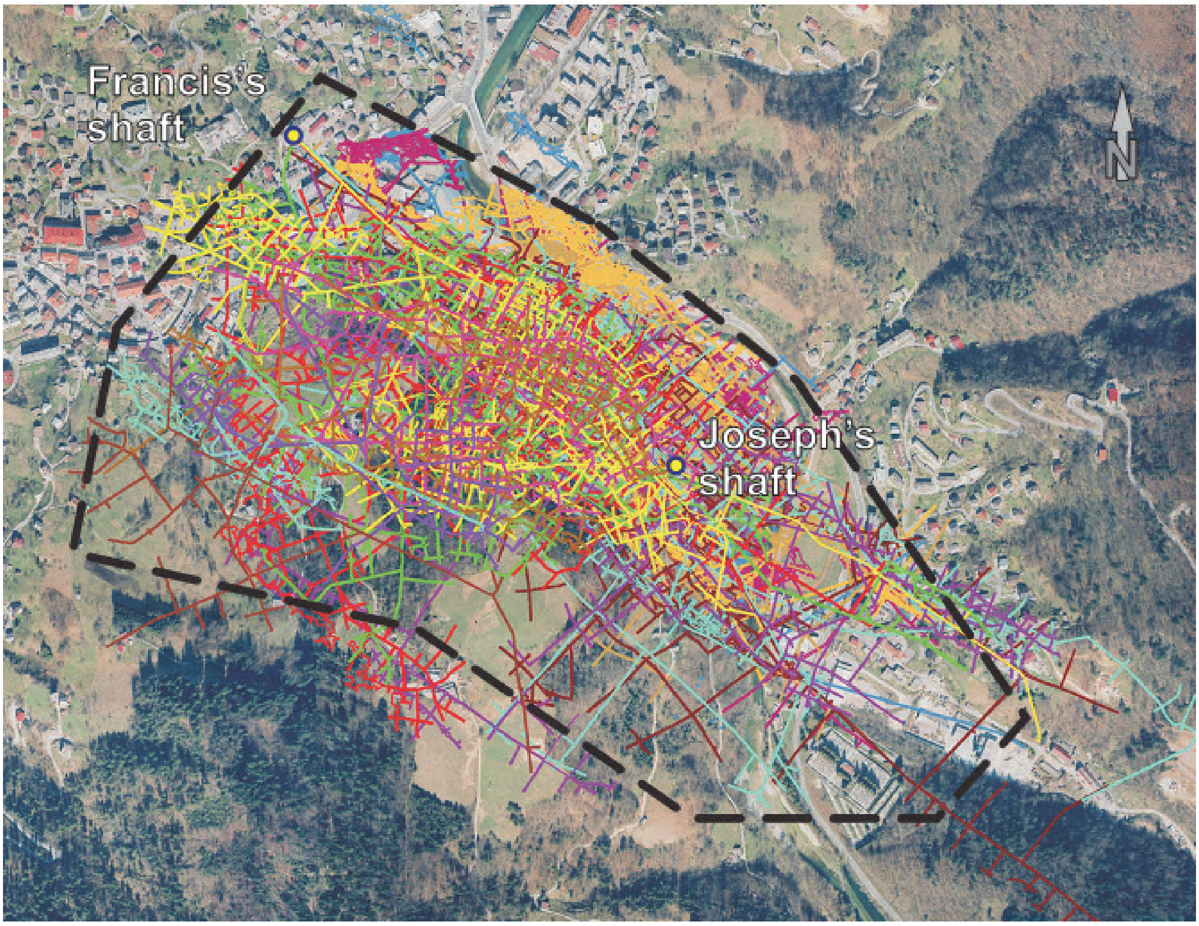

Fig. 1: Layout of the town Idrija with Mercury Mine Structure

The results of measurements and observations give a realistic insight into the actual occurrences, which also enables verification of the effects of consolidated and backfilling works in the mine. Long-term, time-dependent processes which are closely linked to the extent of ore exploitation and the type of mining methods, which were used in the past, and in particular to the geological and geomechanical conditions, are still present. That process is present particularly on the ground surface above Permian-Carboniferous layers and other low-bearing-capacity ground layers. The main goal of mine closure works is the final stabilization of the area which will be able to use land for new construction projects. Fig 1 has shown complex mine structure developed below the town Idrija.

2 Geological and Hydrogeological Interpretation of the Wider Mercury Mine Area

The mercury ore deposit which is 1500 m long and 300 – 600 m wide extends in the directions northwest and southeast. It has a depth of the ore-bearing zone at about 450 m below the surface. The deposit was open in mine history by entrance gallery and vertical shafts. The deepest shaft which is now entirely closed with concrete backfill, reached a depth of 420 m at approx. 20 m below sea level. Over a period of 500 years underground operation, miners have continually excavated more than 700 kilometers of mine roadways, drifts, and blind shafts.
The hydrothermal mercury deposit in Idrija is a geological natural treasure of global significance, and is ranked among the most complex ore deposits in the world.

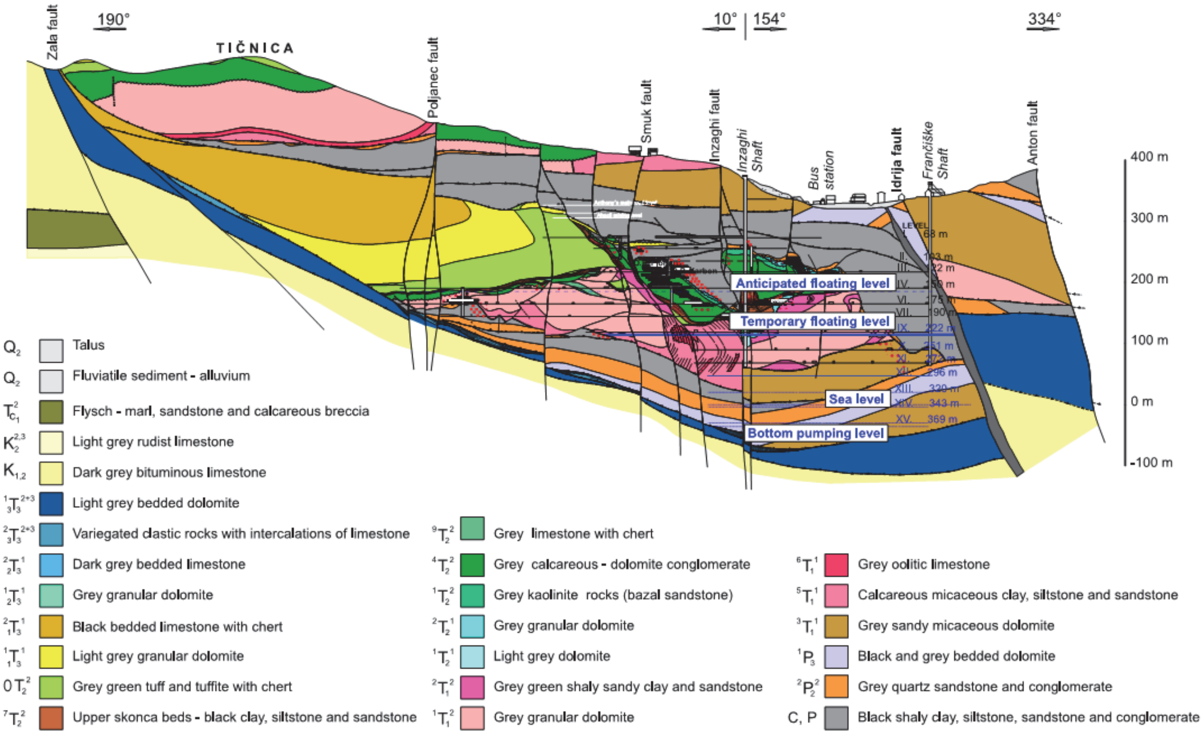

BASED ON: dr. I. Mlakar; 1967, 1969, dr. L. Placer; 1973,1980,1983, dr. J. Čar; 1985, 1990, dr. L. Placer & dr. J. Čar 1975, 1977 **PREPARED:** dr. J. Čar, 1993

Fig. 2: Geological cross section through the Idrija Mercury Mine [6], [7]

The mercury ore deposit is classified as a monometal, as well as a monomineral, deposit and has the second largest concentration of mercury in the world. Most of the mercury appears in the form of cinnabar (HgS, ~70 %), and in the form of native mercury (Hg, ~30 %). Pyrite, marcasite, dolomite, calcite, kaolinite, epsomite, and idrialin (named after Idrija) represent the main gangue or waste rocks [1], [2], [3]. The mercury ore deposit was formed during two phases: in the lower part of the Middle Triassic (Anisian), and in the second, Ladinian phase during a period of intense volcanic activity in Slovenian geological history. Middle Triassic tectonics led to the upwelling of hydrothermal solutions, which expelled their deposits onto the sea bed through a thick layer of Upper Palaeozoic, Permian, Scythian, and Anisian clastic and carbonate rocks [2]. Due to gradually declining temperatures, part of the mercury condensed and was released as pure mercury in the form of drops.

Hydrothermal underwater springs deposited the mercury in littoral swamps forming the synsedimentary ore beds and lenses in the black Skonca shales and tuffs of the Ladinian age [4], [5]. In the final phase of alpine orogenesis, ore bodies were disintegrated and moved along the faults. The Idrija ore deposit has 158 known orebodies, 17 with native mercury are in carboniferous shale, while the remaining 141 are in clastic and carbonate rocks. These ore bodies have extremely different forms and sizes, and are irregularly distributed throughout the entire ore deposit [4], [5]. The geological cross section is shown on Fig 2.

The ore deposit and its surroundings are comprised of several hydrogeological blocks and impermeable hydrogeological barriers. It is also characterized by the presence of backfills (40 % porosity) and filled shafts on different levels of the ore deposit. The impermeable barriers, enclosing the old part of the Idrija ore deposit, are built of Carboniferous shale below the deposit, thrust sheets along the southern edge, and a Carboniferous layers above the deposit. On the north side, the deposit is closed in by an impermeable, clayey zone of the Idrija fault [6], [7]. In all aquifers, the level of ground water is above the level of mine infrastructure. The main inflows of water into the ore deposit occur through shafts, galleries, drilled hydrological barriers or barriers partly demolished due to exploitation works. Due to the geological structure of the Idrija ore deposit, water inflows into the mine facilities are relatively small (average 25 l/s). The flooding of the ore deposit up IXth level (+ 115 m) keeps mine waters within the limits of the abandoned ore deposit, and the only possible source of pollution with pumped mine water into the above-ground water course – the Idrijca River (+ 331 m).

3 Mining Methods Used During the Mine's Operation

In the five centuries of the mine's history the mercury ore mining technologies have employed and adapted to the development of mining science – taking into account existing geomechanics and mining conditions. On the basis of historical sources, the most frequently used the mining method with backfilling from bottom to top, where ore was transported through blind shafts to lower levels and then exported to the surface for further processing. It should be emphasized that throughout the mine's operation, wood was the principal support material used in mining stopes, as well as at the main and auxiliary mine roadways. The cross-stope method which was developed over last 200 years was conducted in several phases, depending on the geometric and geomechanical characteristics of the ore bodies and surrounding rocks. In order to develop an individual level, it was initially necessary to carry out preparations of the main drift on the main level, and install a separate ventilation system so that mining works could be started at individual excavation areas (Fig. 3 A). These were made from a preparatory drift at a 45° or 90° angle with respect to the main drift axis. The dimensions of the cross-sections in drifts were within the limits of 2.0 m to 4.0 m in width, 1.8 m to 3.0 m in height, and a variety of lengths from a few meters to about 50 m to 80 m in some cases. The horizontal and slightly inclined mine stopes were lined with wood supporting. Ore was transported on various levels and roadways using small and medium-sized mine carts (volume from 0.3 to 0.8 m^3) on wooden and steel rails. After the mine's modernization in the 20th century, mine locomotives were used to transport extracted ore and reproductive materials to various levels, while on working levels the ore was mostly transported manually to blinded shaft or chutes.

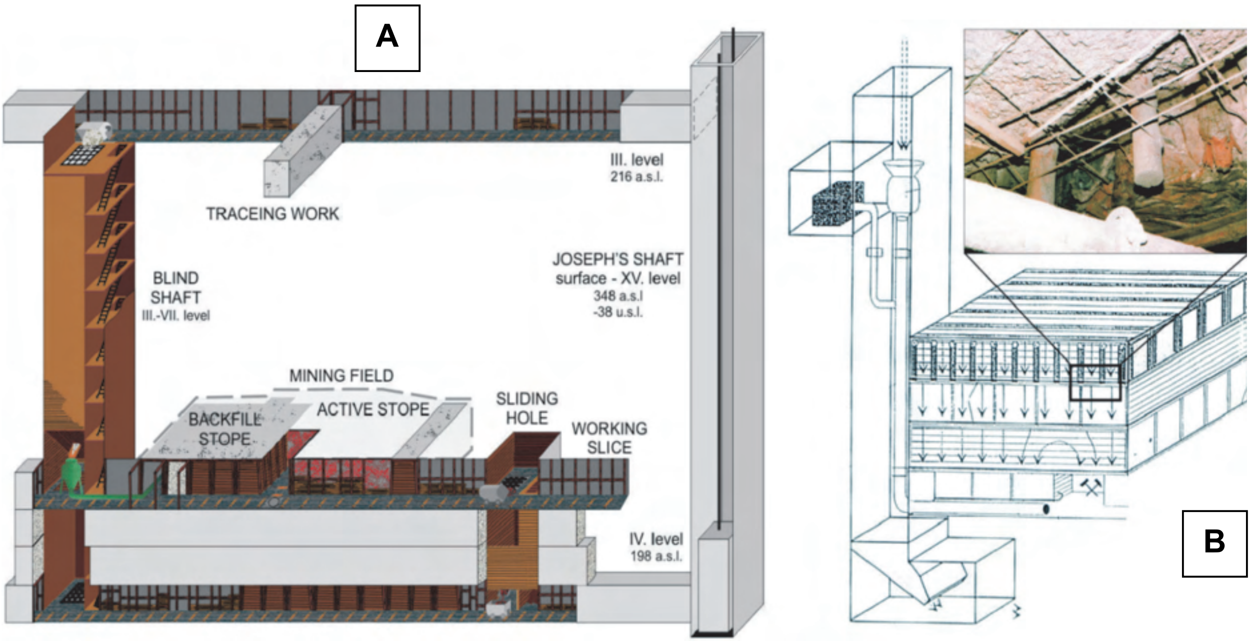

Fig. 3: Cross stopping with backfill and sublevel mining with consolidated backfilling

Technical evaluation of the mining method from bottom to top is shown in Fig. 3 A. The preparation and mining of higher lying levels, was conducted successively after the lower level was backfilled and works had begun on a higher level. The height of each level was approx. 2.5 m to 3.0 m, allowing miners to manually perform all mining works. The relatively complex geological and geotechnical conditions additionally contributed to the worsening mining conditions in higher production levels. In some cases, e.g. when ore was mined from Carboniferous shale, the additional stresses in the rocks on the first level were so intense that mining from bottom to top was practically impossible, because the time-dependent phenomena were so intensive that backfills have still not stabilized. The complex geological and geotechnical conditions accompanying mining works in Carboniferous ore bodies, as well as increased environmental requirements and special concern for the health and safety of miners at work, called for radical changes in the mining method. In the 1970s and 1980s, introduced a new mining method from the top downwards [8], which involved highly different mining and backfilling technologies than had previously been used. The new system of mining from the top downwards represented a significant turning point in the history of the mercury mine, as it completely changed individual technological procedures, particularly those designed to protect miners against caving and collapses in the roof and partly also the side walls.

The use of reinforced backfill with a minimum required compressive strength, the minimum subsidence was developed and the substantial improvement of mining conditions was achieved.

The final requirement based on a test stopes back analysis, backfill with compressive strength 4 MPa, was sufficient for normal mine operation. This was also proven by calculations used the Finite Element Method, taking into account the nonlinear relations between stresses and strains by means of simulations of mining works and successive use of reinforced backfill into each mining area separately [8].

The calculated vertical displacements amounted to maximally 10 cm, which is substantially lower than the subsidence that would have developed when using the old cross-stope method. In addition, mining from the top downwards also has positive effects on the reduction of losses during the mining of mercury ore and native mercury present in Carboniferous shale.

4 Summary of Mine Closure Works

Several reasons influenced the abandonment of mercury ore excavation, initially in the 1970s and finally in the late 1980s. On the one side, an intensive international campaign had been launched against mercury, whose harmful effects were researched in various fields. Another reason was the very low selling price of this metal, which in some cases fell below 100 USD per flask (34.5 kg of mercury). All activities which were done in preparing mine closure works faced particular issues on the long-term effects on the time dependent surface subsidence. More questions were raised, because the town of Idrija location is directly above the mining infrastructure. In addition, the potential instability of the natural and artificial slopes above the mine, and the pollution of the environment with mercury in the town of Idrija itself and far downstream along the Idrijca River and the Soča River, including the Gulf of Trieste, were present as well. The principal tasks were to select and justify the technology required for mine closure works, with the clear goal of attaining the long-term stability of the vibrant surface area above the mine, reducing to the greatest possible extent any possible damage to buildings caused by mining activities, regulating the hydrological and hydrogeological environments, establishing supervision over harmful concentrations of mercury in various forms or aggregate states, and constantly controlling the effects of mercury on miners and other inhabitants of the town of Idrija. Surveying and geometric observations of surface movements in the wider area of the mine from the beginning of the 20th century onwards, as well as the excellent geological and hydrogeological studies and interpretations of the origin of the ore deposit and subsequent tectonic and other occurrences are a useable base for deep interpretation for the complex deformation process. For this purpose, extensive simulations and analyses of the impact of reinforcement processes on the rock structure and old mining works using the finite element method were performed. A specific question was raised in connection with the estimated consequences of possible flooding of the mine up to different height levels, as the considerable worsening of geotechnical conditions was expected in areas where mine water came into contact with rocks and old backfills, which are sensitive to water. In situ investigations in the mine confirmed the fear that increased surface subsidence would develop in the event of uncontrolled flooding of the mine. This is the main reason for anticipated flooding level was deeper instead of the first assumptions. In this context intensive grouting of old mine works and backfills including mine roadways, drifts and vertical mine connections were done over more than 10 years.

5 Measurements of Geotechnical and Hydrogeological Parameters

Geodetic measurements began in the initial years of the 20th century, while extensive geometric observations aimed at monitoring the stabilization of the mine were not performed until year 1990. Measurement was carried out in profiles net installed on the disturbed surface above the mine. Measurements were also performed on important infrastructural buildings and facilities, too. Before the commencement of shutdown works, the horizontal and vertical movements of terrain above the mine were up to 25 mm/year and up to 14 mm/year, respectively.

5.1 Displacements measurements in the mine

The wide mine surveying mesh included measuring points placed on different mine levels connected to main points near the main shafts “Joseph” and “Francis” (Fig. 1.).

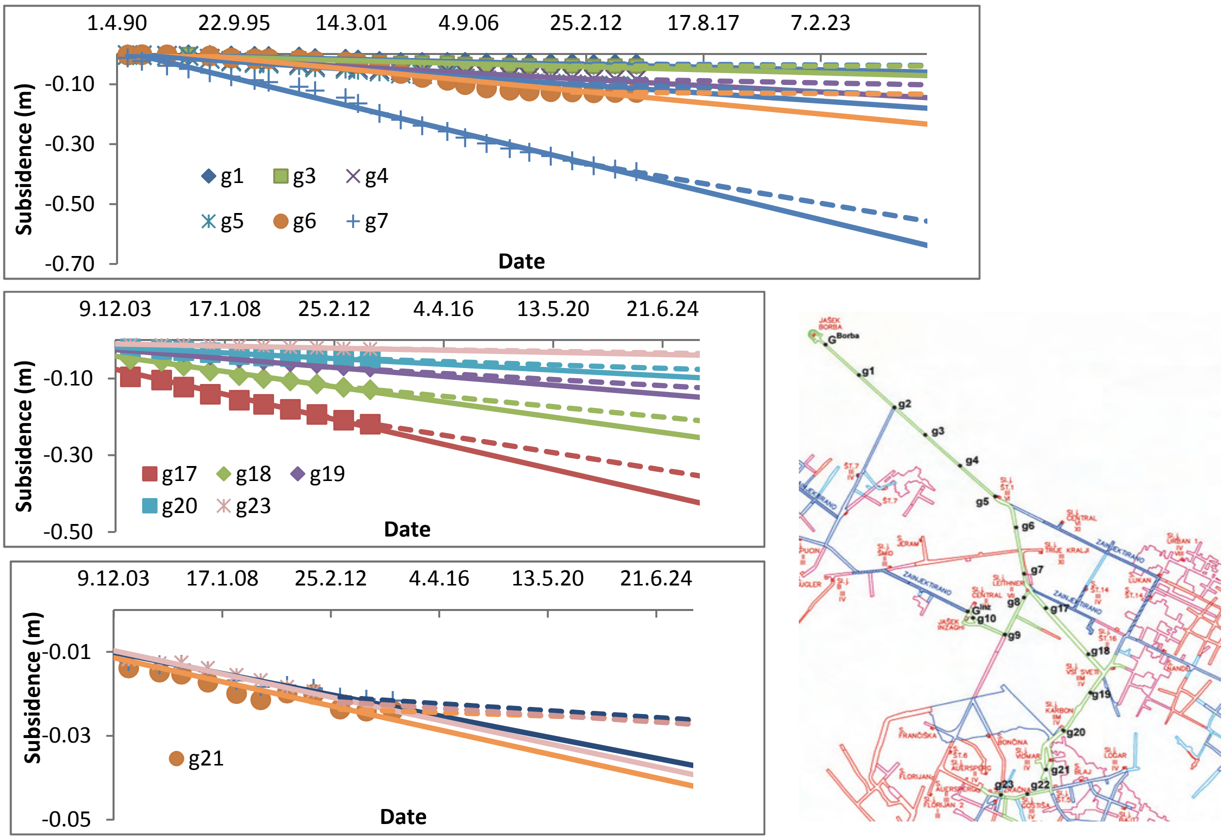

Fig. 4: Measured settlements at the IIIth level

Each measuring point is stabilized on the bottom or in the roof of mine roadways to allow for the measurement of vertical movements and, in some cases, horizontal movements as well. Each measuring cycle was performed twice per year with the aim to keep subsidence control. A trend of vertical displacement similar to that on the surface was also found in the mine. The measurements executed on levels I to XI showed a displacement syncline near the Inzaghi shaft (Fig. 2.), where a maximum subsidence was found. The measured movements gradually decreased and, during the past years, horizontal movements declined to an average 7 mm/year and vertical displacements to 4 mm/year. The typical result of vertical movements is shown in Fig. 4.

5.2 Horizontal displacement measured by inclinometers

Inclinometer measurements in boreholes have been conducted since 1989. In the period from 1989 to 1996, 17 inclinometric boreholes were activated and measurement carried out twice a year, and attained values of up to 21 mm/year and vertical movements of up to 10 mm/year (Fig. 5.). The period from 1996 to 2001 has shown that the terrain above the mine continues to move, but with a decreasing tendency as a result of consolidation and fortifying works. In the last eight years (2003 – 2011), we measured some local increasing deformations in an area with geotechnical, unstable rocks (Carboniferous shale), but these are still in the process of stabilizing and do not present any major hazard.

The results of several years of measurements and observations have shown that not only are different slow slides forming above the mine, but a large subsiding crater is also forming with its center around the Inzaghi shaft (Fig. 2.), where most of the exploitation works took place over the last 100 years.

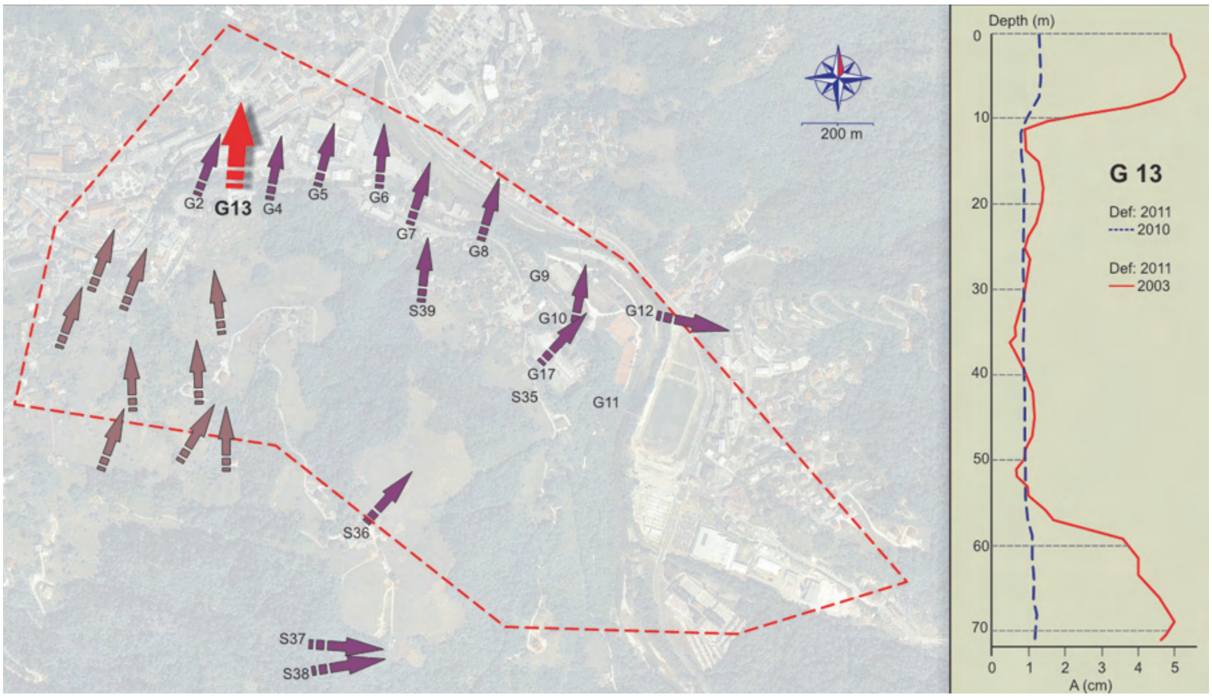

Fig. 5: Results of the inclinometer measurement G13

5.3 Measurements stress changes in rocks and backfills

A very important part of measured data was related to determining secondary stress changes with time in different locations at the deepest levels in the mine. For the purpose of monitoring stress deformation changes in rocks and backfills in the deepest parts of the mine during flooding up to the XIth level, measurement probes, i.e. cells equipped with a strain gauge in the vertical direction tested in the laboratory in biaxial cell, were incorporated into boreholes, and injected with cement grouting material. Since the incorporation of measurement probes at the XIVth and XVth levels in the middle of 1992, measurements of specific deformations in backfill (XIVth level, elevation – 6.45), dolomite (XIVth level, elevation. – 6.45), and shale (XVth level, elevation – 32) have been performed twice yearly. The results of these measurements are shown in Fig. 6 and Fig. 7 at the XIVth and XVth levels where the deformation processes were in progress during the time when the flooding of lower part of the mine was present.

It is evident from the results of measurements shown in Fig. 6 in the form of diagram that the course of time-dependent stress changed in 1995 and partly in 1996, when changes in stresses and deformations in the rock structure occurred as the consequence of mine flooding up to the XIth level. Rapid changes in deformations stopped occurring later on. The results of measurements indicated that the deformation processes are still in progress, but the trends do not point to any major stress changes in surrounding rocks. All measuring points still indicate changes in increasing vertical stresses particularly in shale.

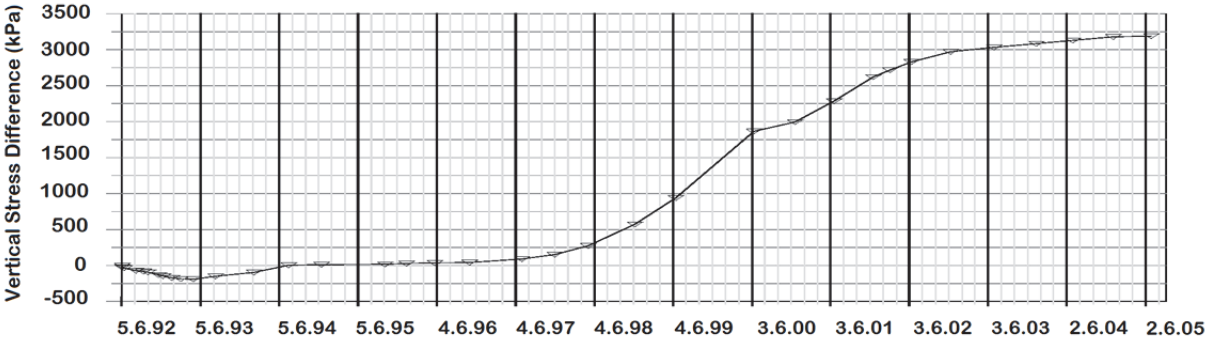

Fig. 6: Results of the additional vertical stress measurement in the shale on the XVth level

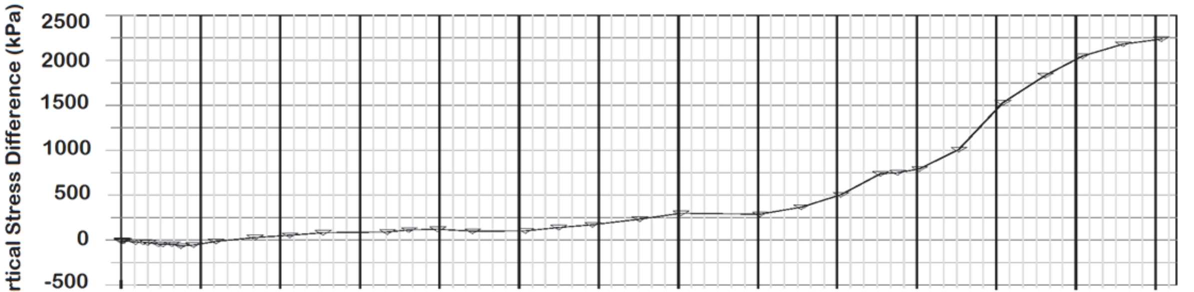

Fig. 7: Results of the additional vertical stress measurement in the dolomite on the XIVth level

It is highly probably that the changes found are linked to the sinking of areas above mine extraction works, and the effects of time-dependent occurrences around the Idrija fault where stress changes have been more intensive in dolomite on the XIVth level, while those in shale on the XVth level are rapidly decreasing.Measurements of secondary stress states on the IVth, VI^{th,} and VIIth levels with triaxial cells for the measurement of stress changes were installed on the IVth level in the beginning of 1996, on the VIIth level in December 1996, and on the VIth level in July 2004. In the most recent period, measurements were performed twice a year in order to determine whether there are any stress changes in consolidated backfills in the broader area, where extensive mining works were performed in the past. The results of measurements shown in Fig. 8 indicate that the time-dependent secondary stresses changes considerably more extensive with no continue trends because consolidated backfills persisted in time intervals.

The substantially increased stress on cells on the IVth level is explained by the fact that the rigidity of old reinforced backfills in the broader areas is incomparably higher than in other backfills, which were not additionally injected or grouted. Results on the VIIth level have shown strain softening deformation process because the lower backfill layers and low bearing ground strata weren’t grouted enough.

6 Evaluation of Adequacy Executed Consolidated Works

It cannot be denied that five centuries of the mine’s operation below the town of Idrija have caused various changes in the mine, the rock structure in the vicinity of the mine, and on the surface. Although mining works were continuously accompanied by backfilling of dug out areas during the mine’s entire operation, the backfills were so deformable that they were unable to prevent surface subsidence.

Also, their rheological characteristics were not such as to reduce subsidence without additional reinforcement measures. Frequent visual inspections of various facilities on the surface have shown that the intensity of time-dependent displacement is gradually decreasing, and that damage in the form of cracks and shear movements has also decreased considerably. In some cases cracks were more open in a specific period, but closed after a number of years.

It may therefore be concluded that the time dependent movements of the surface was not uniform, and that reinforcement measures indirectly influenced the gradual reduction of damage on the surface. Grouted and backfilling works were evaluated based on results of presented measurements and observations which indicate that adequacy of planned and executed procedures were in the expected domain. Retaining walls and other surface civil structures only cracked and damaged to the extent of requiring rehabilitation when the time gradient of deformations will be sufficiently small, or when a differential subsidence rate will be less than 1cm/year. Similar requests can be used in the case of building new structures and rehabilitation works on existing civil facilities.

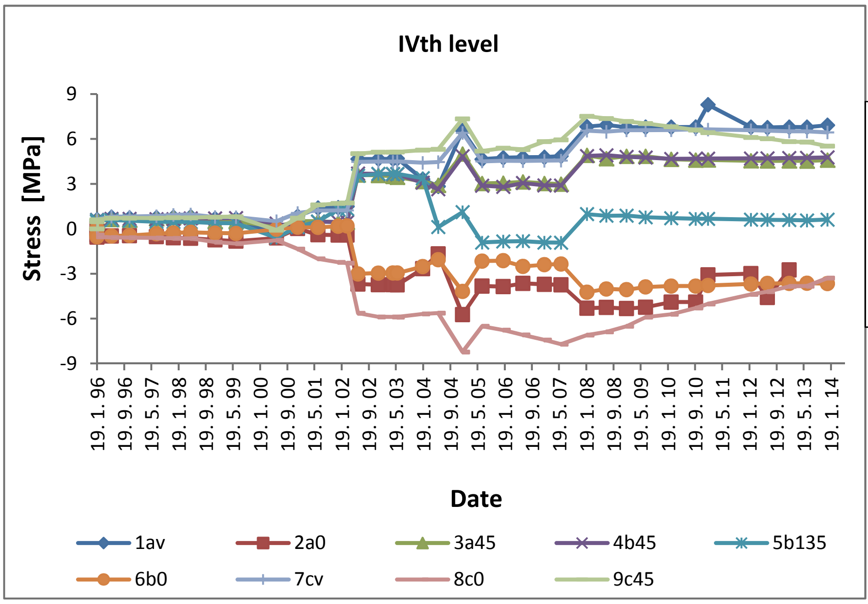

Average Values till January 06

Main stress	σ_1	σ_2	σ_3
Dip (^{0})	61.77	28.22	0.71
Azimuth (^{0})	65.58	153.89	334.27
Value of stress (MPa)	5.06	0.39	-1.42

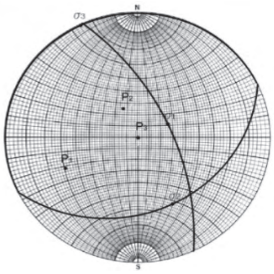

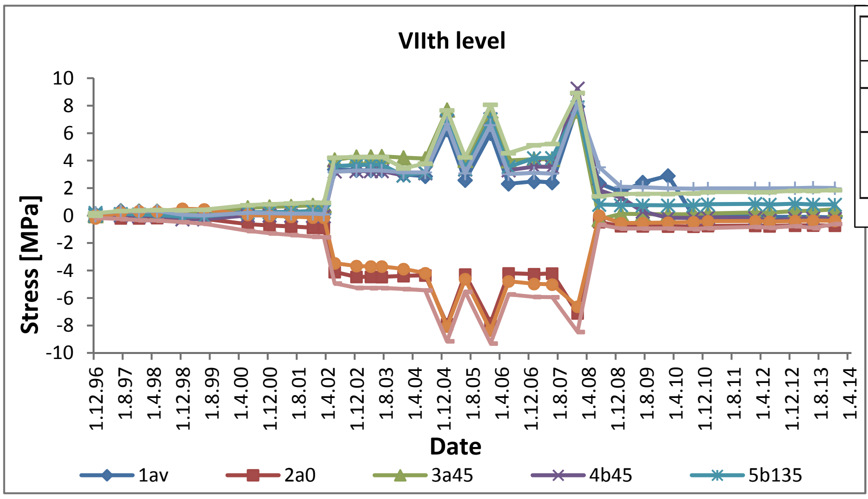

Main stress	σ_1	σ_2	σ_3
Dip (^{0})	59.14	30.77	2.12
Azimuth (^{0})	15.42	110.23	288.97
Value of stress (MPa)	7.84	-0.12	-2.18

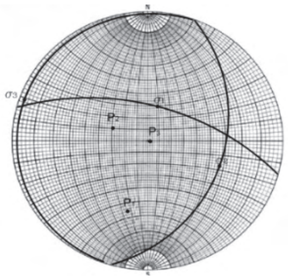

Fig. 8: Stress changes versus time in the consolidated backfill on the IVth level and VIIth level with triaxial cells

The estimation of time-dependent deformations on the surface above the mine has allowed preparing a short time prognosis of the development of the deformation field in the next 10 years. According to the simple linear approximation shown in Fig. 9, the time dependent subsidence can be expected to continue for at least 10 years but with different intensity. A detailed analysis of the time – depend settlements development, which are present in recent years have found lower relative surface deformations which means lower time settlements trends. Some reference measuring points (Fig. 9) have begun to slowly settle around in 2003, and others later, after 2008. This is the result of successfully executed injections and other hardening works at the mine in past decades. Partial settlements increased during intensive injection works were the result of action additional loads that were caused a large amount of mass grouts in the yielding state on the underlying compressible ground layers and old mine backfills.

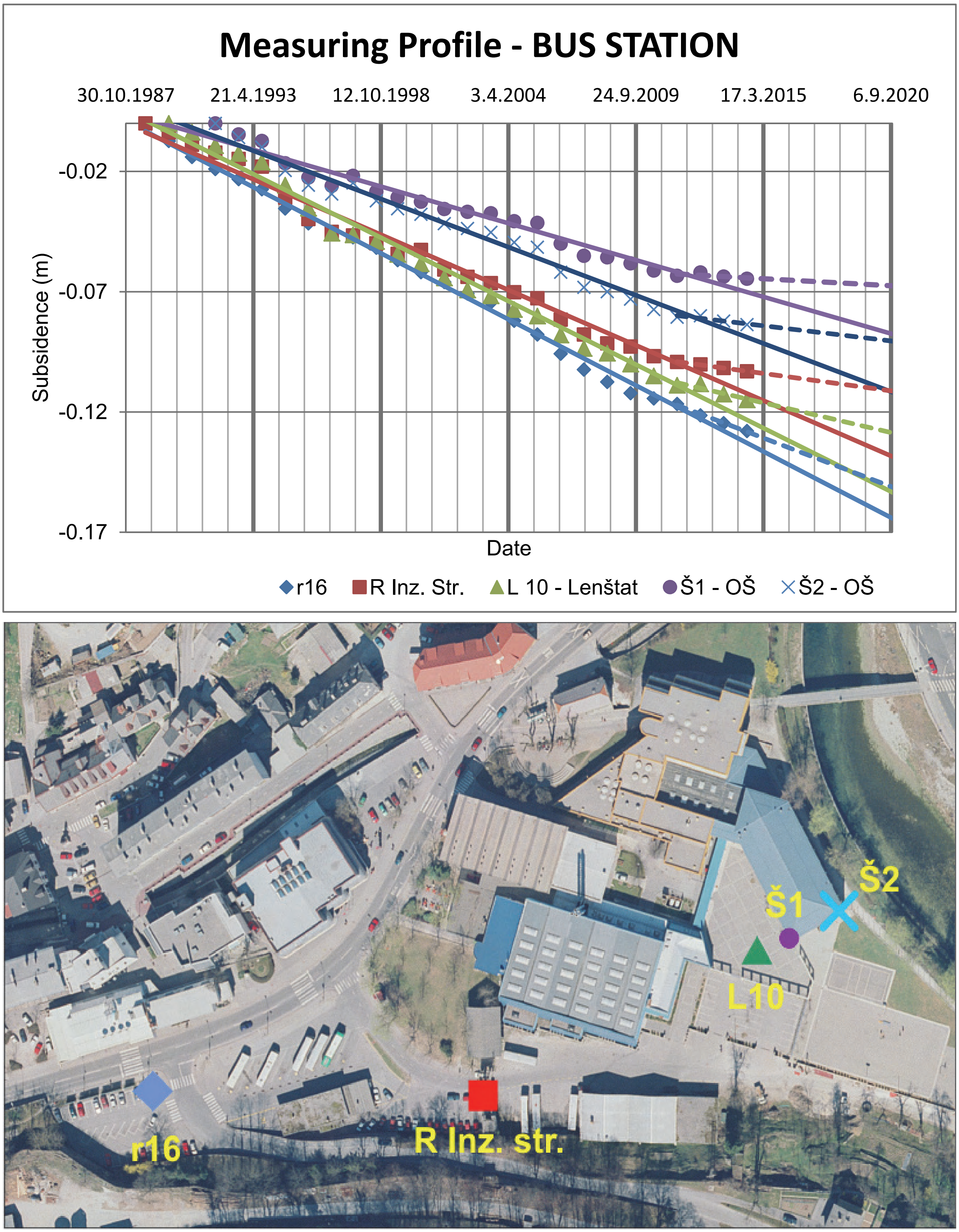

Fig. 9: Estimation of the time dependent settlements of points in measuring profile on the surface above the mine

7 Conclusions

More than five centuries of mining activity in the area below the town of Idrija have caused major changes in the stress strain states of rocks and backfills in the affected areas of the Idrija Mercury Mine. Some implementations of measures for improvement of the rock structure and backfills were done in the period of intensive mercury ore exploitation.

The present complex geological structure in the wider area of the Idrija Mercury Mine, including major tectonic and neo-tectonics occurrences with extreme geological changes are the principal factors which, alongside mining works, continue to influence the development of deformation fields in the mine and on the hilly surface.

In past, before the mine closure works had approved, extensive numerical models were done by checked, proposed, grouted, and other consolidation measures supported by laboratory and in situ investigations in the goal to determine the relevant geotechnical characteristics of rock mass and backfills.

Different measurements and observations were carried out in the mine and on the hilly surface, with particularly attention on making an analysis of time dependent movements of unstable surface areas. Some parts of hilly surface have potential unstable slopes relating to basic very complicated geological structure.

Monitoring which are still active included inclinometric and piezometric measurements, as well as measurements of stress changes using measuring cells, which are still used today and will continue after the completion of the shutdown works and further, depends on risk analysis.

Time-dependent occurrences of potential sliding areas on the surface and in mine rocks and subsidence of artificial backfills are still present, but the intensity of time-dependent movements is considerably reduced.

Analysis and calculation of the development time-dependent surface subsidence shows that in the coming years certain areas can be used to build facilities that will be tolerated by differential settlements around 0.25% (1:400) or smaller.

8 References

[1] Mlakar, I. (1967): Relations between the lower and the upper structure of the Idrija ore deposit (in Sloveni-an). Geologija Spec. Publ., Ljubljana, 10, 87–126.

[2] Mlakar, I. (1969): Krovna zgradba Idrijsko-Žirovskega ozemlja (Upper Structure of the Idrija- Žirovski Vrh Region). Geologija, Ljubljana, 12, 5 –72.

[3] Mlakar, I. and Drovenik, M. (1971): Structural and Genetic Characteristics of the Idrija Ore Deposit (in Slovenian). Geologija, Ljubljana, 14, 67–126.

[4] Mlakar, I. (1974): An Outline of Production of the Idrija Mercury Mine through the Centuries, 1–40 (in Slovenian with English summary).

[5] Placer, L. (1976): Structural Control of the Epigenetic Orebodies of the Idria Ore Deposit (in Slovenian). Rudarsko-metalursˇki zbornik 1, 3–30.

[6] Placer, L. and Čar, J. (1977): Middle Triassic Structure of the Idrija Region
(in Slovenian). Geologija, Ljubljana, 20, 141–166.

[7] Čar, J. (1990): Angular Tectonic-Erosional Unconformity in the Deposit's Part of Idrija Middle Triassic TecTonic Structure (in Slovene with English summary). Geologija, Ljubljana, 31–32, 267–284.

[8] Bajželj,U. 1984. Underhand Cut -and –Fill Stopping Experiments in Carboniferrous
Schists at the Idrija Mine,Symposium AIME, *Society of Mining Engineers of the American Institute of Mining, Metallurgical and Petroleum Engineers ,Inc. New York,* 163-183.

[9]Bajželj, U. & Likar, J. 1991.Analysis of the Stress - deformational State in the
Wider Area of Stopes at the Idrija Mine. *Bolletino della Associazione Mineraria Subalpina, XVIII,n.4, Torino* 699-712.

[10] Cigale, M. 1988. Dolgoročni program postopnega, popolnega in trajnega
zapiranja Rudnika živega srebra Idrija. Idrija1988.

[11] Režun, B. & Dizdarevič, T.1997. The Influence of Surface Waters and Mine Waters on the Closing Down of the Idrija Mercury Mine . *6th IMWA Congress,* Vol. (1): 85-94.

[12] Archive documents, reports, and studies in the Idrija Mercury Mine.

Laboratory and field investigations

Deformation behavior of jointed rock mass-
Lessons learnt from large scale triaxial testing

Zum Deformationsverhalten geklüfteter Felsmasse – Was zeigen uns die Ergebnisse von Großtriaxialversuchen?

T. Mutschler
Karlsruher Institut für Technologie, Institut für Angewandte Geowissenschaften, Karlsruhe

Abstract

The strength and deformation behavior of jointed rock mass (JRM) is a key question of rock mechanics. Rock masses with narrow-spaced systems of discontinuities allow determining this behavior directly on representative elementary volumes (REV) through large scale triaxial tests (LSTT). The strength behavior can be described well by linear boundary conditions of the Mohr-Coulomb type. The stress-strain behavior and the volumetric strain behavior need more complex approaches. This publication summarizes experiences from more than 250 LSTT and shows general results of the deformation behavior of JRM.

Zusammenfassung

Das Festigkeits- und Verformungsverhalten von geklüfteter Felsmasse ist eine Schlüsselfrage der Felsmechanik. Für engständig geklüftete Felsmasse ermöglicht die Großtriaxialversuchstechnik deren Bestimmung direkt an Repräsentativen Elementarvolumen (REV). Während das Festigkeitsverhalten für einen begrenzten Druckbereich sehr gut mit linearen Grenzbedingungen nach Mohr-Coulomb beschreiben lässt, ist das Spannungs-Dehnungsverhalten und das Volumendehnungsverhalten komplexer. Der vorliegende Beitrag fasst die Erfahrungen von mehr als 250 Großtriaxialversuchen zusammen und zeigt grundsätzliche Ergebnisse zum Deformationsverhalten von geklüfteter Felsmasse.

1 Introduction

Large scale sampling and triaxial testing is a method to investigate the mechanical behavior of jointed rock mass (JRM) on representative elementary volumes (REV). It was developed in the 1970ies at Karlsruhe University. The detailed description of the sampling and testing procedure (specimen diameter about 60 cm, height about 120 cm) is given in a Suggested Method of the ISRM-Commission on Testing Methods (Natau, O. and Mutschler, Th., 1989). The wide variety of sedimentary rock masses tested by this method is presented in Natau et. al. (1983).

Fig. 1.1: Sampling equipment (left), flattening of the bottom of the sample (right)

The sampling is based on a drilling technique with a single-core barrel. An annular slot is cut into the rock mass using air-flushing to keep the influence on the water content low and to avoid washout of joint fillings and other loose components. A steal casing is put into the slot and the gap between the sample and the casing is filled-up with plaster. After hardening of the plaster the sample can be pulled out using a truck-mounted crane. The end faces of the sample are flattened and sealed with a layer of plaster in order to avoid desiccation and loosening.

This publication is focused on the evaluation of the testing results and here again on the deformational behavior of JRM. After a short description of the testing procedure and the standard evaluation of the raw data, an extended evaluation of the data within an elasto-plastic concept is presented. JRM behaves elasto-plastic from the very beginning of loading. In most cases viscous behavior occurs too. In order to exclude influences of viscosity the loading rate is kept constant during all tests.

It can be shown that not only the strength behavior but also the deformation behavior is stress dependent. A variation of the confining pressure in the range $0 < \sigma_3 < 1$ MPa e. g. can give a variation of the modulus of elasticity up to a factor of 5. The plastic (anelastic) stress-strain relations are pressure dependent too and can be described by a parabola of 2nd order. The strain reached at the limit stress is pressure dependent too.

2 Testing procedure and evaluation concept

2.1 Testing procedure

Multi-stage testing is used to gain as much as possible information from one sample.

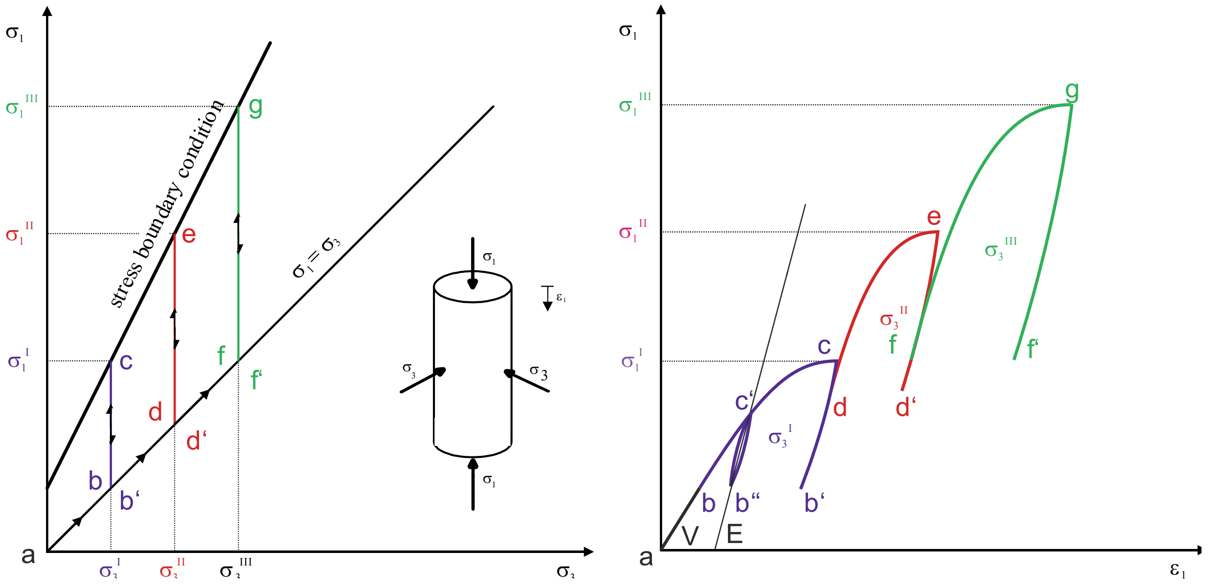

Fig. 2.1: Loading path (left) and stress-strain curve (right)

Fig 2.1 left side shows the loading path of a multi-stage triaxial test (MST). The loading starts with an isotropic increase of the principle stresses σ_1 and σ_3 (a-b). At the desired first confining stage $\sigma_3{}^{I}$ is kept constant (b) and the deviatoric loading is started (b-c). In order to exclude effects of viscosity the loading rate $d\varepsilon/dt$ is kept constant. Unloading-reloading cycles (c'-b''-c') allow separating reversible (elastic) from irreversible (anelastic) behavior. The inclination of a secant on the curve c'–b'' gives the modulus of elasticity E. When the limit state of stress (point c, tangent stiffness zero or below a defined value) is reached, the deviatoric loading is stopped and an unloading to the isotropic state is done (b'). The next testing stage (II) starts again with the isotropic increase of the principle stresses σ_1 and σ_3 to the next confining stage $\sigma_3{}^{II}$ (d). The procedure is repeated up to two times thus having a MST with three confining stages. Sometimes the material allows one or two further confining stages.

2.2 Extended evaluation of testing results

A synopsis of the extended evaluation is given in fig. 2.2. The stresses and strains are calculated from the raw data of the test. Step I is the conventional plotting of the deviatoric stress $q = \sigma_1 - \sigma_3$ over the axial strain ε_1. Unloading-reloading cycles give the modulus of elasticity E. Plotting E vs. σ_3 (II) shows the pressure dependence which can be described by a linear relation (eq. 2.1).

$$E(\sigma_3) = e_1 \cdot \sigma_3 + E_0 \qquad (2.1)$$

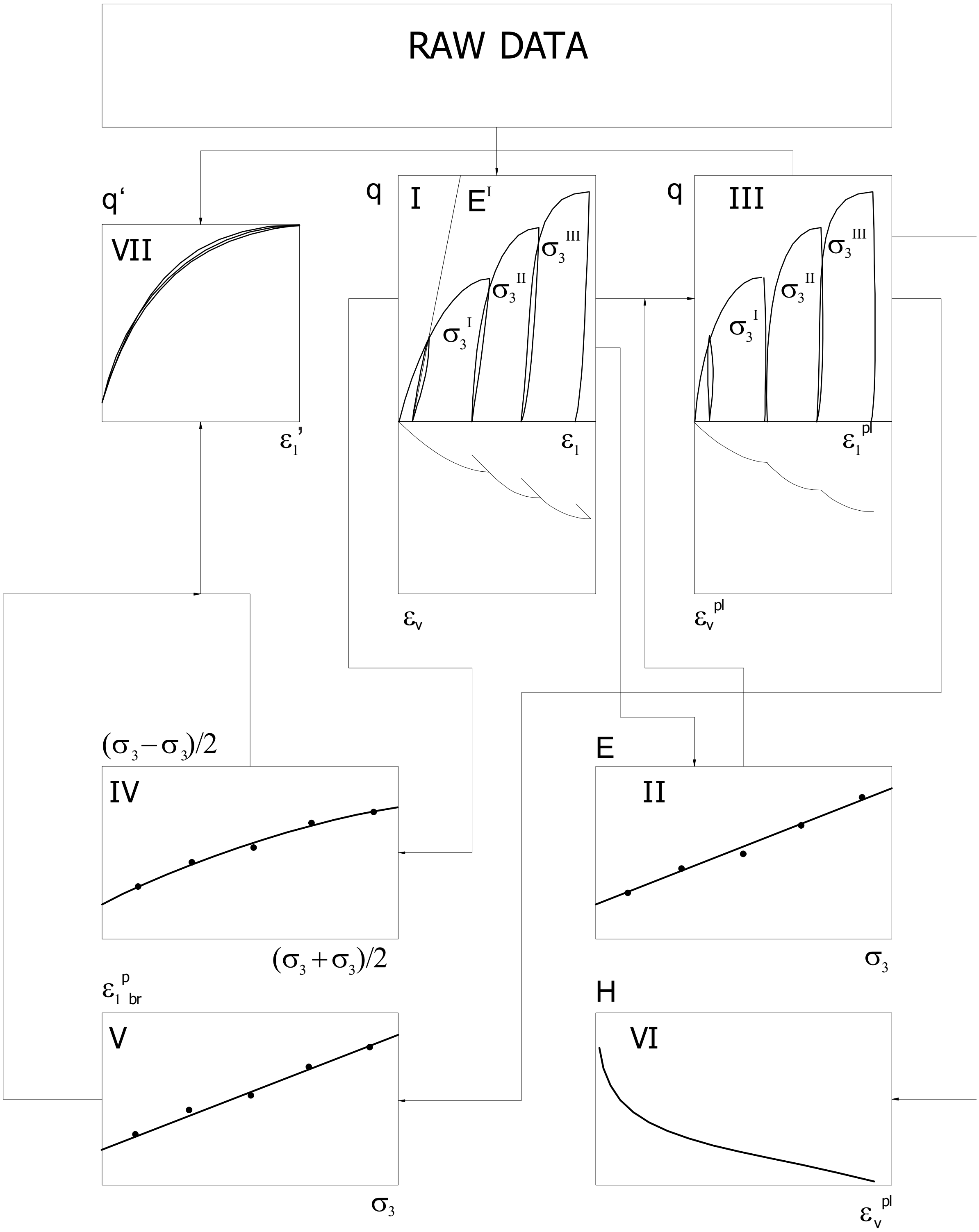

Fig. 2.2: Extended evaluation of LSTT within an elasto-plastic concept: Conventional stress-strain behavior (I), stress dependence of E (II), plastic stress-strain behavior (III), strength behavior (IV), stress dependence of the ultimate strain at the limit deviatoric stress $\varepsilon_1{}^{pl}{}_{br}$ (V), depencence of the tangent stiffness H of the plastic strain $\varepsilon_1{}^{pl}$

The plastic strain ε_1^{pl} (eq. 2.2) is used to plot the plastic stress-strain curve (III).

$$\varepsilon_1^{pl} = \varepsilon_1 - (\sigma_1 - \sigma_3)/E(\sigma_3) \tag{2.2}$$

The limit state of stress is evaluated in a diagram $(\sigma_1^i - \sigma_3^i)/2$ vs. $(\sigma_1^i + \sigma_3^i)/2$ (IV). The stresses σ_1^i and σ_3^i denote the stresses at the limit state (see fig. 2.1). For a limited pressure range a linear boundary condition (eq. 2.3) can be used

$$\frac{\sigma_1 - \sigma_3}{2} = \frac{\sigma_1 + \sigma_3}{2} \sin\varphi + c \cos\varphi \text{ or } \sigma_1 - \sigma_3 = (2\sigma_3 \sin\varphi + 2c \cos\varphi)/(1 - \sin\varphi) \tag{2.3}$$

where φ stands for the friction angle and c for the cohesion.

The plastic strain at the limit deviatoric stress $\varepsilon_1{}^{pl}{}_{br} = \varepsilon_1^{pl}$ $(\sigma_1^l - \sigma_3^l)$ in the first confining is plotted vs. the confining pressure σ_3^l (V). It can be described by a linear relation.

$$\varepsilon_{1,br}^{pl} = D_1 \cdot \sigma_3 + D_0 \tag{2.4}$$

The tangent stiffness of the plastic stress-strain curve $H = dq/d\varepsilon_1^{pl}$ decreases linearly with the plastic strain ε_1^{pl} (VI). This means the plastic stress-strain curve can be approximated by a parabola of 2nd order.

The step (VII) is plotting the normalized plastic stress-strain-curve $q' = q/q_{br}$ vs. $\varepsilon_1^{pl'} = \varepsilon_1^{pl}/\varepsilon_{1,br}^{pl}$ where q_{br} is the deviatoric stress at the limit state and $\varepsilon_{1,br}^{pl}$ is the associated plastic strain.

3 Results

Results are given for a series of LSTT on weathered granodiorite which was sampled from the lower beds of the Grube Messel near Darmstadt. The JRM consists of a green-yellow to green-brown rock substance. The joints are coated with a black-brownish film of a few millimeters thickness. The joint system in the vertically drilled samples is governed by two sets (KK 1: 270°± 20°/50°±15°;KK 2: 000°± 30°/50°± 10°). The joint spacing was 10 to 20 cm. The rock strength was very low. Joint body could be crushed by hand. The grain size distribution gave 55 to 70% silt, 25 to 40 % sand and about 7 % clay. The water content was about 25%.

Fig. 3.1: Weathered Granodiorite from Grube Messel, near Darmstadt, Hessen

The tests were carried out at a confining pressure range $0.1 < \sigma_3 < 1.2$ MPa. The deformation rate was $d\varepsilon/dt = 0.03$ %/min. One test (B2) was carried out with a stepwise variation of the deformation rate over two orders of magnitude.

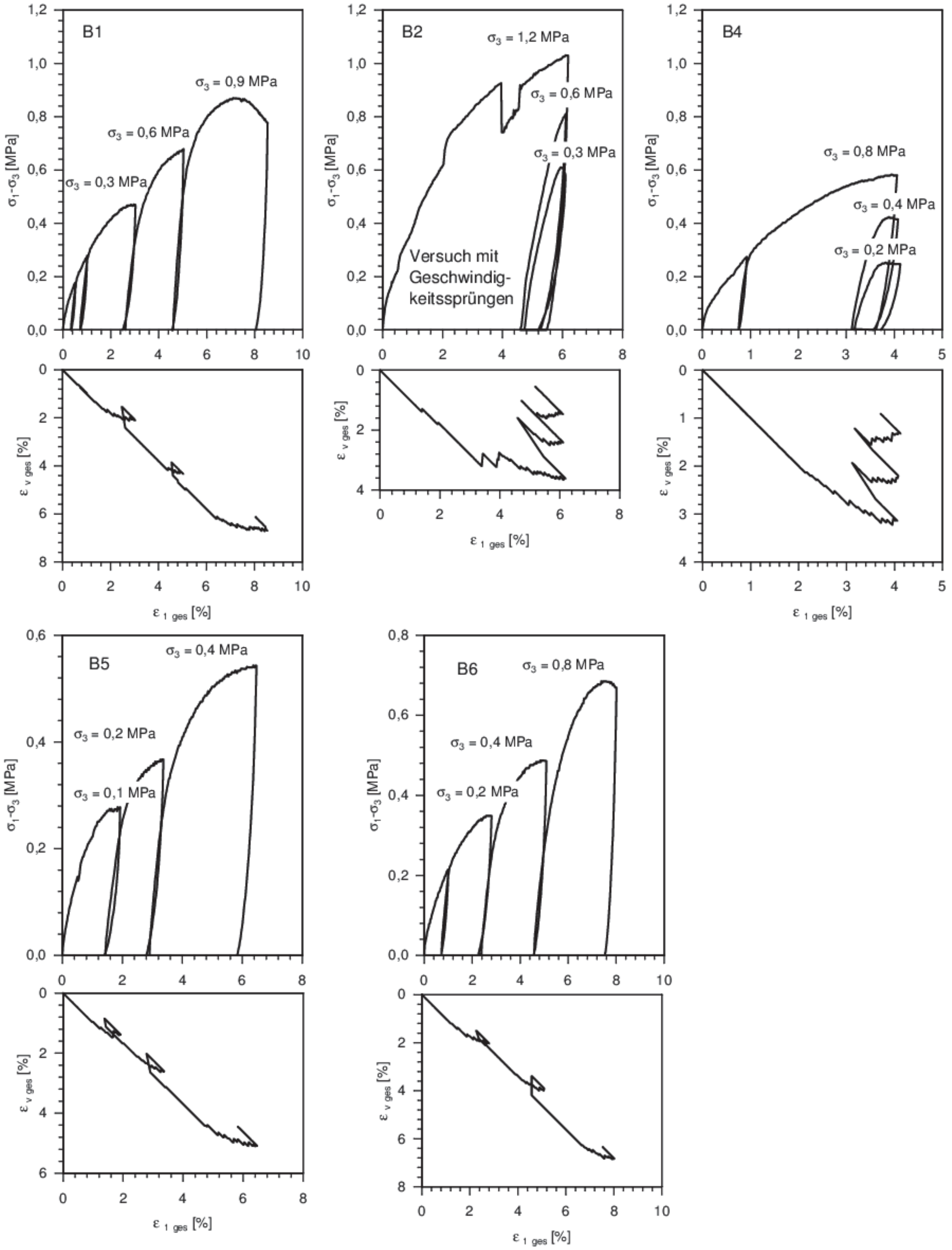

Fig. 3.2: Five LSTT in MST on a weathered granodiorite from Grube Messel near Darmstadt, Hessen, step I plotting the deviatoric stress vs. the total strain (here denoted $\varepsilon_{1,ges}$) and volumetric strain (here denoted $\varepsilon_{v,ges}$) respectively. Test B2 was carried out with stepwise variation of the loading rate, which shall not be handled here.

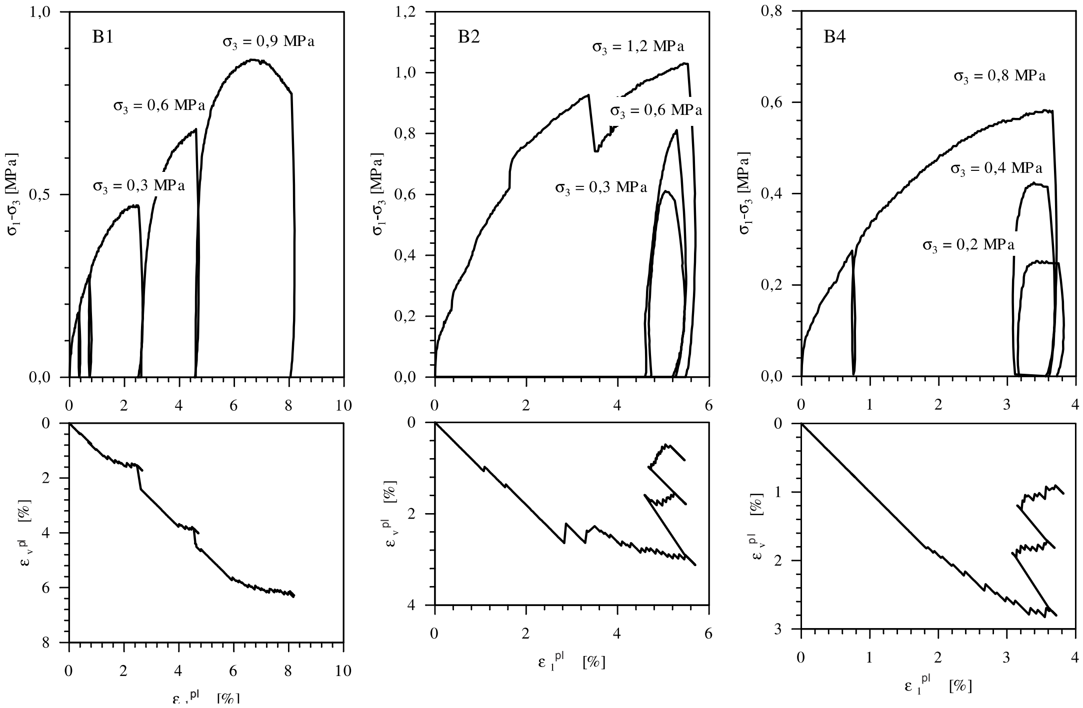

Fig. 3.3: Three of five LSTT in MST on a weathered granodiorite from Grube Messel near Darmstadt, Hessen, step III plotting the deviatoric stress vs. the plastic strain (here denoted $\varepsilon_{1,ges}$) and volumetric strain (here denoted $\varepsilon_{v,ges}$) respectively. Test B2 was carried out with stepwise variation of the loading rate, which shall not be handled here.

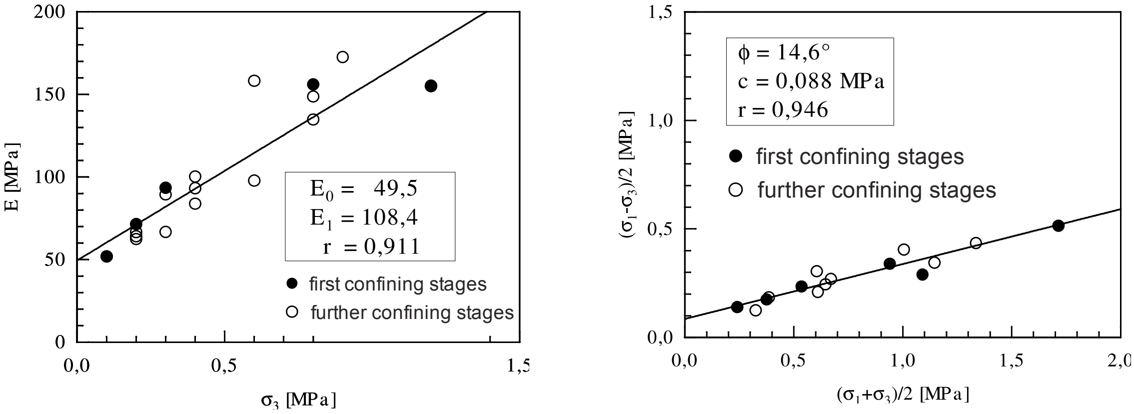

Fig. 3.4: Five LSTT in MST on a weathered granodiorite from Grube Messel near Darmstadt, Hessen, step II plotting of the modulus of elasticity E vs. the confining pressure σ_3 (ledt), step IV plotting of the stress boundary condition

Fig 3.4 shows a good linearity of the stress boundary condition and the dependence of the modulus of elasticity E from the confining pressure σ_3. Fig. 3.5 shows the strain boundary condition which can also be described by an linear relation.

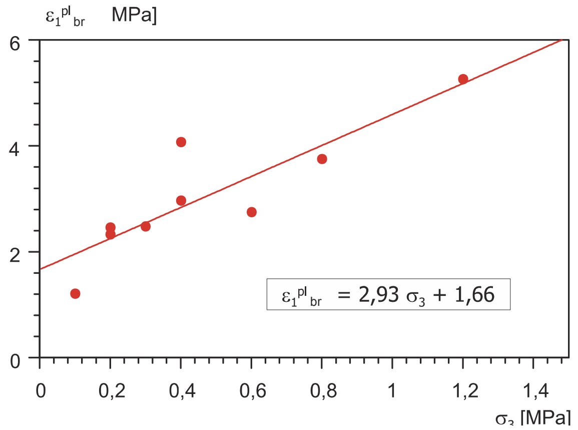

Fig. 3.5: Five LSTT in MST on a weathered granodiorite from Grube Messel near Darmstadt, Hessen, step V plotting of the plastic strain at the limit state of stress $\varepsilon_1{}^{pl}{}_{br}$ vs. the confining pressure σ_3

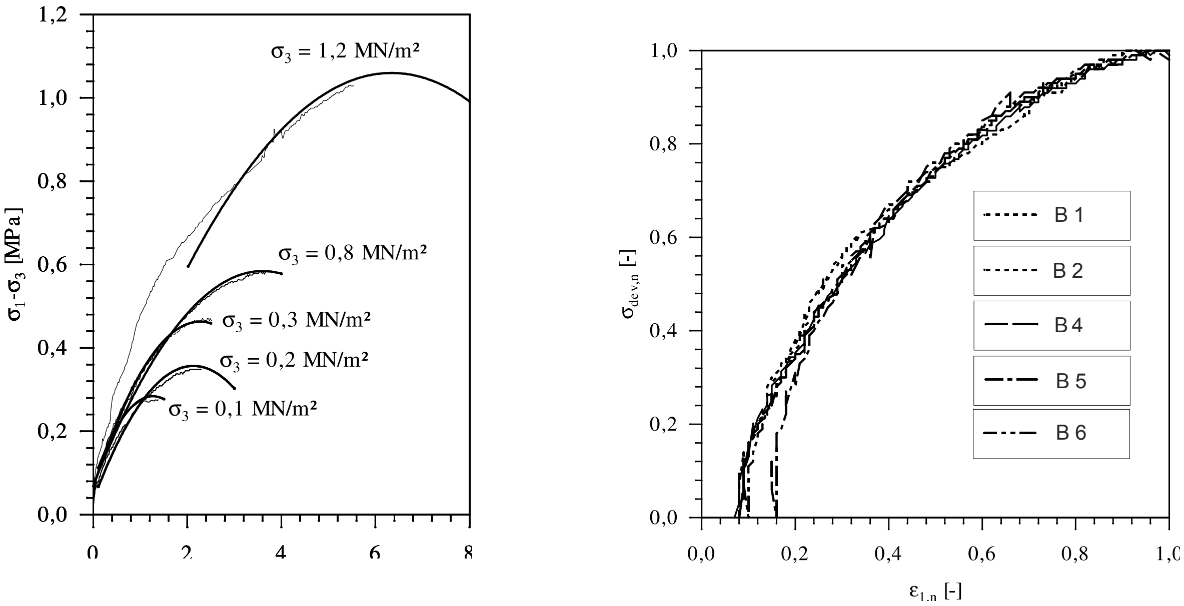

Fig. 3.6: Five LSTT in MST on a weathered granodiorite from Grube Messel near Darmstadt, Hessen, regression of the of the plastic stress-strain curve with parabolas of 2nd order (left) and normalized plastic stress-strain curves (right)

4 Conclusions

The full behavior of JRM can be described by three equations. They are the stress boundary condition (eq. 2.3 left), the stain boundary condition (eq. 2.4) and the pressure dependence of the elasticity (eq. 2.1). In the case of reloaded material (e. g. if an overburden is removed) a boundary of elasticity might be necessary. The curvature between the boundary conditions can described by a parabola of 2nd order (see fig 3.6, right).

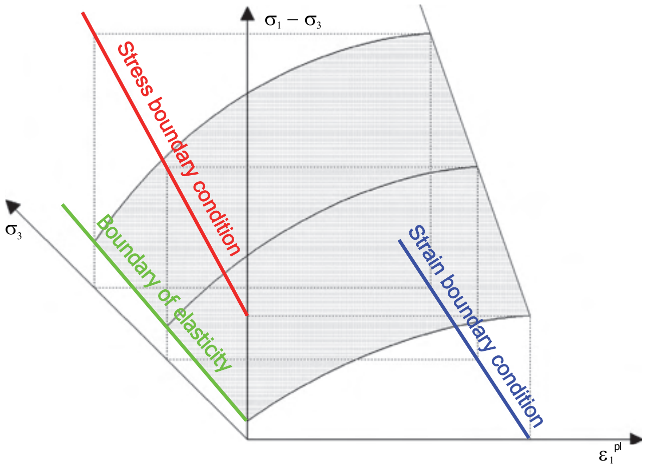

Fig. 4.1: Material law for JRM.

5 References

Natau, O. and Mutschler, Th. (1989): *Suggested Method for large scale sampling and triaxial testing of jointed rock*. Int. J. Rock. Mech. Min. Sci. & Geomech. Abstr. Vol. 26, No. 5. pp. 427-434

Natau, O., Fröhlich, B. and Mutschler, Th. (1983): *Recent developments of the large-scale triaxial test.* 5. Int. Kongress der ISRM, Melbourne, 1983

Experimental Evaluation of Frozen Red Sandstone at Water-rich Mesozoic Strata in Northwest-China

Experimentelle Untersuchungen von gefrorenem roten Sandstein aus wasserreichen mesozoischen Schichten im Nordwesten Chinas

B. Liu, N. Liu, D. Li
School of Mechanics and Civil Engineering, China University of Mining
and Technology at Beijing

Abstract

The mechanical properties of frozen red sandstone in water-rich Mesozoic strata in northwest territory were measured in uniaxial compression and triaxial compression tests under freezing temperature of -5°C, -10°C and -15°C. The strength properties, (UCS, internal friction angle and cohesion) of saturated red sandstone at three different freezing temperature were measured. Under each confinement, when temperature drops from -5°C to -15°C the strength of red sandstone increases by 37 % at the maximum. The internal friction angle increases by 11.6 % but the cohesion does not change. The ultimate axial strain increases little when the temperature decreases and the plasticity deformation capacity of frozen red sandstone is improved. The elastic modulus only slightly decreases with the drop of temperature.

Zusammenfassung

Die mechanischen Eigenschaften von gefrorenem roten Sandstein aus wasserreichen mesozoischen Schichten aus dem nordwestlichen Territorium wurden bei -5°C, -10°C und -15°C mittels einaxialer und triaxialer Druckversuche untersucht. Die Festigkeitseigenschaften (einaxiale Druckfestigkeit, Reibungswinkel und Kohäsion) des gesättigten roten Sandsteins wurden bei 3 unterschiedlichen Frosttemperaturen gemessen. Bei jedem Manteldruck stieg die Festigkeit des roten Sandsteins bis um 37 %, wenn die Temperatur von -5°C auf -15°C erniedrigt wurde. Der Reibungswinkel erhöhte sich um 11.6 %, die Kohäsion aber blieb konstant. Die axiale Deformation im Bruchpunkt erhöht sich leicht, wenn die Temperatur sinkt und das Potential der plastischen Deformation des gefrorenen Sandsteins verbessert sich. Der Elastizitätsmodul verringert sich nur wenig, wenn die Temperatur sinkt.

1 Introduction

More and more coal mines will be constructed in Northwest coal-rich region in China to meet the nation’s energy demand. In these regions, deeply buried coal seam, thin alluvium, fissured water-rich rock layers make water-inrush at work face a very serious problem and freezing method becomes a unique way to construct deep coal mine shaft[1]. The research on physical and mechanical properties of water-rich soft rock in freezing condition has significant engineering value.

Frozen rocks were encountered in mining engineering[2], underground liquefied natural gas storage engineering[3] and gas hydrate exploitation engineering[4], but there were only a limited number of experiments that have been performed to study the physical and mechanical properties of frozen rocks[5]. Kodama investigated the effects of water content, temperature and loading rate on frozen tuff and andesite and suggested that the increase of frozen rock is caused by the reduction in the stress concentration within the samples and the increase of tensile strength [6]. Tang and Wang conducted uniaxial and triaxial compression tests on Jinzhou granite under different temperatures and showed that the strength increases nonlinearly with the decrease of temperature but becomes stabilized when temperature is below -40°C. The cohesion and internal friction angle of saturated granite also increases with the drop of temperature[3].Li conducted uniaxial compression test on both dry and saturated granite and argued that the increase of strength under freezing condition is caused by thermal effect, and the expansion force of pore ice plays a secondary role[7]. All these research subjects were tackling hard rocks in construction, but they are rarely present in mining shaft construction in west China.

Yang[5] conducted uniaxial and triaxial compression tests on coal rock, sandstone and sandy mudstone and found that, because of the increase of water content, sandstone was more sensitive to temperature, the strength increases more with the decrease of temperature. Confinement improves the plastic deformation ability of coal rock and sandstone[8-11]. Xu[12] studied how the strength (cohesion and internal friction) and stiffness of Jiangxi red sandstone and Hubei shale with different water content vary with temperature from -20°C to +20°C and suggested that uniaxial compressive strength changes very little when the temperature is above -5°C, but increases with further drop of temperature; cohesion and internal friction angle of saturated red sandstone increase when temperature drops. Liu and Wang[13] suggested that the relationship between the strength of cretaceous rock and temperature fits well with quadratic function and sandstone property is impacted more significantly by temperature.

The Mesozoic strata in northwest China are coal-bearing strata, more and more new-built coal mines have to penetrate through Jurassic strata and Cretaceous strata, the rocks in these strata have weak cementation, high porosity and low strength. The properties of the rock in these regions are not very clear. In order to meet the need of design and construction of freezing shaft sinking in water-rich Mesozoic strata, uniaxial and triaxial compression experiments at different low temperatures are necessary.

2 Experimental conditions

The red sandstone samples used in the experiments were drilled from water-rich Mesozoic strata at 500 – 600 m below the ground surface in Meilinmiao main shaft at

Erdos in Inner Mongolia. The samples appeared in reddish-brown and contained coarse grain. In water circumstances, the samples had low strength and demonstrated argillic alteration phenomenon.

2.1 Sample preparation

Fresh big masses of rocks from the construction site were wrapped with fresh-keeping film and delievered to the laboratory for sampling immediately. In order to control the discreteness of the physical and mechanical properties of the samples, the rocks were visually inspected before sampling, the rocks with obvious different color and ingredient were abandoned. The rocks were drilled, cut and polished into cylinder samples following Chinese national standard[14], the samples were 80 mm in height and 39.1mm in diameter, dimensional variation of the samples met the demand of the relevant standards, as shown in Fig.2.1. All samples were immersed in water for 7 days to make sure they were fully saturated, the water on the surface of the samples was dried, then the samples were wrapped with fresh-keeping film and put into cryostat cooler. When the temperature dropped to the test temperature, all samples were preserved in the cryostat for another 24 hours. The basic physical properties are listed in table 1.1.

Fig. 2.1: Red sandstone specimen

Tab. 1.1: Physical parameters of red sandstone

Lithology of the samples	Dry density g/cm^3	Saturated density g/cm^3	Porosity %	Saturated water content %
Red sandstone	1.941	2.150	20.9	10.81

2.2 Test parameters

The compression tests with or without confinement were conducted with TDW-200 frozen rock triaxial test system. The system is configured with servo control system, axial loading system, confinement loading system, measuring system and cryogenic system, the schematic diagram of TDW-200 is presented in Fig. 2.2. There are two heat exchangers inside and outside the pressure cell and the heat transfer rate can be adjusted by cryogenic system, which can provide a stable negative temperature environment to the samples. Three temperature sensors are laid inside the pressure cell to monitor the temperature at the upper, middle and lower part of the testing sample. Loading system can provide 200 kN axial force and 30 MPa confining pressure. Cryogenic system can provide -40°C testing environment with accuracy of ±0.2°C

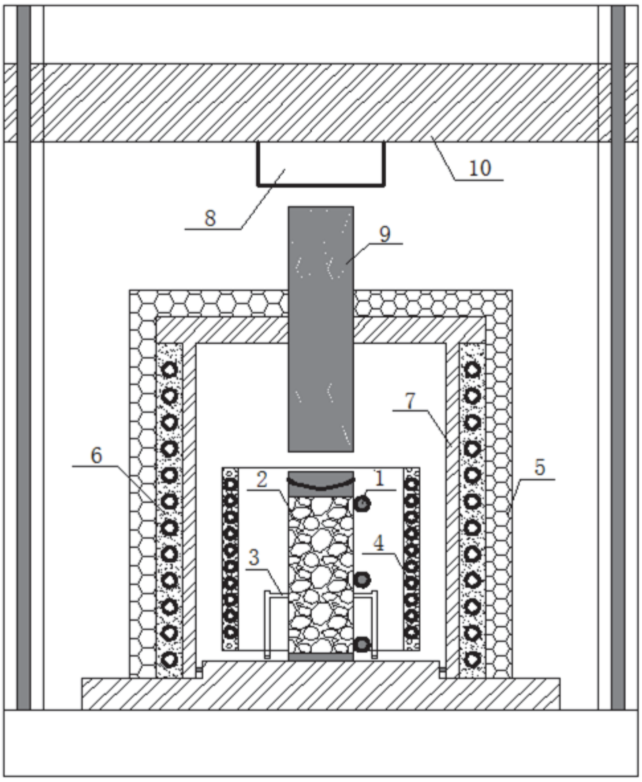

1 - temperature sensor; 2 - sample; 3 - radial extensometer; 4 - internal heat exchanger; 5 - heat preservation cover; 6 - outside heat exchanger; 7 - pressure cell;8 - pressure sensor; 9 - axial loading bar; 10 - axial loading beam

Fig. 2.2: Schematic diagram of frozen rock triaxial apparatus

The confining pressure applied on the testing sample was calculated by the formula:

$$P = 0.013H \qquad (1)$$

where P is horizontal formation pressure in unit of MPa, H is stratum depth in unit of m.

The rocks in this experiment were taken from strata 500 ~ 600 m below ground, but in field construction, the depth of the mining shaft reached 800 m. In order to represent stress conditions at different depths, the confining pressure was set to 0 MPa, 4 MPa, 8 MPa and 12 MPa.

2.3 Testing Temperature

In reference to Chinese coal industry standard about physical and mechanical tests of frozen soil[15], -10°C was chosen as one of the test temperature, in consideration of the limit of test system, - 15°C was the minimum temperature of the testing temperature, and at construction site, the temperature of outer ring of the frozen wall was relatively high, i.e., around -5°C. Therefore, the testing temperatures were set to -5°C, -10°C and -15°C.

2.4 Experimental process

After the testing machine was ready, the sample was taken from the cryostat, wrapped with latex film and then placed on the testbed quickly. After centering, the pressure cell was put down and covered with heat preservation cover and filtered with low temperature silicon oil. The sample was preserved in pressure cell for another 2 hours after the temperature dropped to testing temperature, assuring the uniformity of temperature in the sample.

Axial loading mode in the test was displacement-controlled loading with a rate of 0.1 mm/min. Confining pressure loading rate was 0.5 MPa/sec. During loading confining pressure, axial load and confinement were applied synchronously.

3 Test results and analysis

The stress-strain curves of frozen red sandstone under different confinements at the temperature of -5°C, -10°C and -15°C are presented in Fig. 3.1.

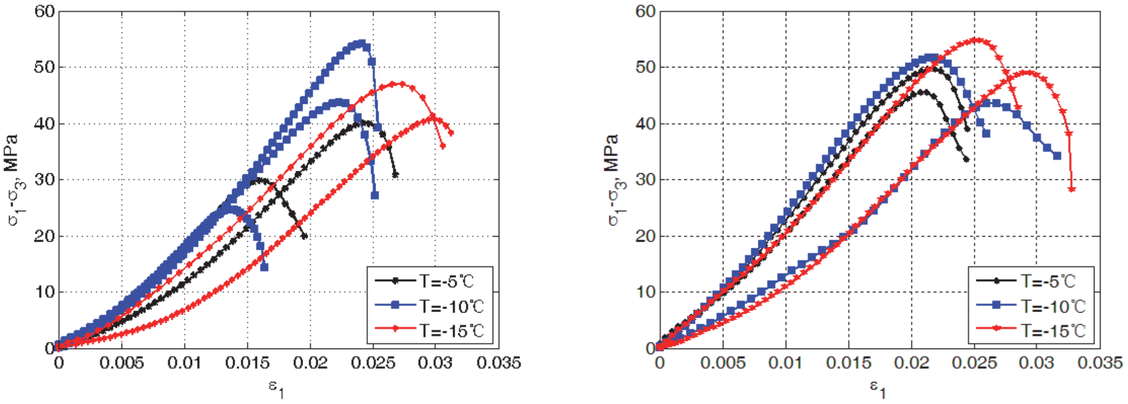

(a) σ_3=0 MPa (b) σ_3=4 MPa

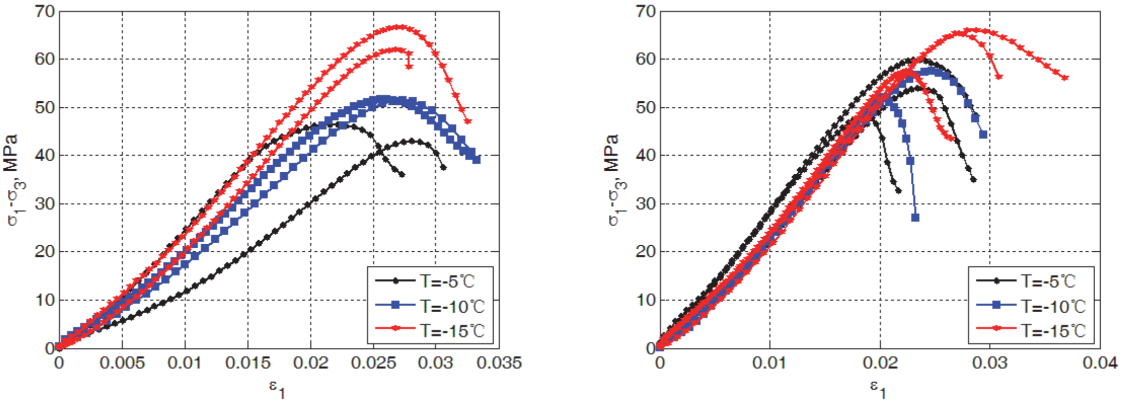

(c) σ_3=8 MPa (d) σ_3=12 MPa

Fig. 3.1: Deviator stress vs. axial strain curves of red sandstone

The stress-strain curves of red sandstone may be divided into four phases: initial compaction phase, linear increase phase, plastic yielding phase and plastic softening phase. As the strength of pore ice is lower than that of red sandstone grain, at initial compaction stage, the closure of micro crack and the crushing of red sandstone particle into pore ice is producing large sample deformations. The lower the temperature, the larger the frost damage, so in general, under each confinement, the slopes of stress-strain curves at -15°C were smaller than those at -5°C in the initial phase. With the increase of confinement, the slopes of the curves in initial phase and linear increase phase show less and less difference and the distances between the curves decreased. When the confinement reached 12 MPa, slopes of the curves in the first two phases had very little difference, this indicated that the confinement of 12 MPa can compact the frozen samples at different temperature to the same compactness. Under this confinement, the elastic properties of skeleton and cementation were almost the same, i.e., the temperature only had little influence. The stress-strain curves with confinement of 12 MPa under three negative temperatures were perfectly coincided before plastic yielding took place, which indicated that temperature did not influence the properties of frozen red sandstone under high confinement before yielding. But, after yielding, the curves varied a lot, and the peak stress varied with temperature too.

3.1 The influence of temperature and confinement on strength properties

The strength of red sandstone under different confinement at temperature of -5°C, -10°C and -15°C are reported in Table 3.1.

Tab. 3.1: Strength of red sandstone

T(℃)	Compression strength σ_f (MPa)							
	σ_3 =0 MPa		σ_3 =4 MPa		σ_3 =8 MPa		σ_3 =12 MPa	
-5	40.02	29.92	53.73	49.48	51.02	54.39	71.79	66.00
-10	43.67	48.22	47.61	55.63	59.44	59.61	69.56	64.03
-15	47.02	40.69	52.93	58.73	69.86	74.52	77.30	77.93

As seen in Table 3.1, confinement has evident influence on the strength of red sandstone. At the temperature of -5°C, -10°C and -15°C as the confinement increased from 0 MPa to 12 MPa, the strength of red sandstone increased by 72.16 %, 45.38 % and 76.97 %. The linear fitting between the strength and confinement is shown in Fig. 3.2. The correlation coefficients are 0.9126, 0.9447 and 0.9384, respectively. Relatively good match is observed.

Under each confinement, the relationship between the strength of red sandstone and the temperature is shown in Fig. 3.3.

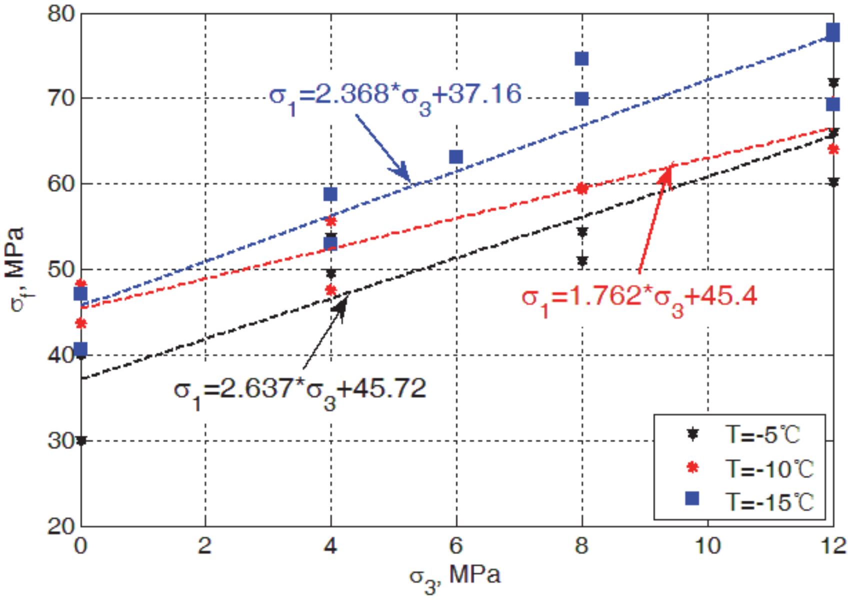

Fig. 3.2: Relationship between sandstone strength and confining pressure

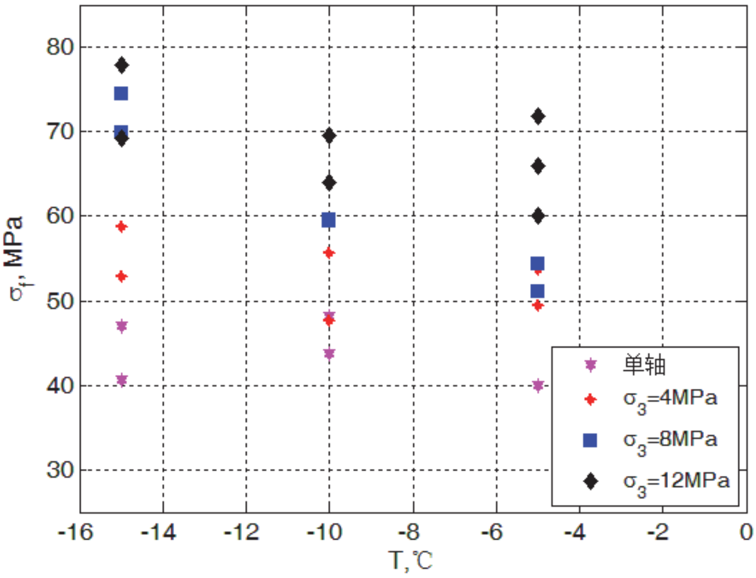

Fig. 3.3: Relationship between red sandstone strength and temperature

As seen from Table 2 and Fig. 5, the uniaxial compression strength (UCS) increased by 31.4 % when temperature dropped from -5°C to -10°C, but when the temperature dropped to -15°C, the uniaxial compression strength did not increase. Under the confinement of 4 MPa, 8 MPa and 12 MPa, when the temperature dropped from -5°C to -15°C, the triaxial compression strength increased by 7.9 %, 37.0 % and 12.7 %. Under frozen condition, temperature had a limited impact on the strength of red sandstone, so in freezing construction in red sandstone, it was not necessary to lower the temperature of the freezing wall too much, e.g., it was acceptable as long as the freezing wall can seal the water.

3.2 The influence of temperature on shear strength parameters

Based on Mohr-Coulomb criterion, Mohr circles and strength envelopes were drawn as shown in Fig. 3.4. The shear strength parameters are list in Table 3.2.

Tab. 3.2: Shear strength parameters of red sandstone at different temperatures

T(℃)	tan(φ)	Internal friction angle φ (deg)	cohesion c (MPa)
-5	0.45	24.22	13.0
-10	0.41	22.29	14.5
-15	0.55	28.81	13.0

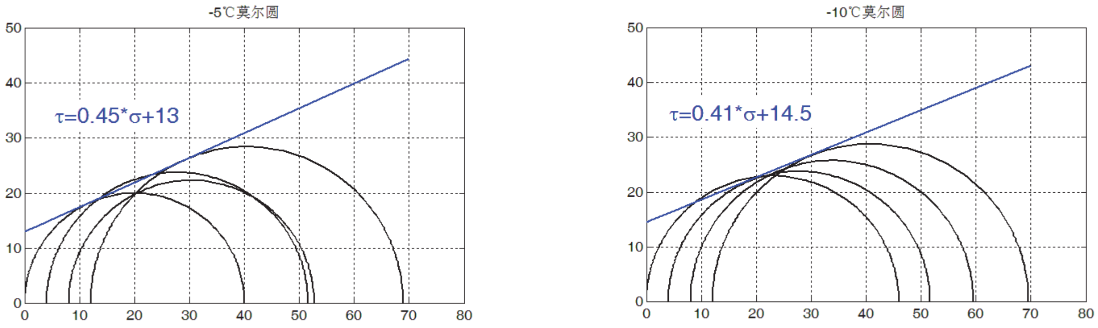

(a) T=-5℃ (b) T=-10℃

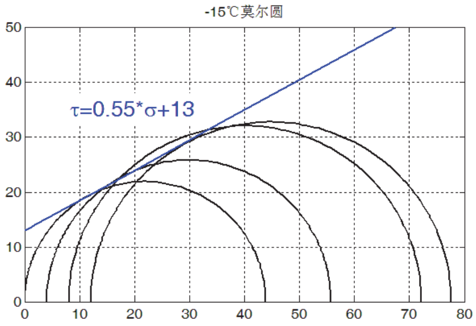

(c) T=-15℃

Fig. 3.4: Relationship between red sandstone strength and temperature

Internal friction angle increased by 11.6 % when the temperature dropped from -5°C to -15°C. With the decrease of temperature, the unfrozen water content reduces, which reduces the lubricative effect. Pore ice with increasing strength made the shear surface tougher. These two factors increased the internal friction angle. But, the pore ice content was not very high, so the increase of internal friction angle was limited.

As shown in Fig. 3.2, the slope of fitting line at -10°C was obviously smaller than the others, which is acceptable considering that the strength of frozen red sandsone under confinement of 12 MPa was abnormally low. So cohesion at -10°C was relatively high. But, when temperature dropped to -15°C the cohesion equaled to that at -5°C. This suggested that temperature had little influence on the cohesion of frozen red sandstone.

3.3 The influence of temperature on elastic modulus

Testing standard[15] stated that the modulus of frozen soil should be calculated based on the definition of secant modulus. But discreteness of the samples and testing conditions can increase the discreteness of stress-strain curves[16], especially in the initial compaction phase, furthermore, in practical engineering, rocks are exposed to specific stress conditions, so the average elastic modulus which is the slope of a straight line along the stress-strain curve is preferable to reflect the properties of the rocks. Hence, the average elastic modulus is chosen in the analysis.

Some individual abnormal data were eliminated and the average elastic modulus of each sample under different testing conditions are listed in Table 3.3. The relationship between elastic modulus and temperature is shown in Fig. 3.5.

Tab. 3.3: Elastic modulus of red sandstone

T(℃)	Average elastic modulus *E*(Mpa)								
	σ_3 = 0 MPa		σ_3 = 4 MPa		σ_3 = 8 MPa		σ_3 = 12 MPa		
-5	2217.09	2242.84	2653.14	2441.01	1890.20	2859.93	2997.48	2608.45	2889.57
-10	2289.88	1143.41	1888.54	2823.05	2221.97	2344.76	2775.68	2719.57	-
-15	2113.67	1899.45	2164.46	2400.53	2764.11	2825.77	2820.70	2643.95	2643.95

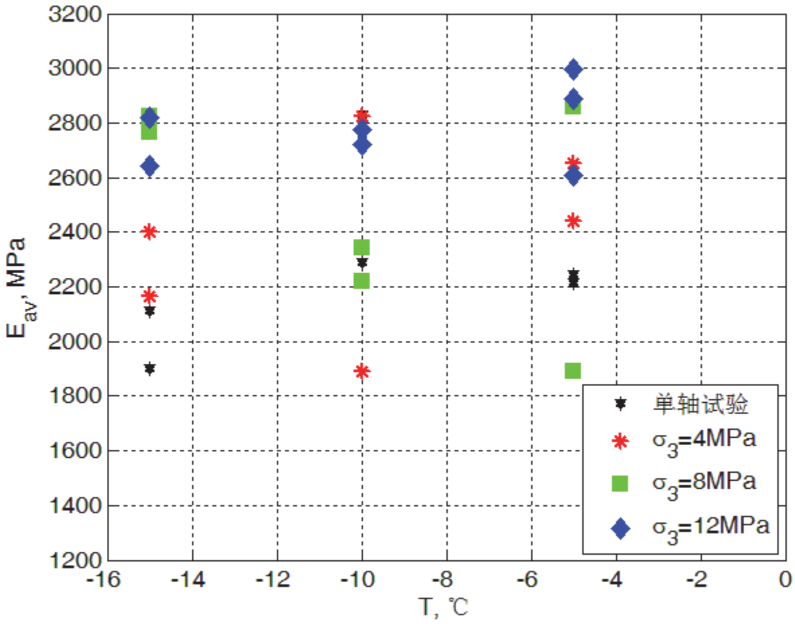

Fig. 3.5: Relationship between elastic modulus and temperature of red sandstone

As seen in Fig. 3.5, three sets of data with the confinement of 0 MPa, 4 MPa and 12 MPa indicated that the elastic modulus decreased with the drop of the temperature, but not that much. This may be explained by the damage induced by freezing heave, i.e., as the temperature dropped, the damage increased, but because the porosity of red sandstone is small and the pore water content is low, the influence of this damage is limited, therefore, the modulus decreased only slightly.

4 Conclusion

Uniaxial compression and triaxial compression tests with confinement of 4 MPa, 8 MPa and 12 MPa were conducted on the red sandstone drilled from water-rich Mesozoic strata under the temperatures of -5°C, -10°C, -15°C. Based on the experimental results, three conclusions can be drawn:

(1) the strength of red sandstone increases with the drop of temperature, but not that much.
(2) the internal friction angle increases by 11.6 % at the maximum, but the temperature has little influence on the cohesion of frozen red sandstone.
(3) the stiffness only slightly decreases when the temperature drops, in other words, the temperature has very limited influence on the stiffness.

5 Acknowledgment

The authors sincerely thanks the following agents for their financial supports: National Natural Science Foundation of China (Grant No. 51274209, 41472259, 51304215, U1261212), The National Science and Technology Support Program Project (Grant No. 2012BAK24B0201), Research Fund for the Doctoral Program of Higher Education (Grant No. 20110023110004). The authors thank Dr. Yanhui Han for his valuable suggestions.

6 Reference

[1] Cui Guangxin. Frozen soil mechanics for deep alluvium- a new field of frozen soil mechanics[J]. Journal of Glaciology and Geocryology, 1998, 20(2): 97-99.

[2] S.A. Ghoreishi-Madiseh, F. Hassani, A. Mohammadian, et al. Numerical modeling of thawing in frozen rocks of underground mines caused by backfilling[J]. International Journal of Rock Mechanics & Mining Sciences, 2011, 48: 1068-1076.

[3] Tang Mingming, Wang Zhiyin, Sun Yili, et al. Experimental study of mechanical properties of granite under low temperature[J]. Chinese Journal of Rock Mechanics and engineering, 2010, 29(04): 787-794.

[4] Naval Goel, Joao Tadeu V De Sousa, Joseph Flenniken, et al. Fabrication and testing of apparatus for laboratory simulation of Alaska frozen rock encountered during hydrate gas reservoir coring[J]. Journal of Cold Regions Engineering, 2004, 18: 53-69.

[5] Yang Gengshe. A review on frozen rock mechanics [J]. Mechanics in Engineering, 2009, 31(2): 9-16, 29.

[6] J. Kodama, T. Goto, Y. Fujii, et al. The effects of water content, temperature and loading rate on strength and failure process of frozen rocks[J]. International Journal of Rock Mechanics & Mining Sciences, 2013, 62: 1-13.

[7] Li Yunpeng, Wang Zhiyin. Uniaxial compressive mechanical properties of rock at low temperature[J]. Journal of University and Technology Beijing, 2011, 33(6): 671-675.

[8] Yang Gengshe, Xi Jiami, Wang Zongjin, et al. Study on rock mechanical properties of frozen wall of main shaft in Hujiahe coal mine[J]. Journal of China Coal Society, 2010, 35(4): 565-570.

[9] Yang Gengshe, Xi Jiami, Shao Xuemin, et al. Experimental test on the strength of rocks underfreezing condition[J]. Journal of Xian University of Science and Technology, 2010, 30(01):14-18.

[10] Yang Gengshe, Xi Jiami, Li Huijun, et al. Experimental study of rock mechanical properties under triaxial compressive and frozen conditions[J]. Chinese Journal of Rock Mechanics and engineering, 2010, 29(03): 459-464.

[11] Yang Gengshe, Lv Xiaotao. Experimental study on the sandy mudstone mechanical properties of shaft sidewalls under the frozen conditions[J]. Journal of Mining & Safety Engineering,2012, 29(4): 492-496.

[12] Xu Guangmiao, Liu Quansheng, Peng Wanwei, et al. Experimental study on basic mechanical behaviors of rocks under low temperatures[J]. Chinese Journal of Rock Mechanics and engineering, 2006, 25(12): 2502-2508.

[13] Liu Ying, Wang Renhe, Chen Junhao. Experimental study on physical mechanics performances of cretaceous system rock under minus temperature[J]. Coal Engineering, 2011, 1:82-84.

[14] National Standard of People‘ Repulic of China. GB/T 23561-2009 China Standard Book Number[S]. Beijing: Standards Press of China, 2009

[15] Coal Industry Standard of People‘ Repulic of China.MTT 593-2011 China Standard Book Number[S]. Beijing: China Coal Industry Publishing House, 2009

[16] You Mingqing. Mechanical properties of rocks[M].Beijing: Geological Publish House, 2007. 91-92

Hydraulic fracturing – laboratory experiments, acoustic emissions and fracture mechanics

Hydraulische Risserzeugung – Laborexperimente, Schallemissionsanalyse und Bruchmechnik

F. Stoeckhert, S. Brenne, M. Molenda, M. Alber
Ingenieurgeologie / Felsbau, Ruhr-Universität Bochum

Abstract

To examine hydraulic fracturing processes in highly anisotropic rocks like slate, we performed a series of hydraulic fracturing laboratory experiments under uniaxial as well as triaxial loading. Cubic specimens with edge lengths of 150 mm and a central borehole with a diameter of 13 mm were prepared from Fredeburg slate. An experiment using Bebertal sandstone as a rather isotropic rock was also performed. Hydraulic fractures were generated using the sleeve-fracturing technique, where a polymer tube placed inside the borehole is pressurized to generate the fractures. This technique was used in order to exclude fluid-rock interaction and poroelastic effects.

In the uniaxial test series, the loading was varied in order to observe the transition from strength-dominated fracture propagation at low loading magnitudes to stress-dominated fracture propagation at high loading magnitudes.

Zusammenfassung

Um hydraulische Rissausbreitungsprozesse in stark anisotropen Gesteinen wie Schiefer zu untersuchen, wurde eine Reihe von Hydrofrac-Laborversuchen unter einaxialer und dreiaxialer Belastung durchgeführt. Kubische Proben mit Kantenlängen von 150 mm mit einem zentrischen Loch von 13 mm Durchmesser wurden aus Fredeburg-Schiefer hergestellt. Ebenfalls wurden Experimente am eher isotropen Bebertal-Sandstein durchgeführt. Hydraulische Risse wurden mittels ‚sleeve-fracturing‘-Technik erzeugt, wobei eine Polymer-Röhre ins Bohrloch eingesetzt und mit Druck beaufschlagt wurde, um Risse zu erzeugen. Diese Technik wurde eingesetzt, um eine hydro-mechanische Interaktion sowie poren-elastische Effekte zu vermeiden. In der einaxialen Testserie wurde die Belastung variiert, um den Übergang von festigkeitsdominierter Rissausbreitung bei geringen Lastmagnituden zur spannungsdominierenden Rissausbreitung bei hohen Lastmagnituden zu untersuchen.

1 Introduction

Hydraulic fracturing is used in a vast field of applications, e.g. increasing productivity from hydrocarbon or geothermal reservoirs, stress measurements, stress relief for tunneling or subsurface mining techniques like block caving. In these applications we are confronted with a wide range of lithologies, stress magnitudes and desired fracture dimensions.

The process of hydraulic fracturing is well understood for homogenous and isotropic media (see e.g. Valkó & Economides (1995)), but the problem gets much more complex if the mechanical properties of the surrounding rock deviate from being isotropic. Basically all rocks exhibit in-situ a certain degree of anisotropy due to e.g. bedding, cleavage or pre-existing discontinuities such as joints or faults. This anisotropy might have a strong influence on the fracture propagation direction, the overall fracture geometry and the injection pressures (Warpinski & Teufel, 1987).

To generate hydraulic fractures under confining pressure in the laboratory two different experimental setups are most commonly used: One uses core specimens with a central injection borehole that are loaded isostatically by a Hoek-Cell (Haimson & Fairhurst, 1970; Lockner & Byerlee, 1977; Rummel, 1987; Brenne *et al.*, 2013). A fluid is then injected into the borehole until the specimen is split into two parts. The second setup makes use of cubic or cuboid specimens that are loaded independently in three directions to induce a true triaxial stress field more similar to in-situ conditions (Haimson & Avasthi, 1975; Zoback *et al.*, 1977; van Dam *et al.*, 2000; Ishida *et al.*, 2004; Frash *et al.*, 2013). The recording of acoustic emissions is a useful tool to gain insights into fracturing processes (Stanchits *et al.*, 2014). Due to typical specimen dimensions in laboratory experiments, with specimen's outer dimensions being only several times the borehole diameter, such experiments are mainly suitable for the examination of mechanical processes near the borehole (fracture length in the order of few borehole diameters) like fracture initiation or borehole failure.

To simplify the boundary conditions in the experiments and to exclude complex poroelastic and leakoff effects, a polymer tube can be pressurized inside the borehole instead of injecting fluid directly into an open borehole (Clifton *et al.*, 1976; Abou-Sayed *et al.*, 1978; Schmitt & Zoback, 1992). This also brings the positive side-effect, that quasi-static fracture propagation can be achieved and fracture processes can be investigated at very low velocities. A similar technique (sleeve fracturing) is also used in-situ for stress measurements (O.Stephansson, 1983; Serata & Kikuchi, 1986).

1.1 Continuum models

In a basic model for impermeable rock, the initiation of hydraulic fracture propagation is only controlled by the orientation and magnitude of the external stress field as well as the strength of the rock. The borehole breakdown pressure P_b can be calculated as

$$P_b = 3\sigma_3 - \sigma_1 + T - P_0 \ , \tag{1}$$

where σ_3 and σ_1 are the minimum and maximum horizontal far field stress, T is the tensile strength of the rock and P_0 is the pore pressure (Hubbert & Willis, 1957).

When the rock near the wellbore is assumed to be poroelastic, Poisson's ratio v and the Biot poroelastic parameter ($\alpha = 1 - C_r / C_b$, C_r is the rock matrix compressibility, C_b is the material bulk compressibility) are introduced as additional parameters into this equation (Haimson & Fairhurst, 1967):

$$P_b = \frac{3\sigma_3 - \sigma_1 + T}{2 - \alpha \frac{1-2\nu}{1-\nu}} - P_0 \ . \tag{2}$$

For the impermeable case ($\alpha=0$, $P_0=0$), instead of reducing to the equation of Hubbert & Willis, this equation gives

$$P_b = \frac{3\sigma_3 - \sigma_1 + T}{2} \ . \tag{3}$$

From this discrepancy it follows that the correlation between far field stress $\sigma = (\sigma_1 + \sigma_3)/2$ and breakdown pressure for an impermeable medium could be either $P_b \propto 1\sigma$ *or* $P_b \propto 2\sigma$.

Furthermore, laboratory experiments indicate that small specimen dimensions as well as high pressurization rates and fluid viscosity increase the breakdown pressure (Haimson & Zhao, 1991; Schmitt & Zoback, 1992). This effect is not covered by the continuum models mentioned above.

1.2 Linear elastic fracture mechanics

The classical approaches for calculating breakdown pressures are only valid for a homogenous, defect free continuum. These assumptions are not met by most rocks, at the latest when a hydraulic fracture is present. To overcome these shortcomings, the principles of fracture mechanics have been successfully applied in the evaluation of hydraulic fracturing experiments (Abou-Sayed *et al.*, 1978; Rummel, 1987; Haimson & Zhao, 1991; Detournay & Carbonell, 1997; Stoeckhert *et al.*, 2014).

Linear elastic fracture mechanics deal explicitly with the stress distribution around fractures and the conditions that let fractures propagate. The magnitude of the stress field at the tip of a sharp fracture can be characterized by one single parameter – the stress intensity factor K (Irwin, 1957). The stress intensity factor is depending on the stress acting on the fracture as well as the fracture length. For the simple case of a fracture of the length a in an infinite plate that is loaded by a tensile stress σ perpendicular to the fracture, the stress intensity factor K_I (the subscript $_I$ refers to tensile fracturing mode) is given by

$$K_I = \sigma\sqrt{a\pi} \ . \tag{4}$$

Accordingly, a corresponding material parameter called fracture toughness K_c (or K_{IC} for tensile fracturing, respectively) can be defined, at which the fracture propagates:

$$K = K_C \quad . \tag{5}$$

This parameter can be determined by standardized laboratory tests like the chevron notched three point bending test (Ouchterlony, 1988). Typical fracture toughness values for the rocks used in our experiments can be found in Tab. 2.

For a hydraulic fracture emanating from a borehole in an infinite isotropic medium the stress intensity factors can be calculated by superposition of known solutions for simple problems (Rummel, 1987). However, the influence of the specimen geometry should be taken into account, as the distance between borehole and outer walls is quite small. The calculation of stress intensity factors for such complex geometries can be done numerically. Stress intensity factors can be calculated from finite element method (FEM) simulations using the J-integral (Parks, 1977) which requires the mesh to be adjusted at the fracture tip for good solutions. Another approach is the extended finite element method (XFEM) where the fracture path is independent of the mesh.

As the fracture grows, parameters like the hydraulic properties of the injection fluid and the surrounding rock have an increasing influence on the further propagation. This case is not considered in our models as we only want to examine near-borehole process and exclude all hydraulic effects by the sleeve-fracturing technique.

2 Methods

2.1 Experimental set-up and specimen preparation

Within this work two series of hydraulic fracturing (HF) experiments on cube specimens (edge length = 150 mm) were carried out using the sleeve-fracturing technique. Fig. 1 shows the true-triaxial loading frame construction. Loading is maintained by four servo-controlled pressure intensifiers simultaneously controlled by a MTS Teststar IIm system. Principal stresses σ_2 and σ_3 are applied by super flat cylinders with a maximum capacity of 525 kN. The maximum principle stress (σ_1) is applied via a hydraulic ram with a maximum capacity of 4.5 MN. External loading is performed in stress rate control. Accuracies of all sensors used in the experiments can be found in Tab.1. During the injection phase the borehole is pressurized through a pressure intensifier in volume rate control. The injection medium is deionized water. The borehole wall is sealed off by an elastic but tough polymer tube to exclude hydraulic effects in the rock matrix completely during the pressurization phase (see Brenne et al. (2014) and Stoeckhert et al. (2014)).

Tab.1: sensors used in experiment and signal accuracy for each measured parameter.

parameter	sensor for raw signal acquisition	data accuracy
σ_1	force transmitter 2000 kN ±200 N	±0.01 MPa
σ_2	pressure sensor 70 MPa ±0.02 MPa	±0.007 MPa
σ_3	pressure sensor 70 MPa ±0.02 MPa	±0.007 MPa
injection volume	LVDT 100 mm ±0.08 mm	±0.5 ml
injection pressure	Pressure sensor 300 MPa	±0.06 MPa
specimen deformation (D_1, D_2, D_3)	LVDT 6.35 mm	±0.9 µm

Specimen cubes are cut with a water flushed CNC saw with a diamond blade. A central borehole of 13 mm diameter was drilled perpendicular to cube specimen's surface. Each specimen was dried to mass constancy before the experiment.

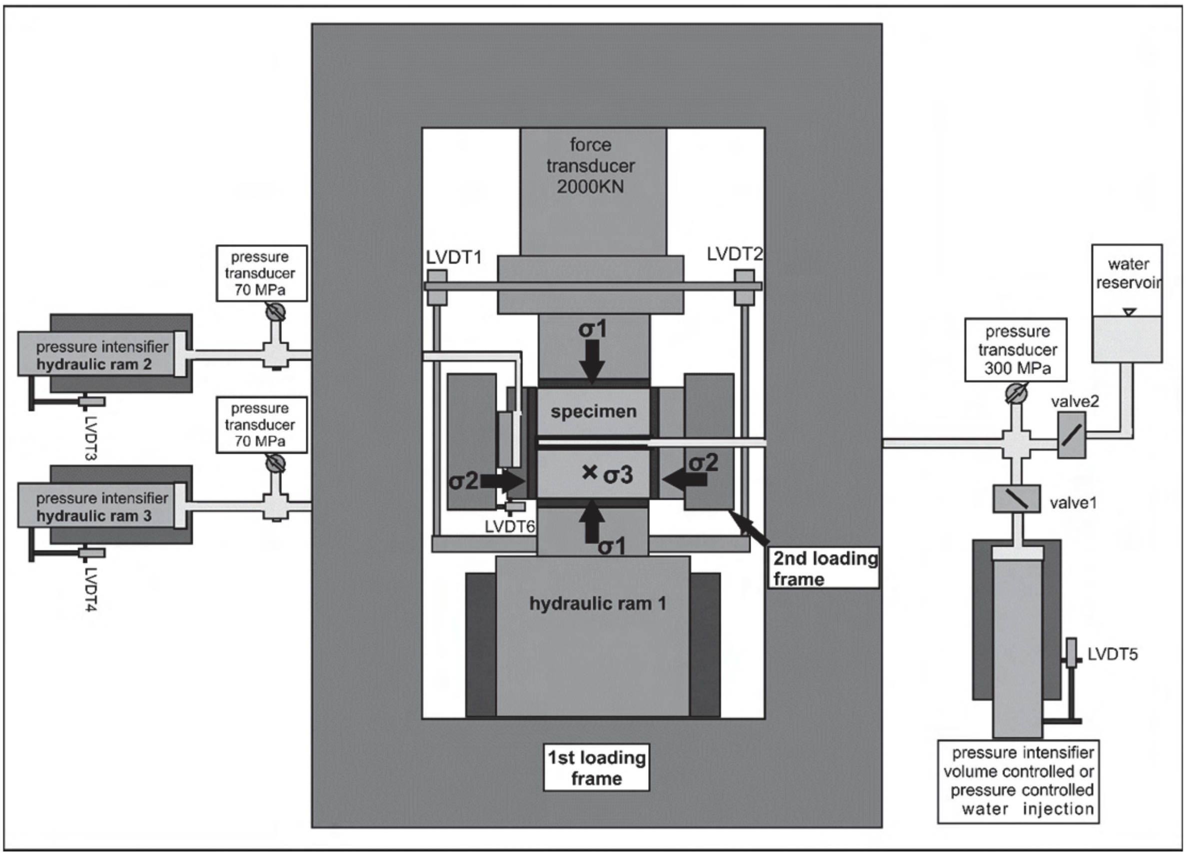

Fig. 1: Schematic drawing of the experimental setup

2.2 Acoustic emission monitoring and event localization

Information about fracture initiation, growth and geometry during HF experiments is collected using a 10-channel Acoustic Emission (AE) monitoring system (AMSY-5, Vallen Systeme GmbH, Germany). AE P-wave piezo sensors are mounted within notches in all six loading plates surrounding the specimen. Locations of the sensors can be seen in Fig.3. High-vacuum grease is used to improve sensor-specimen coupling by reducing the impedance contrast. The sensors are pushed to the specimen's surface with constant force of 39.9 N by springs to ensure a constant contact pressure. This guarantees for optimal and constant sensor coupling during the experiments.

The AMSY-5 AE monitoring system captures transient waveforms of all 10 channels with a sampling frequency of 10 MHz. Recording of all 10 channels is triggered as soon as one channel exceeds a predefined fixed threshold. The waveforms have a page length of 1024 samples including 256 pre-trigger samples, resulting in a captured time frame of 0.1024 µs per Event. AE sensors of type VS600-Z2, also provided by Vallen GmbH, are used. These sensors have a resonance frequency of 600 kHz and deliver very high sensitivity with respect to the specimen size. The small size of the sensors (4.75 mm diameter) guarantees precise sensor coordinates for localization purposes. The sensor signals are pre-amplified with 34 dB pre-amplifiers for each channel. AE data are post-processed using a self-written program.

In a first step the event-arrival-times are estimated by applying an AIC-Trigger (Akaike Information Criterion) routine (Akaike, 1974). The technique yields more precise arrival times compared to a fixed threshold method (cf. Fig.2). This precision is needed for the localization within the given specimen size. After arrival-time estimation the arrival-times are put into groups. This event-building process searches for arrival-times within a certain time interval that is based on the slowest compressional wave velocity in the sample. Events are localized by minimizing the time-differences of the measured and theoretical arrival-times. Theoretical arrival-times are calculated using an estimated source and calculating the travel-times to each sensor using a known velocity field. Minimizing was performed using the Nelder-Mead Downhill-Simplex algorithm (Nelder & Mead, 1965) that starts at an initial guessed source position and minimizes the arrival-time differences via approximation towards the local optimum in a tetrahedron for three dimensions. This method yields fast and numerically stable results. Localization uncertainties are calculated from the fitting time residuals and the compressional wave velocities.

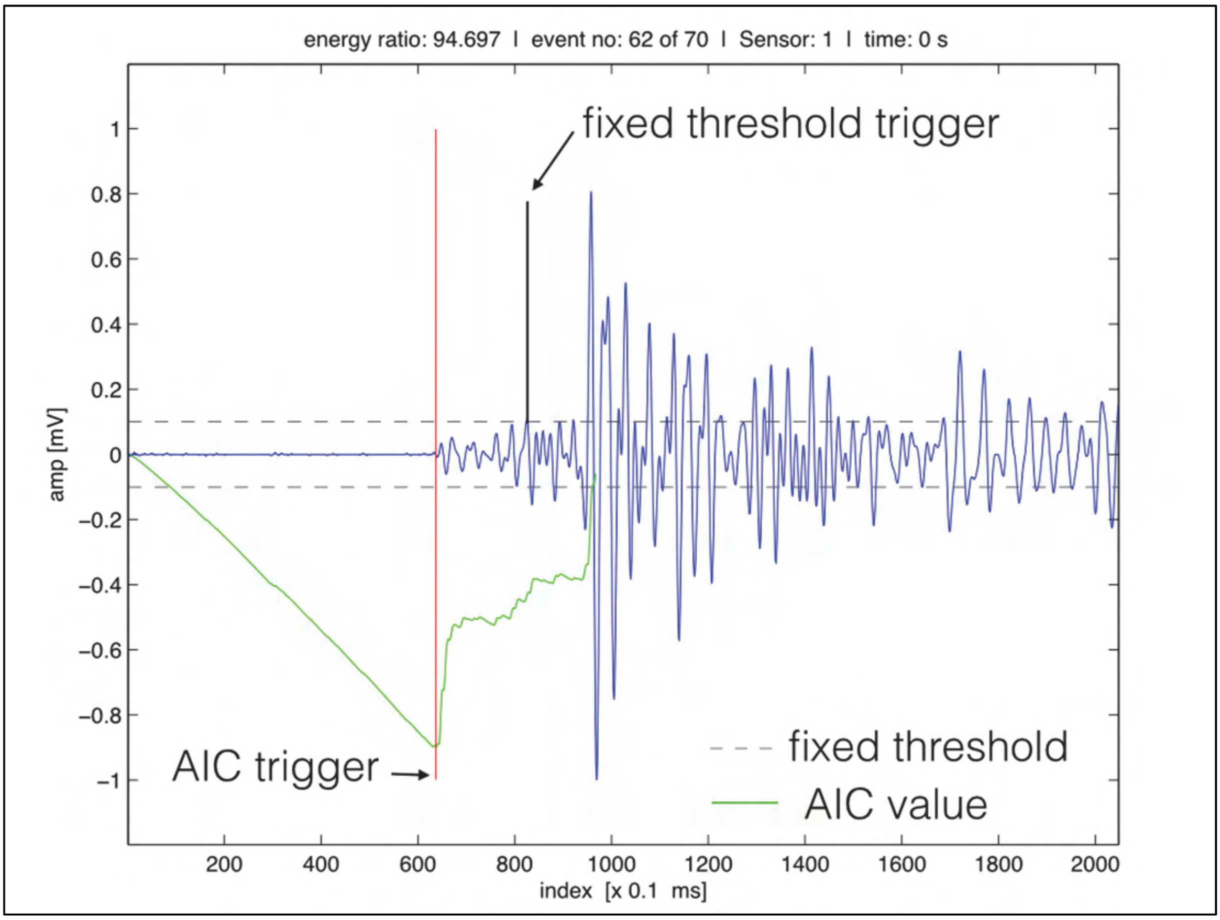

Fig.2: Signal detected from an acoustic emission event. Vertical red line marks the arrival-time picked by the AIC trigger. Green line is calculated using the AIC algorithm.

The velocity field used for the calculations of the theoretical arrival times is of type transverse isotropic. The velocity field is measured by active sensor pulsing. Each sensor is used as an active source while the other sensors record the arriving signal. From the position information and arrival times a transverse isotropic (due to foliation or bedding) velocity field is estimated. The borehole was neglected for the velocity model. The velocities are measured after the application of external loading and before fracturing.

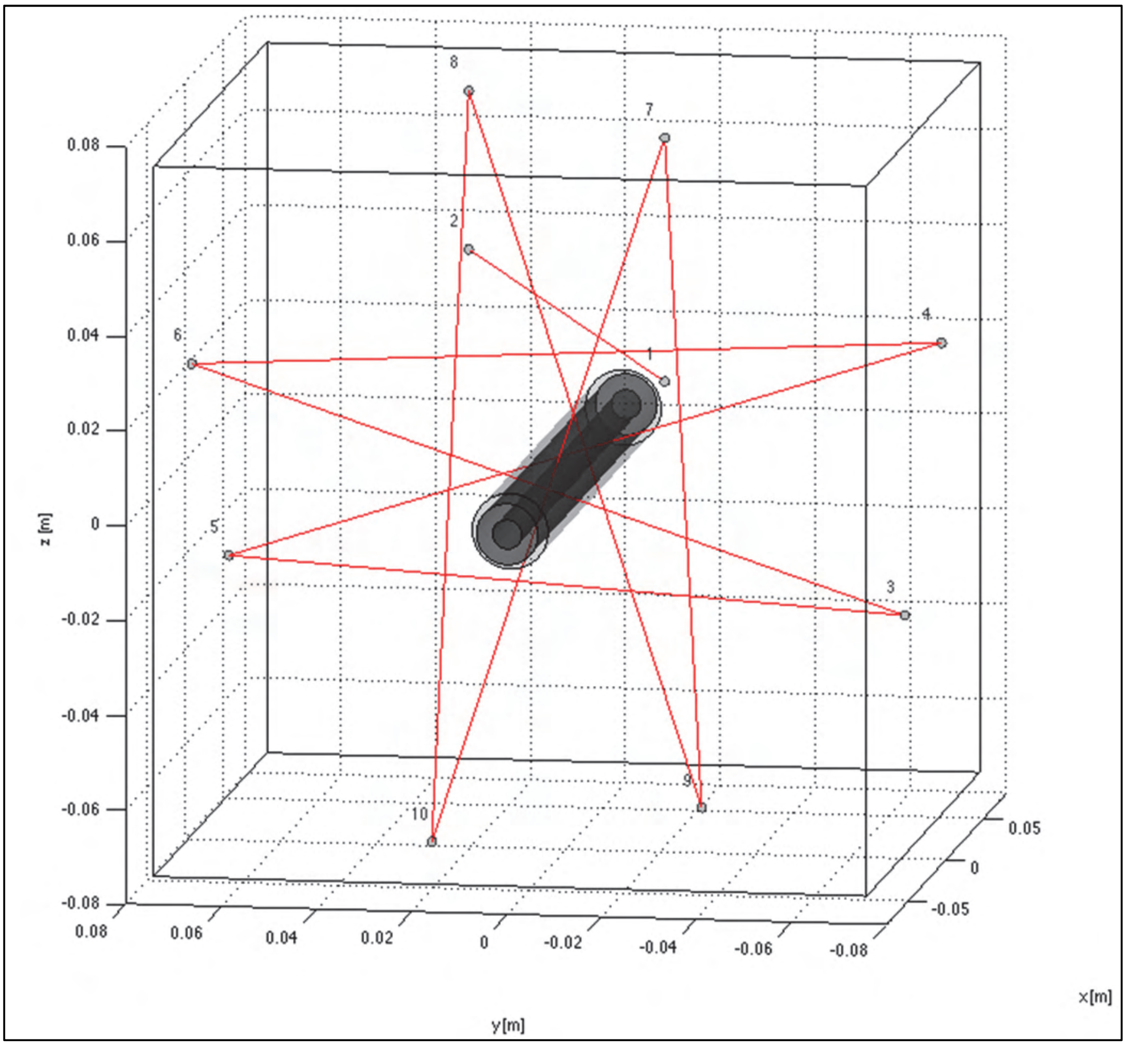

Fig.3: Acoustic emission sensor positions with pulsing paths used for velocity model.

For a better imaging of the localizations a collapsing method was applied (cf. Fig. 4). This method uses the localization uncertainty to move each event within this uncertainty in space. The direction of movement is calculated to be normal to the best fitting plane within a predefined sphere of 20 mm radius instead of moving the events towards the center of gravity. This method was chosen because of the circumstances that the expected features (localization results formation in space) are thought to be planar. This assumption is based on the expected planar fracture geometry.

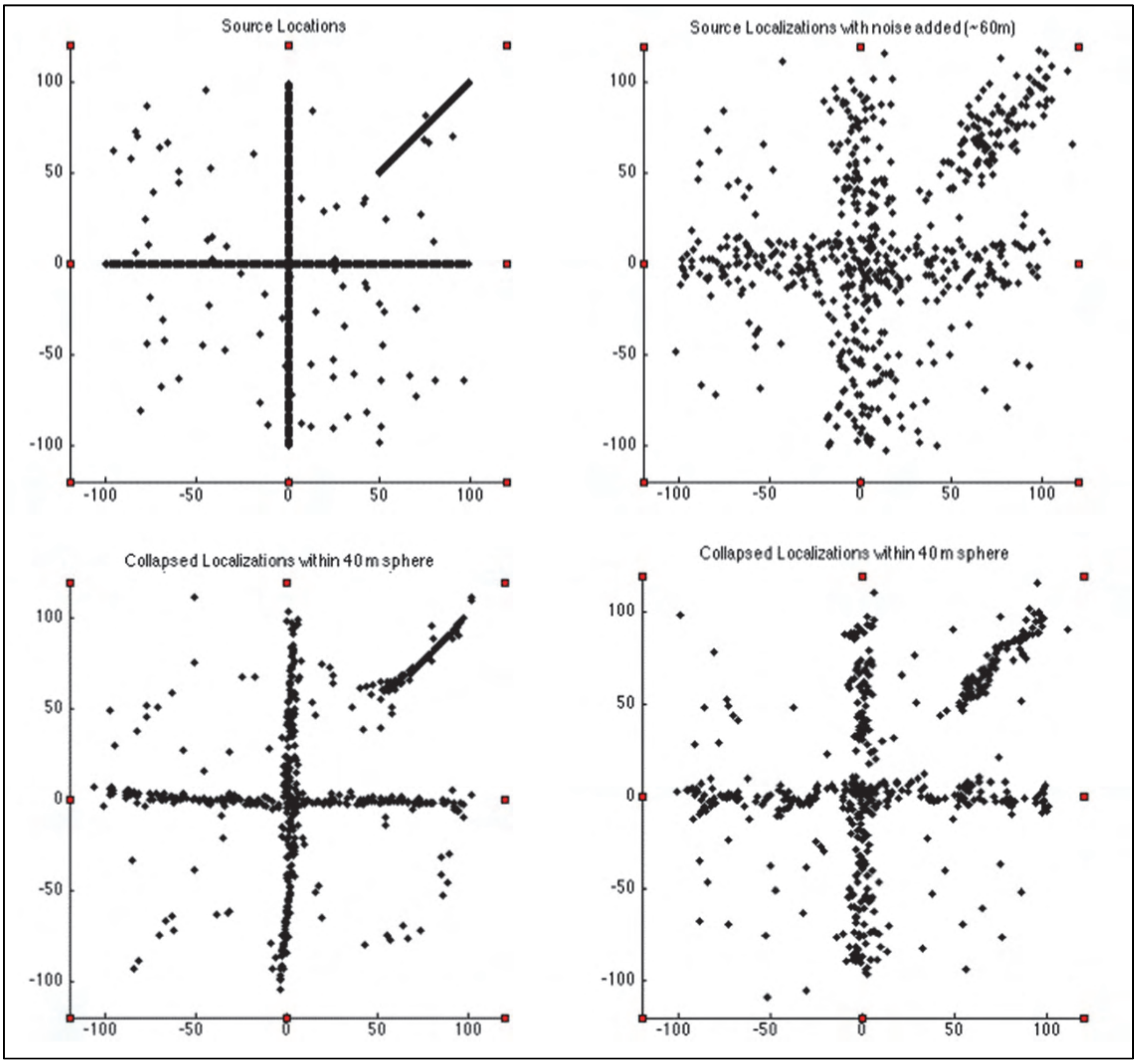

Fig. 4: Example for the application of the collapsing method described in text.

Source mechanisms are approximated using the first p-wave polarities *pol* that is defined as

$$pol := \frac{1}{k}\sum_{i=1}^{k} sign\left(A_i\right), \tag{6}$$

where *i* is the channel and *k* is the number of channels (Zang *et al.*, 1998). The variable $sign\left(A_i\right)$ stands for the first p-wave motion polarity of *i*th event. For *pol*-values of $-1 \le pol \le -0.25$ the event is classified as tensile (T-type). For *pol*-values of $0.25 \le pol \le 1$ the event is classified as compressional (C-type). Events with *pol*-values of $-0.25 \le pol \le 0.25$ are classified as shear or mixed mode (S-type).

Good quality events can be localized within a localization uncertainty of around 5 mm (cf. Figure 5). These localizations are characterized by more than 6 triggered sensors with energy ratios of > 10. Energy ratios are calculated by squaring and integrating the signal over an equal time length before and after the AIC arrival-time. The signal in Fig.2 has a calculated energy ratio of 94.679, for example.

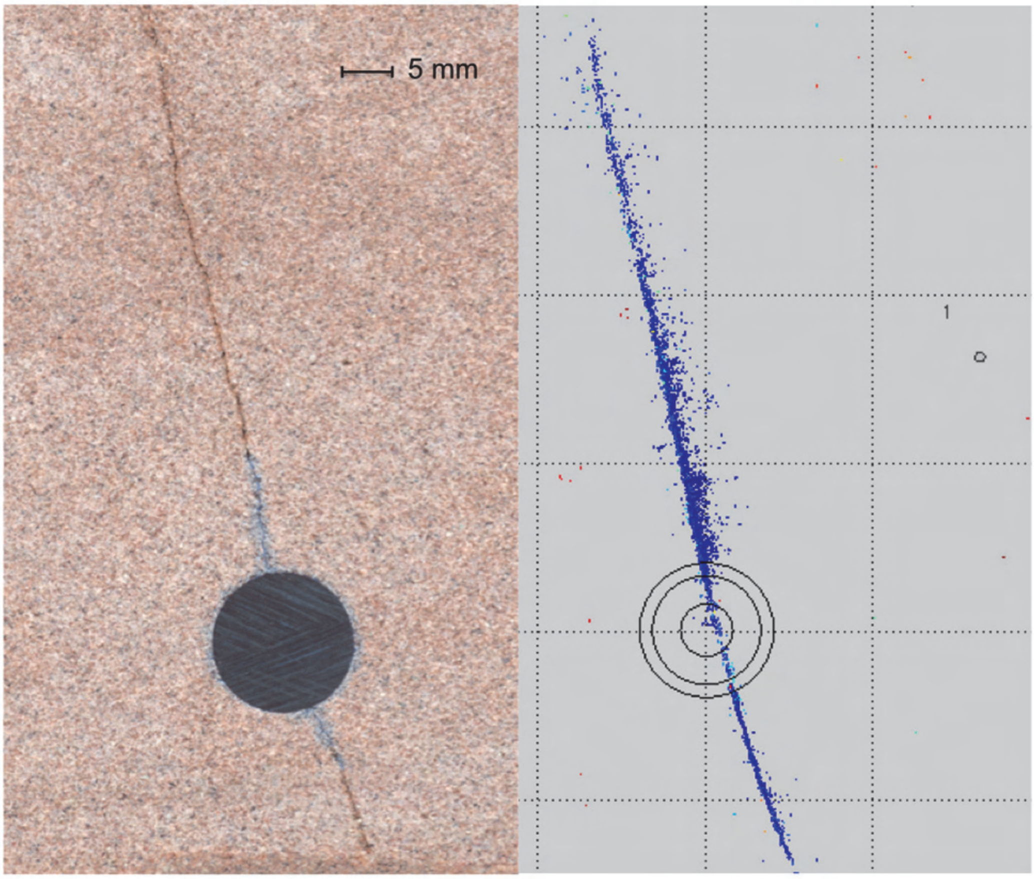

Figure 5: Comparison of fracture geometry from thin-section (left) and acoustic emission localization (right). Same scale for both pictures.

2.3 *Procedures for hydraulic fracturing experiments*

2.3.1 True triaxial sleeve frac experiments

A Bebertal sandstone and a Fredeburg slate cube have been tested using external loading magnitudes of $\sigma_1 = 5\text{MPa}$, $\sigma_2 = 3.75\text{MPa}$ and $\sigma_3 = 2.5\text{MPa}$. The experimental procedure for these true triaxial hydraulic fracturing experiments can be divided in four phases (cf. Fig. 6): First external loading cycle (to ensure correct positioning of specimen and loading plates), application of final external loads, borehole pressurization cycles and unloading of external loads.

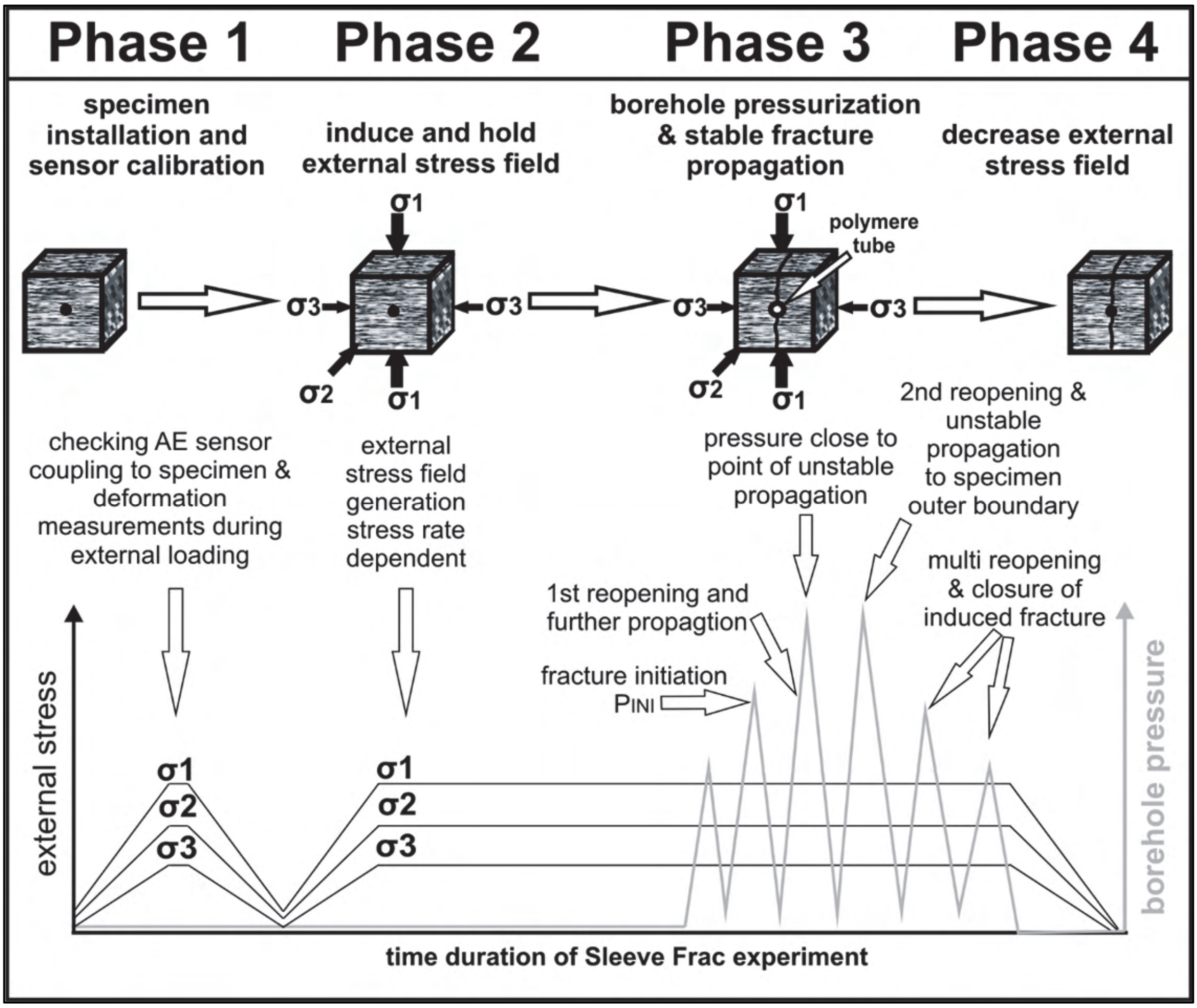

Fig. 6: Workflow for hydraulic fracturing experiments under triaxial loading.

Ratios between external loads are kept constant at *2:1* for $\sigma_1 : \sigma_3$ and *1.5:1* for $\sigma_1 : \sigma_2$ throughout the experiment to keep the rate of tangential stress increase around the borehole constant. Therefore we used following stress rates: $d\sigma_1/dt = 0.1 \text{ MPa}/s \quad d\sigma_2/dt = 0.075 \text{ MPa}/s$. Such stress ratios are similar to those found in horizontal wells drilled parallel to maximum principal horizontal stress in depth ranges between 3 to 5 km in the North German Basin (Moeck *et al.*, 2009).

Wellbore pressurization (Phase 3) is driven in volume control to perform a cyclic stable fracture propagation (see Figure 6).

2.3.2 Sleeve frac experiments under uniaxial compression

Additionally, a series of 5 sleeve frac experiments with 5 different magnitudes of σ_1 from 2 MPa up to 20 MPa acting normal to cleavage planes have been performed. σ_2 and σ_3 are set to a value of 0.5 MPa to guarantee specimen deformation measurements and AE sensor coupling within loading plates (see also Chapters AE and Results). Apart from that, the workflow is similar to the triaxial experiment series.

2.4 Sample material

We used a permian sandstone (Bebertal sandstone) with low porosity from a quarry in the Northern German Basin as well as a Devonian slate (Fredeburg slate) from an underground mine in the Rhenish Massif. Geomechanical parameters were determined according to ISRM suggested methods (Ulusay & Hudson, 2007). The properties of slate are strongly anisotropic (depending on the angle between loading direction and cleavage planes), therefore we determined an upper and lower boundary of material strength, toughness and elasticity (see Tab. 2 as well as Brenne *et al.* (2014) and Stoeckhert *et al.* (2014) for further information).

Tab. 2: Rock mechanical parameters (cohesion/angle of internal friction c/ϕ, Young's modulus E, tensile strength T, fracture toughness K_{IC}, ultra-sonic wave velocity V_P) of Bebertal sandstone and Fredeburg slate perpendicular ($\perp$) as well as parallel (II) to bedding/cleavage.

lithology	c/ϕ [MPa]/[°]	E [GPa]	T [MPa]	K_{IC} [$\mathrm{MPa}\sqrt{\mathrm{m}}$]	Vp [km/s]
Bebertal sandstone	26/48	19 ±1.3	5.5 ±0.5	1.21 ±0.27	II 3.98 ±0.24 $\perp$ 4.10 ±0.19
Fredeburg slate	8.6-34.1/ 21.7-37.6	14.5- 35.5	3.5 21.1	0.3 (assumed) 2.5(determined)	II 5.92 ±0.13 $\perp$ 2.69 ±0.14

3 Results

Information about fracture processes is gained from both, the AE as well as deformation measurements. When external stresses are applied, we often receive acoustic emissions from preexisting discontinuities. The magnitude of deformation in each direction is proportional to the respective external loading (biggest amount in direction of σ_1, smallest amount in direction of σ_3) (cf. Fig. 7).

In the first phase of injection (the pre-fracture phase) no significant acoustic emissions are received. Small amounts of negative deformation (the cube is getting bigger) can be measured at the loading plates. There is a linear relation between deformation and injection pressure in this first phase. The beginning of the second phase (the fracture propagation phase) is either determined by the detection of first acoustic events close to the borehole wall or the deviation of the ratio between external deformation and injection pressure from being linear. The injection pressures at which this occurs are named $P_{INI}(AE)$ and $P_{INI}(D)$, respectively. After this point successive acoustic emissions are recorded and deformation rate is constantly increasing.

The final stage is marked by the specimen breakdown, where the injection pressure is at a maximum and cannot be further increased. Just before, the deformation rate also reaches its maximum. Acoustic emission localizations reach the specimens outer walls in this stage. When the injection pressure is reduced to zero afterwards, a residual deformation perpendicular to the fracture is measurable.

Further injection cycles typically show smaller amounts of acoustic emissions and higher rates of deformation at the respective injection pressures compared to preceding cycles.

3.1 Triaxial experiment - sandstone

A sleeve frac experiment using a Bebertal sandstone cube with an external loading of σ_1 = 5 MPa, σ_2 = 3.75 MPa and σ_3 = 2.5 MPa was performed with 4 pressurization cycles up to a maximum injection pressure of 47.7 MPa in polymer tube.

Sensor signals recorded during this experiment can be seen in Fig. 7. The specimen expands parallel to the direction of σ_3 during injection. Pressure vs. deformation curve of cycle 1 shows a significant change of deformation rate at $P_{INI}(D_1)$ = 30.9 MPa, while first significant AE events already occurred at a $P_{INI}(AE)$ = 20 MPa. In cycles 2 and 3 a nearly penny shaped axial bi-wing fracture grew stepwise in each pressurization cycle to the specimen surface. In cycle 4 there was no further fracture propagation, only fracture reopening occurred as indicated by lower acoustic emission activity. Therefore, fracture was propagated over an injection pressure range of about 30 MPa. Fig. 8 shows the measured D_3 signal and the emerged residual deformation between the pressurization cycles in detail.

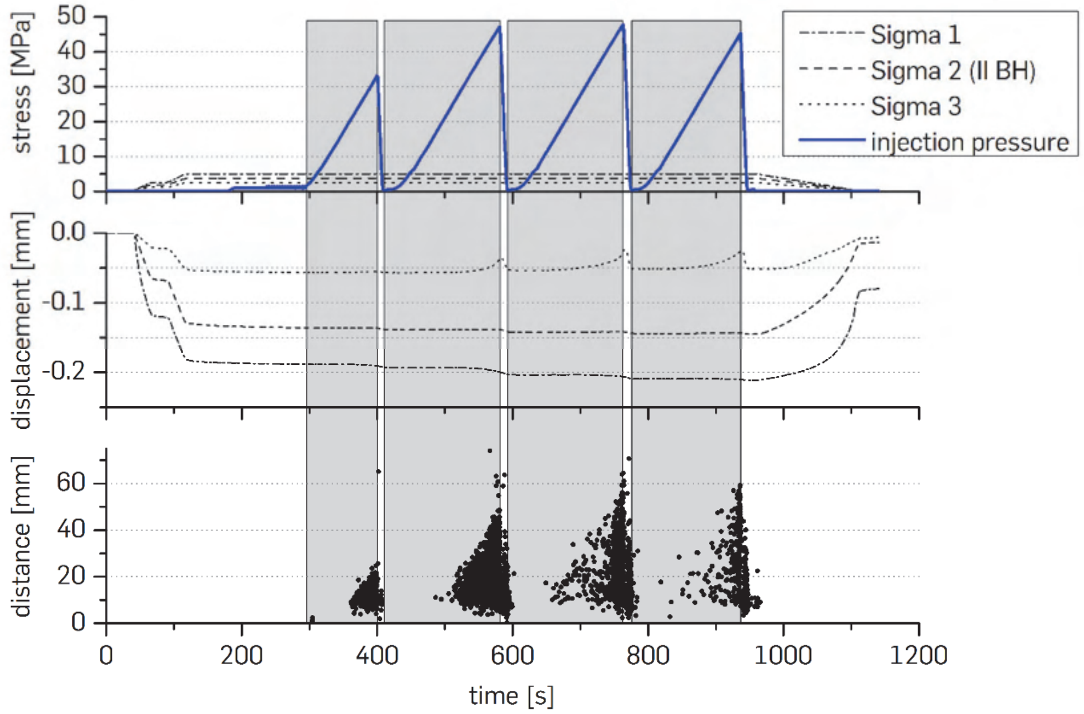

Fig. 7: stress, pressure, displacement and AE signals detected during hydraulic fracturing experiment under triaxial loading with a Bebertal sandstone cube. External loading magnitudes as well as injection pressure (upper), loading plate displacements (middle) and distance of AE localizations from borehole axis (lower) vs. experiments time. Four subsequent injection cycles were run in this experiment. Compression results in negative displacement.

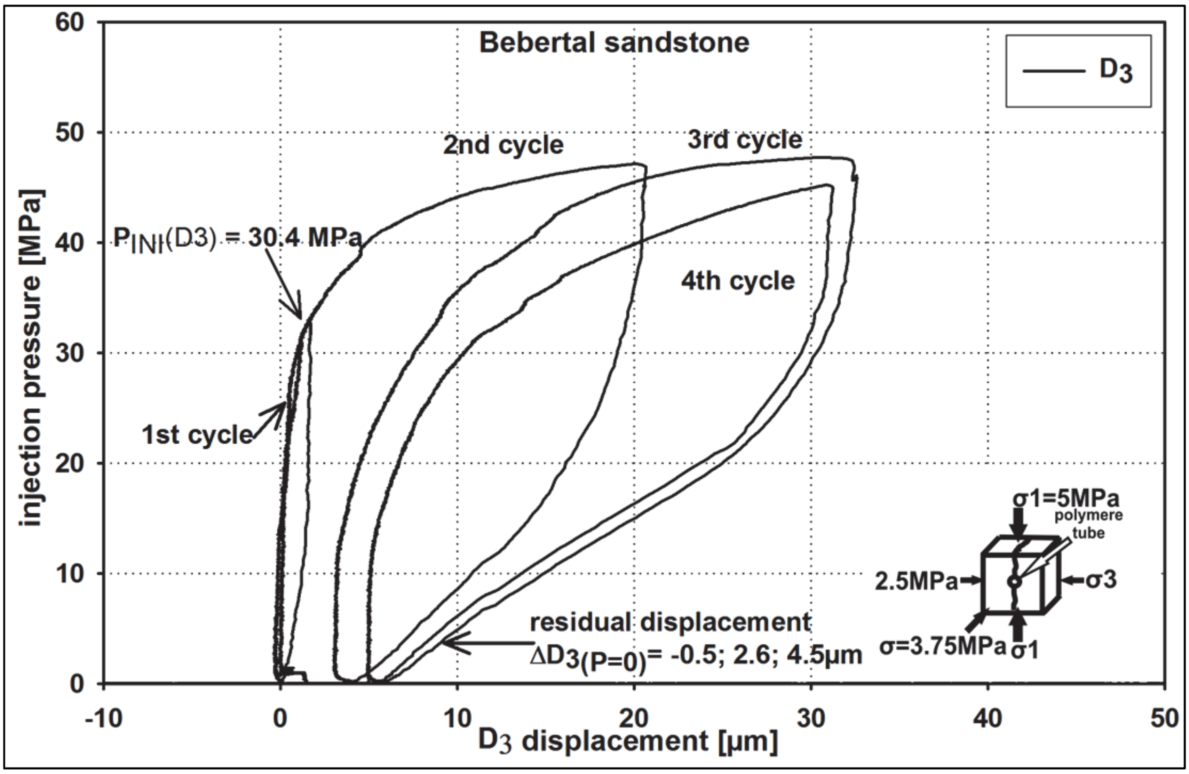

Fig. 8: Displacement vs. injection pressure plots for hydraulic fracturing experiments under triaxial loading. D_3 is the specimen deformation parallel to the directions of the minimum loading (σ_3), respectively. Dilatation results in positive displacement. Signal was reset to zero after the external loading phase.

During the experiment over 31000 AE events were successfully localized. These events are based on a minimum of 6 triggered sensors with energy ratios > 10. The velocities from the pulsing yields following results: $V_P(x)$ = 3593 m/s, $V_P(y)$ = 3459 m/s and $V_P(z)$ = 3516 m/s. Therefore, the acoustic properties of this sandstone specimen can be assumed to be isotropic.

Localizations reveal that the fractures start to grow at the borehole wall diametrically opposed. The fracture grows stable over several centimeters. We observed a stepwise and discrete fracture growth process, meaning that each fracture wing grows in an alternating way and not simultaneously.

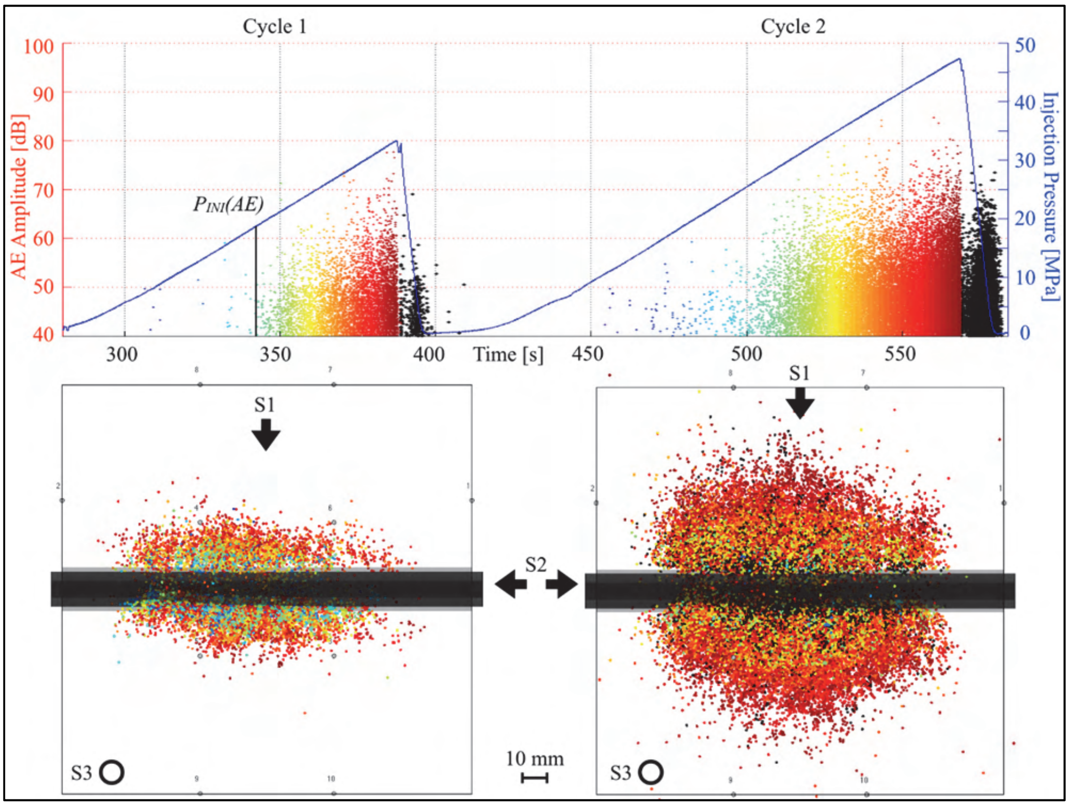

Fig. 9: AE localization for the experiment with Bebertal sandstone under triaxial loading for injection cycle 1 and 2.

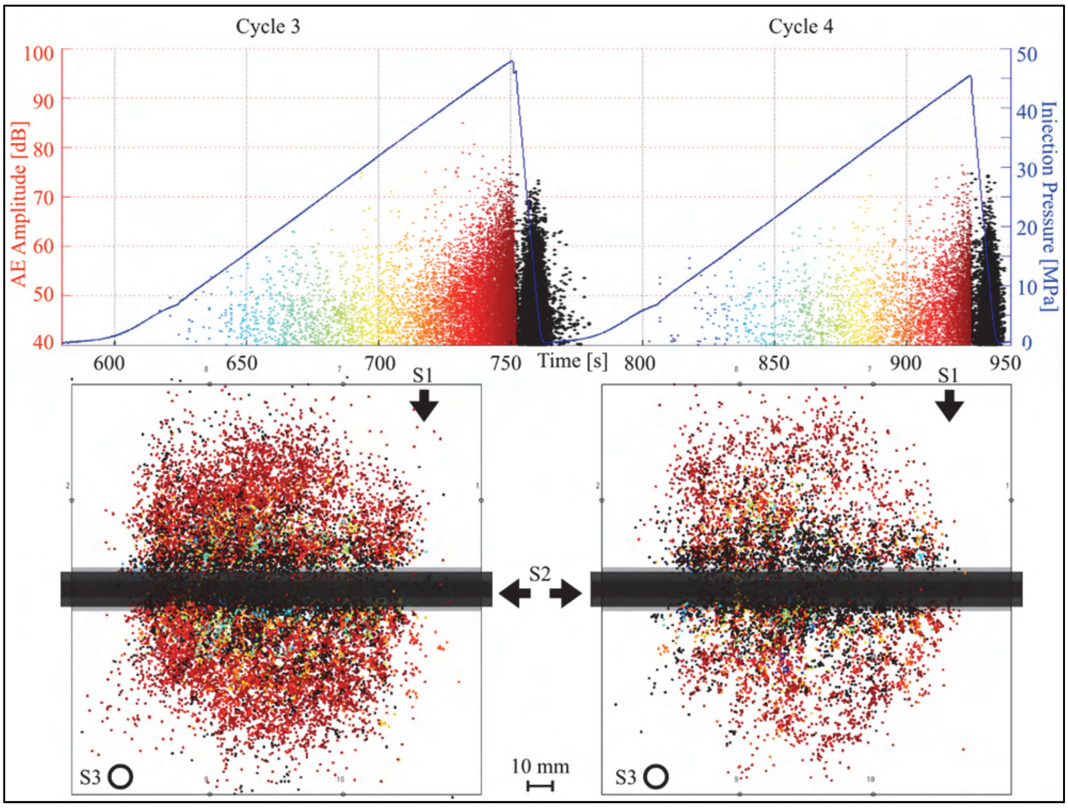

Fig. 10: AE localization for the experiment with Bebertal sandstone under triaxial loading for injection cycle 3 and 4.

Fracture length from the borehole wall at a given injection pressure can be measured using the localizations. The re-onset or further fracturing in successive cycles is marked by an increase in AE activity.

Source mechanism evaluation showed that there are differences in the source types between pressurization and pressure release. Events during pressurization are dominated by T-type (62 %) and S-type (34 %) events. When the fracture closes during pressure release the main source type mechanisms are C-type (58 %) and S-type (26 %). The fracturing process is mainly a tensile and shear dominated process whereas the fracture closing is characterized by compressional and shear type events.

3.2 *Triaxial experiment - slate*

In an experiment using a slate cube under the same external loading (σ_1 = 5 MPa, σ_2 = 3.75MPa, σ_3 = 2.5 MPa; σ_1 perpendicular to cleavage plane) the fracture propagated in the unfavorable direction perpendicular to σ_1. This is related to the preexisting planes of weakness due to the cleavage. Deformation measurements also indicate a dilatation parallel to σ_1, while the specimen is compressed parallel to σ_3 (see Fig. 11). As fracture initiation pressure from deformation measurements parallel to σ_1 direction $P_{INI}(D_1) = 22.5$ MPa could be detected in pressurization cycle 2. The maximum pressure was 42.7 MPa. At that pressure the induced deformations are 8 µm in D_1 and -5 µm in D_3 direction.

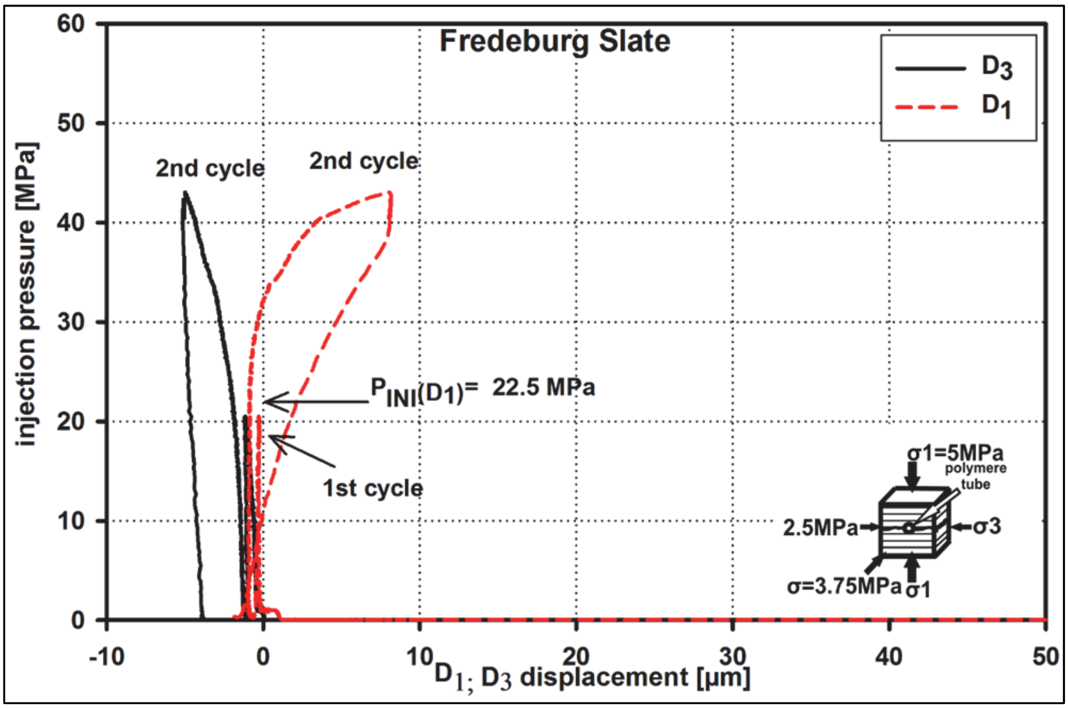

Fig. 11: Displacement vs. injection pressure plots for hydraulic fracturing experiments under triaxial loading. D_1 and D_3 are the specimen deformation parallel to the directions of the maximum loading (σ_1) and the minimum loading (σ_3), respectively. Dilatation results in positive displacement. Signal was reset to zero after the external loading phase.

A much lower AE activity was recorded during this experiment resulting in 612 localizable events with a minimum of 6 triggered sensors with energy ratios > 10. The reason for the low AE activity is presumably the high acoustic wave attenuation in slates compared to sandstones, especially perpendicular to the cleavage plane. From pulsing data a transverse isotropic velocity model is assumed for the slate: $V_P(x)$ = 5839 m/s, $V_P(y)$ = 5562 m/s and $V_P(z)$ = 4446 m/s. The z-velocity, orthogonal to the cleavage planes, is 22 % slower than the x- and y-velocities that are within the cleavage planes.

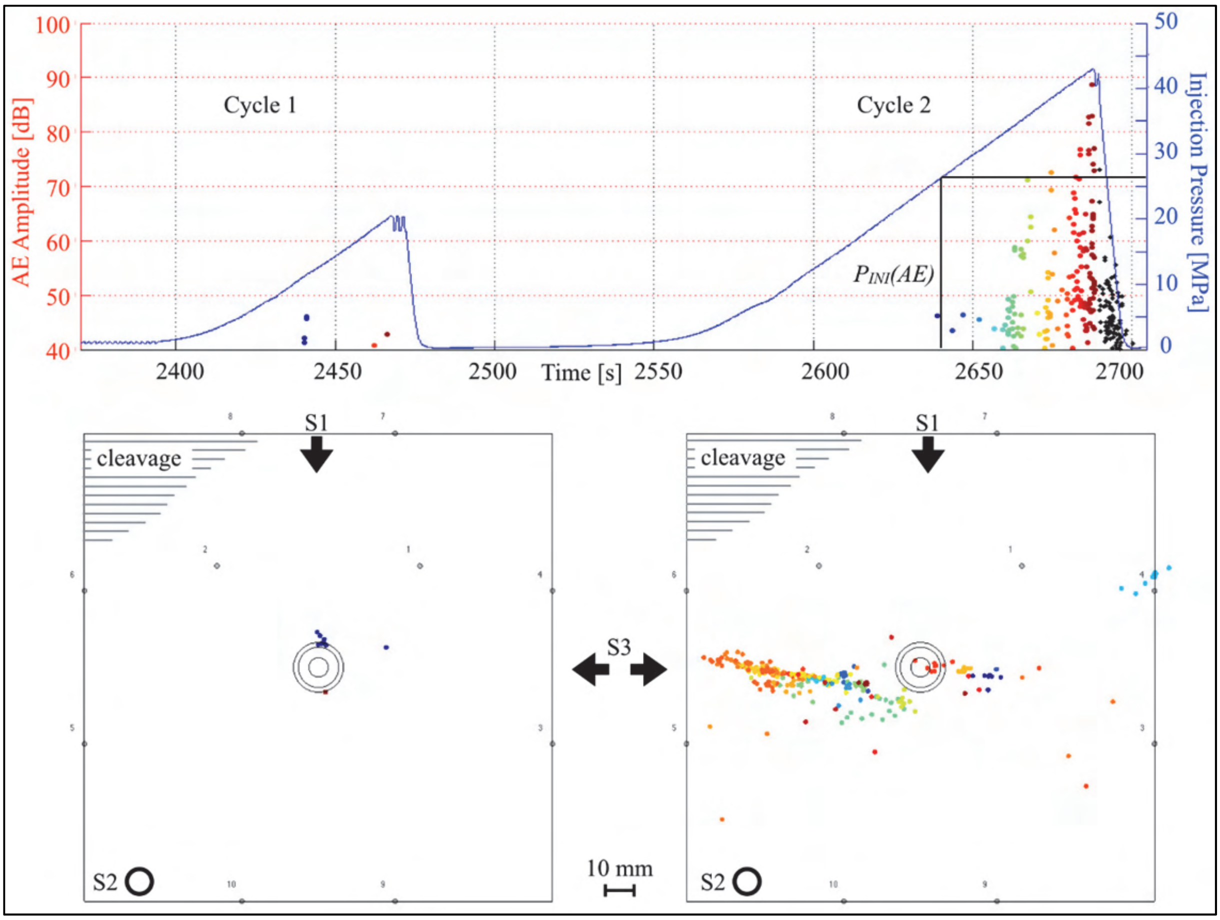

Fig. 12: AE localization for the experiment with slate under triaxial loading.

According to acoustic emissions the fracture starts to grow within the cleavage plane in the direction of σ_3 at $P_{INI}(AE)$ 26.3 MPa injection pressure. Successive pressurization forces the fracture to grow without changing the direction.

Source Type AE results of the slate fracturing are different to the results from the Bebertal sandstone. During pressurization (fracture growth) the dominant source type is S-type with 62 %. During fracture closure the total amount of the S-type events stays roughly the same with 57 %. The only difference between fracture propagation and closure source types is the relative amount of C-type to T-type events. During fracture propagation there are twice as much T-type (24 %) events as C-type (14 %) ones. This relation reverses during fracture closure where there are twice as much

C-type (29 %) events compared to T-type (14 %) ones. Basically, both fracturing and closure seem to be shear-dominated processes in the slate.

The fracture propagation direction is controlled by rock properties instead of the stress field in this experiment. We performed a series of uniaxial sleeve frac experiments to examine the transition from stress-dominated to strength-dominated fracture propagation.

3.3 Results uniaxial experiments

Unfortunately, during most uniaxial experiments the AE measurement was disturbed by strong electrical ground noise. The AE signal to noise ratio was such low that only a few AE events could be localized with huge spatial errors. Therefore, the use of AE localization data is restricted for these experiments. Deformation measurements still yield useful information on fracture processes.

Tab. 3: Results of uniaxial experiments with magnitude of axial loading (σ_1), specimen breakdown pressure (P_B), fracture initiation pressures as determined by acoustic emissions ($P_{INI}(AE)$) and deformation measurement parallel to σ_1 ($P_{INI}(D_1)$) and σ_3 ($P_{INI}(D_3)$).

specimen	σ_1	P_B	$P_{INI}(AE)$	$P_{INI}(D_1)$	$P_{INI}(D_3)$
S1-W99	2	19.6	12	9	10
S1-W06	5	39.8	34	36	39
S1-W05	7.5	40.2	40.5	--	37
S1-W09	10	34.02	34	33	33
S1-W03	20	23.1	23	--	21

We varied the uniaxial loading from 20 MPa (where the fracture clearly propagates perpendicular to the cleavage plane) down to 2 MPa with strength-dominated fracture propagation in the cleavage plane. The transition from stress to strength-dominated fracture propagation somewhere between 5 and 10 MPa uniaxial stress is marked by complex fracture geometries (also cf. Fig. 15). Fracture initiation pressures (as determined by both acoustic emissions and deformation) increase with the magnitude of uniaxial loading up to the strength-stress transition. After this point fracture initiation pressure slightly decrease with increasing uniaxial loading (see Tab. 3).

4 Discussion

4.1 Acoustic emissions

The existence of stable fracture propagation and the fracture plane geometry could be verified and visualized by Acoustic Emission analysis for both triaxial experiments. The outer rim of the plane formed by the localizations are assumed to correlate with the actual fracture front position. Based on this assumption the fracture length at a given injection pressure can be measured using the AE localizations.

Source type analysis of the AE events give insights into the predominant source types being active during fracturing. One would expect the fracturing process being predominated by tensile failure and fracture closure a mixed mode of compressional and shear events. For the sandstone these expectations correlate with the source type analysis. During fracturing tensile (T-type) failure is dominant and during closure the predominant source types are mainly compressional (C-type) and shear type (S-type) events. The slate fracture draws a different source type picture. The fracturing within a cleavage plane in the slate in a strength-dominated manner seems to be preliminary based on shear (S-type) failure. A similar observation is made during fracture closure. The source type analysis indicates that the fracturing and closure process in the slate is accompanied by microshearing events which overlays the tensile and compressional events. This might also be due to higher amplitudes of shear events compared to tensile and compressive events in slate. This effect seems not to be present in the sandstone experiment.

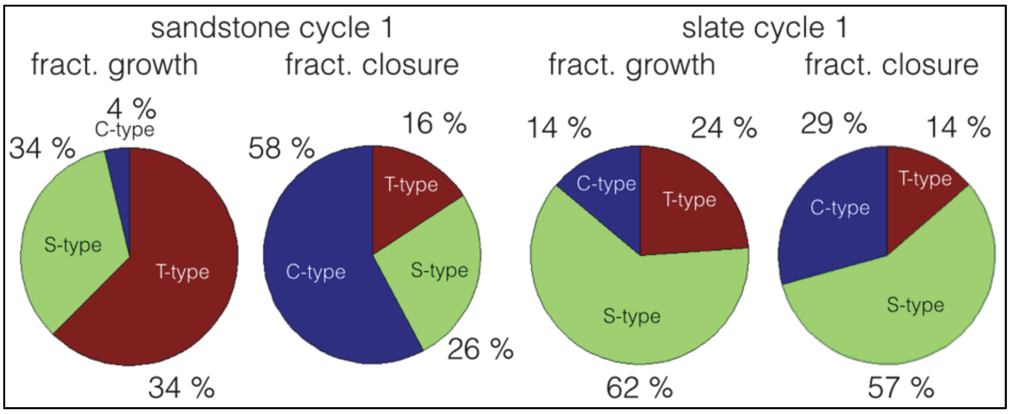

Fig. 13: AE source types during fracture propagation and fracture closure in triaxial experiments.

There is a significant difference in localized AE between the sandstone and slate experiment for a similar sized fracture plane. Given a similar fracturing time the sandstone emits 10 times as much localizable AE events compared to the slate. One reasonable explanation is the difference in attenuation between both lithologies. Another reason may arise from the assumption that the fracture in the slate is composed of a larger number of low energy emitting fracture steps compared to the sandstone fracture. Most of these low energy AE may be under the detection sensitivity of the AE system and therefore only a few large energy AE events are being recorded.

4.2 Deformation measurements

Deformation measurements in test series 1 of Bebertal sandstone and Fredeburg slate at the same external stresses provide the different fracturing mechanism described above. Tensile-dominated fracture propagation and opening parallel to cleavage planes lead to measurable displacements at the loading plates. Magnitudes of deformation perpendicular to the stimulated fracture plane were in a range of 0-35 µm for the Bebertal sandstone and of 0-5 µm for the Fredeburg slate. During the first pressurization cycle fracture initiation pressures as determined by deformation ($P_{INI}(D)$) are higher than those determined by acoustic emissions ($P_{INI}(AE)$) for the Bebertal sandstone. In the slate specimen the relation between $P_{INI}(D)$ and $P_{INI}(AE)$

is reversed. Between pressurization cycles residual deformations of a few microns as a result of fracturing can be seen.

The 5 experiments of test series 2 the determination of fracture initiation pressures for deformation measurements is less straightforward. At highest normal stresses (σ_1 = 10; 20 MPa) an abrupt increase of deformation in σ_3 direction was detected simultaneously with the detection of first AE events. The pressure interval between first deformation attributed to fracture initiation and the final specimen breakdown is very small. This indicates either that the injection pressure range for stable fracture propagation was only a few MPa or deformation was to low to be detectable during fracturing parallel to σ_1. At low uniaxial stress (σ_1 = 2 MPa) an increase of deformation rate in σ_1 direction was observed some 10 MPa below specimen breakdown. The correlation of fracturing processes to deformation measurements yields good results for single planar fractures perpendicular to one of the loading directions. When multiple, inclined, branched or tortuous fractures propagate, this relation gets more ambiguous.

As the total displacement of the loading plate is measured it might not only be related to fracture opening, but also to other types of plastic deformation inside the specimen and at the contacts between loading plates and the specimen. Thus, it is difficult to infer accurate fracture opening widths from the deformation measurements. The effect of plastic deformation was minimized by an external loading cycle (phase 1 in Fig. 6) prior to the actual experiment.

4.3 Numerical modeling

Although triaxial experiments are 3D Problems, we model a cutting plane perpendicular to the borehole using a 2D plane-strain simplification as a first approximation. We assume simple linear elastic, impermeable and non-poroelastic material behavior.

We modeled a square geometry with two fractures emanating radially from an central borehole with the commercial FEM package Abaqus (Dassault Systèmes, 2012) and the XFEM software roxol (geomecon GmbH, 2013). External loading as well as the pressure inside the borehole is supplied by Neumann boundaries. The fracture faces are traction free. This accounts for the sealing of the borehole by the polymer tube.

The critical injection pressures for which the fracture propagation criterion is satisfied at a given fracture length were calculated for a range of typical fracture toughness values and external stress magnitudes. This gives us a theoretical relation between the fracture length and the injection pressure required for stable fracture propagation at this length.

The results suggest that in the experiments using the polymer sleeve at short fracture lengths there is stable fracture propagation, i.e. the pressure inside the borehole has to be increased to propagate the fracture. Therefore the fracture growth rate can be controlled through the injection rate.

We assume the minimum of the fracture length vs. propagation pressure curve to be the pressure at which a fracture is initiated. Specimen breakdown occurs at a pressure corresponding to the maximum of this curve. After this point the fracture propagates fast and unstable until it reaches the specimens outer walls.

Our approach to modeling material with an anisotropic strength is the assumption of a directional variation of fracture toughness. For our case, where a slate specimen is loaded perpendicular to the foliation plane, we simulated two configurations: a) the propagation of a fracture in a direction parallel to the maximum principle stress in a medium with high fracture toughness and b) the propagation perpendicular to the maximum principle stress in a medium with a low fracture toughness.

4.3.1 Numerical modeling of triaxial experiments

Numerical modeling using a fracture toughness of 1.2 MPa $m^{0.5}$ as determined for Bebertal sandstone in three-point bending tests and assuming two radial fracture emanating from the borehole parallel to σ_1 yields a relation between fracture length and injection pressure required for stable fracture propagation. These curves can be compared to the localization of acoustic emission events. The front of the acoustic emission cloud is assumed to be the fracture tip at the respective injection pressure.

In Fig. 14 the distance of this front from the borehole wall is in rather good agreement with the numerical models for short fracture length. Injection pressure for specimen breakdown is strongly underestimated by the model. This might be due to border effects like friction on the interface between specimen and loading plates. It is also likely, that the assumption of plane-strain conditions (and the neglection of σ_2) is an over-simplification. The fracture geometry in the experiment is penny-shaped, which cannot be reproduced by a plane-strain model.

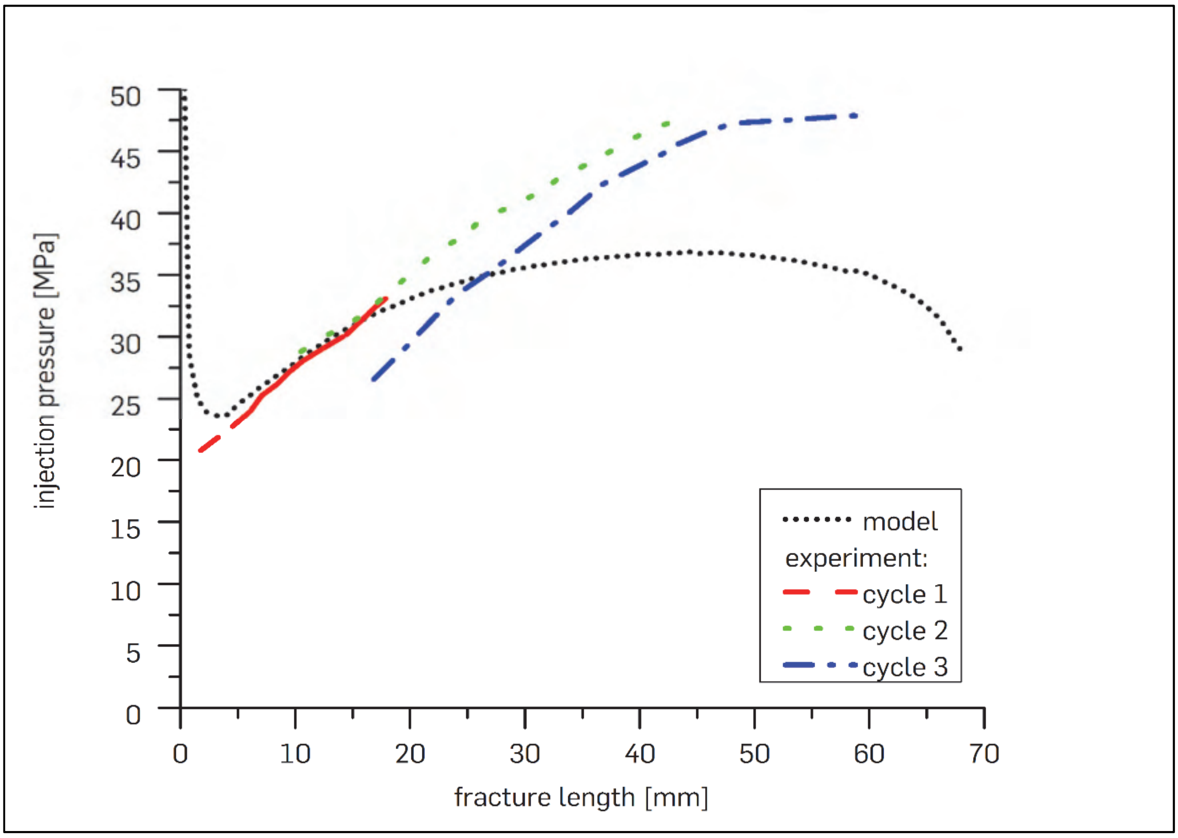

Fig. 14: Fracture length vs. Injection pressure modeled using fracture mechanics (dotted black line) for the triaxial experiment with Bebertal sandstone. Color lines are the fracture lengths determined by acoustic emission localization for the respective injection cycles.

4.3.2 Numerical modeling of uniaxial experiments

For the numerical modeling of the uniaxial experiments we focused on the two end-members of fracture propagation being purely stress-controlled (parallel to σ_1, perpendicular to foliation) and purely strength-controlled (perpendicular to σ_1, parallel to foliation). This is due to the fact, that the numerical simulation of fracture propagation (and especially the fracture propagation direction) in anisotropic material is quite complex. By limiting to the two end-members, we can make use of isotropic models and only vary the fracture toughness.

In the strength-controlled case, a fracture toughness of 0.3 MPa $m^{0.5}$ is assumed, according to the fracture toughness determined for fracture propagation in the foliation plane. This yields a relation between fracture initiation as well as breakdown pressures and confining pressures with positive gradients of about 3 and 10, respectively (cf. Fig. 15 – red lines).

The stress-controlled fracture propagation regime where the fracture cuts through layers of sheet silicates is modeled using a much higher fracture toughness of 2.5 MPa $m^{0.5}$. This is supported by the magnitude of fracture toughness determined for the slate in three-point bending tests perpendicular to the cleavage plane. The calculated fracture initiation and breakdown pressures for this configuration at low uniaxial stresses are much higher than in the strength-dominated model. However, they are decreasing with increasing uniaxial stress. Gradients are -0.44 for fracture initiation and -0.16 for specimen breakdown (cf. Fig. 15 – black lines).

The intersections between the curves for stress-dominated and for the strength dominated configuration are at about 10 MPa uniaxial stress for fracture initiation and at about 4 MPa uniaxial stress for specimen breakdown.

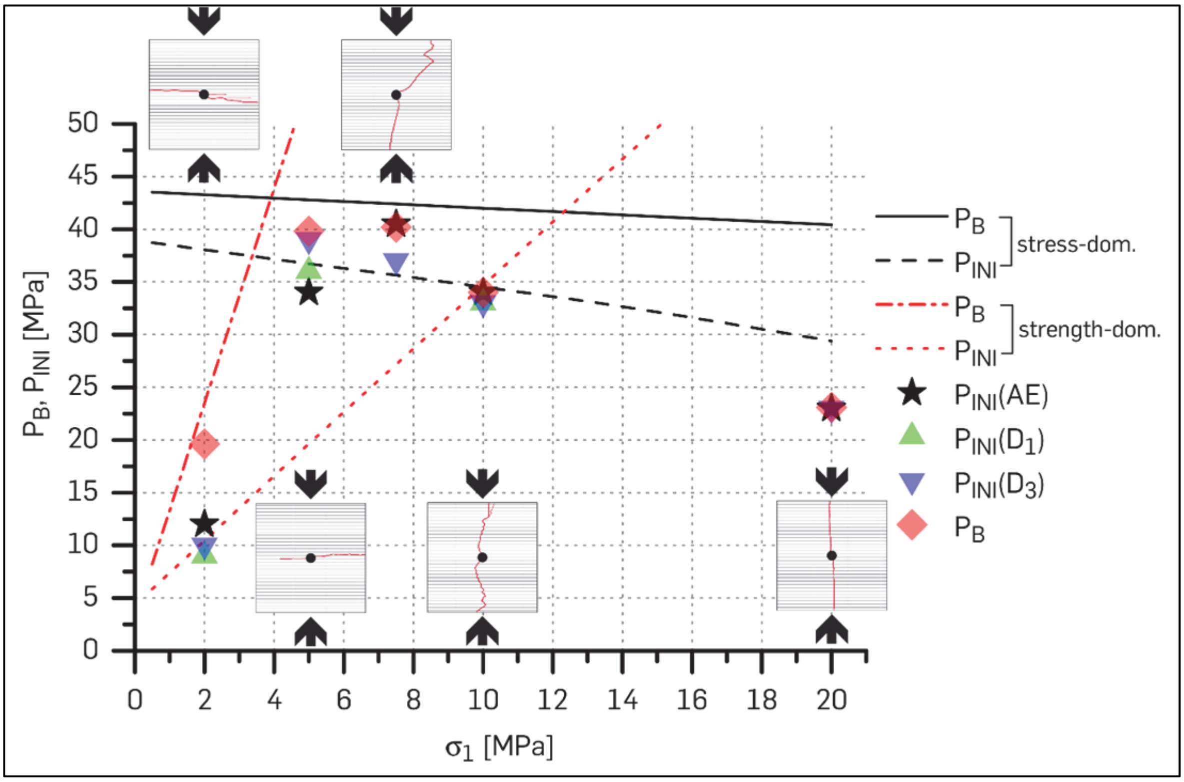

Fig. 15: Fracture initiation as determined by deformation ($P_{INI}(D_1)$) and ($P_{INI}(D_3)$) and acoustic emissions ($P_{INI}(AE)$) vs. uniaxial loading σ_1. Fracture geometries after the experiment are also shown at the respective uniaxial loading. Lines are fracture initiation (P_{INI}) as well as specimen breakdown (P_B) pressures calculated by numerical modeling. Black lines are for a stress dominated fracture parallel to σ_1, red lines are for strength-dominated fracturing in the foliation plane perpendicular to σ_1.

Experimental results show a similar trend. Fracture initiation pressures as determined by acoustic emission as well as breakdown pressures increase up to a uniaxial loading of 7.5 MPa. At 20 MPa uniaxial loading, fracture initiation and breakdown pressures are significantly lower. However, the numerical model seems to fail in predicting the absolute magnitudes of initiation and breakdown pressures at such high loading magnitudes. This might be specific for slate or in general material with high anisotropy. An experimental series using cylindrical specimens under isostatic confining pressures performed before gave similar findings. The simple fracture mechanical model overestimates the breakdown pressures at high confining pressure for slate specimens, while for other rock types it seemed to fit much better (Stoeckhert *et al.*, 2014).

From Fig. 15 it is evident, that at 2 MPa uniaxial loading, there is only fracture propagation in the foliation plane and no fracture parallel to σ_1. On the other hand, at

20 MPa uniaxial loading there is only one single planar fracture parallel to σ_1 and no visible fracture in the direction of the cleavage plane. In the transitional range at 5, 7.5 and 10 MPa uniaxial loading, the fracture geometry is complex including opening of cleavage planes, inclined fractures at varying angles to the direction of σ_1, stepped fractures and multiple branched fractures.

In the model, this is the range where the pressure to initiate a fracture parallel to the foliation plane is lower than for one perpendicular to it. However, the breakdown pressure for the latter is below that required for specimen breakdown by a fracture in the foliation plane. An interpretation of this modeling data could be that at first a fracture parallel to foliation is initiated. When injection is further increased a second fracture set perpendicular to the initial set and parallel to σ_1 is initiated and propagated until breakdown.

The fracture geometries are much more complex in our experimental results but we find evidence for fracturing parallel to foliation as well as fractures perpendicular (or at some high angle) to it in all three specimens under intermediate loading.

5 Conclusion

We performed hydraulic fracturing experiments under uniaxial and triaxial loading in the laboratory. Deformation measurements and detection of acoustic emissions gives insight in fracturing processes. The localization of acoustic emission events provides detailed information about fracture propagation and fracture geometry. Numerical modeling using fracture mechanics can reproduce most observations from laboratory experiments. However, the models fail to predict magnitudes of injection pressures at specimen breakdown in some experiments.

Hydraulic fracturing of anisotropic rocks in the laboratory results in complex fracture geometries. We found a transition from strength-dominated to stress-dominated fracturing in experiments with slate under uniaxial compression. In the strength-dominated regime, the fracture plane strongly deviates from the idealized model, where fracture propagation is parallel to σ_1. The detection of acoustic emissions in experiments with slate involves some difficulties that are not yet resolved. Transverse isotropic rocks like slate might be modeled using a directional anisotropy of strength parameters like fracture toughness.

Acknowledgements

This project is funded by the German Federal Ministry for Economic Affairs (FKZ 0325279B). The authors also gratefully acknowledge the support by our research partners at geomecon GmbH Potsdam for providing their software roxol™ and fruitful discussions.

6 References

Abou-Sayed, A.S., Brechtel, C.E., and Clifton, R.J., 1978, In Situ Stress Determination by Hydrofracturing: A Fracture Mechanics Approach: *J. Geophys. Res.*, v. 83, B6, p. 2851–2862, doi: 10.1029/JB083iB06p02851.

Akaike, H., 1974, A new look at the statistical model identification: *IEEE Transactions on Automatic Control*, v. 19, no. 6, p. 716–723, doi: 10.1109/TAC.1974.1100705.

Brenne, S., Molenda, M., Stöckhert, F., and Alber, M., 2014, Hydraulic Fracturing of a Devonian Slate under confining pressure – with emphasis on cleavage inclination, *in* Alejano, R., Perucho, Á., et al., eds., *Rock engineering and rock mechanics:* Structures in and on rock masses. EUROCK 2014, ISRM European Regional Symposium, Vigo, Spain. 26-28 May, CRC Press.

Brenne, S., Molenda, M., Stoeckhert, F., and Alber, M., 2013, Hydraulic and Sleeve Fracturing Laboratory Experiments on 6 Rock Types, *in* Jeffrey, R., ed., *Effective and Sustainable Hydraulic Fracturing*, InTech.

Clifton, R., Simonson, E., Jones, A., and Green, S., 1976, Determination of the critical-stress-intensity factor K_{Ic} from internally pressurized thick-walled vessels: *Experimental Mechanics*, v. 16, no. 6, p. 233–238, doi: 10.1007/BF02329274.

Dassault Systèmes, 2012, Abaqus: www.simulia.com.

Detournay, E., and Carbonell, R., 1997, Fracture-Mechanics Analysis of the Breakdown Process in Minifracture or Leakoff Test: *SPE Production & Operations*, v. 12, no. 3, p. 195–199, doi: 10.2118/28076-PA.

Frash, L., Gutierrez, M., and Hampton, J., 2013, Scale Model Simulation of Hydraulic Fracturing for EGS Reservoir Creation Using a Heated True-Triaxial Apparatus, Effective and Sustainable Hydraulic Fracturing.

geomecon GmbH, 2013, roxol: www.roxol.de.

Haimson, B., and Fairhurst, C., 1967, Initiation and Extension of Hydraulic Fractures in Rocks: *Society of Petroleum Engineers Journal*, SPE 1710-PA, doi: 10.2118/1710-PA.

Haimson, B., and Fairhurst, C., 1970, In-situ stress determination at great depth by means of hydraulic fracturing, *in* Somerton, W.H., ed., *Rock Mechanics - Theory and Practice:* Proceedings 11th Symposium on Rock Mechanics. 11th Symposium on Rock Mechanics, University of California, Berkeley, California. June 16-19, 1969, p. 559–584.

Haimson, B.C., and Avasthi, J.M., 1975, Stress measurements in anisotropic rock by hydraulic fracturing, *in* Hoskins JR, Earl R., ed., *Applications of Rock Mechnics:* Proceedings - Fifteenth Symposium on Rock Mechanics. Fifteenth Symposium on Rock Mechanics, Custer State Park, South Dakota. September 17-19, 1973, p. 135–156.

Haimson, B.C., and Zhao, Z., 1991, Effect of Borehole Size And Pressurization Rate On Hydraulic Fracturing Breakdown Pressure, *in* Roegiers, J., ed., *Rock Mechanics as a Multidisciplinary Science*, A. A. Balkema, Rotterdam.

Hubbert, M., and Willis, D., 1957, Mechanics of hydraulic fracturing: *Petroleum Transactions*, v. 210, p. 153–168.

Irwin, G.R., 1957, Analysis of stresses and strains near the end of a crack traversing a plate: *Journal of Applied Mechanics*, v. 24, p. 361–364.

Ishida, T., Chen, Q., Mizuta, Y., and Roegiers, J.-C., 2004, Influence of Fluid Viscosity on the Hydraulic Fracturing Mechanism: *Journal of Energy Resources Technology*, v. 126, no. 3, p. 190–200, doi: 10.1115/1.1791651.

Lockner, D.A., and Byerlee, J.D., 1977, Hydrofracture in Weber Sandstone at High Confining Pressure and Differential Stress: *J. Geophys. Res*, v. 82, no. 14, p. 2018–2026, doi: 10.1029/JB082i014p02018.

Moeck, I., Schandelmeier, H., and Holl, H.-G., 2009, The stress regime in a Rotliegend reservoir of the Northeast German Basin: *International Journal of Earth Sciences*, v. 98, no. 7, p. 1643–1654, doi: 10.1007/s00531-008-0316-1.

Nelder, J.A., and Mead, R., 1965, A Simplex Method for Function Minimization: *The Computer Journal*, v. 7, no. 4, p. 308–313, doi: 10.1093/comjnl/7.4.308.

O.Stephansson, 1983, Rock Stress Measurement by Sleeve Fracturing, *in* International Society for Rock Mechanics, ed., *Proceedings of the 5th Congress of the International Society for Rock Mechanics:* Proceedings, Melbourne/1983 = Congrès international de mécanique des roches comptes-rendus = Internationaler Kongress über Felsmechanik Berichte. --. International Congress on Rock Mechanics, Melbourne, Australia: Rotterdam, Balkema, p. F129-F137.

Ouchterlony, F., 1988, Suggested methods for determining the fracture toughness of rock: *International Journal of Rock Mechanics and Mining Sciences*, v. 25, no. 2, p. 71–96.

Parks, D.M., 1977, The virtual crack extension method for nonlinear material behavior: *Computer Methods in Applied Mechanics and Engineering*, v. 12, no. 3, p. 353–364, doi: 10.1016/0045-7825(77)90023-8.

Rummel, F., 1987, Fracture Mechanics Approach to Hydraulic Fracturing Stress Measurements, *in* Atkinson, B.K., ed., *Fracture mechanics of rock*: London, Academic Press. Academic Press geology series, p. 217–239.

Schmitt, D.R., and Zoback, M.D., 1992, Diminished pore pressure in low-porosity crystalline rock under tensional failure: Apparent strengthening by dilatancy: *Journal of Geophysical Research: Solid Earth*, v. 97, B1, p. 273–288, doi: 10.1029/91JB02256.

Serata, S., and Kikuchi, S., 1986, A diametral deformation method for in situ stress and rock property measurement: *International Journal of Mining and Geological Engineering*, v. 4, no. 1, p. 15-38, doi: 10.1007/BF01553754.

Stanchits, S., Surdi, A., Gathogo, P., Edelman, E., and Suarez-Rivera, R., 2014, Onset of Hydraulic Fracture Initiation Monitored by Acoustic Emission and Volumetric Deformation Measurements: *Rock Mechanics and Rock Engineering*, p. 1-12, doi: 10.1007/s00603-014-0584-y.

Stoeckhert, F., Brenne, S., Molenda, M., and Alber, M., 2014, Fracture mechanical evaluation of hydraulic fracturing laboratory experiments, *in* Alejano, R., Perucho, Á., et al., eds., *Rock engineering and rock mechanics:* Structures in and on rock masses. EUROCK 2014, ISRM European Regional Symposium, Vigo, Spain. 26-28 May, CRC Press.

Ulusay, R., and Hudson, J.A., editors, 2007, The complete ISRM suggested methods for rock characterization, testing and monitoring: 1974-2006, 2007th ed.: Ankara, Commission on Testing Methods, International Society of Rock Mechanics, 628 p.

Valkó, P., and Economides, M.J., 1995, Hydraulic fracture mechanics: Chichester, Wiley, 298 p.

van Dam, D.B., C. J. de Pater, and Romijn, R., 2000, Analysis of Hydraulic Fracture Closure in Laboratory Experiments: *SPE Production & Operations*, v. 15, no. 3, p. 151–158, doi: 10.2118/65066-PA.

Warpinski, N.R., and Teufel, L.W., 1987, Influence of Geologic Discontinuities on Hydraulic Fracture Propagation (includes associated papers 17011 and 17074): *Journal of Petroleum Technology*, v. 39, no. 02, p. 209–220, doi: 10.2118/13224-PA.

Zang, A., Christian Wagner, F., Stanchits, S., Dresen, G., Andresen, R., Haidekker, M.A., Zang, A., Stanchits, S., Dresen, G., Andresen, R., and Haidekker, M.A., 1998, Source analysis of acoustic emissions in Aue granite cores under symmetric and asymmetric compressive loads: *Geophysical Journal International*, v. 135, no. 3, p. 1113–1130, doi: 10.1046/j.1365-246X.1998.00706.x.

Zoback, M.D., Rummel, F., Jung, R., and Raleigh, C.B., 1977, Laboratory hydraulic fracturing experiments in intact and pre-fractured rock: *International Journal of Rock Mechanics and Mining Sciences & Geomechanics Abstracts*, v. 14, no. 2, p. 49–58, doi: 10.1016/0148-9062(77)90196-6.

Salt mechanics / fracture mechanics

Steady State Creep of Rock Salt

Improved Laboratory Test Method for Parameter Determination and extended Model Approach

Stationäres Kriechen von Steinsalz

Verbessertes Verfahren zur Bestimmung der stationären Kriechrate im Dauerstandversuch und numerische Nachrechung von Kriechversuchen mit einem weiterentwickelten Stoffmodell für stationäres Kriechen

R.-M. Günther, K. Salzer, T. Popp
Institute for Rockmechanics GmbH (IfG), Leipzig, Germany

Abstract

Actual problems in geotechnical design, e.g. of underground openings for radioactive waste repositories or high-pressure gas storages, require sophisticated constitutive models and consistent parameters for rock salt that facilitate reliable prognosis of stress-dependent deformation and associated damage from the initial excavation to long times. In the long term the response of salt masses is governed by its steady state creep behavior. However, because in experiments to reaching the "true" steady creep rate time periods of some few days up to years may be required (dependent mainly on temperature) an improved but even relatively simple test regime is proposed. A series of multi-step tests with loading and un-loading cycles allow a more reliable estimate of stationary creep rates in a reasonable time frame. In completion, the advanced strain-hardening approach of Günther/Salzer is used which describes all relevant deformation properties of rock salt, e.g. creep and damage induced rock failure, comprehensively within the scope of an unified creep approach. The capability of the combination of improved creep testing procedures and accompanied modelling is demonstrated by recalculating multi-step creep at different loading and temperature conditions. Thus reliable extrapolations relevant to in-situ creep rates (10^{-9} to 10^{-13} s^{-1}) become possible.

Zusammenfassung

An untertägige Bauwerke im Steinsalz werden immer komplexere gebirgsmechanische Anforderungen gestellt. Das betrifft ganz besonders die langzeitsichere Verwahrung von Gefahrstoffen und die damit verbundenen Fragestellungen zur Stabilität, Barriereintegrität und zum Konvergenzverhalten für lange Prognosezeiträume. Aber auch in anderen Bereichen wie z. B. der Kavernenspeicherung, deren Speicherzyklen einer zunehmenden Intensivierung unterliegen, werden die Aufgabenstellungen zunehmend komplexer. Aus diesem

Grund kommt einer konsistenten Beschreibung des Spannungs-Verformungs-Verhaltens von Steinsalz sowie der Ableitung belastbarer gesteinsphysikalischer Parameter eine immer größere Bedeutung zu. Während unmittelbar nach der Hohlraumschaffung Schädigungs- und Entfestigungsprozesse das Verformungsverhalten z. T. stark beeinflussen können, ist das langzeitige Kriechverhalten von Steinsalz hauptsächlich vom stationären Kriechen abhängig. Für Langzeitprognosen über mehrere hundert bis hunderttausend Jahre ist daher das stationäre Kriechen der maßgebliche Prozess. Im Dauerstandversuch stellt sich die “wahre” stationäre Kriechrate (abhängig von Temperatur und Spannung) nach Wochen oder aber bei geringer Spannung und Temperatur auch erst nach Monaten bzw. Jahren ein.

Mit dem vorliegenden Beitrag wird ein vergleichsweise einfaches Verfahren zur Durchführung von Dauerstandversuchen vorgestellt, mit dem die stationäre Kriechrate in akzeptablen Zeiträumen und mit höherer Genauigkeit ermittelt werden kann. Dazu werden Mehrphasenkriechversuche durchgeführt, die eine Kombination von Be- und Entlastungsstufen beinhalten.

Zusätzlich werden mit dem Erweiterten Dehnungs-Verfestigungsansatz (Günther/Salzer) Kriechversuche mit einem einheitlichen Parametersatz nachgerechnet sowie Prognoserechnungen für unterschiedliche Temperaturen durchgeführt und anschließend mit den entsprechenden Versuchen verglichen. Die Kombination zwischen dem verbesserten Untersuchungsverfahren und der Modellierung zeigt, dass für die langzeitig relevanten in-situ Kriechraten (10-9 bis 10-13 s-1) eine zuverlässigere Extrapolationen möglich ist.

1 Introduction

The mechanical properties of rock salt are extensively investigated in the past, not only motivated by its enormous economic importance, e.g. for extraction by conventional or solution salt mining, but in particular by its unique properties, i.e. tightness and plasticity. The latter facts justify its suitability as natural geological barrier, e.g. for gas storage purposes and final disposal of hazardous chemo-toxic or radioactive waste [1, 2]. However, to exclude a threat to actual and future generations the salt barrier integrity has to be demonstrated during construction, operation and in the post-closure phase of a repository. For model calculations one needs detailed knowledge and understanding of material behavior under relevant loading conditions, e.g. the elastic properties, creep, dilatancy, damage fracture development, creep failure, failure and permeability.

In our contribution we focus on the time-dependent stress-strain characteristics of rock salt which is usually denoted as creep. The creep may be subdivided as well documented by experimental studies into the following three phases representing the typically observed behavior in creep tests:

(i) Primary creep – also denoted as transient or non-stationary creep,
(ii) Secondary or stationary creep, and
(iii) Tertiary creep or creep failure.

These three creep phases are one-after-another related, and their change results from the action of different intra-crystalline deformation processes, as described below. However, creep depends, in addition to external factors, i.e. magnitude of the applied load (difference stress: $\sigma_{Diff} = \sigma_1 - \sigma_3$), temperature and time, on lithological parameters, such as rock structure, size and distribution of accessory components (e.g. anhydrite), as documented for instance in many papers presented during the seven conferences on the mechanical behavior of salt since 1984. The last conference took place 2012 in Paris [3]. With respect to the variety of influence parameters reliable experimental investigations are of urgent need to characterize the material and site-specific long-term behavior of rock salt.

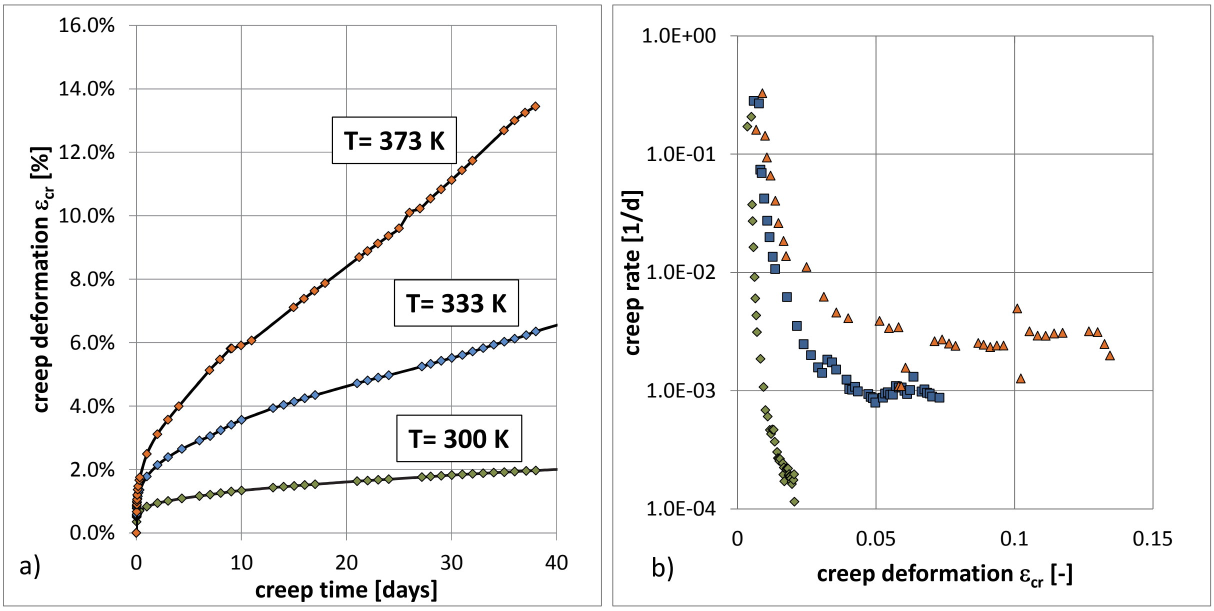

Fig. 1: Creep of rock salt (Asse-Speisesalz from the Asse salt mine, Germany) at elevated temperatures: σ_3 = 20 MPa, σ_1 = 38 MPa, σ_{Diff} = 18 MPa: a) deformation vs. time; b) creep rates vs. deformation

In the long term where only moderate stresses are acting as documented microstructural studies of subgrain sizes [4] the response of salt masses is governed by its steady state creep behavior, i.e. the transient creep has been vanished.

Thus, the experimental challenge is to ensure that “true” stationary creep is acting during the test, i.e. that the primary creep is truly finished. Exemplarily, in Fig. 1 creep curves on homogenous rock salt samples (i.e. lithological differences may be neglected) are depicted, which were performed at σ_3 = 20 MPa, i.e. the loading conditions are below the dilatancy boundary. The results clearly document that despite the moderate high difference stress of σ_{Diff} = 18 MPa at room temperature which represents the usual creep test standard no stationary creep is reached (ongoing drop of the green symbols in Fig 1b). The results even show that for higher temperatures the steady state creep rate is faster achieved (Fig 1b - constant getting values for T=333 K and T=373 K).

The change of creep rate in the course of transient creep is caused by the changing relation of work hardening due to the entangling of the increasing number of dislocations and of recovery due to the annihilation of dislocations. In steady state creep these processes are in balance whereas work hardening dominates after a stress increase causing a decreasing strain rate (normal transient creep), and recovery is dominant after a stress decrease causing an increasing strain rate (inverse transient creep). This fact can be used to overcome the usual experimental deficits of standard creep tests. In addition, the creep test results clearly document increased temperature conditions accelerate creep significantly.

Thus we suggest the following new creep test approach consisting of two parts:

(i) an improved testing procedure with a series of two-step creep tests at increased temperature, where after a hydrostatic consolidation phase, (1) a primary loading step and (2) an un-loading step to a lower load level is performed;
(ii) verification of the experimental test results by numerical modelling with re-calculation of the tests facilitating, thereby, a more reliable extrapolation of the data.

We used the advanced strain-hardening approach of Günther/Salzer which describes all relevant deformation properties of rock salt, e.g. creep and damage induced rock failure, comprehensively within the scope of an unified creep approach [5, 6].

2 Principles / Methodology

2.1 Dislocation creep / micro mechanics

At natural conditions at increased effective mean stress and especially at elevated temperatures dislocation creep is the dominating deformation mechanism in salt, i.e. polycrystalline halite can deform to large strains by this mechanism without microcracking and dilatancy [4].

Simulating natural creep in the lab with constant load conditions demonstrates that firstly primary creep occurs which is characterized by initially high deformation rates. They decrease continuously until a stationary creep rate is reached, i.e. the secondary creep. The creep rate controlling processes for primary creep are the dislocations which are present within the lattice structure and which start to move when stress increases. With ongoing deformation, new dislocations will be produced within the lattice. Thus, the dislocation density rises, and this process will cause an increasing resistance against deformation itself so that for maintaining a constant deformation rate an increasingly higher force is necessary or the deformation rate will decrease even when load is kept constant. This material hardening which increases with ongoing deformation is counteracted by the recovery of dislocations. This process results in stationary creeping if the formation rate becomes equal to the annihilation rate of the dislocations. In this phase the dislocation density (microscopic scale), the deformation resistance and consequently also the (macroscopic) creep rate evolve to constants [8]. Tertiary creep is caused by intra-crystalline fissures or micro-cracks i.e. denoted as damage. The formation of damage only occurs if the acting stress exceeds the dilatancy boundary [9]. Closely associated with local damage development is the volume dilatancy. If the damage reaches critical values, the creeping will transferred into its tertiary phase and creep-failure occurs.

2.2 Laboratory creep test procedure

The standard equipment to perform triaxial creep tests consists usually of a load frame, to apply the axial forces and a triaxial cell where a defined oil pressure acts as confinement. Despite the required accuracies of the applied stresses respectively the strain measurement conventional servo-controlled testing machines are only limited suitable for long-term creep tests due to economic considerations and the questionable long-term stability, e.g. risk of interruption due to a loss of electrical power. In addition, several tests have to be performed at the same time to increase the data base. Therefore IfG developed small and efficient creep test rigs, representing both hydraulic and mechanical loadings systems, as depicted in Fig. 2. A number of 48 test facilities are available in climate-controlled laboratories (room temperature: 25°C ±1°C). The standard samples are cylindrical cores, with 80 mm respectively 120 mm length and a diameter of 40 / 60 mm (depending on the grain size), i.e. the aspect ratio is always 2 : 1. The triaxial cells, used for testing at compressional and extensional stress regimes, can be heated up to 120°C. The test condition can be varied applying confining pressures up to 30 MPa, while the axial load is in a range up to 250 kN, depending on the creep rig. The axial load is determined by a calibrated load cell before each experiment. The confining pressure results from a hydraulic system and is kept constant by pressure accumulator as checked by digital pressure gauges. Both parameters are kept constant with accuracy better than 1% during the tests.

After installing the test samples in the triaxial cell, both, the axial and the radial stresses are increased simultaneously with a rate of 0.1 MPa/min. After a specified waiting phase for sample consolidation (we suggest 10 days, see below) the samples are loaded by increasing the axial stress with a rate of 1 MPa/min.

The first deformation measurement immediately after the loading phase leads to the start values for creep deformation $\Delta h_{cr}(0)$ and lifetime ($t = 0$). The deformation measurement are being carried out using three dial gauges fixed around the samples, each one 120° hocked. The accuracy of the measured deformations is ±0.002 mm.

To ensure constant stresses during the test the axial load was stepwise increased by correcting the axial load corresponding to the lateral strain assuming that the cross section is

$$A(\varepsilon)=\frac{A_0}{(1-\varepsilon)} \tag{1}$$

with $$\varepsilon=\frac{\Delta h}{h_0} \tag{2}$$

All test parameters like deformation, confining pressure and temperature are manually checked and recorded daily.

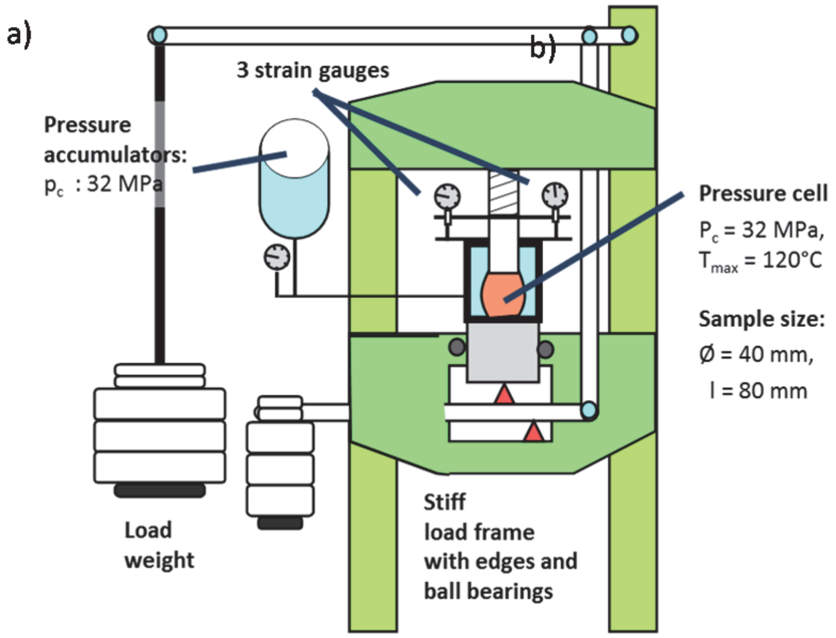

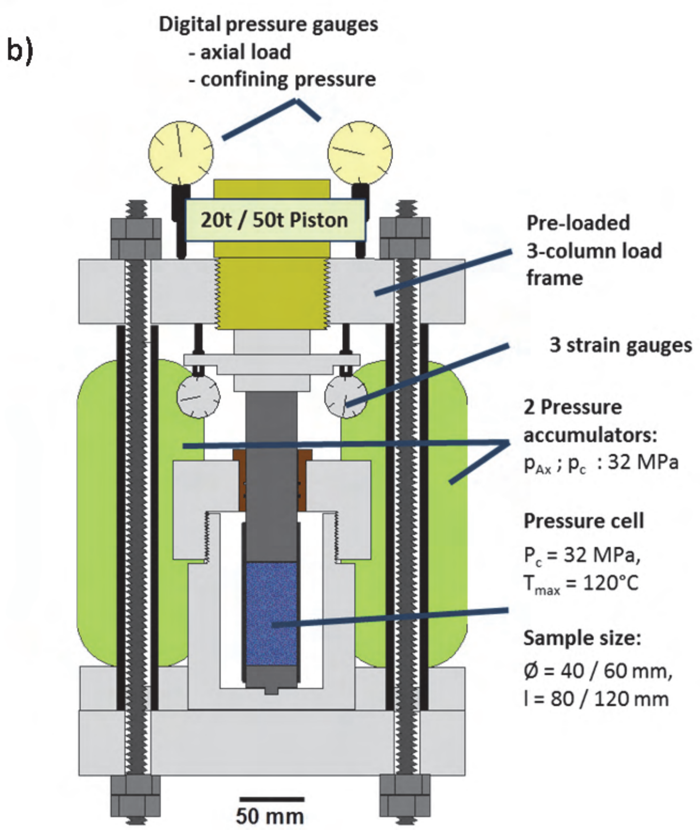

Fig. 2: Long-term creep test devices, available at IfG. a) Mechanical load rig with a cantilever system, amplifying the applied dead-load weight by a factor 50. Maximum load capacity: around 120 kN. b) Hydraulic load frame with an axial hydraulic cylinder: Maximum load capacity: 150 kN respectively 250 kN (depending on the creep rig and the used pressure accumulators).

2.3 Material

As reference material for creep testing we used the so-called “Asse-Speisesalz” (“z2Sp”) which is one of the most and best investigated rock salt types in Germany. The grain-shape texture of the almost pure halite is largely isotropic, with a grain size varying from 2 – 12 mm. The total water content is in the order of 0.05 wt%. The micro-structure of Asse rock salt suggest that natural deformation was accommodated by dislocation and dissolution-precipitation creep [10]. This material has been also subject in the German Joint Project III on the “Comparison of Constitutive Models for the Thermo-Mechanical Behavior of Rock Salt” [11].

3 The improved Creep test approach

3.1 Methodology

The new approach makes use of the fact that in steady state creep work hardening due to increasing number of dislocations and stress recovery due to the annihilation are in balance. Thereby work hardening dominates after a stress increase causing a decreasing strain rate (normal transient creep), and recovery is dominant after a stress decrease causing an increasing strain rate (inverse transient creep). However, in both cases the creep rates are approaching finally the same steady state creep rate. This physical fact has been used to improve the reliability of the experimental determination by applying both experimental loading conditions during a two-step creep test. This is demonstrated in Fig. 3.

The creep curves show, that as already learned, rock salt responds on loading with a high transient (primary) creep rate. But it is important to note that, at least in the beginning of deformation, primary creep is always overlapped by compaction depending on the initial state of unavoidable sample disturbance. To overcome these effects, firstly a compaction phase of 10days is initiated (not shown here). To ensure that no damage acts during the creep test application of high confining pressure (e.g. 20 MPa) is required to suppress the occurrence of micro cracks. In addition, the sample needs to be consolidated to eliminate sample disturbance, here a consolidation phase of 10 days also at 20 MPa isostatic stress is applied. Thus, the obtained creep curves reach more efficient stationary creep than it is observed in standard tests.

For the first “real” loading step, the axial load is increased up to the designated difference stress, whereas the confining pressure remains at 20 MPa. Directly after the loading the creep rate becomes initially quite high, but because of the acting hardening the creep rate decreases and approaches finally the steady state creep rate.

At the 2nd loading step, the applied stress difference is reduced by 2 MPa, but the creep rate switches not directly to that new value, which would be correspond to the new stress conditions. As the result of an “over-hardening” effect the creep movement is firstly disrupted. The reason for this is that the current dislocation density within the crystal lattice corresponds to the former higher loading. Because the dislocation flow depends on the dislocation density to the acting differential stress after the loading reduction is too low to maintain the dislocation flow. Therefore stops the macroscopic creeping but by recovery processes the dislocation density is reduced in time, whereby the creeping slowly restarts, i.e. onset of inverse transient creep. It has to be noted that a stress drop of not more than 2 MPa results in a tolerable time for creep recovery.

However, we found that the strain rate recovery during an unloading cycle approximates more reliable a steady state creep rate than in the pure loading cycle, especially if the temperature is increased.

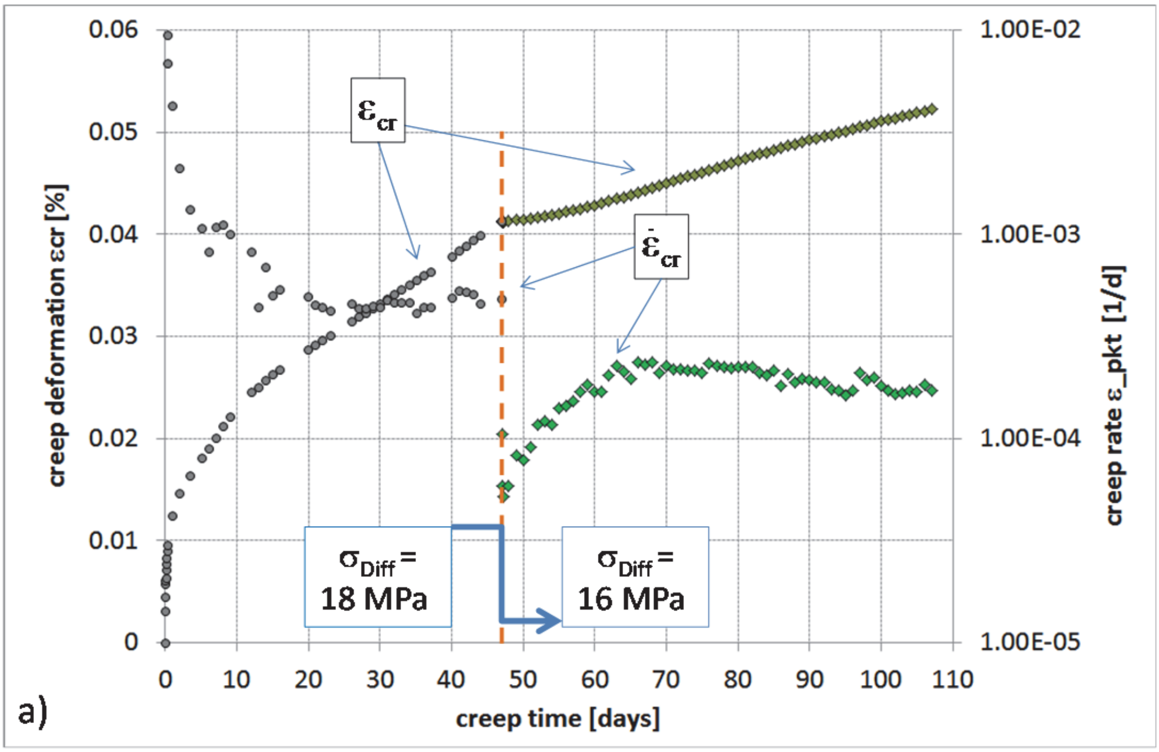

Fig. 3a: Evaluation of two 2-step creep tests as a function of time at T = 333K (60°C) and σ_3 = 20 MPa with a loading and an un-loading step - 1st test: σ_{Diff} = 18MPa ⇒ 16 MPa

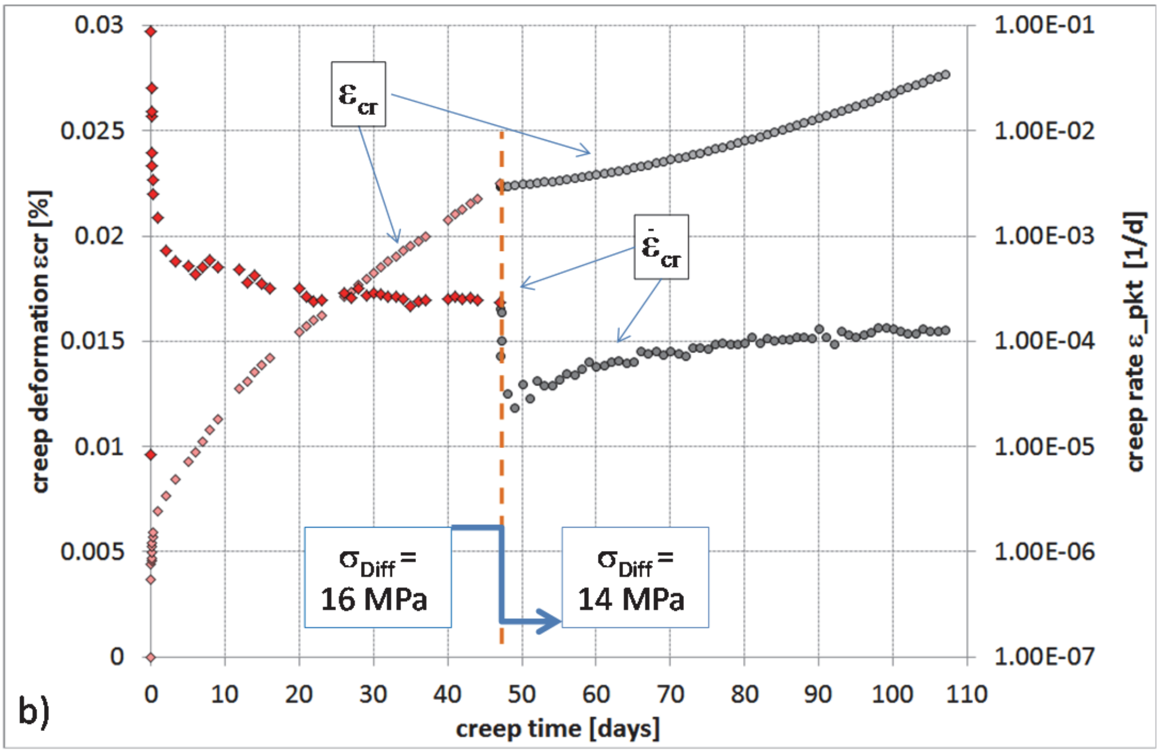

Fig. 3b: Evaluation of two 2-step creep tests as a function of time at T = 333K (60°C) and σ_3 = 20 MPa with a loading and an un-loading step - 2nd test: σ_{Diff} = 16 MPa ⇒ 14 MPa

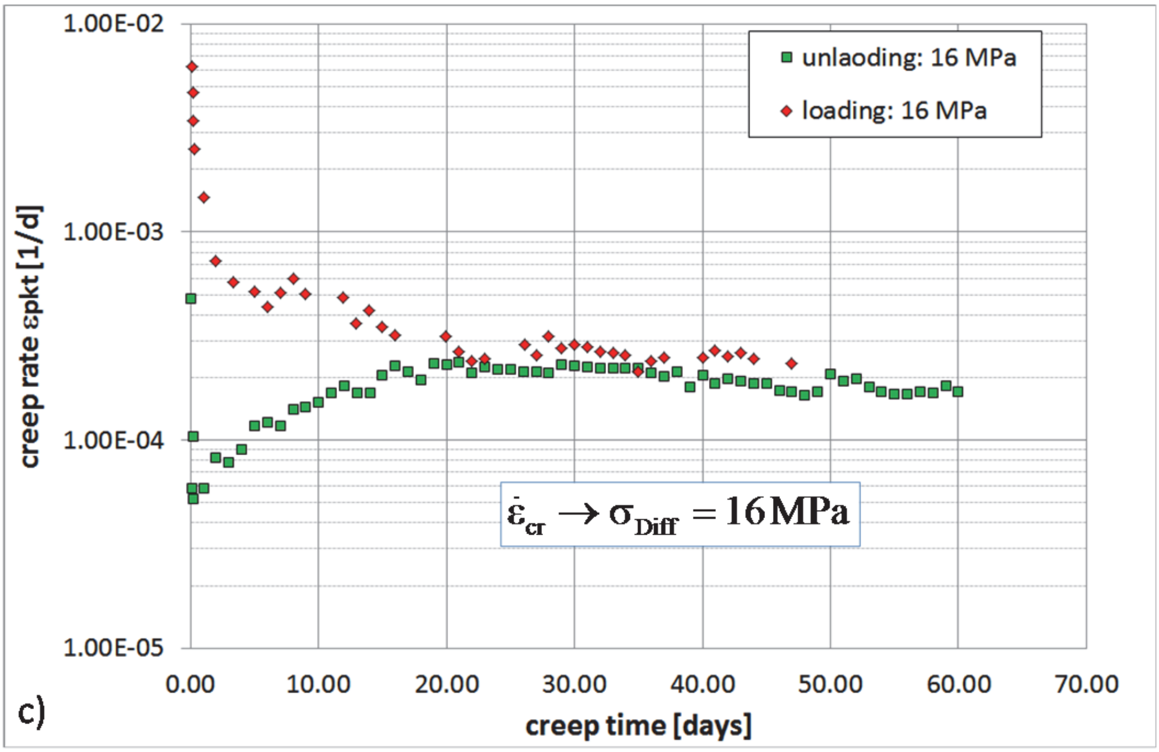

Fig. 3c: Evaluation of two 2-step creep tests as a function of time at T = 333K (60°C) and σ_3 = 20 MPa with a loading and an un-loading step - Comparison of the creep rates for both test steps at: σ_{Diff} = 16MPa.

3.2 Test-matrix

For parameter determination one needs a comprehensive large database, which has to be obtained by systematical variation of the applied experimental conditions, i.e. a complete test series. An example with a series of six creep tests on Asse-Speisesalz, loaded at around 60°C, is given in Tab. 1. Note, that always the difference stresses of the first and second step of the consecutive creep tests are equal. Thus, experimental verification of all test results is ensured. In addition, also the temperature dependence is investigated in additional single creep tests at room temperature and at around 90°C to facilitate extrapolations.

Exemplarily, the test results of the complete series (performed at 60°C) are shown in Fig. 4 demonstrating the impact of increasing difference stress on creep. The effect of temperature is illustrated in the Figs. 8 and 9.

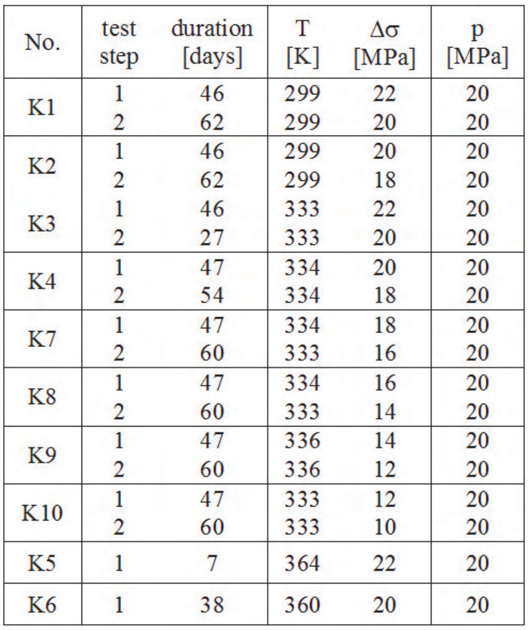

No.	test step	duration [days]	T [K]	Δσ [MPa]	p [MPa]
K1	1	46	299	22	20
	2	62	299	20	20
K2	1	46	299	20	20
	2	62	299	18	20
K3	1	46	333	22	20
	2	27	333	20	20
K4	1	47	334	20	20
	2	54	334	18	20
K7	1	47	334	18	20
	2	60	333	16	20
K8	1	47	334	16	20
	2	60	333	14	20
K9	1	47	336	14	20
	2	60	336	12	20
K10	1	47	333	12	20
	2	60	333	10	20
K5	1	7	364	22	20
K6	1	38	360	20	20

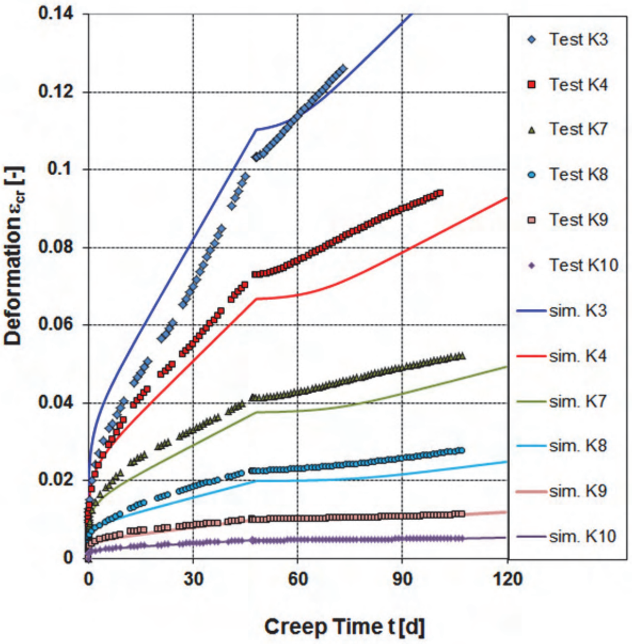

Fig. 4: Left: Table 1. Creep test matrix on Asse-Speisesalz with indicated temperatures T, stress differences Δσ, axial strain rate $d\varepsilon_1/dt$, and confining stress p for the parameter determination. Right: A series of two-step creep tests at 333 K (60°C) with Asse-Speisesalz, see Tab. 1. In addition, numerically calculated model curves are given after adjustment with the IfG-Günther/Salzer model and a unique parameter set for this salt type.

4 Verification of test results

4.1 Modelling of damage free creep

The constitutive Günther/Salzer model was used for subsequent modelling and numerical verification of the experimental test results. It is based on macroscopic-phenomenological description of the competition between the effective strain hardening and recovery given by the strain-hardening theory [12] where the creep deformation rate is described as follows:

$$\dot{\varepsilon}_{cr} = f(\sigma_{eff}, \varepsilon_{cr}^{V}) = A_p \frac{\sigma_{eff}^{n_p}}{(\varepsilon^{V,0} + \varepsilon_{cr}^{V})^{\mu}} \tag{3}$$

where A_p, n_p, μ being material parameters and σ_{eff} is the effective stress.

Because the macroscopically salt-creep results mainly from the movement of intra-crystalline lattice dislocations the deviatoric stress-induced dislocations density has an important effect to the creep rate. It follows, that the material hardening can be described by means of the creeping. (thus, strain or also deformation hardening). The parameter $\varepsilon^{V,0}$ is a value for the initial hardening.

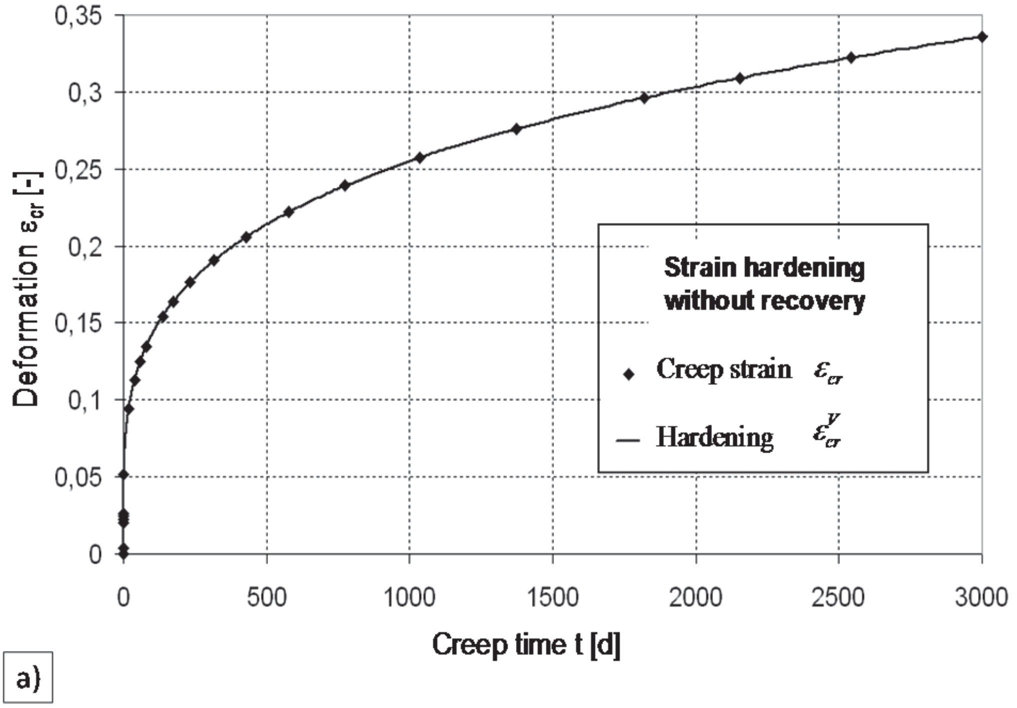

Fig. 5a: Modeling of only primary creep deformation – exemplary behavior. - only strain-hardening without recovery and damage/ dilatancy and b) strain-hardening with recovery but still without damage/ dilatancy.

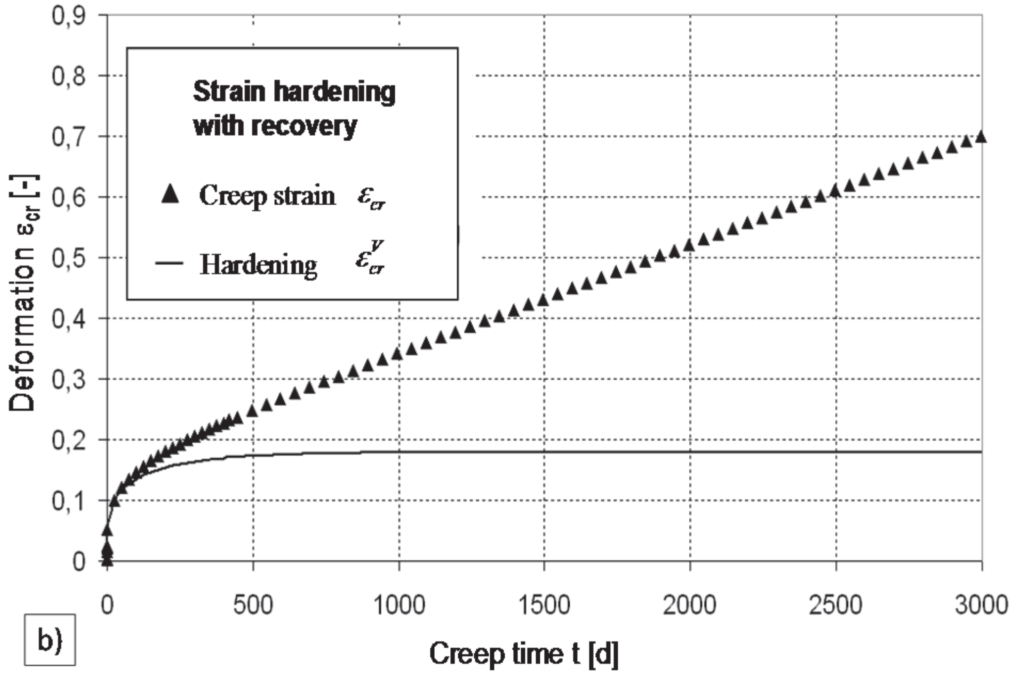

Fig. 5b: Modeling of only primary creep deformation – exemplary behavior. - strain-hardening with recovery but still without damage/ dilatancy.

Fig. 5a shows exemplarily the model response of Eq. (3) for primary creep (hardening and total creep deformation are equal: $\varepsilon_{cr}^{V} = \varepsilon_{cr}$, and also the therewith associated rates $\dot{\varepsilon}_{cr}^{V} = \dot{\varepsilon}_{cr}$). The creep parameters of Eq. (3) are evaluated on the base of creep tests which have to be carried out in the laboratory over a long period at sufficient high minimum stresses to suppress any dilatancy effect. Recovery processes develop only slowly at room temperature, so that after test periods of few months their effect is yet unimportant. This allows describing quite well the creep behavior using the strain-hardening approach, as shown below.

The process of dislocation annihilation is denoted as recovery which is counteracting the deformation hardening. The recovery is mainly a thermal activated process which runs quicker at higher temperatures. With growing dislocation density, also the recovery rate increases.

With involvement of the recovery the total creep rate $\dot{\varepsilon}_{cr}$ is the sum of both deformation components (resulting from hardening $\dot{\varepsilon}_{cr}^{V}$ and recovery $\dot{\varepsilon}_{cr}^{E}$), it follows [13]:

$$\dot{\varepsilon}_{cr} = \dot{\varepsilon}_{cr}^{V} + \dot{\varepsilon}_{cr}^{E} . \tag{4}$$

For the hardening associated strain follows from Eq. (4):

$$\dot{\varepsilon}_{cr}^{V} = \dot{\varepsilon}_{cr} - \dot{\varepsilon}_{cr}^{E} \tag{5}$$

with:

$$\dot{\varepsilon}_{cr}^{E} = A_{s1} \cdot \exp\left[\frac{-Q_1}{R \cdot T}\right] \sigma_{eff}^{n_{s1}} + A_{s2} \cdot \exp\left[\frac{-Q_2}{R \cdot T}\right] \sigma_{eff}^{n_{s2}} \tag{6}$$

where A_{s1}, n_{s1}, A_{s2} and n_{s2} are material properties determined at creep tests. It is possible to assign different activation energies (Q_1, Q_2), for a more precise adaption of the temperature dependence. For the hardening rate follows Eq. (7) from the Eq. (3), (5) and (6) with :

$$\dot{\varepsilon}_{cr}^{V} = A_p \frac{\sigma_{eff}^{n_p}}{(\varepsilon^{V,0} + \varepsilon_{cr}^{V})^{\mu}} - \dot{\varepsilon}_{cr}^{E} \tag{7}$$

The stationary creep phase is reached if the hardening rate tends toward to zero, because the accumulated hardening strain ε_{cr}^{V} will become constant (Fig. 5b).

In extension to the description of creep, only based on strain hardening, Fig. 5b shows exemplarily the model response of Eq. 3 for primary and secondary creep with consideration of recovery of hardening (hardening deformation $\dot{\varepsilon}^{V}_{cr}$ according Eq. 7).

With respect to onset of tertiary creep, i.e. for stress conditions above the dilatancy boundary, this effective strain hardening is reduced by damage softening. When the difference between both deformation rates become zero, failure occurs automatically. A special feature of the Günther/Salzer model is that the damage evolution rate is found to be equal to the volumetric strain rate. For more details about this approach, see [5, 6].

4.2 Back-calculation of creep test results

In a first step creep parameters were derived from a multi-parameter fit of the various experimental test regimes, also under consideration of temperature effects, i.e. with determination of the activation energy. For the Asse rock salt variety, the following creep parameters for the Günther/ Salzer model have been determined:

Transient creep:

$$A_p = 5{,}5 \cdot 10^{-40}\,[d^{-1}], \quad n_p = 19{,}6 \quad \mu = 5{,}25$$

Secondary creep:

$$A_{s1} = 0{,}05\ [d^{-1}]\ \ n_{s1} = 2{,}7\ \ Q_1 = 40\,{}^{kJ}\!/_{mol}$$
$$A_{s2} = 0{,}02\ [d^{-1}]\ \ n_{s2} = 6{,}8\ \ Q_2 = 65\,{}^{kJ}\!/_{mol}$$

Fig. 6a-6c shows the model response for the steady state creep rate depending on stress and temperature for three different temperatures corresponding to the test regime. In a first approximation the well-known (one component) BGR-a power law with a constant stress exponent of n = 5 is depicted in Fig. 6. However, it becomes obvious that the shape of the creep rate dependency at lower differential stresses is strongly non-linear, i.e. the creep rates become higher. Thus, because a non-constant stress exponent appears, we suggest the two component power law (eq. 6) which gives a much more realistic curved approximation.

However it has to be stated, that in contrast to other creep approaches in our constitutive model the transient creep parameters are mainly derived from strain-controlled triaxial strength tests at various confining pressures, for details see [11]. This considers the fact, that also in strain-controlled strength tests creep processes are dominating up to the failure limit.

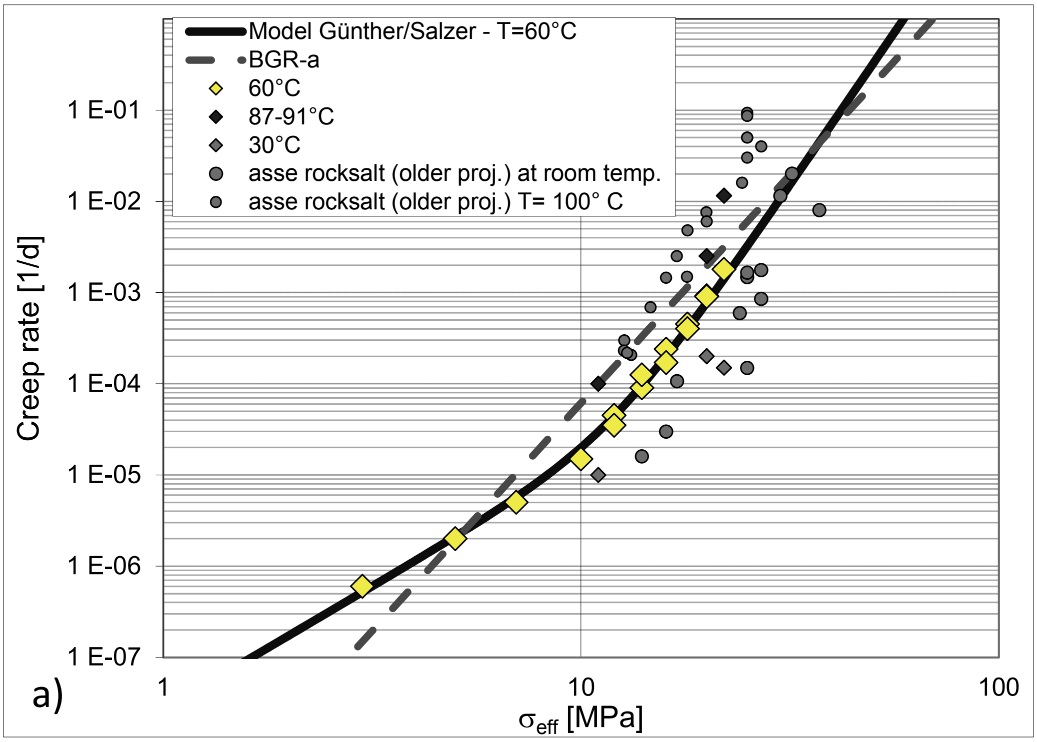
Model Günther/Salzer - T=60°C
BGR-a
60°C
87-91°C
30°C
asse rocksalt (older proj.) at room temp.
asse rocksalt (older proj.) T= 100° C
Creep rate [1/d]
1 E-01
1 E-02
1 E-03
1 E-04
1 E-05
1 E-06
1 E-07
1
10
100
σ_{eff} [MPa]
a)

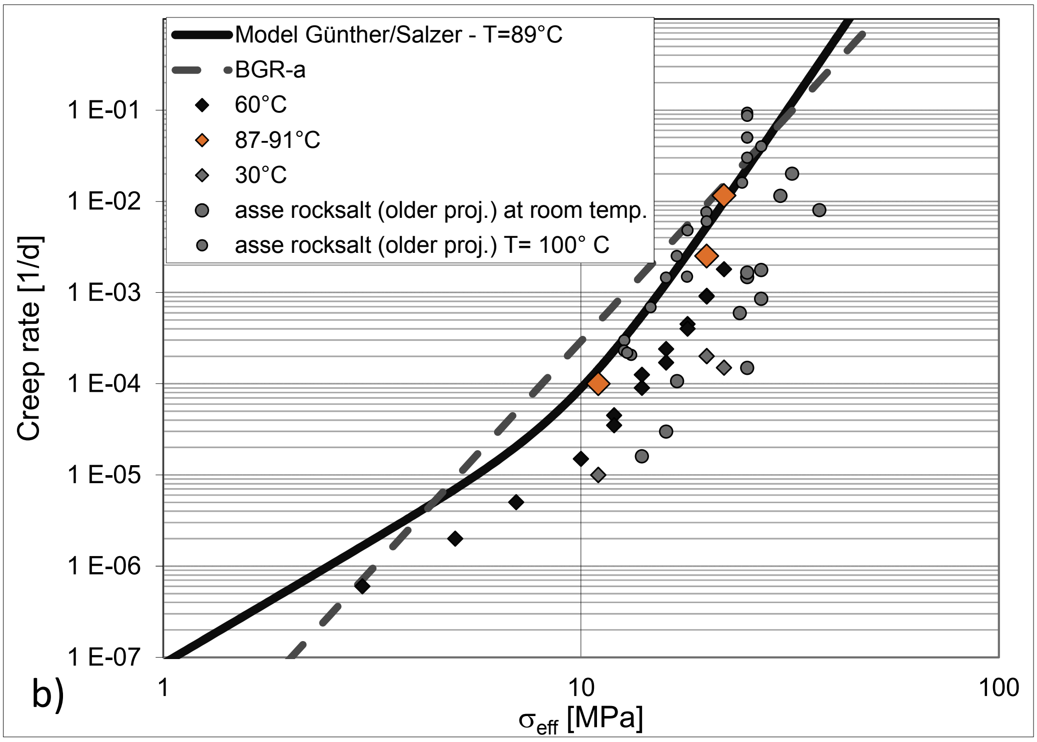
Model Günther/Salzer - T=89°C
BGR-a
60°C
87-91°C
30°C
asse rocksalt (older proj.) at room temp.
asse rocksalt (older proj.) T= 100° C
Creep rate [1/d]
1 E-01
1 E-02
1 E-03
1 E-04
1 E-05
1 E-06
1 E-07
1
10
100
σ_{eff} [MPa]
b)

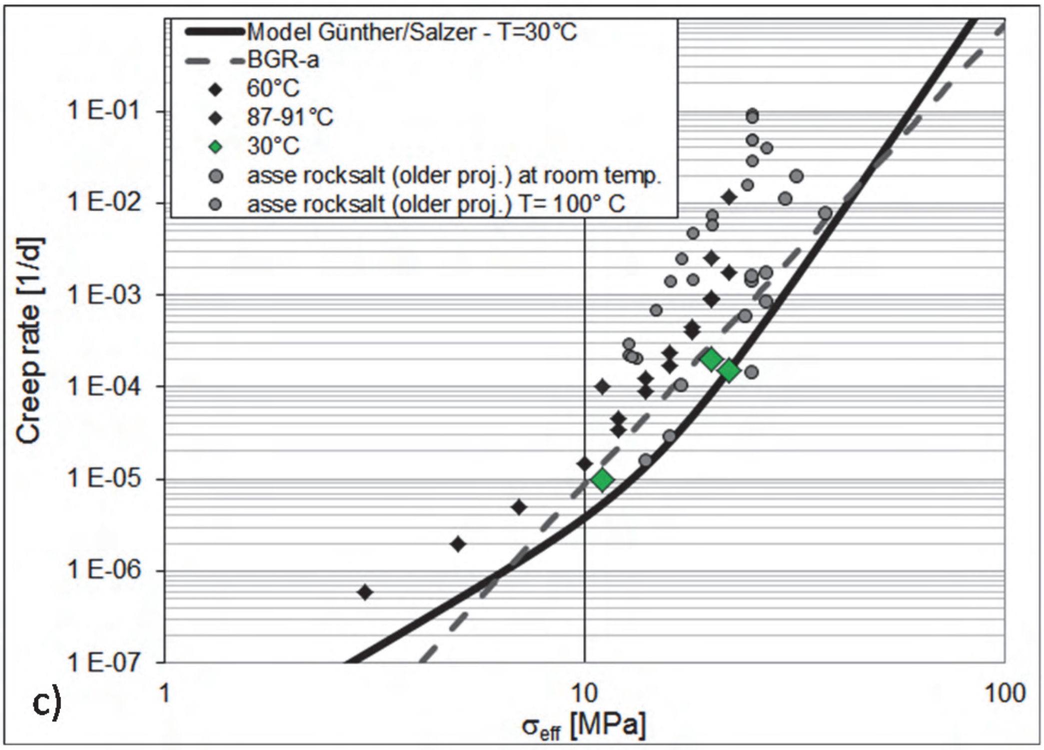

Fig. 6: Validation of the steady state creep behavior with the Günther/Salzer creep model in consideration of stress and temperature dependencies; a) 60°C; b) 88.5°C and c) 30°C. For comparison, comprehensive datasets for the room temperature and 100°C are given, taken from [11] are given.

Using the complete parameter set, given above, recalculations of all available creep tests were performed. Examples are presented in the Figs. 4, and 7. The set of creep curves in Fig. 4 illustrates nicely the increasing strain at higher difference stresses. In addition, also the effect of temperature, resulting in creep acceleration, has been recalculated in a good manner, as demonstrated in both Figs. 7a and 7b.

It has to been pointed out that all creep calculations were made with a unique parameter sets, demonstrating the capability of the Günther/Salzer, which also holds for coupled strength and dilatancy tests (given in [6, 11]).

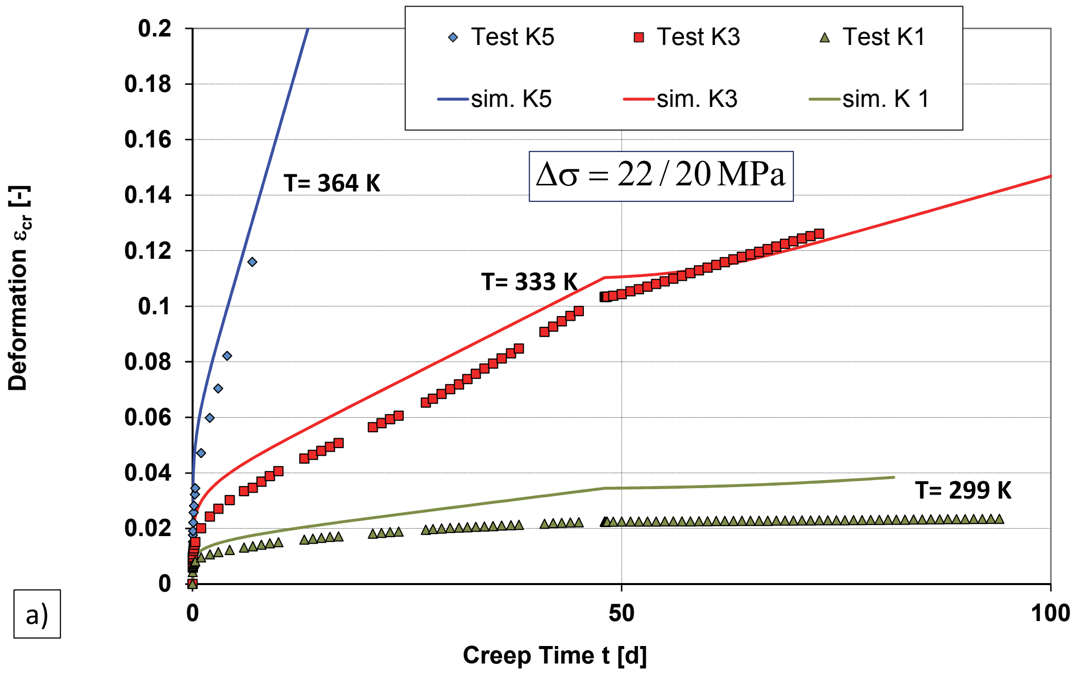

Fig. 7a: Recalculation of three two-step creep tests with σ_{Diff} = 22 MPa and 20 MPa at different temperatures (Tab. 1) with the Günther/ Salzer model and the unique parameter set.

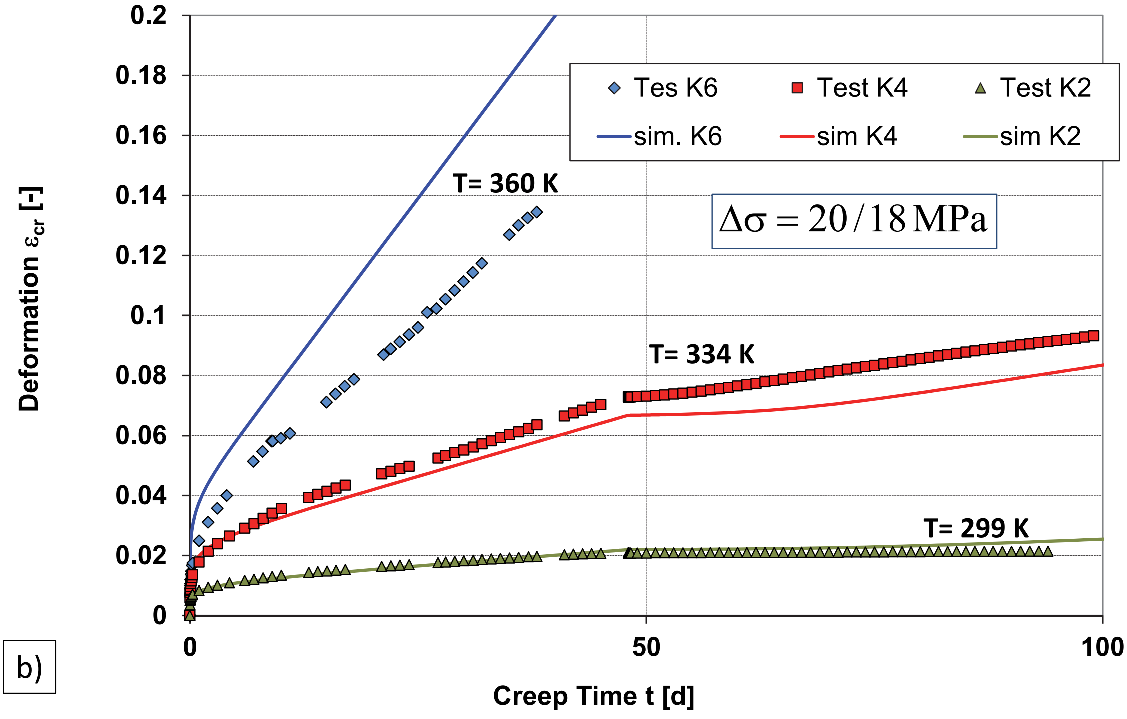

Fig. 7b. Recalculation of three two-step creep tests σ_{Diff} = 20 MPa and 18 MPa at different temperatures (Tab. 1) with the Günther/ Salzer model and the unique parameter set.

5 Summary and Conclusions

A new experimental testing approach for performing creep tests on rock salt is suggested which significantly improves the reliability of such tests, i.e. the determination of the stationary creep rate which is essential for predicting the long-term behavior of the salt mass.

Generally, the approach rests:

- on a series of two-step creep tests with previous consolidation at increased temperature with a primary loading and a subsequent unloading step of ≤ 2 MPa and
- on the verification of the experimental test results by numerical modelling with re-calculation of the test results.

The usability of the new test procedures was proven by a test series for Asse Speisesalz, where also temperature effects were considered. The creep tests were performed in two special triaxial test setups which were designed as simple as possible but with a high long-term reliability regarding the external load conditions (better than 1 %).

Generally, both mechanical and hydraulical axial load systems were found to be usable but the hydraulical system is more flexible than a dead-weight controlled cantilever system.

As prerequisites, it is recommended that

(1) the tests are performed at increased temperatures, e.g. 60°C, and

(2) that an initial consolidation phase of the samples is performed to reduce e.g. preparation-induced sample disturbances before the creep test is virtually started.

The test results document that if the load is changed, the sample behavior shows transient or primary creep, but reaches after some time a constant rate. Whereas in pure loading tests the stationary creep rate is usually over-estimated it becomes clear that creep rates resulting from a recovery (inverse) creep process after an unloading step corresponds to more realistic lower level. Additionally marks the inverse transient creep rate also a lower boundary for the extrapolation of the steady state creep rate.

However, due to the increased temperature, for both testing regimes (load and unload) nearly equal stationary creep rates were found. It has to be confirmed, that the use of increased temperature does not only limit the test duration to a tolerable time period but that, in addition, also creep tests at small difference stresses can be realized. Based on the help of the experimentally determined activation energy the obtained creep properties can be extrapolated to the respective in-situ-conditions.

The subsequent back-calculation demonstrated not only the quality of the various experimental creep curves itself but also the performed modelling. It has to mention that the macroscopic-phenomenological description of the competition processes between the effective strain hardening and recovery, as realized with the Günther/Salzer-model, allows the description of the realized test series with a unique parameter-set in a remarkably well manner.

In addition, the creep dependency as a function of stress is much better described by the preferred two-component creep law than only by simple power law, e.g. BGRa. However, the micro-mechanical process which is responsible for this non-linear behavior is lively debated [4, 7]. Nevertheless, the bandwidth of results gives an impression and a measure of the accuracy of simulation results that has to be taken into account when conclusions about the trustiness of extrapolations relevant to in-situ creep rates (10^{-9} to 10^{-13} s^{-1}) are drawn.

Acknowledgement

Financial support by the Federal Ministry of Education and Research (BMBF, projects I and II) and the Federal Ministry of Economics and Technology (BMWi, project III), and advisory support by the Project Management Agency Karlsruhe (PTKA-WTE) is gratefully acknowledged. The partners in the “Comparison of Constitutive Models for the joint projects “Thermo-Mechanical Behavior of Rock Salt” is thanked for the long-lasting and fruitful cooperation.

References

1. Minkley, W. and Popp, T., 2010. Final Disposal in Rock Salt - Geomechanical Assessment of the Barrier Integrity. In *Proceedings of the 44th US Rock Mechanics Symposium (ARMA-10), Salt Lake City/Utah, 27-30 June 2010*, American Rock Mechanics Association (ARMA), 10-492.
2. Hansen, F.D. and C.D. Leigh. 2011. Salt Disposal of Heat-Generating Nuclear Waste. Sandia Report SAND 2011-0161, Sandia National Laboratories.
3. Berest, P., Ghoreychi, M., Hadj-Hassen, F. & Tijani, M. (eds.) 2012. *Mechanical Behavior of Salt VII. Taylor & Francis group, London N, ISBN 978-0-415-62122-9.*
4. Urai, J. L., C. J. Spiers. 2007. The effect of grain boundary water on deformation mechanisms and rheo-logy of rock salt during long-term deformation. In *Proc. 6th Conference on the Mechanical Behavior of Salt “Saltmech6” Hannover, 22-25 May 2007,* 149 – 158.
5. Günther, R.-M., K. Salzer, and T. Popp. 2010. Advanced Strain-Hardening Approach Constitutive Model for Rock Salt Describing Transient, Stationary and Accelerated Creep and Dilatancy. In *Proceedings of the 44th US Rock Mechanics Symposium (ARMA-10), Salt Lake City/Utah, 27-30 June 2010*, American Rock Mechanics Association (ARMA).

6. Günther, R.-M. and K. Salzer. 2012. Advanced strain-hardening approach: A powerful creep model for rock salt with dilatancy, strength and healing. . In *Proceedings of the 7th Conference on Mechanical Behavior of Salt, Paris, 16–19 April 2012,* eds. P. Bérest, M. Ghoreychi, F. Hadj-Hassen, and M. Tijani, 13–22. Leiden: CRC Press/Balkema.
7. Carter, N.L., Horseman, S.T., Russell, J.E. and Handin, J. 1993. Rheology of rocksalt. *J. Struct. Geol.,* 15, 1257-1271.
8. Blum, W. 1993. Plastic Deformation and Creep of Crystalline Materials. In: *Plastic Deformation and Fracture of Materials, volume 6 of Materials Science and Technology,* ed. H. Mughrabi, 359–405, Weinheim, VCH Verlagsgesellschaft.
9. Hunsche, U., O. Schulze, F. Walter, I. Plischke. 2003. *Thermomechanisches Verhalten von Salzgestein.* Abschlussbericht Projekt Gorleben. Hannover: Bundesanstalt für Geowissenschaften und Rohstoffe (unpubl.).
10. Urai J.L. Spiers CJ. Peach C.J. Franssen R.C.M.W. and Liezenberg J.L. 1987. Deformation mechanisms operating in naturally deformed Halite rocks as deduced from microstructural investigations. Geol. Mijnbouw 66: 165-176.
11. Hampel, A., Argüello, J.G., Hansen, F.D., Günther, R.M., Salzer, K., Minkley, W., Lux, K.-H., Herchen, K., Düsterloh, U., Pudewills, A., Yildirim, S., Staudtmeister, K., Rokahr, R., Zapf, D., Gährken, A., Missal, C., Stahlmann, J. 2013. Benchmark Calculations of the Thermo-Mechanical Behavior of Rock Salt – Results from a US-German Joint Project. *Proceedings of the 47th US Rock Mechanics Symposium (ARMA-10), San Francisco, CA, USA, 23-26 June 2013*, American Rock Mechanics Association (ARMA), 10-456.
12. Odqvist, F. K. G. & H. Hult. 1962. Kriechfestigkeit metallischer Werkstoffe. Berlin: Springer Verlag.
13. Salzer, K. 1993. Ableitung eines kombinierten Kriechgesetzes unter Berücksichtigung der Erholung. Teilbericht zum BMFT Vorhaben 02 C 00 628. Leipzig: Institut für Gebirgsmechanik (unpubl.).

A mechanism-based creep constitutive model for salt rock to simulate all creep phases

Ein komplexes Kriechstoffgesetz für Steinsalz zur Abbildung aller Kriechphasen

H. W. Zhou[a], D. Liu[a], J.Y. Ding[a], J.F. Liu[b]
[a] State Key Laboratory of Coal Resources and Safe Mining, China University of Mining and Technology, Beijing
[b]College of Water Resource and Hydropower, Sichuan University, Chengdu

Abstract

Research on creep behavior of salt rock is of great significance for long-term operation of many salt-based underground facilities. A computer-controlled creep system with acoustic emission (AE) sensors was employed to investigate creep behavior of salt rock. To get a better understanding of damage evolution in salt rock, real-time AE signals are monitored during whole process of creep test up to 359 days. It is shown that the accumulated AE counts have the same trend as the strain curve, reflecting a trend of the evolution of strain. In addition, based on the Weibull distribution of AE events during creep test, a variable-viscosity Abel dashpot is established by means of definition of damage variable. By replacing the Newtonian dashpot in the classical Nishihara model with the variable-viscosity Abel dashpot, a new fractional derivative constitutive model for salt rock is proposed based on acoustic emission. Furthermore, the parameters in the new constitutive model are determined by fitting analysis of experimental data. The comparison of modeling approach with experimental data indicates an agreement between theoretical modeling and experimental data in the three stages of creep of rock salt.

Zusammenfassung

Die Erforschung des Kriechverhaltens von Salzgestein ist von großer Bedeutung für viele langzeitlich betriebenen unterirdischen Einrichtungen im Salzgestein. Eine computergesteuerte Kriech-Versuchseinrichtung mit akustischer Emissionsanalyse (AE) wurde eingesetzt, um das Kriechverhalten von Salzgestein zu untersuchen. Um ein besseres Verständnis zum Schädigungsverhalten von Steinsalz zu erhalten, wurden durch Echtzeit AE-Aufzeichnungen der gesamte Kriechprozess bis zu einer Dauer von 359 Tagen untersucht. Es wurde erkannt, dass die akkumulierten AE-Counts denselben Trend aufwiesen wir die Deformations-Kurven und damit die Deformationen widerspiegeln. Basierend auf der während der Tests beobachteten Weibull-Verteilung der AE-Ereignisse wurde ein viskositätsveränderlicher Abel-Dämpfer eingeführt, über den eine Schädigungsvariable definiert wird. Dadurch, dass der Newton-Dämpfer durch einen klassischen Nishihara-Dämpfer mit viskos-variablem Abel-Dämpfer ersetzt wurde, konnte ein partiell neues Materialgesetz für Steinsalz auf Basis der AE abgeleitet werden. Darüber hinaus konnten die Parameter des neuen Materialgesetzes durch Kurven-Fitting aus den experimentellen

Versuchen bestimmt werden. Ein Vergleich der Modellierungsergebnisse mit denen des Experimentes zeigt eine Übereinstimmung für alle drei Stadien des Kriechprozesses von Steinsalz.

1 Introduction

Research of the creep behavior of salt rock is of great importance for many salt-based underground engineering projects and many efforts have been focused on the mathematical modeling of creep of salt rock. The strain curve of creep in salt rock can be characterized by typical three stages: primary creep stage, steady stage and accelerated creep stage. Generally the constitutive models of salt rock also has been divided into three kinds, which are named empirical models, component models and mechanism-based creep constitutive models (Zhou *et al*., 2011; 2012; 2013a; 2013b). Many efforts have been devoted to application of micro mechanical theory (Miura *et al*., 2003) or endochronic theory (Auberin *et al*., 1991) to develop creep constitutive models in order to describe the three stages of creep in salt rock, especially the tertiary stage. Hou and Lux proposed a damage variable creep constitutive model of salt rock called Hou/Lux model, which shows the development of dilatancy, damage and healing of salt caverns (Hou *et al*., 1999). Adolfsson *et al*. (2005) proposed a fractional order viscoelastic model based on the concept of internal variables. They found that the corresponding rate equations can be formulated by the fractional order integrals rather than the fractional order derivatives.

The theory of fractional calculus is focused on the study of calculus of any order and has an increasing research application in many fields. Rogers (1983), Bagleyand, Torvik (1983, 1985), and Koeller (1984) established a solid foundation in fractional derivative models. Fu *et al*. (2013) developed a novel boundary meshless approach (LTBPM) for numerical modeling of time fractional diffusion equations. By replacing a Newtonian dashpot in the classical Nishihara model with the fractional derivative Abel dashpot, Zhou *et al*. (2012) proposed a new creep constitutive model on the basis of time-based fractional derivative. The results estimated by the new model are in better agreement with the experimental data.

In their experiments, the authors used a computer-controlled creep approach under uniaxial compression accompanied by acoustic emission (AE) monotoring to investigate creep behavior of salt rock. AE signals are monitored during whole process of creep tests for a better understanding of damage evolution in salt rock. It is suggested that the accumulated AE counts have the same trend as the strain curve, but ahead in time. It can reflected the trend of the evolution of strain. In addition, based on the Weibull distribution of AE events gained from the experiment, a variable-viscosity Abel dashpot is established by means of definition of damage variable. The author replaced Newtonian dashpot in the classical Nishihara model with the variable-viscosity Abel dashpot, and established a new fractional derivative constitutive model of salt rock based on acoustic emission. The comparison of modeling approach with experimental data indicates that the fractional derivative constitutive model can reflect the three stages of creep of rock salt.

2 Experimental studies of salt rock

2.1 *Sample preparation*

The salt rock samples were taken from the PT Well No.1 at a depth of 1719 m below ground surface, Pingdingshan, Henan Province, Central China. The specimens used in the experimental study were prepared with required dimensions of 80 mm in diameter and 160 mm in height. These samples are of high quality which means there is quite a little impurity inside, so it appears milk white from observation (Fig.1a).

2.2 *Experimental setup*

The creep tests were completed in Sichuan University by using computer-controlled creep test setup with acoustic emission (AE) sensors (Fig.1b). The required experimental parameter settings are: uniaxial load: 0~600 kN; confining pressure: 0~30 MPa; temperature: 22°C. The AESMART 2000 supervisor control system produced by DECI corporation is adopted in this acoustic emission (AE) test. 8 AE sensors are fixed on the surface of sample symmetrically both on the top and bottom. Frequency is 150 kHz (Fig.1c). The creep tests were carried out by using a constant uniaxial load of 80 kN and lasted for 359 days.

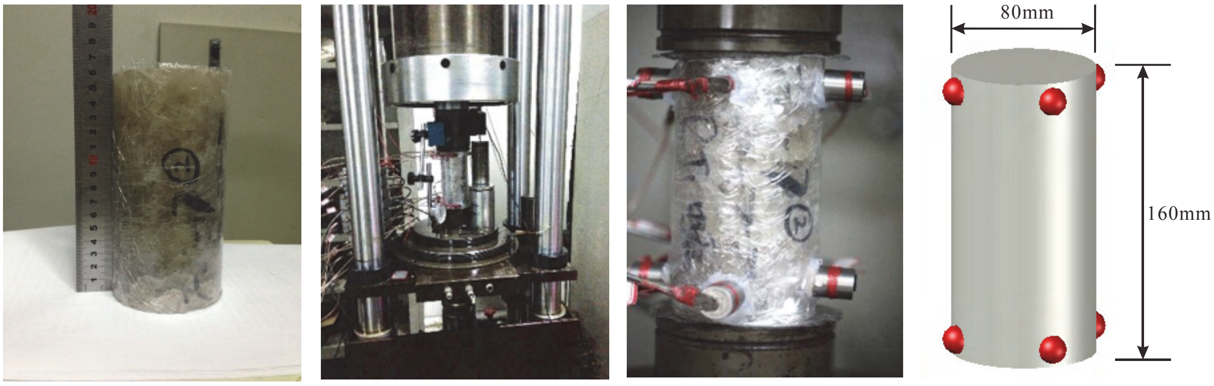

(a) (b) © (d)

Fig.1 Experimental set-up of creep test of salt rock
(a) specimen of salt rock; (b) computer-controlled creep test set-up; (c) AE sensors fixed on the specimen; (d) model for salt rock with dimensions

2.3 *Results of experiment*

The creep curve under uniaxial load and the strain rate curve are shown in Fig.2a and Fig.2b, respectively. During the experiment, the 8 AE sensors collect AE signals from the sample under uniaxial load and confirmed the position in 3D space at the same time. Actually, an AE signal can be received by one or more sensors, there are sure some tiny distinction in parts of the AE event frequency data collected from different sensors. The frequency of AE events collected from sensor 5 is shown in Fig.3a, which increases nonlinearly with time. The accumulated AE counts-time curve is shown in Fig. 3b.

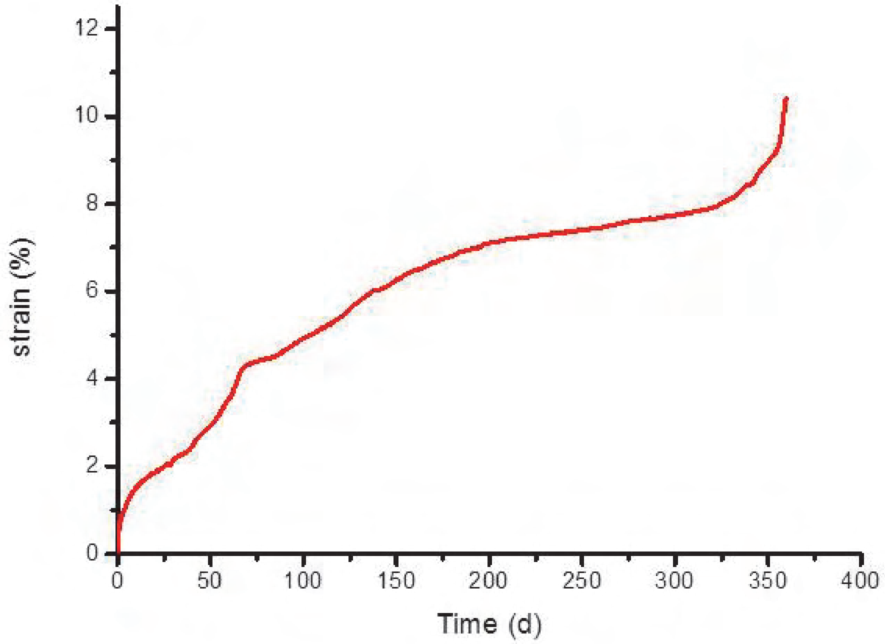

(a)

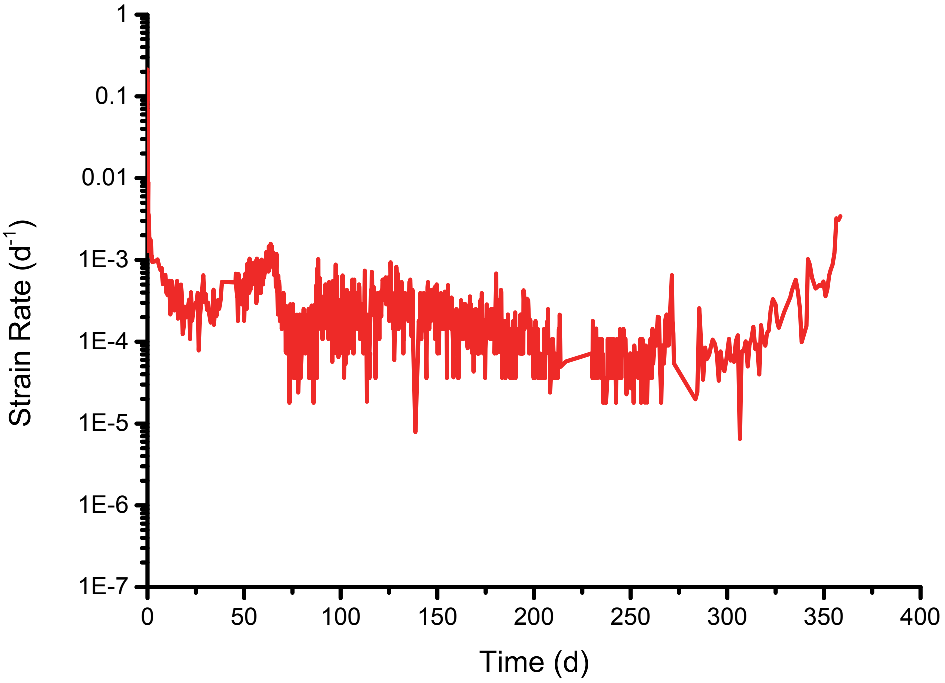

(b)

Fig.2 Data of creep test for salt rock
(a) Strain curve of salt rock; (b) Strain rate curve of salt rock

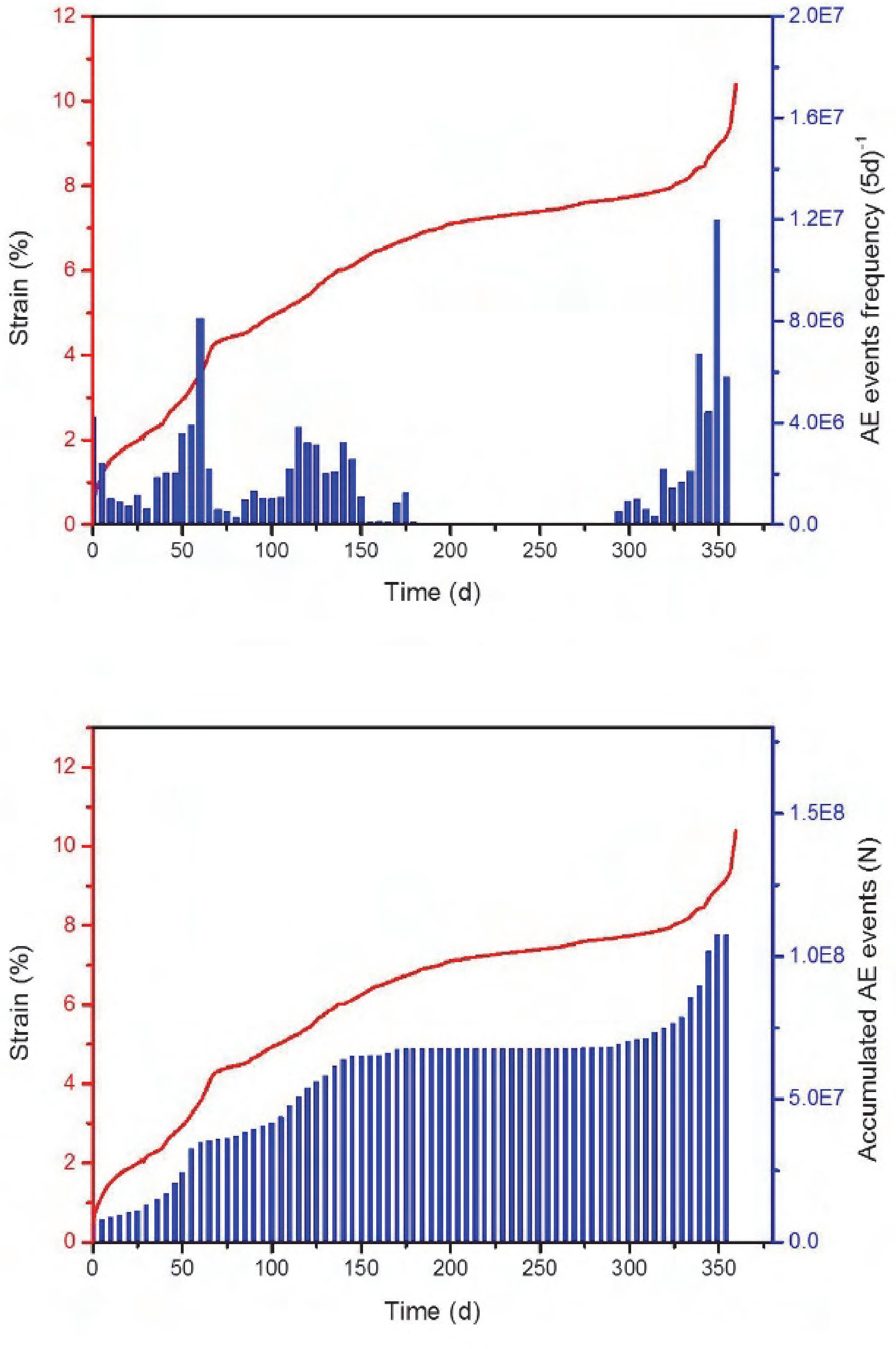

(a) (b)

Fig.3 Data of creep-acoustic emission test for salt rock
(a) Frequency of AE events; (b) Accumulated AE events

There are many kinds of failure modes in rock materials, but brittle failure and flexible failure take the dominant position. This can easily be distinguished by human eyes. If there are bursts and cracks observed by eyes, it’s brittle failure. If there are not any obvious cracks, it is flexible failure. The flexible failure is usually caused by sliding or dislocation between crystals. In this experiment, the failure of salt rock samples is bulging failure, belonging to flexible failure type. Damage and deformation pattern at different time is shown in Fig.4.

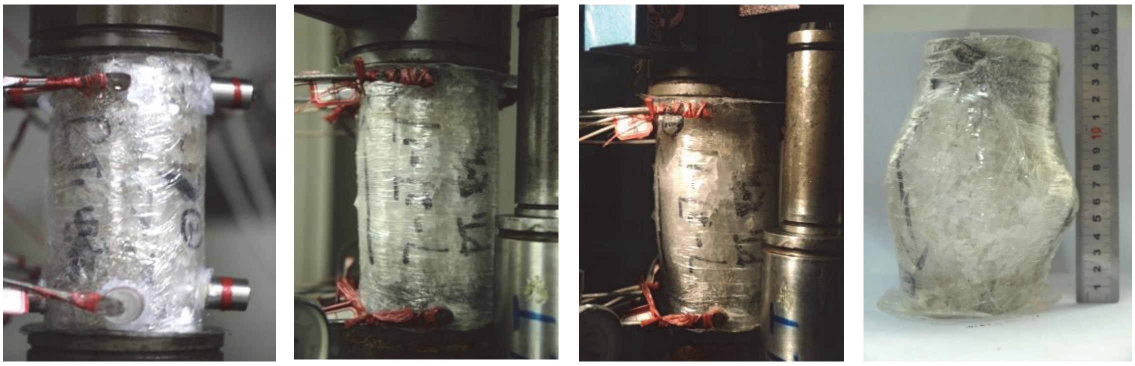
(a) (b) (c) (d)

Fig.4 Salt rock during the whole procedure of experiment
(a) Sample before creep test; (b) 120 days after beginning of creep test; (c) 340 days after beginning of creep test; (d) Sample after creep test (359 days)

2.4 *Analysis of results*

Fig. 2a shows the creep curve of salt rock for a uniaxial load creep test. The strain curve of specimen reflects the typical 3 stages of creep in salt rock: primary creep stage, longer steady stage and accelerated creep stage. The strain rate curve in Fig. 2b indicates that after a sharp descend during a short time at the beginning, the strain rate is slowly rising until 70 days which then plummeted. After that, it experienced a long dynamic stability stage before final ascended to the extreme value. Actually the two actions ‘hardening’ and ‘recovery’ are involved in the whole process of creep in salt rock. Hardening can be concluded as the dislocation confined inside the crystals, so the internal stresses increase and hinder the growth of strain. Recovery can be recognized as the annihilation of dislocation or the dislocation crossing the barrier which results in climb and cross-slip. During the primary creep stage hardening take the leading position. In the longer steady stage, the two actions are in dynamic competition, then recovery action takes the leading position during the final stage of creep.

Fig. 3 shows the data of creep-acoustic emission test for salt rock under a fixed uniaxial load. It is indicated that in transient creep stage, there are abundant AE signals. AE counts soar conspicuously first after the initial load on samples. This is according to the generation and disappearance of micro-fractures as well as dislocations and glide accompany by load up. Then AE counts descend slowly for a short while the cracks has been compressed. After that the counts of AE signals ascended to maximum value. This also can be reflected in the strain curve of salt rock at around 70 days, the stain rate experienced a fluctuation that time. During the beginning of longer steady stage, the AE signals are quite active, it is because of the expanding of micro-fracture under recovery action afford the help for growth of strain and balanced with hardening. From 150 days to 300 days, the AE signals nearly disappear as hardening and recovery are in an inactive balanced stage, the strain energy is accumulated till the next stage. In accelerated creep stage, the cracks grow quickly and AE signals soared to the peak value until there's bulging failure appeared in the salt rock sample. It also can be observed in Fig. 3b that the accumulated AE counts have the same trend as the strain curve of salt rock.

3 A creep model of salt rock based on acoustic emission

The acoustic emission phenomenon is the result of the internal damage evolution, so a model which can reflect the characteristics of acoustic emission based on damage theory can be established. For isotropic damage under uniaxial stress, *d* is defined as the damage variable. According to the method of Kachanov, the definition of *d* is given by

$$d = \frac{A}{A_d} \tag{1}$$

where A_d is the total area of micro-defects in instant bearing surface, A is the area of the non-destructive cross-section.

The definition of *N* is given by

$$N = \frac{N_m}{A} A_d \tag{2}$$

where *N* is the cumulative number of the acoustic emission events when section micro-defects area is A_d , N_m is the cumulative number of the acoustic emission events when the rock fails (section area A completely destroyed).

By combining Eqs. (1) and (2), one gets

$$d = \frac{N}{N_m} \tag{3}$$

The rock is divided into a number of microelements based on microscopic damage mechanics during the damage evolution process. Assuming that the number of acoustic emission events correspond to the failed number of salt rock internal elements and the probability density function of microelement failure, the Weibull statistical law holds, namely,

$$p(t) = \frac{m}{n}\left(\frac{t}{n}\right)^{m-1} e^{-\left(\frac{t}{n}\right)^m} \tag{4}$$

where m and n are parameters characterizing the damage influenced by experimental conditions and factors of specimen itself.

The number of failed elements at any time (t) is given by

$$n(t) = N_m p(t) = N_m \times \frac{m}{n}\left(\frac{t}{n}\right)^{m-1} e^{-\left(\frac{t}{n}\right)^m} \tag{5}$$

where N_m represents the total number of microelements failed (cumulative number of the acoustic emission events when the rock salt failed).

The total number of the microelement failure when section of micro-defects area reached A_d can be written as

$$N = \int_0^t N_m p(x)dx = N_m[1 - e^{-(\frac{t}{n})^m}] \tag{6}$$

Combining Eqs.(3), (4), (5) with (6), one gets

$$d = 1 - e^{-(\frac{t}{n})^m} \tag{7}$$

Eq. (5) correlates acoustic emission event number with loading time, and Eq.(7) is a damage function based on Weibull distribution. The constitutive relation of the Abel dashpot is given by

$$\sigma(t) = \eta^\beta D_t^\beta\left[\varepsilon(t)\right] \quad (0 \le \beta \le 1) \tag{8}$$

where η^β is the viscosity coefficient. If $\beta = 0$, the Abel dashpot becomes the Hookean model and Eq. (8) gives the stress-strain relation for an perfect solid; if $\beta = 1$, the Abel dashpot becomes the Newtonian dashpot and Eq. (8) represents the stress-strain relation of an perfect fluid. As a result, if $0 < \beta < 1$, Eq. (8) characterizes the creep property of a soft material whose rheological property is between the elastic Hookean model and the Newtonian dashpot.

If the Newtonian dashpot in the Nishihara model is replaced by Abel dashpot, the new model can describe the creep characteristic of rock. If the stress is lower than the yield limit, the viscoelastic strain of rock induces non damage; if the stress is larger than the yield limit, the damage threshold is reached with the unrecoverable damage accumulation, and the rock reaches the accelerated creep stage. However, in the Nishihara model, when the stress in salt rock reaches the yield limit, the viscoplastic strain continuously increases linearly with time. However, the linear increase of the viscoplastic strain does not coincide with the actual accelerated creep stage of salt rock. So, based on the Abel dashpot, the viscosity coefficient η^β in the viscoplastic body in Fig. 5 is defined as a damage accumulation-related variable.

$$\eta^{\beta'} = (1-d)\cdot\eta^\beta \tag{9}$$

where d is the damage variable.
Combining Eq. (7) and Eq. (9), one obtains:

$$\eta^{\beta'} = (1-d)\cdot\eta^\beta = \eta^\beta e^{-(\frac{t}{n})^m} \tag{10}$$

Combining Eq. (8) and Eq. (10), a constitutive equation of the Weibull distribution-based Abel dashpot is given by:

$$\sigma(t) = (\eta^\beta e^{-(\frac{t}{n})^m})D_t^\beta\left[\varepsilon(t)\right] \quad (0 \le \beta \le 1) \tag{11}$$

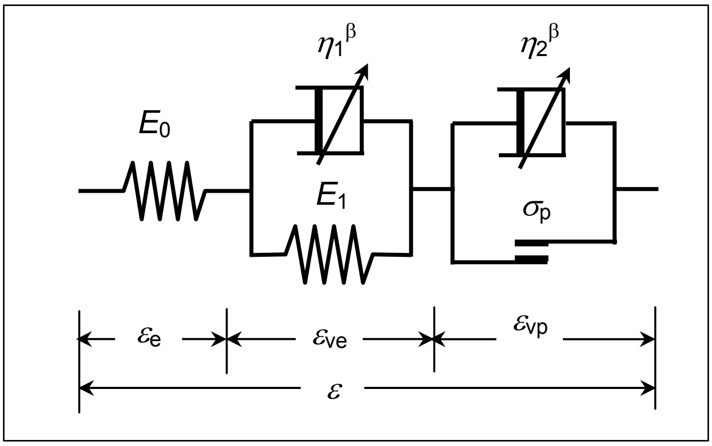

Fig.5 Fractional derivative model of rock salt (Zhou et al., 2013a)

In Fig.5, if the strain of the Hooke body (H), the viscoelastic body (N/H) and viscoplastic body are assumed to be ε_e, ε_{ve} and ε_{vp}, respectively, then the total strain of the constitutive model is:

$$\varepsilon = \varepsilon_e + \varepsilon_{ve} + \varepsilon_{vp} \tag{12}$$

The strain-stress relation of the Hooke body is given by

$$\varepsilon_e = \frac{\sigma}{E_0} \tag{13}$$

where E_0 is the elastic modulus of the spring.

The strain-stress relation of the viscoelastic body (N/H) is given by (Zhou *et al.*, 2011)

$$\varepsilon_{ve} = \frac{\sigma}{\eta_1^\beta} \sum_{k=0}^{\infty} \frac{\left(-\frac{E_1}{\eta_1^\beta}\right)^k t^{\beta(1+k)}}{\beta(1+k)\Gamma[(1+k)\beta]} \tag{14}$$

where E_1 and η_1^β are the elastic modulus of the spring and the constant viscosity coefficient of the Abel dashpot in the mechanical model of the viscoelastic body.

In the mechanical model of a viscoplastic body (N/St.V), the stress σ_p carried by the plastic element is given by

$$\sigma_p = \begin{cases} \sigma, & \sigma < \sigma_s \\ \sigma_s, & \sigma \geq \sigma_s \end{cases} \tag{15}$$

where σ_s is the yield limit

The total stress will be the sum of the stress applied on the dashpot and the plastic element:

$$\sigma = \sigma_d + \sigma_p \tag{16}$$

where σ is the total stress, σ_d is the stress applied on the dashpot with variable viscosity coefficient and σ_p is the stress by the plastic element.

If $\sigma < \sigma_s$, combining Eq. (15) and Eq. (16), one gets $\sigma_d = 0$, then considering Eq. (11):

$$\varepsilon_{vp} = 0 \tag{17}$$

If $\sigma \geq \sigma_s$, combining Eq. (15) with Eq. (16), one gets $\sigma_d = \sigma - \sigma_s$, then considering Eq. (11):

$$\sigma(t) = (\eta_2^\beta e^{-(\frac{t}{n})^m}) D_t^\beta \left[\varepsilon_{vp}(t) \right] + \sigma_s \quad (0 \leq \beta \leq 1) \tag{18}$$

Solving Eq. (18) with the method of fractional order differential equations, one obtains:

$$\varepsilon_{vp} = \frac{\sigma - \sigma_s}{\eta_2^\beta \Gamma(\beta)} \int_0^t (t-\tau)^{\beta-1} e^{(\frac{\tau}{n})^m} \, d\tau \tag{19}$$

So the constitutive relationship of the viscoplastic body (N/St.V) is given by:

$$\varepsilon_{vp} = \begin{cases} 0, & \sigma < \sigma_s \\ \dfrac{\sigma - \sigma_s}{\eta_2^\beta \Gamma(\beta)} \displaystyle\int_0^t (t-\tau)^{\beta-1} e^{(\frac{\tau}{n})^m} \, d\tau, & \sigma \geq \sigma_s \end{cases} \tag{20}$$

By substituting Eqs. (13-14) and Eq. (20) into Eq. (12), the constitutive relationship of the Weibull distribution-based fractional derivative creep model of salt rock is given by (Zhou *et al*, 2013b):

$$\varepsilon(t) = \frac{\sigma}{E_0} + \frac{\sigma}{\eta_1^\beta} \sum_{k=0}^{\infty} \frac{\left(-\frac{E_1}{\eta_1^\beta} \right)^k t^{\beta(1+k)}}{\beta(1+k)\Gamma[(1+k)\beta]} \quad (\sigma < \sigma_s) \tag{21a}$$

$$\varepsilon(t) = \frac{\sigma}{E_0} + \frac{\sigma}{\eta_1^\beta} \sum_{k=0}^{\infty} \frac{\left(-\frac{E_1}{\eta_1^\beta} \right)^k t^{\beta(1+k)}}{\beta(1+k)\Gamma[(1+k)\beta]} + \frac{\sigma - \sigma_s}{\eta_2^\beta \Gamma(\beta)} \int_0^t (t-\tau)^{\beta-1} e^{(\frac{\tau}{n})^m} \, d\tau \quad (\sigma \geq \sigma_s) \tag{21b}$$

We use least-squares fitting method for the parameter determination of the fractional derivative model. The parameters in Eq. (21b) are presented in Table 1. The fitting curves for fractional derivative model given in this paper are shown in Fig.6. The comparison of modeling approach with experimental data indicates that the fractional derivative constitutive model can reflect the three stages of creep of salt rock.

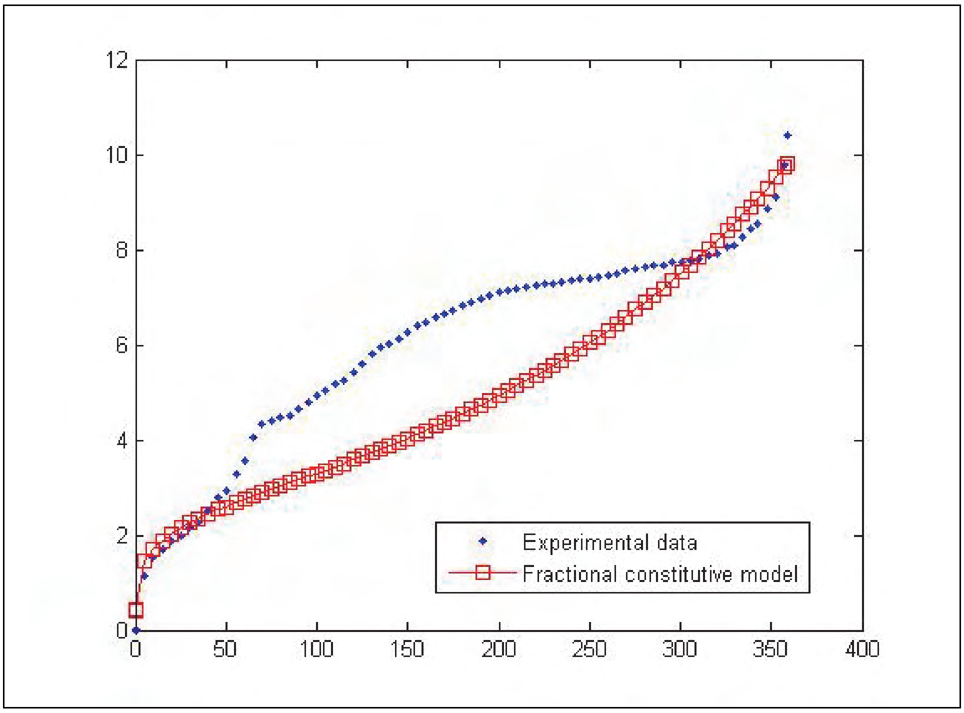

Fig.6 Experimental data and fitting curve by fractional derivative model

Table 1. Parameters determined by fitting analysis based on creep tests of salt rock

	E_0 (GPa)	E_1 (GPa)	η_1^β (GPa·h$^\beta$)	η_2^β (GPa·h$^\beta$)	β	$1/n$	m	LSF errors
Fractional derivative model	3.9	0.8	3.2	6.76	0.48	0.0002	0.58	0.0149

4 Conclusions

In this paper, on the basis of creep-acoustic emission tests of salt rock under the condition of uniaxial compression, AE events are monitored during the whole creep process to get a better understanding of damage evolution in salt rock. In addition, based on the Weibull distribution, a new variable-viscosity Abel dashpot is established by means of definition of a damage variable. By replacing the Newtonian dashpot in the classical Nishihara model by the variable-viscosity Abel dashpot, a new creep constitutive model is suggested based on acoustic emission statistics accompanied by damage evolution and fractional derivative. It is indicated that the fractional derivative constitutive model can better reflect the three stages of creep of salt rock, especially the tertiary one. The main conclusions are drawn as follows:

(1) Based on the AE counts-time curve, it is indicated that the AE counts soar conspicuously first, then descend slowly for a short time, which corresponds to the transient creep region. During the beginning of longer steady stage, the AE signals are active, then nearly disappeared before the third stage of creep.

In the accelerated creep region, the AE counts increase sharply, macroscopic cracks are generated and grow fast.

(2) The accumulated AE counts have the same trend as the strain curve and are ahead of time, it can reflected the trend of the evolution of strain.

(3) Assuming that the number of AE events correspond to the failure number of salt rock internal elements and the probability density function of microelement failure meets the Weibull distribution, a relation between acoustic emission event number and time, as well as a damage function with time is established, which is in agreement with the experimental data.

(4) The new fractional derivative constitutive model of salt rock based on acoustic emission proposed in the paper is capable of giving a well approach to describe all creep phases in salt rock.

Acknowledgements

The present work is supported by the National Natural Science Foundation of China (11172318, 51120145001), and the 111 Project (B14006). The financial supports are gratefully acknowledged.

References

Adolfsson, K., Enelund, M., Olsson, P.: On the fractional order model of viscoelasticity. Mech. Time-Depend. Mat. **9**, 15–34 (2005)

Bagley, R.L., Torvik, P.J.: Fractional calculus - a different approach to the analysis of viscoelastically damped structures. AIAA J. 21, 741–748 (1983)

Bagley, R.L., Torvik, P.J.: Fractional calculus in the transient analysis of viscoelastically damped structures. AIAA J. 23, 918–925 (1985)

Barpi, F., Valente, S.: A fractional order rate approach for modeling concrete structures subjected to creep and fracture. Int. J. Solids Struct. 41, 2607–2621 (2004)

Bazant, Z.P., Xi, Y.: Drying creep of concrete: constitutive model and new experiments separating its mechanism. Mater. Struct. 27, 3–14 (1994)

Carter, N.L., Hansen, F.D.: Creep of rocksalt. Tectonophysics 92, 275–333 (1983)

Carter, N.L., Horseman, S.T., Russell, J.E., Handin, J.: Rheology of salt rock. J. Struct. Geol. 15, 1257–1272 (1993)

Chan, K.S., Bodner, S.R., Fossum, A.F., Munson, D.E.: A damage mechanics treatment of creep failure in rock salt. Int. J. Damage Mech. 6, 121–152 (1997)

Cristescu, N.D.: A general constitutive equation for transient and stationary creep of rock salt. Int. J. Rock Mech. Min. 30, 125–140 (1993)

Herrmann, R.: Fractional Calculus: An Introduction for Physicists. World Scientific, Singapore (2011)

Homand-Etienne, F., Houpert, R.: Thermally induced microcracking in granites: characterization and analysis. Int. J. Rock Mech. Min. 26, 125–134 (1989)

Hou, Z.: Mechanical and hydraulic behaviour of salt in the excavation disturbed zone around underground facilities. Int. J. Rock Mech. Min. 40, 725–738 (2003)

Jin, J., Cristescu, N.D.: An elastic/viscoplastic model for transient creep of rock salt. Int. J. Plasticity 14, 85–107 (1998)

Kilbas, A.A., Srivastava, H.M., Trujillo, J.J.: Theory and Applications of Fractional Differential Equations. Elsevier, Amsterdam (2006)

King, M.S.: Creep in model pillars of Saskatchewan potash. Int. J. Rock Mech. Min. 10, 363–371 (1973)

Koeller, R.C.: Application of fractional calculus to the theory of viscoelasticity. J. Appl. Mech.-T. ASME 51, 299–307 (1984)

Koeller, R.C.: Toward an equation of state for solid materials with memory by use of the half-order derivative. Acta Mech. 191, 125–133 (2007)

Koeller, R.C.: A theory relating creep and relaxation for linear materials with memory. J. Appl. Mech.-T. ASME 77, 1–9 (2010)

Krishnan, B., Jitendra, S.V., Raghu, V.P.: Creep damage characterization using a low amplitude nonlinear ultrasonic technique.Mater. Charact. 62, 275–286 (2011)

Mainardi, F.: Fractional Calculus and Waves in Linear Viscoelasticity. World Scientific, Singapore (2010)

Metzler, R., Nonnenmacher, T.F.: Fractional relaxation processes and fractional rheological models for the description of a class of viscoelastic materials. Int. J. Plasticity 19, 941–959 (2003)

Ortigueira, M.D.: Fractional Calculus for Scientists and Engineers. Springer (2011)

Podlubny, I.: Fractional Differential Equations: An Introduction to Fractional Derivatives, Fractional Differential Equations, to Methods of Their Solution and Some of Their Applications. Academic Press, San Diego (1999)

Rogers, L.: Operators and fractional derivates for viscoelastic constitutive equations. J. Rheol. 27, 351–372 (1983)

Senseny, P.E., Hansen, F.D., Russell, J.E., Carter, N.L., Handin, J.: Mechanical behavior of rock salt: phenomenology and micromechanisms. Int. J. Rock Mech. Min. 29, 363–378 (1992)

Scott Blair, G.W.: The role of psychophysics in rheology. J. Colloid Sci. 2, 21-32 (1947)

Tan, T.K., Kang, W.F.: Locked in stresses, creep and dilatance of rocks constitutive equation. Rock Mech. Rock Eng.13, 5–22 (1980)

Tang, S., Green, M.S., Liu, W.K.: Two-scale mechanism-based theory of nonlinear viscoelasticity. J. Mech. Phys. Solids 60, 199–226 (2012)

Urai, J.L., Spiers, C.J., Hendrik, H.J., Zwart, H.J., Lister, G.S.: Weakening of rock-salt by water during long-term creep. Nature 324, 554–557 (1986)

Welch, S.W.J., Rorrer, R.A.L., Duren, J.R.G.: Application of time-based fractional calculus methods to viscoelastic creep and stress relaxation of materials. Mech. Time-Depend. Mat. 3, 279–303 (1999)

Yang, C.H., Daemen, J.J.K., Yin, J.H.: Experimental investigation of creep behavior of salt rock. Int. J. Rock Mech. Min. 36, 233–242 (1999)

Zhou, H.W., Wang C.P., Duan Z.Q., Han B.B.: Time-dependent constitutive model of rock salt based on Caputo fractional derivative, in: Hou, Z.M., Xie, H., Yoon, J.S. (eds.) Underground Storage of CO2 and Energy. CRC Press, Leiden, pp. 161–165 (2010)

Zhou, H.W., Wang, C.P., Han, B.B., Duan, Z.Q.: A creep constitutive model for salt rock based on fractional derivatives. Int. J. Rock Mech. Min. 48, 116–121 (2011)

Zhou, H.W., Wang, C.P., Duan, Z.Q., Zhang, M., Liu, J.F.: Time-based fractional derivative approach to creep constitutive model of salt rock. Sci. Sin.-Phys. Mech. Astron. 42, 310–318 (in Chinese) (2012)

H. W. Zhou, C. P. Wang, L. Mishnaevsky Jr., Z. Q. Duan, J. Y. Ding. A fractional derivative approach to full creep regions in salt rock. Mechanics of Time-Dependent Materials, 17, 413-425 (2013a)

H.W. Zhou, J.Y. Ding, J.D. Liu et al. A Weibull distribution-based constitutive model of creep of salt rock. In: Kwasniewski & Lydzba eds. Rock Mechanics for Resources, Energy and Environment, London: Taylor & Francis Group, 497-503 (2013b)

Risk-assessment of the consolidation of a baroque tombstone of Cottaer sandstone

Risikobewertung der Festigung eines barocken Grabmals aus Cottaer Sandstein

J. Wichert, T. Frühwirt, H. Konietzky
TU Bergakademie Freiberg, Institut für Geotechnik

Abstract

A baroque tombstone made of Cottaer Sandstone was consolidated under real-life conditions by means of the in-situ Vacuum Conservation Method (VCM) in cooperation with the company Studio Erich Pummer PLC (Austria). The effect of consolidation to the tombstone was examined by accompanied scientific investigations.

Common superficial impregnations for the consolidation of damaged surfaces often do not migrate deep enough into the object. In contrast, consolidation by full impregnations require the demounting, stabilisation and transport of the object, leading to high costs and an endangerment of the object. In the case of a successfull application of the VCM it is expected to have a new exemplary solution for small sized objects of Cottaer sandstone.

We apply numerical simulation by means of UDEC to evaluate the behaviour of the material, especially a possible development of cracks due to the consolidation. We describe the different investigations and steps of conservations as well as the different approaches of the generation of geometric models. The simulation itself is not finished yet so we will introduce it later.

Zusammenfassung

In Kooperation mit der Firma Atelier Pummer GmbH (Österreich) wurde das in-situ Vakuum Kreislauf Verfahren (VKV) zur Festigung/Volltränkung eines barocken Grabmal aus Cottaer Sandstein unter Praxisbedingungen angewandt und seine Wirkung detailliert naturwissenschaftlich dokumentiert.

Herkömmliche Oberflächentränkungen zur Festigung der zerstörten Oberflächen erreichen oft nicht die notwendigen Eindringtiefen des Wirkstoffs. Volltränkungsverfahren erforderten dagegen bisher einen aufwendigen Abbau, die Stabilisierung und den Transport der Objekte, die neben höheren Kosten auch mit Risiken für die Substanz verbunden sein können. Von der in-situ-Applikation des VK-Verfahrens wird im Erfolgsfall eine „Musterlösung“ für Objekte aus Cottaer Sandstein erwartet.

Mit der numerischen Simulation mittels UDEC möchten wir das Materialverhalten, insbesondere mögliche Rissbildung nach der Tränkung bewerten. Wir beschreiben die Untersuchungen und restauratorischen Schritte sowie verschiedene Ansätze zur Generierung der Modelle. Die eigentlichen Simulationen sind noch nicht beendet, so dass sie hier keinen Eingang finden.

1 Introduction

Damages of monuments of Cottaer sandstone are often caused by specific fabric elements: The clay minerals (kaolinite, illite) lead to inhomogenity of the fabric due to their low porosity and they are those parts where salt weathering starts (Siedel 2007, 2010). In addition, the clay minerals are problematic zones for the consolidation of weathered stone surfaces because they can reduce the migration depths of the consolidants. Former tests have shown that the migration depths of the consolidants can be significantly increased by applying a negative pressure (Ibach & Sobott 2007). Thus, the same phenomenon can be expected for the Cottaer sandstone.

Besides the migration depths, a particular crucial point is whether the consolidant migrates into the finer parts of the mica flakes because they are especially susceptible to weathering (Siedel 2007).

This is not only a question of the pore sizes but also of the surface properties of the single minerals. In frequently moisture-penetrated parts the Elbe sandstones show a thin black patina after decades, resulting in a reduction of the water uptake under atmospheric pressure. Concerning the Cottaer sandstone also the water vapour diffusion will be reduced (Siedel 2007). The behavior of such surfaces is difficult to estimate and will be tested.

Fig. 1.1: Occurrence of cracks after consolidation with unknown cause.

Especially in the case of severely damaged objects in complicated constructional situations like sculptures mounted on buttresses an in-situ treatment is desireable because removal and transportation prior to treatment and consolidation may be impossible or threaten the structural integrity. The VCM applied on several objects has shown to be very promising for desalination and consolidation of stone objects. Thus, the application of this technique is carried out on an object which is severely weathered to determine the migration depth and distribution of the consolidant.

After a consolidation of stone objects sometimes cracks or scaling occur, although the properties of the object were analyzed before the treatment (Fig. 1.1). The phenomenon of crack development concerns former as well as actual consolidation techniques.

Cause and mechanisms can not be explained in detail. Although influencing variables like hygric and/or thermal stresses are basically known, a quantification is not yet possible. This leads to uncertainties in the interpretation of the cause of the different damage types. In addition, no reliable predictions of possible crack developments or scalings due to a consolidation can be given.

In the field of the consolidation of stone monuments numerical simulation techniques are poorly developed. One aim is therefore to introduce the simulation for risk-assessment as a new method within the science of conservation.

For the investigation we chose a baroque tombstone. It is located in the ‘Innerer Neustädter Friedhof’ in the city of Dresden and due to its bad condition it was given up by the heritage authority (Landesamt für Denkmalpflege Dresden) so that we could carry out detailed investigations.

Fig. 1.2: Damage pattern of the baroque tombstone. **A:** Original place of the tombstone; **B:** Translocation of object before treatment; **C:** Relief, complete loss of original surface; **D:** Cracks; **E:** Missing part; **F:** Flaking

The tombstone was erected in memoriam of Johann Christoph Richter (1701-1763) and his second wife Ursula Juliane (1705-1774). This very nice exemplar of a barocque sepulchral culture is 2.5 m high and comprises two putti, three cartouches for inscriptions and two heads of angels in a gloriole. It consists of Cottaer sandstone which is a variety of the Elbe sandstone (Fig. 1.2: A, B).

The original surface is largely lost and shows the typical black patina. Especially at the base this loss is mainly caused by flaking (in accordance to the ICOMOS Glossary). Thin scaling leads to a partly loss of the inscriptions in the cartouches while in other areas missing parts and spalling is observed.

The intensive biological colonisation by moose and the patina does not lead to damages. Within niches black crusts and in one case efflorescence occur.

The investigations carried out are listed in table 4.1 (b./a.t.= before / after treatment)

Tab. 1.1: Overview on investigations

Parameter	Method
hydrophobic properties b./a.t.	Karsten-measurements on surfaces with different conditions (patina, crust, relief)
dyn. Young's modulus and Poisson ratio b./a.t.	measurement of ultrasonic wave speed
water-vapor permeability (μ-Wert) und hydric dilatation b./a.t.	on discs prepared for ring bending strength determination
viscosity of the consolidants: KSE 300E + 10% accelerator & KSE 500E + 10% accelerator	rotational rheometry
thermal dilatation unconsolidated and consolidated (KSE 300E + 10% accelerator & KSE 500E + 10% accelerator)	dilatometry with DIL 402 C by NETZSCH
uniaxial compressive strength, deformation modulus, Young's modulus, Poisson ratio b./a.t.	on cylindric samples (13 x 5 cm) in accordance to the recommendation no. 1 of DGGT e.V.
indirect tensile strength (Brazilian test), bulk density and water content fo Cottaer sandstone before treatment	on cylindric samples (2.5 x 5 cm) in accordance to the recommendation no. 10 of DGGT e.V.
ring bending strength b./a.t.	testing machine, own construction of the Geotechnical Institute
drilling resistance b./a.t.	Tersis
porosity	polarisation microscopy, image analysis, mercury porosimetry
grain size distribution and grain shapes	polarisation microscopy, image analysis

2 Short introduction of the Vacuum Conservation Method (VCM)

The in-situ VCM allows the desalting and consolidation especially of degraded architectural elements in complicated architectural situations in which dismounting is impossible or their removal and transportation prior to treatment and consolidation may threaten their structural integrity (comp. Fig. 2.1). The objects are shrink-wrapped within an airtight solvent-resistant film. Afterwards, the remaining air trapped inside the film and within the pore space is then drawn out with the vacuum-circling preserver so that a negative pressure is created in the object itself.
If a negative pressure of 300–900 mbar is achieved the appropriate consolidant is injected by means of a precise dosing system, distributed evenly and deeply into the stone thanks to the low pressure. The open pores and damaged areas are firstly filled, followed by a slow filling of the parts which are less damaged.

Fig. 2.1: **First and second photograph:** In-situ consolidation of 3-metre tall Attic sculptures of the National Library in Vienna which could not be dismounted. Two apparatuses (on the truck and at the sculpture) were coupled together to span the height of 30 m. **Third photograph:** Desalination of a brick wall over the full cross section. The wall was sealed on the front side to enable negative pressure on it. On the backside regular water was pressed into drilled injection valves. The desalination took six days of continuous flushing and about 2500 litres of water.

3 Desalting and consolidation of the object

The analysis about the salt content showed a high amount especially of gypsum so that we decided to carry out a desalting by the VCM before the consolidation. For the desalting regular water was flushed 'through' the tombstone. This procedure is based on the assumption that the water really flushes through the whole object, washing out the salts. This needs a repeated re-plugging of the tube for water in- and outlet, leading to this high effort and high water consumption. In our case it took four days, about 200 times re-plugging and 7,500 l water (see Fig. 3.2).

By measuring the electrical conductivity of the flushed water we determined the progress of desalting during the treatment. The diagramm in Fig. 3.1 shows a typical serrated history of the curve with a peak in the morning at the beginning of the daily desalting towards a decreasing conductivity each day and in total.

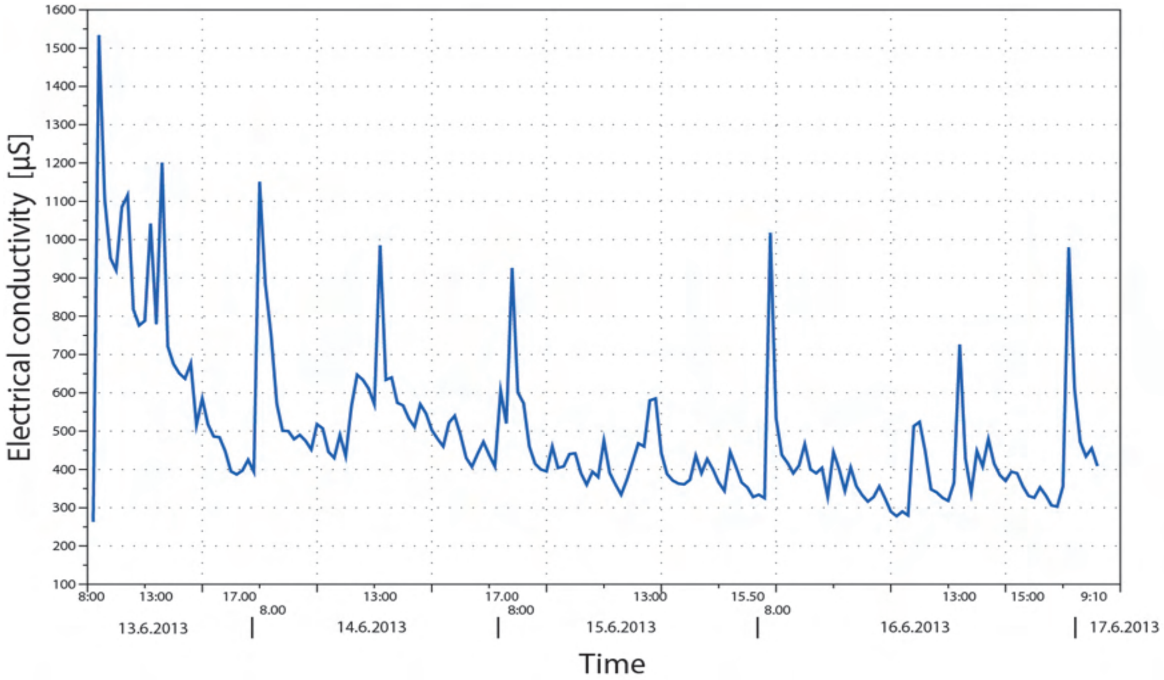

Fig. 3.1: Electrical conductivity of the water used during desalting of the tombstone

The company Pummer carried out the desalting by flushing water in June 2013. With the subsequent application of compresses the salts which remained close and/or on the surface can migrate into the compresses, making possible an almost complete desalting.

We expected that the tombstone would dry up within some months without active drying. Yet in October we examined remaining moisture so that the tombstone was dried actively for three days. After a sufficient drying the object was consolidated with the consolidant KSE 300E + 10 % catalyst from the company Remmers over a period of 6 hours.

At the same time we investigated the consolidation of “dummy”-samples, using two different consolidants to compare the penetration depth and degree of strengthening: KSE 300E + 10 % catalyst and KSE 500E + 10 % catalyst.

KSE is the shortcut for ‘Kieselsäurester’ which is the German term for ethyl silicates. The numbers describe the gel deposit rate and the size of the molecules and E means “elasticized”. For KSE 300E the gel deposit rate is approx. 30 % and für KSE 500E it is approx. 50 %. The size of the molecules of the KSE 300E is smaller than those of the KSE 500E. The consolidant KSE 300E is usually applied for the consolidation of the Cottaer Sandstone because it migrates deeper into the object and leads to a balanced strength profile between the consolidated and untreated parts. It was also used to consolidate the tombstone. The VCM needs 10 % additional catalyst to obtain a higher penetration speed into the object.

Fig. 3.2: Treatment of the tombstone with VCM from upper left to lower right: Covering with fleece for protection, desalting by flushing water through the tombstone; covering with a compress for final desalting; drying; consolidation.

4 Investigations of the material properties before and after the consolidation

The term Elbe-Sandstone comprises the varities Cottaer Sandstone and Postaer Sandstone. Elbe-Sandstone has been used for buildings and sculpturing not only in Saxony for almost 1000 years. Postaer Sandstone is harder than the Cottaer type and is therefore used for architectonical elements like stairs or cornices. The softer Cottaer Sandstone is easily processable and very popular among sculptors.

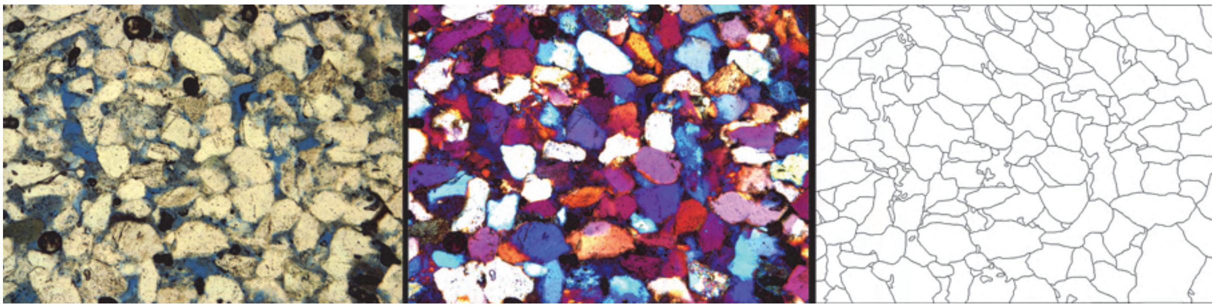

Fig. 4.1: Microimages of Cottaer Sandstone. On the left photograph the darker parts correspond with the porosity. The photograph in the middle shows the different quartz grain (crossed nichols). The right drawing shows the grain boundaries obtained by image processing (width of view = 1.3 mm).

Both are siliceous sandstones with over 90 % quartz as a main component (Fig. 4.1). Supplementary minerals are feldspar and glauconite. The pore space of the Cottaer sandstone is partly filled, consisting mainly of fine grained minerals like quartz, illite and kaolonite. These parts are vulnerable to weathering and damages due to salts like gypsum.

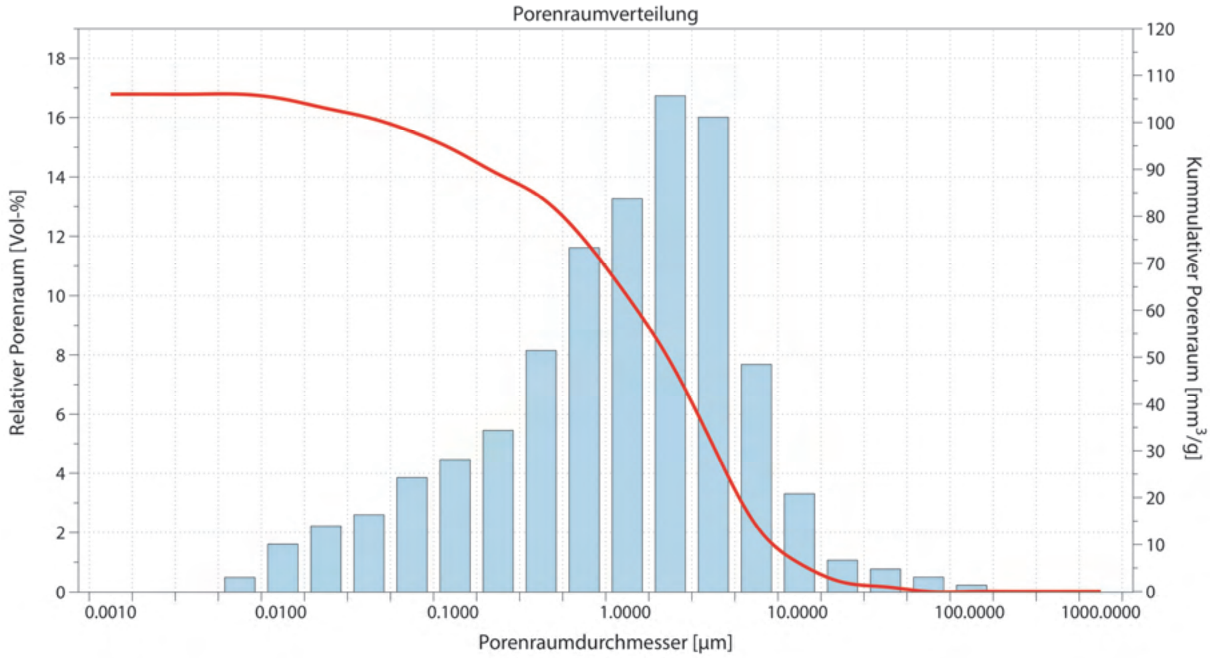

Fig. 4.2: Porosity vs. pore diameter for Cottaer Sandstone.

We performed rock mechanical testing on (weathered) samples from the monument as well as on reference samples of fresh (unweathered) Cottaer Sandstone. Four blocks where obtained from an active quarry near Pirna and identified as having representative properties for Cottaer Sandstone. The blocks were of cubic shape with an edge length of 200 mm. Each of the blocks was treated by a classical consolidation (brushes) with KSE 300E, by VCM with KSE 300E + 10% catalyst and by VCM with KSE 500E + 10% catalyst. One block was left untreated. Comparing the parameters obtained on each single block we were able to document the alteration of the rock properties in accordance to the specific consolidations.

As a reference we selected 25 samples of freshly broken Cottaer Sandstone from various locations to determine standard rock mechanical parameters and to get an estimation of the natural variability of the rock mass. From these samples we prepared cylindrical specimens according to the regulations of ISRM and DGGT. Testing was done according to the recommendation no. 1 of DGGT (Option 6: Uniaxial compressive test with measurement of axial and lateral deformation, including cycling loading in the pre-failure range) and recommendation no. 10 of DGGT (Determination of indirect tensile strength by the Brazilian test). In addition, we determined the compressive wave speed, Young's modulus and Poisson's ratio, using ultrasonic pulsing equipment to measure pulse-runtime and resonance frequency.

Deformation properties were determined as secant moduli in stress intervals of 40 to 60% of maximum load level in the unloading-branches of the loading-cycles and the ultimate load, respectively.

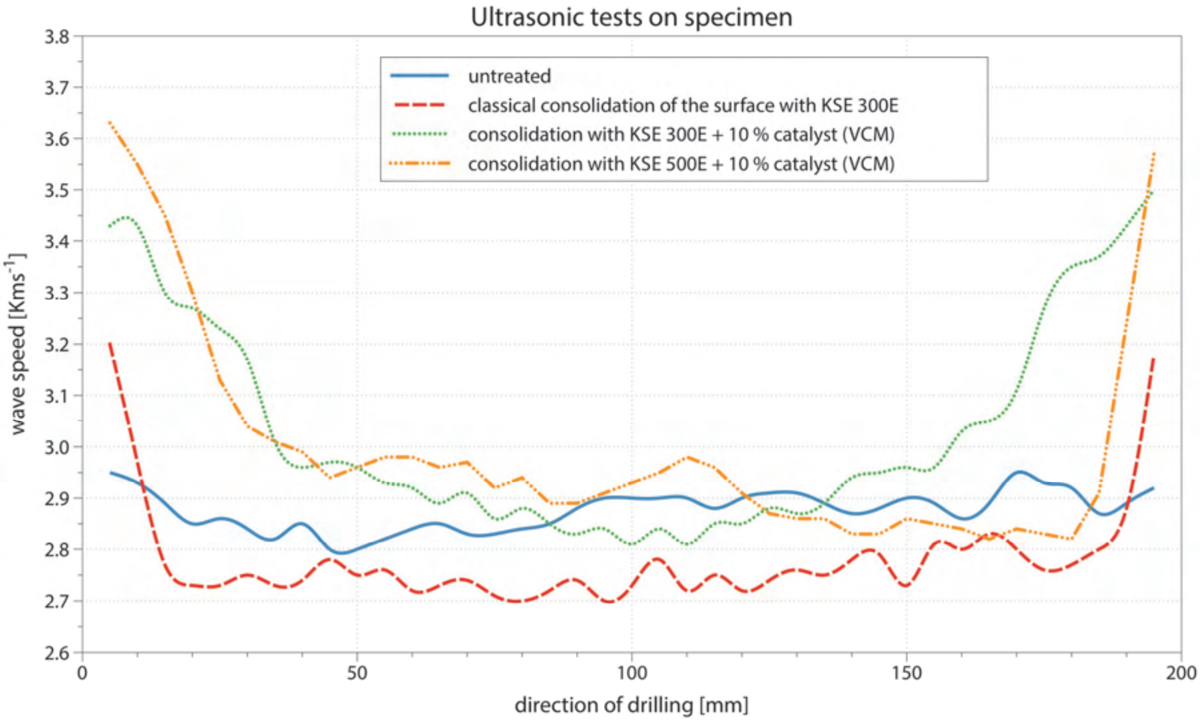

Fig. 4.3: Ultrasonic tests on untreated and consolidated samples (edge length of blocks 20 x 20 x 20 cm), showing the difference of the migration depth of the different consolidants.

Tab. 4.1: Properties of untreated Cottaer Sandstone (uniaxial compressive test)

Direction of loading to bedding		Bulk density	Uniaxial compressive Strength	Deformation Modulus	Elastic Modulus (static)	Poisson’s ratio (static)
		[g/cm³]	[N/mm²]	[kN/mm²]	[kN/mm²]	[-]
parallel	average value	2.10	35.00	12.19	12.43	0.11
	coefficient of variation	0.01	0.04	0.02	0.02	0.10
normal	average value	2.10	31.29	10.45	10.50	0.09
	coefficient of variation	0.01	0.06	0.03	0.03	0.06

After the treatment of the cubic rock samples we drilled cylindrical samples out of each block. Because we wanted to investigate the dependence of alteration of properties as a function of distance from the free (treated) surface, care was taken to drill at sufficient distance from the edges of the blocks and to drill right through the core of the blocks. Compressional wave speed as a measure of elastic properties of the rock was determined using an ultrasonic measurement device with a pulse-runtime method. By comparison of the depth-profile of the untreated cylindrical specimen with the consolidated specimens it is clear to see that the depth of penetration is going along with an increase of dynamic properties.

The results shown in Fig. 4.3 were gained from specimens with a length of 200 mm, which means that they go right through the cubic rock blocks in their total thickness and show the effect of the free surface at both ends. The compressive wave speed of the untreated sample is – besides some slight variations – constant over the whole depth and similar to freshly broken samples parallel to the bedding (see table 4.2 for comparison).

The classical consolidation treatment using a brush at the free surface shows migration depth of about 20 mm and a relatively low strengthening effect even in near-surface regions. VCM using KSE 500E leads to the expected higher strengthening than the KSE 300E; and conversely, a lower migration depth. Using KSE 500E, deformation properties of rock are enhanced up to a depth of 20 to 40 mm from the free surface. With KSE 300E the thickness of the strengthened zone is at least 40 to 60 mm. In all of the tested samples the compressional wave speed in the middle section was proven to be more or less unchanged compared to the untreated reference samples. The penetration depth varied up to 20 mm when penetration of the consolidant was parallel and perpendicular to the bedding planes, respectively (data not shown here).

This leads to the conclusion, that even using the VCM only rock volume relatively close to surface is strengthened by the consolidation treatment, forming a shell around a relatively unaltered core. However, the degree of strengthening regarding the depth of penetration (strengthened rock volume) and the extent of the change of deformation properties is largely enhanced compared to the classical consolidation technique.

Tab. 4.2: Properties of untreated Cottaer Sandstone (ultrasonic pulse test, Brazilian disc test)

Direction of loading to bedding		**Propagation speed of compressional wave**	**Elastic Modulus (dynamic)**	**Poisson's ratio (dynamic)**	**Tensile strength**
		[m/s]	[kN/mm²]	[-]	[N/mm²]
parallel	average value	2864	16.68	0.12	
	coefficient of variation	0.01	0.02	0.14	
normal	average value	2642	13.85	0.13	
	coefficient of variation	0.01	0.01	0.40	
parallel (SPZ 3)	average value				2.58
	coefficient of variation				0.14
normal (SPZ 2)	average value				2.73
	coefficient of variation				0.08

After completing the ultrasonic tests, two cylindrical specimens of every cubic rock block were tested in uniaxial compression to determine the strength and deformability properties. One specimen with axis parallel and one with axis perpendicular to the bedding plane. Because the dimension of the cylindrical specimen (diameter: 50 mm, length: 115 to 125 mm) was larger than the maximum migration depth of the consolidant (max. 60 mm), the strength and deformability can be assumed to be very inhomogeneous over the total volume of the specimen. The cylindrical specimen have an “end-cap” of relatively competent (consolidated) rock material with unaltered (not strengthened) properties in the middle section.

In uniaxial compression tests fractures typically accumulate in the middle section of the cylindrical specimen, where a relatively homogenous uniaxial state of stress exists with only little influence of the clamping pressure caused by elastic mismatch of the rock material and the steel loading platens. Axial and lateral deformation are measured in the central section of the specimen. Even in the case of specimen prepared from the treated cubic samples, the middle section of the specimen is relatively unaltered. Neither uniaxial strength nor deformation values show a significant strengthening effect due to consolidation treatment (Fig. 4.4 and Fig. 4.5).

The analysis of the fracture patterns of all tested specimen has shown evidence for intense fracturing in the middle section of the specimen. However, in the case of treated samples we observed only local cracks (mainly tensile-type) which did not propagate through the strengthened end-caps whereas in the untreated material classical shear fractures developed (Fig. 4.6).

In order to be able to provide specimens with a homogeneous penetration (in shape and size) of the consolidant and to investigate the depth-dependent strengthening effect by documentation of depth profiles we adapted a novel testing technique. This laboratory technique relies on the testing of disc shaped rock specimens in a biaxial flexural stress state. This method of measuring rock strength is well established in the field of stone conservation but is rather unknown in classical rock mechanical testing so far. The method provides the biaxial flexural strength and the Young's modulus of the specimen.

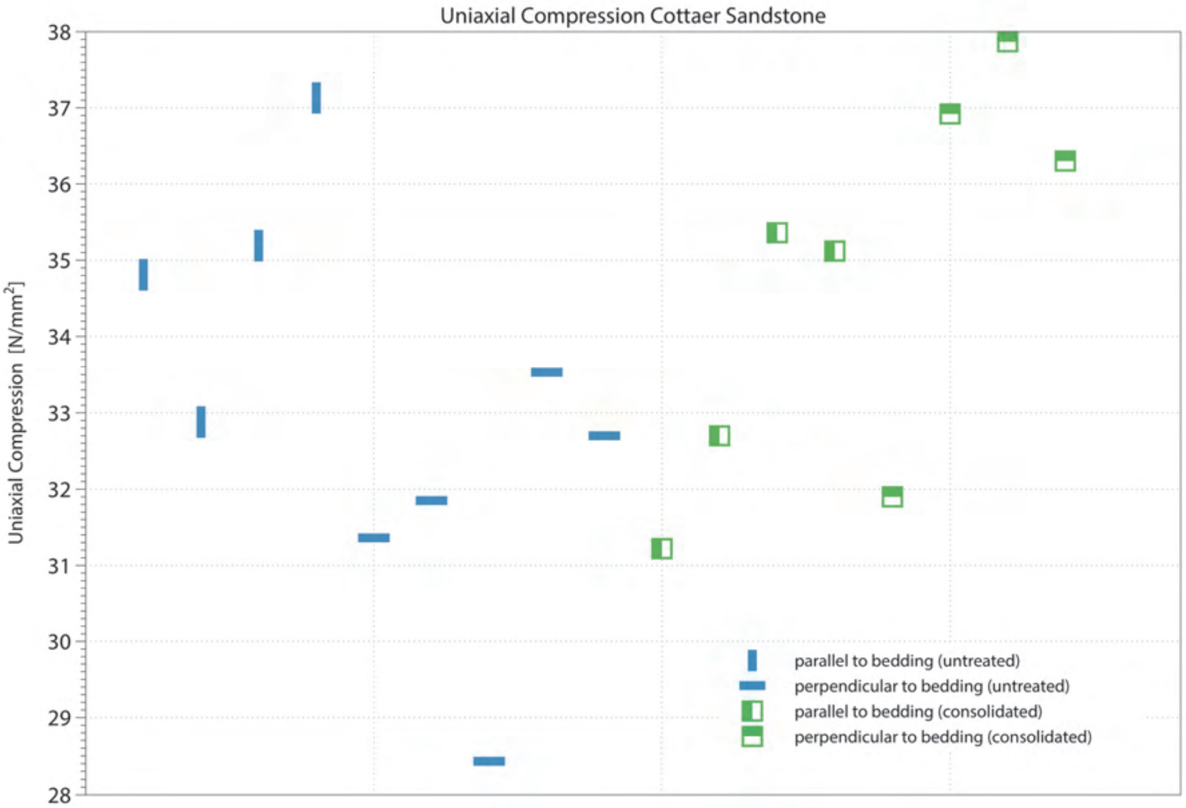

Fig. 4.4: Comparison of uniaxial compressive strength data of Cottaer Sandstone with/without treatment (treatment: VCM KSE300 E + 10 % catalyst).

Fig. 4.5: Comparison of deformation modulus and Young's modulus of Cottaer Sandstone with/without treatment (treatment: VCM KSE300 E + 10 % catalyst).

The biaxial flexural strength is defined as the attained maximal flexural strength generated by the annular-shaped load transmission onto the disc-shaped rock plate. The circular plate of rock is hereby laid upon a larger ring (bearing ring) while pressure is applied centrically by a second smaller ring (loading ring). The elastic modulus is calculated from measurement of the deflection of the central point of the specimen by an inductive displacement transducer. The key advantages of this method are primarily the relative small number of samples necessary to run the test, the opportunity to analyze complete profiles with regard to their strengths and the simultaneously conductible determination of the elastic modulus (Kozub, 2008). The tested specimens were disc-shaped with diameter of 50 mm and thickness of 5 mm. They were attained by slicing the cylindrical specimen drilled from the cubic rock samples on which the ultrasonic wave speed had been determined. The typical fracture pattern shows cracks radiating from the central point of the plate (Fig. 4.7).

Profiles of flexural strength (Fig. 4.8) as well as elastic modulus (Fig. 4.9) reveal that the VCM greatly enhances the migration depth of the consolidant as compared to the traditional treatment. With the traditional surface-treatment a strengthening effect can be recorded in rock mass up to a distance of about 10 mm from the treated surface. Using KSE 500E with VCM the effective depth can be increased up to 30 to 40 mm. With the consolidant KSE 300E a strengthening effect can be documented up to a distance of about 60 mm from the free surface. However, the strengthening effect in the near-surface region is less pronounced as compared to KSE 500E consolidant. This effect fits very well to the observation we made with our non-destructive testing technique by determining the p-wave velocity distribution in the specimen.

Fig. 4.6: Comparison of fracture pattern of untreated (left picture) and treated (VCM with KSE 300E, right picture) specimen after uniaxial compression test

From the graphs in Fig. 4.8 and Fig. 4.9 it is clear, that the consolidation can only be documented in a shell-like volume close to surface of the sample blocks. The central region of the rock core was not strengthened. As we inferred from the test data from the ultrasonic tests there is no evidence that any of the applied consolidation techniques alters the mechanical properties of the whole volume of rock sample. In none of the tested specimens we could find an alteration effect on strength or deformability parameters at distances greater than 60 mm from the free surface.

Fig. 4.7: Typical fracture pattern of specimen after biaxial flexural test

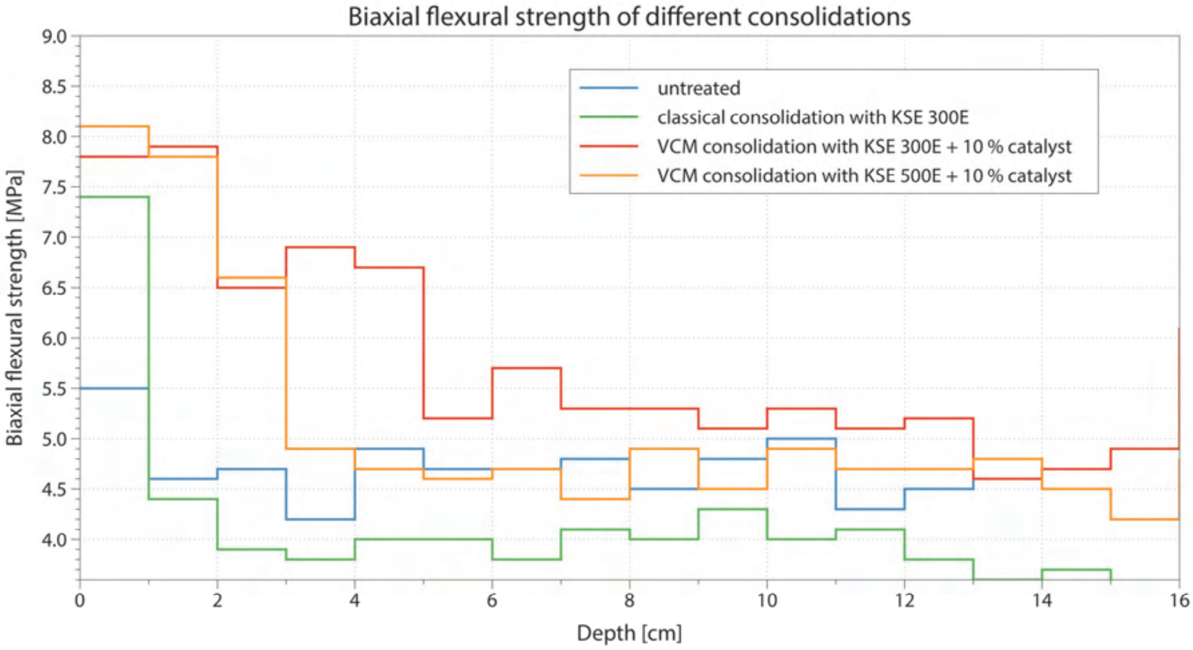

Fig. 4.8: Biaxial flexural strength vs. depth below surface

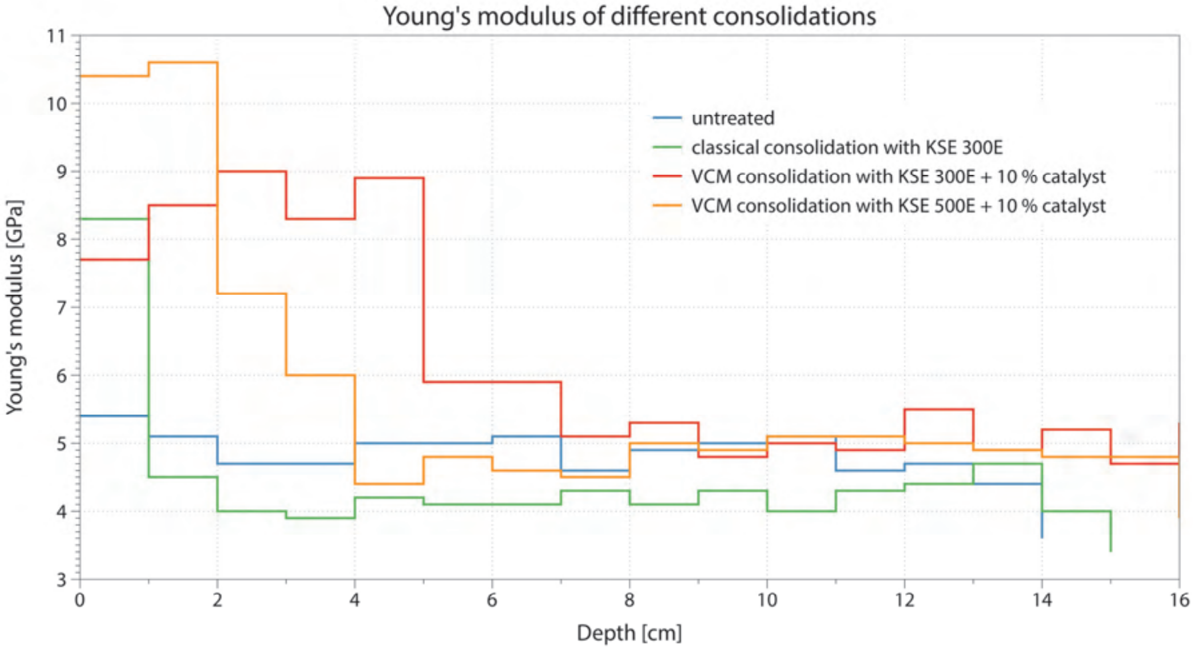

Fig. 4.9: Young’s modulus vs. depth below surface

5 Numerical Simulation

Microscopic image analysis

We applied image analysis on thin sections to quantify the quartz components and to analyze the shape factors as well as to measure the porosity of the Cottaer sandstone.

The scaled RGB-micro images were gained from a live image by the software Axiovision with the polarization mikroskop Axioskop 40 - both Carl Zeiss. This was followed by an image processing to enhance the images. The image analysis itself was carried out with the Java written freeware „ImageJ“. It runs on all common operating systems (Mac OSX, Linux, Windows) and provides numerous options for image processing and – analysis.

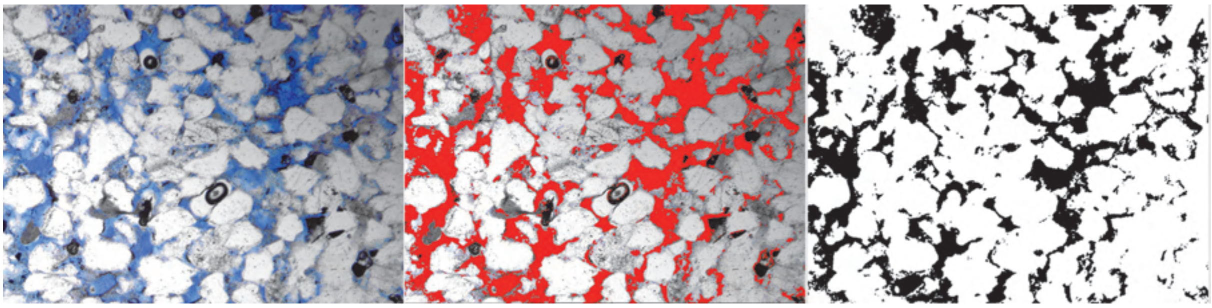

Fig. 5.1: Determination of the porosity by image analysis on thin sections. The left picture shows the thin section with blue colored resign to optically enhance the porosity. The picture in the middle shows the masking within ImageJ. The right one shows the binary image which is ready for the measurement (width of view = 1.3 mm).

During the image processing it turned out that final tracing by hand leads to more exact images in respect to the grain boundaries, although it is very time-consuming. For the measurement of the porosity no tracing was needed. We turned the gray images into binary images by means of thresholds, where the black pixels correspond to the objects of interest. A binary image is the prerequisite for the image analysis. „ImageJ“ offers core functions for the measurement of objects. These functions can be extended by macros, for example, for the measurement of additional shape factors. The following shape factors were measured:

- area, perimeter
- shape factor = 4 Pi • area/perimeter^2
- axial ratio = minor axis/major axis
- solidity = area/convex area

With the macro „ConvexitySolidarity.txt“, the following parameter were analyzed:

- CH Perim = perimeter of the convex hull
- CH Area = area of the convex hull

This macro comes with the freeware „Fiji“, which is a modification of „ImageJ“. It cannot be used for any class struggle.

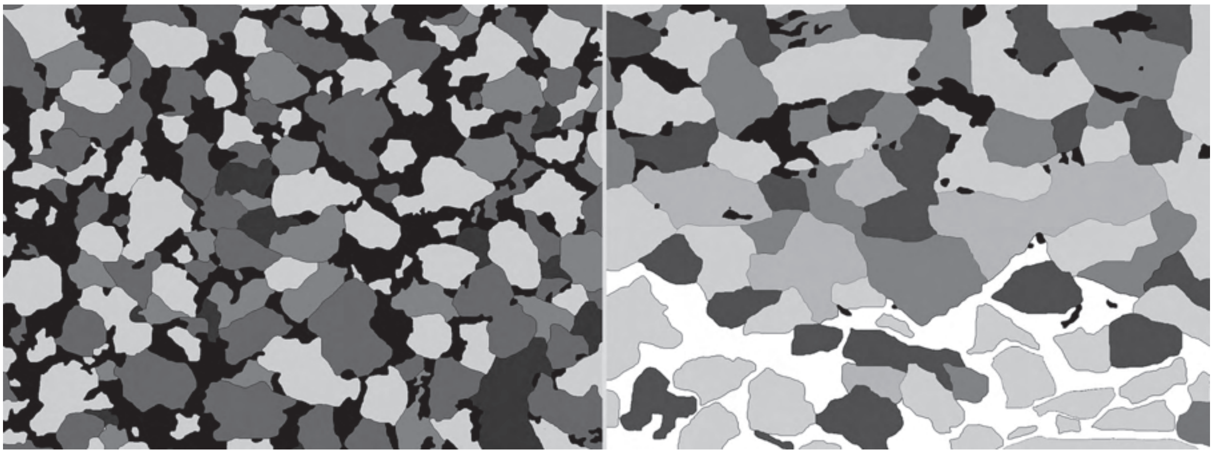

Fig. 5.2: From thin sections generated micro images for image analysis and the generation of geometric models for UDEC (black = porosity, grey = quartz grains, white = mica flake, width of view = 1.3 mm).

The grain parameters (compare left graphic in Fig. 5.3) are the starting point for further analysis. The axial ratio determines the degree of roundness, where 1.0 is a perfect circle and the more it moves towards 0.0 the more it becomes elliptical. The axial ratio is not sufficient for a grain shape analysis, i.e. only for elliptical objects one can measure differences and classify.
In most cases the shape is irregular so that additional grain shape parameters are necessary. There are a plenty of approaches. We used the calculation method of Heilbronner & Barett (2013). They developed routines (freeware „IMAGE SXM“) which only runs under Mac OSX but can be transferred to „ImageJ“. Additional parameter used are deltA, deltP and radius Δ:

We measured CH Perim and CH Area to compare the particular relations of the perimeter (CH Perim) and area (= CH Area) of the convex hull with the perimeter (P) and area (A) of the real grain:

$\Delta P = P - \text{CH Perim}$ with $\text{CH Perim} \leq P$

$\Delta A = \text{CH Area} - A$ with $\text{CH Area} \geq A$

With these parameters we got the ’excess’ length and defect area to calculate the aforementioned shape parameter:

$\text{deltP} = \Delta P/P \cdot 100\ \%$

$\text{deltA} = \Delta A/A \cdot 100\ \%$

The shape parameter deltP und deltA are independent of each other. By combining both we got the degree of bulge:

radius $\Delta = (\text{deltA}^2 + \text{deltP}^2)^{\frac{1}{2}}$

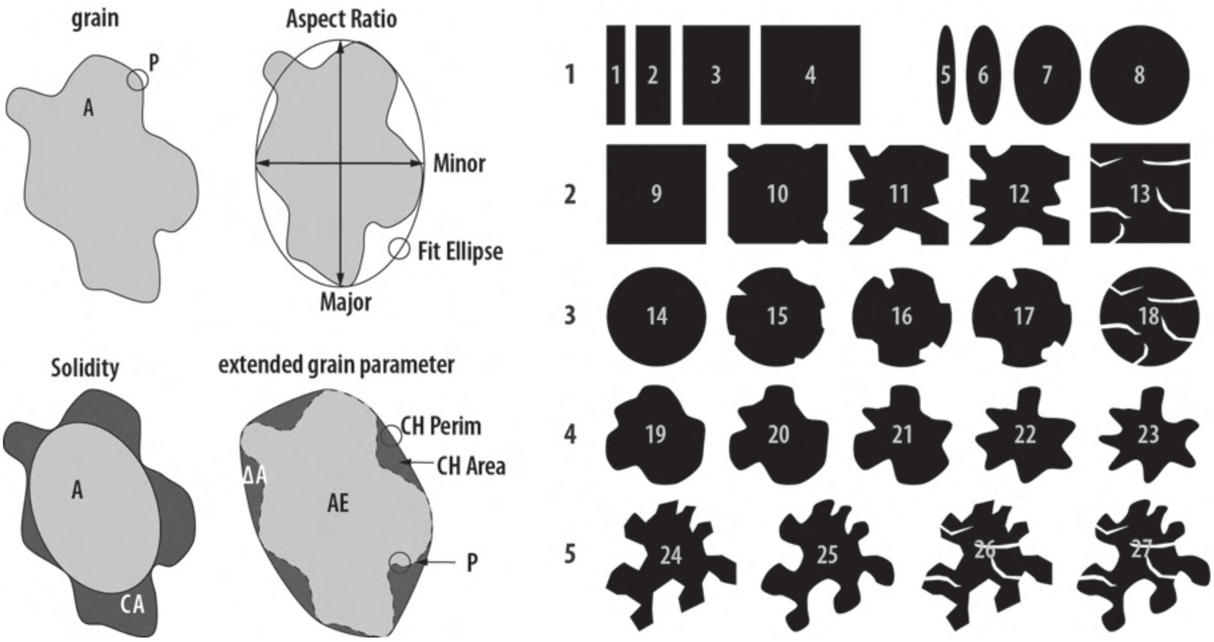

Fig. 5.3: Grain parameters (left) and exemplary shapes to illustrate the importance of an appropriate image analysis (after Heilbronner & Barett, 2013)

The relevance of the shape descriptors is illustrated in Fig. 5.3 and in the diagram of Fig. 5.4. In Fig. 5.3 the first row shows regular and only convex grains so that the analysis of the axial ratio could be sufficient for a classification. In the second and third row the shapes become more and more irregular, whereas between no. 11 and 12 as well as 16 and 17 only the edge roundings are different. Grain 13 and 18 show additional cracks. The fourth and fifth row show very irregular shapes.
If one reads the values of the axial ratio, no differences would be found because the value of the square (4,9) and the circle (8,14) are almost equal to the values of most of the other grains. Comparing deltP and deltA the values from grain 1 to 9 are zero because they all have a convex shape and therefore the convex hull is equal to the grain.

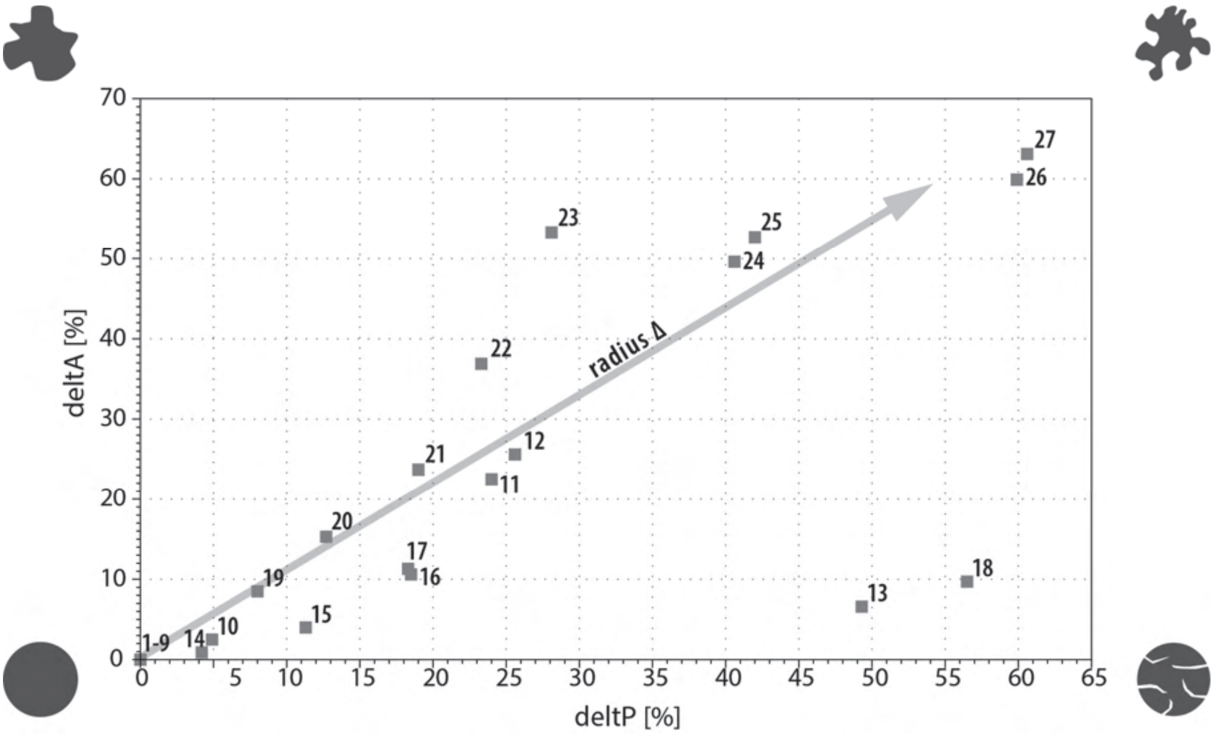

Fig. 5.4: Exemplary shapes using the shape factors delP versus deltA (after Heilbronner & Barrett, 2013).

The shape descriptors become important for irregularly shaped grains. The diagram in Fig. 5.4 makes clear that deltP depicts objects with cracks while deltA is an expression of the bulge: for grain 13 and 18 the values are high for deltP and low for deltA. In contrast for grain 23 the value is moderate for deltP and high for deltA. The grains 24 to 27 are very irregular. Additional cracks are detected for grains 26 and 27. While the values for deltA between grains 24/25 and 26/27 differ only little, the differences in deltP are obvious. It is therefore possible the make statements of the shape for a large number of grains and to classify them.

We have classified the grains in accordance to deltP vs. deltA and subsequently grouped in accordance to the axial ratio. Within these groups the grains were sorted in accordance to their size, using the equivalent diameter:

$$d_{equ} = 2 \cdot \sqrt{\frac{A}{\pi}}$$

Generation of the geometrical models using grey image values

The microimages comprise only a small range of grey values, making the subsequent steps easier. In 'ImageJ' the grey value and corresponding x,y-coordinate of each pixel is read-out and saved in a text file.

The model generated in UDEC corresponds to the size of the microimage (1.3 x 0.97 mm) and is filled with Voronoi-blocks. The text file will be read-in by UDEC to assign the grey values to the Voronoi-blocks (see Fig. 5.5).

The colored polygons depict the merged Voronoi-blocks, corresponding either to a grain or to porosity. Due to the very fine Voronoi-block structure the generated geometric model is more or less identical with the real fabric. Finally the constitutive laws and corresponding parameters are assigned to the different minerals.

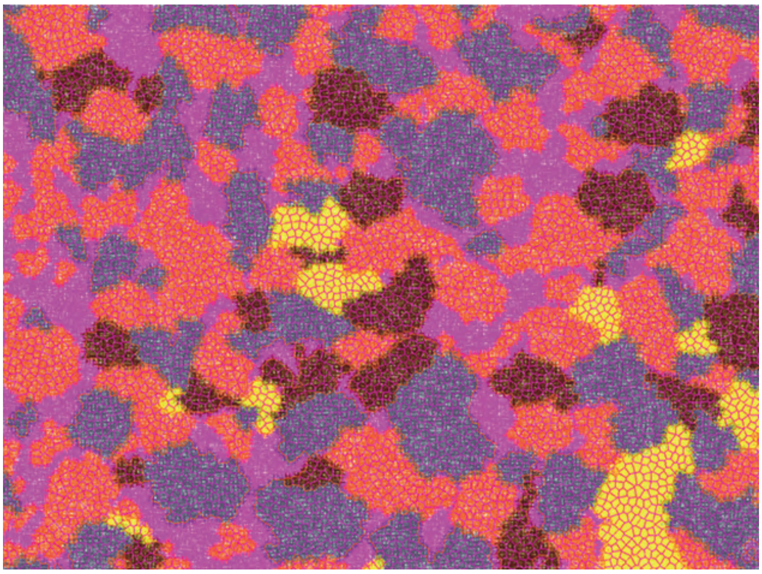

Fig. 5.5: Generated geometrical model using grey level images
(compare left image in Fig. 5.2)

Generation of the geometrical models using clumps

Clumps in PFC-2D are generated by overlapping particles to reconstruct the real grain shape. The number, degree of overlapping and the size of the clumps can differ. Fig. 5.6 shows the procedure schematically: Firstly, circular particles are generated in a ’box’. Secondly, predefined clumps replace particles having the same area and point of origin but arbitrary orientations.

All information is saved in a text-file, i.e. x,y-coordinates of the center, radius and data of the material type. UDEC reads-in this file, assigns Voronoi-blocks and generates clusters. With PFC-2D it is possible to build „grain shape libraries“.

We measured the shape and size of the generated clumps with ’ImageJ’ to ensure that they correspond to the real grain size distribution and shapes. 200 clumps combining 5 to 15 particles were generated and it turned out that the combination with 7 particles covers most of the grain shapes. Only certain shapes couldn’t be generated or only with great effort by combinations of 10 to 15 particles.

Clumps were grouped in accordance to the deltA and deltP values and their ellipticity. By comparing the number of objects in the particular group of ellipticity we assigned the same number of clumps to this groups.

Both, the generation of the clumps and the image analysis are fast and simple methods but the selection of the clumps appropriate to the real grain shapes turned out to be very time-consuming. On reason is the random generator - Nomen est omen – which has no influence to the generated grain shapes.

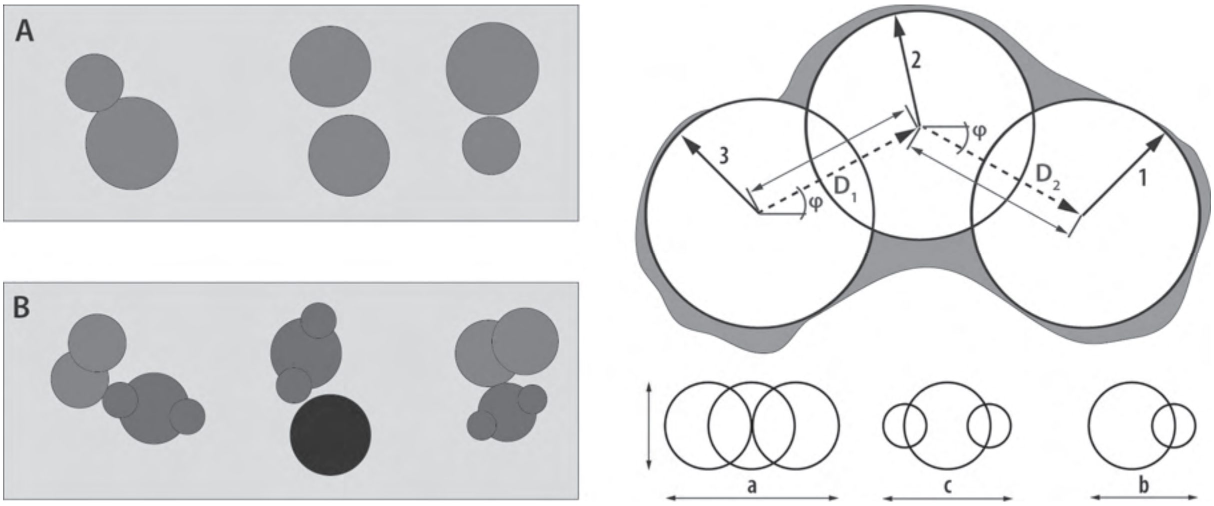

Fig. 5.6: Replacement of particles by clumps (left). Right: generation of a clump by three particles. Particle 1 has a defined position, whereas particle 2 and 3 are randomly generated. The combinations reconstruct the real grain seen in the background. The lower row shows different simple combinations with variations in number and size of the particles.

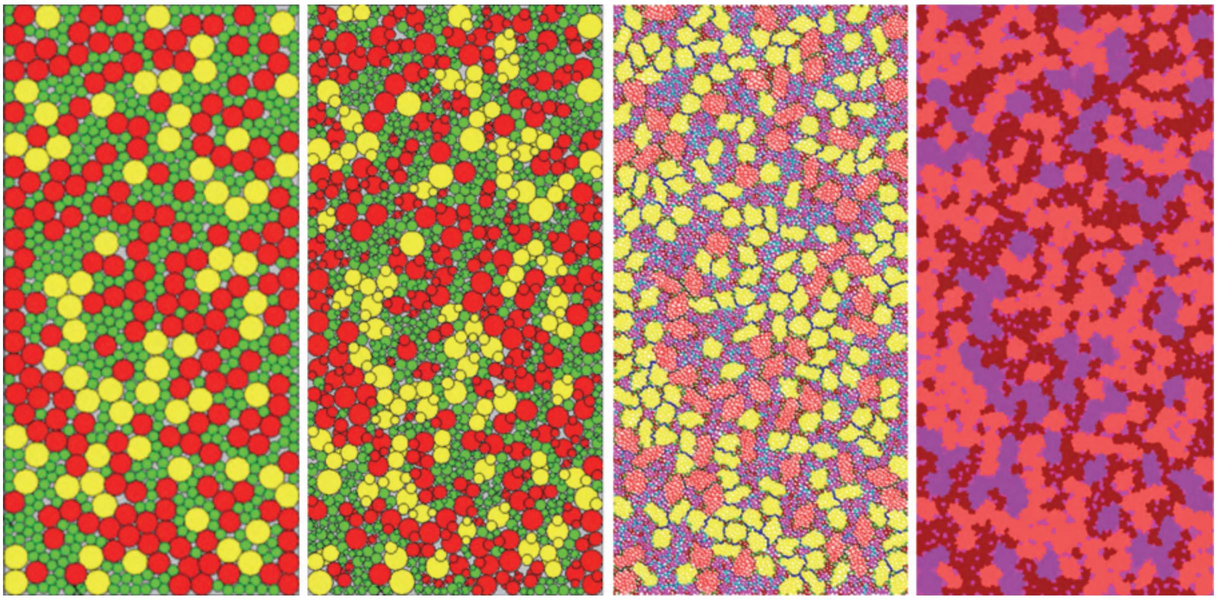

Fig. 5.7: Generated geometric model based on clumps: [a] particle, [b] replacement of particles by clumps, [c] geometric model by import of text file into UDEC, [d] material blocks

6 Prospects

After the generation of the different models calibration is performed and final simulations will follow. The simulations consider a thermal load of about 50-60 °C under consideration of different thermal dilatation parameters and gradients as well

as different strength properties for the untreated and treated parts. Main aim is to evaluate the treatment, i.e. to access whether it will lead to cracks and/or scaling within the object or not.
Another topic is the comparison of the results in respect to the different approaches of model generation. In other words, to evaluate if there is a scientific advantage to the common model generation by random assignments, for example, for porosity or grains.

7 Preferences

Heilbronner, R. & Barrett, (2014): Image Analysis in Earth Sciences. Springer, Berlin Heidelberg

IBACH, W., SOBOTT, R. (2007): Vollkonservierung von Cottaer Sandstein, In: Elbsandstein, S. 113-119, H. Siedel, C. Franzen and S. Weise. Dresden, Institut für Diagnostik und Konservierung IfD e.V.

ICOMOS (2008): Illustrated glossary on stone deterioration patterns - Illustriertes Glossar der Verwitterungsformen von Naturstein

Kozub, P. (2008): To the determination of the Young’s modulus from the biaxial flexural strength. In: Lukaszewicz, J.W. & Niemcewicz P. (Eds.): 11th International Congress on the Deterioration and Conservation of Stone, 15.-20. Sept. 2008, Torun, Poland. Volume 1, p. 407-4.13

Pummer, E. (2007): Die Kremser Dreifaltigkeitssäule - European Commission Research Projekt 2007 (Vakuum-Kreislauf-Festigung), Eigenverlag.

SIEDEL, H. (2007): Verwitterung von Elbsandstein am Bauwerk. – In: SIEDEL, H.; FRANZEN, C. & WEISE, S. (Hrsg.): Elbsandstein. Beiträge zur Tagung des Arbeitskreises zur Erhaltung von Kulturgütern aus Stein (ARKUS) in Dresden, 59-71.

SIEDEL, H. (2010): Alveolar weathering of Cretaceous building sandstones on monuments in Saxony, Germany. - In: TÖRÖK, A. & PŘIKRYL, R. (eds.): Natural Stone Resources for Historical Monuments. Geological Society, London, Special Publications 333. - S. 11 - 23.

Waste repositories / Geothermal energy

Swiss repositories for radioactive waste: Status of site selection and technical feasibility demonstration

Geologische Tiefenlager für radioaktive Abfälle in der Schweiz: Standortauswahl und Demonstration der technischen Machbarkeit

T. Vietor, H. R. Müller
Nagra, Wettingen, Schweiz

Abstract

In order to select the sites for geological repositories for nuclear waste Switzerland follows a step-wise approach. After identification of 6 candidate sites in phase 1, in the ongoing phase 2 Nagra as the implementing organization is currently preparing the proposal for the selection of the candidate sites to be investigated in detail in the upcoming phase 3. For high-level waste the host rock is Opalinus Clay a 100 m thick shale that is intercalated in the Mesozoic sequence of clay rich rocks of Northern Switzerland. In this paper we describe the field activities and rock characterization program that is being assembled as a scientific base for the host rock and site selection. Secondly we depict selected underground laboratory experiments that demonstrate the disposal concept at large scale. We focus on the current understanding of THM coupled effects and the feasibility of the high-level waste repository concept.

Zusammenfassung

Zur Standortauswahl für die geologischen Tiefenlager für radioaktive Abfälle hat die Schweiz ein mehrstufiges Verfahren gewählt. Zunächst wurden in einer ersten Phase 6 mögliche Standorte identifiziert. In der gegenwärtigen zweiten Phase bereitet die Nagra die Standortvorschläge für die erdwissenschaftlichen Untersuchungen der Phase 3 vor. Für die hochaktiven Abfälle ist der Opalinuston als Wirtgestein bereits festgelegt worden. Diese etwa 100 m mächtige tonreiche Formation ist eingeschaltet in weitere tonreiche Formationen des Mesozoikums der Nordschweiz. Hier berichten wird über das Programm der Nagra zur Standort- und Wirtgesteinscharakterisierung auf dem der Auswahlprozess basiert. Weiterhin werden Experimente aus den Felslaboren vorgestellt, die das Lagerkonzept der Schweiz grossmassstäblich demonstrieren. Dabei liegt der Schwerpunkt auf dem gegenwärtigen Verständnis von THM Effekten und der technischen Machbarkeit des Lagerkonzepts für hochaktive Abfälle.

1 Swiss Program for the implementation of radioactive waste repositories

Nagra's mission is to develop safe geological repositories for all radioactive wastes arising in Switzerland. The procedure for site selection foresees application within the next 7 to 8 years for general (site) licenses for two repositories, one for low and intermediate level waste (L/ILW) and one for spent fuel, vitrified high level waste (HLW) and long-lived ILW (referred to hereafter as the HLW repository). The candidate disposal siting regions are located in sedimentary rocks in Northern Switzerland, except for one region in Central Switzerland for L/ILW. Within the current second phase of the regulatory process Nagra is preparing the documents for the proposal of the sites to be investigated in detail until the general license application.

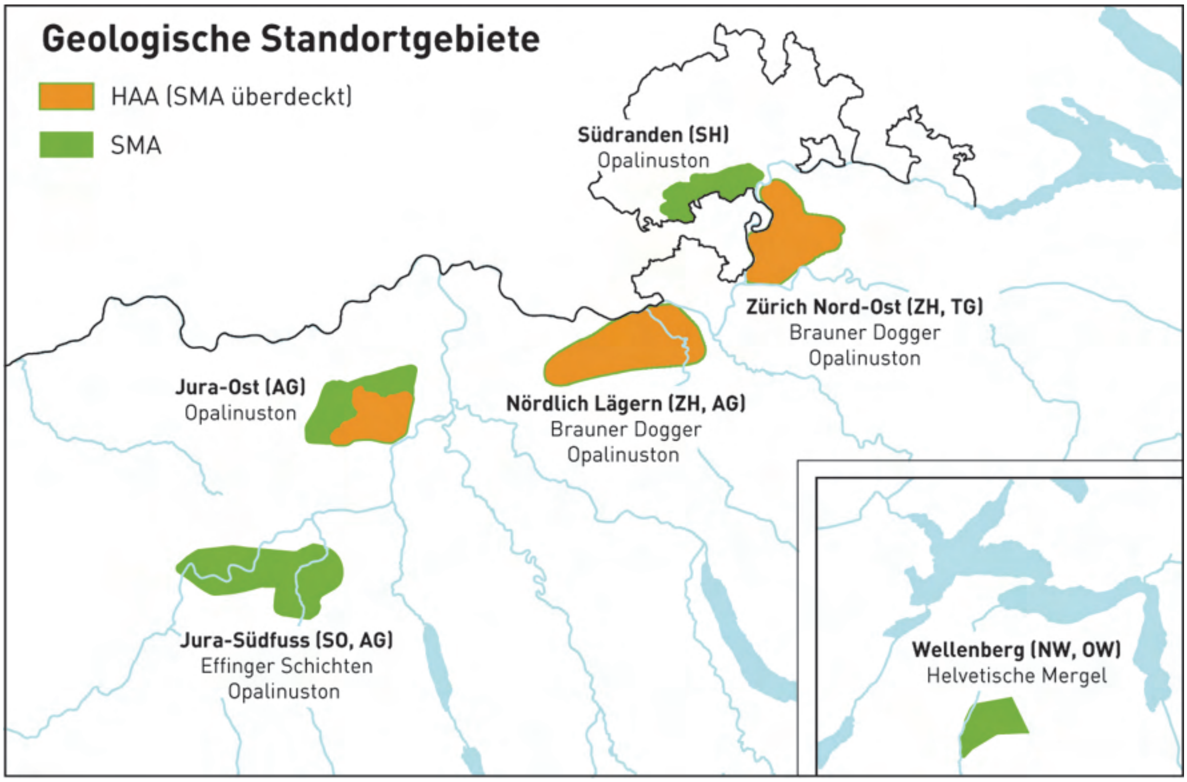

Fig. 1.1: Candidate regions for the geological repositories in Northern Switzerland

2 Nagra's site and host rock characterization program

An important part of Nagra's activities are focused on the Opalinus Clay formation, the host rock selected for the HLW repository and a host rock candidate for the L/ILW repository (Nagra, 2008). In the proposed siting regions the Opalinus Clay has a very low hydraulic conductivity in the range of 10^{-12} to 10^{-14} ms^{-1} and a porosity of 0.12 and 0.15. The Opalinus Clay formation is generally around 100 m thick and is surrounded by other clay-rich confining units. The Opalinus Clay formation has the following favourable characteristics (Nagra, 2002):

- The Opalinus Clay is an indurated claystone (clay shale) with reasonable engineering properties, allowing small, unlined tunnels and larger, lined tunnels to be constructed at depths of several hundred metres.
- The properties of the Opalinus Clay ensure that repository-induced and natural fractures will be of very low hydraulic conductivity due to the self sealing capacity of the Opalinus Clay; i.e. their effect on the hydraulic properties of the Opalinus Clay will be negligible.
- The Opalinus Clay has such a low hydraulic conductivity that solute movement through the formation is predominantly by diffusion rather than advection.
- The geochemical conditions in the Opalinus Clay are reducing, slightly alkaline and moderately saline and favour the preservation of the engineered barriers and radionuclide retention.
- The geochemical environment in the Opalinus Clay and surrounding formations is expected to remain effectively stable for several million years.

The geochemical, hydrogeological and hydromechanical characterisation from the microscale to the regional scale show that the Opalinus Clay is a suitable host rock for geological repositories of nuclear waste. Natural tracer profiles have been instrumental for demonstrating the extremely low transport capacity of the Opalinus Clay. At the large scale 2D and 3D seismics and deep drilling in the recent years have successfully refined the geosphere models. At the very small scale hyperspectral scans are contributing to the mineralogical characterisation. Further efforts will aim to enhance the correlation between mineralogy and petrophysical parameters. While these elements contribute to the development of accurate static geomodels, several activities are already anticipating the development of the dynamic models for the proposed sites. The understanding of the constitutive behaviour of the Opalinus Clay will be enhanced (e.g. using novel large strain experiments and adequately assessing the role of the hydraulic state of the samples). Detailed geochemical analysis and modelling are accurately assessing the pore water compositions in support of the long-term safety assessment.

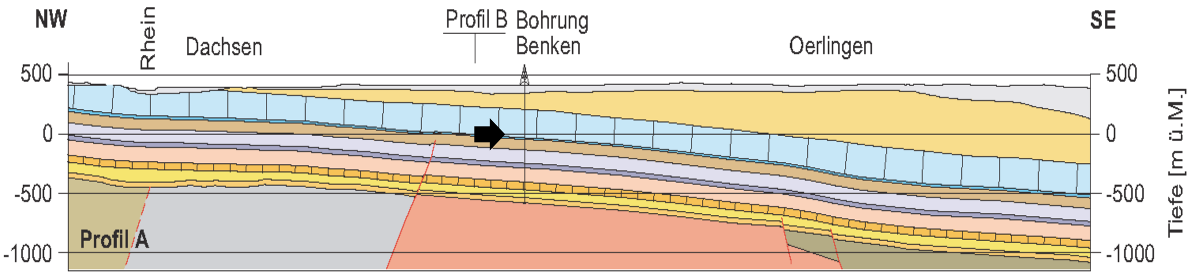

Fig. 2.1: Geological cross section in the candidate siting region Zürich Nordost.
The 100 m thick Lower Dogger Opalinus Clay (arrow) is surrounded by other clay rich formations.

Another part of Nagra's work focusses on the the impact of the repository on the Opalinus Clay from a long term safety point of view. This includes gas migration and thermo-hydro-mechanical impacts as well as excavation damaged zone (EDZ) characterisation and clay interface reactions. With the results of large-scale gas related experiments (HG-A and HG-D) available, the conceptual picture on how gas is transported in the EDZ and the disturbed OPA can be refined while advanced numerical models (FEM-DEM) provide insight into the formation of the EDZ. A series of increasingly complex heater tests (HE-D, HE-E, FE) are significantly contributing to the understanding of thermally induced stresses in the Opalinus Clay and the bounding of induced overpressures. Important observations to confirm these bounding assumptions are expected in the years to come.

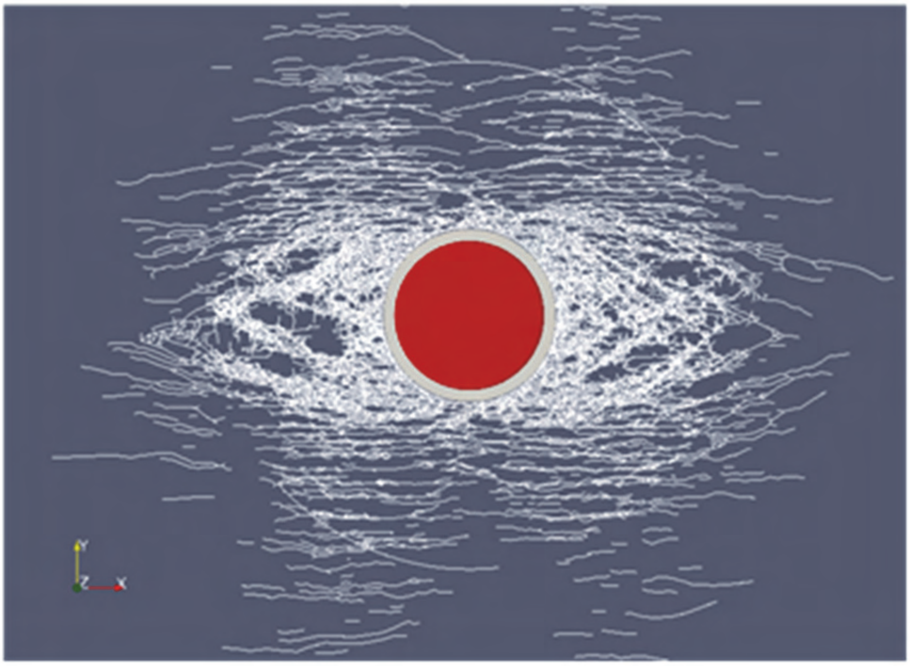

Fig. 2.2: Such induced fracture networks derived from FEM-DEM simulations are used as a basis for the abstracted long-term safety assessment models.

Finally activities supporting engineering and planning of repository construction are presented. As the plans for the repository are targeted to be at the concept stage at the time of the license application, these activities will remain mainly desk-based (e.g. geomechanical modelling studies). The 1:1 scale heater test at Mont Terri (FE-experiment), for which the implementation is completed in December 2014, had a strong demonstration component (as part of the LUCOEX 7th Framework project) regarding the feasibility of the horizontal emplacement concept as proposed by Nagra and accepted by the Swiss Government (Nagra, 2002).

Fig. 2.3: Multiple-screw-conveyor machine used to emplace the bentonite backfill material in the triple-heater repository scale test at the Mont Terri rock laboratory. Here the machine is used in a mock-up pre-test. Note the dummy canister between the conveyor pipes at left.

References

Nagra (2002): Project Opalinus Clay: Safety report: Demonstration of disposal feasibility for spent fuel, vitrified high-level waste and long-lived intermediate-level waste (Entsorgungsnachweis). Nagra Technischer Bericht. NTB 02-05. Nagra, Wettingen.

Nagra (2008): Vorschlag geologischer Standortgebiete für ein SMA- und ein HAA-Lager: Geologische Grundlagen (Bericht zur Geologie). Nagra Technischer Bericht. NTB 08-04. Nagra, Wettingen.

Numerical modelling of shallow and deep geothermal systems

Numerische Modellierung oberflächennaher und tiefer geothermischer Systeme

O. Kolditz[1,2], N. Watanabe[1], U.-J. Görke[1], A. Bucher[4], H. Shao[1,3]
[1]Helmholtz-Zentrum für Umweltforschung UFZ, Leipzig
[2]Technische Universität Dresden
[3]Technische Universität Bergakademie Freiberg
[4]Hochschule für Technik , Wirtschaft und Kultur, HTWK, Leipzig

Abstract

Modelling of geothermal systems is an important tool for different aspects of using geothermal energy resources, e.g., gaining a better understanding of thermodynamic, physico-chemical processes in natural and man-made geothermal reservoirs (in particular deep geothermal systems), optimising geothermal heat pump installation for domestic heat supply (in particular shallow geothermal systems), and assessing any kind of environmental impacts of anthropogenic interference to natural geothermal systems. Recently, heat storage in the subsurface at higher temperatures from industrial processes came into discussion. The value of modelling is in particular the analysis of coupled processes based on fundamental thermodynamic and mechanical principles and providing predictive power for future forecasts of geothermal systems evaluation. The current work provides a framework for both shallow and deep geothermal systems.

Zusammenfassung

Die Modellierung geothermischer Systeme ist ein wichtiges Werkzeug für verschiedene Aspekte der Nutzung geothermischer Ressourcen, z. B. für ein verbessertes Verständnis der thermodynamischen, physiko-chemischen Prozesse in den natürlichen und stimulierten Systemen (insbesondere tiefe Geothermie), die Optimierung von Erdwärmepumpenanlagen (insbesondere flache Geothermie) und die Bewertung möglicher Umweltwirkungen durch die anthropogenen Eingriffe in das geothermische System. Seit kurzen ist auch die mögliche Wärmespeicherung im Untergrund Gegenstand der Geothermieforschung. Durch die numerische Modellierung können insbesondere gekoppelte Prozesse auf der Basis thermodynamischer und kontinuums-mechanischer untersucht werden und Vorhersagen für die Entwicklung geothermischer Reservoire getroffen werden. Die vorliegende Arbeit gibt einen Rahmen für die Modeliierung oberflächennaher und tiefer geothermischer Systeme.

1 Introduction

“Geothermal energy is a promising alternative energy source as it is suited for baseload energy supply, can replace fossil fuel power generation, can be combined with other renewable energy sources such as solar thermal energy, and can stimulate the regional economy” is cited from the Editorial to a new open access journal Geothermal Energy (Kolditz et al. 2013) in order to appraise the potential of this renewable energy resource for both heat supply and electricity production.

Geothermal energy became an essential part in many research programmes worldwide. The current status of research on geoenergy (including both geological energy resources and concepts for energy waste deposition) in Germany and other countries recently was compiled in a thematic issue on “Geoenergy: new concepts for utilization of geo-reservoirs as potential energy sources” (Scheck-Wenderoth et al. 2013). The Helmholtz Association dedicated a topic on geothermal energy systems into its next five-year-program from 2015 to 2019 (Huenges et al. 2013).

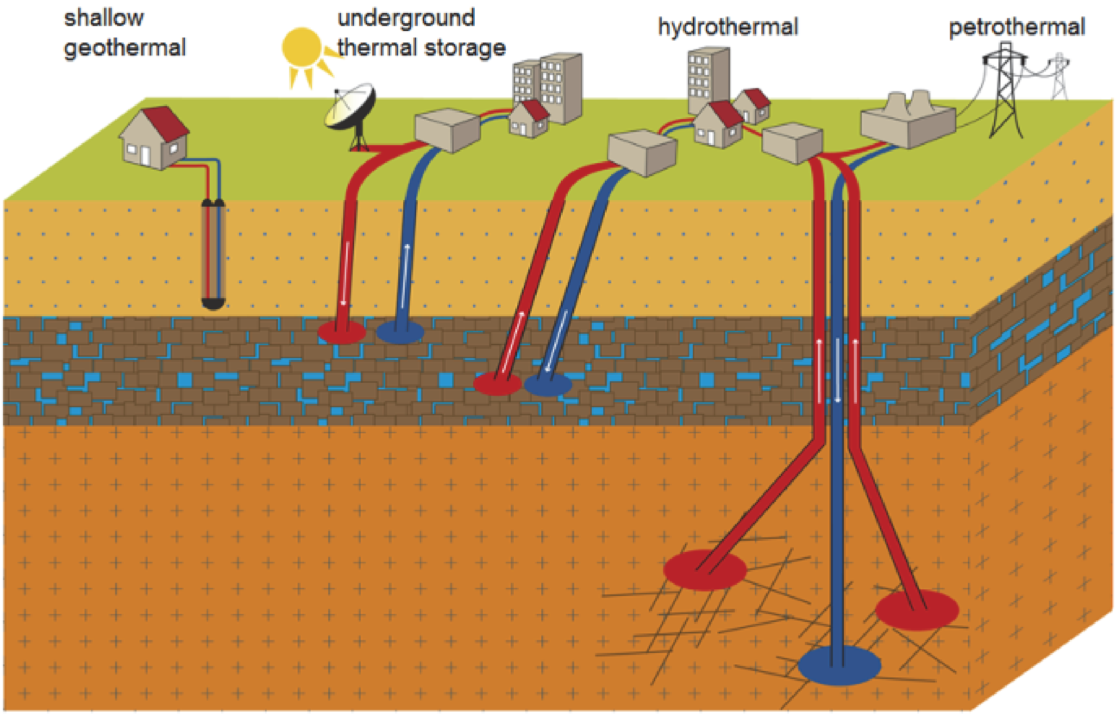

Fig. 1: Overview of different types of geothermal systems (Huenges et al. 2013)

Looking at different types of geothermal systems it can be distinguished between shallow, medium, and deep systems in general (Figure 1). Installations of shallow systems are allowed down to 100 m by regulation, and include soil and shallow aquifers, therefore. Medium systems are associated with hydrothermal resources and may be suited for underground thermal storage (Bauer et al. 2013). Deep systems are connected to petrothermal sources and need to be stimulated to increase hydraulic conductivity for heat extraction by fluid circulation (Enhanced Geothermal Systems - EGS). In general, the corresponding temperature regimes at different depths depend on the geothermal gradient. Some areas benefit from favourable geothermal conditions with amplified heat fluxes, e.g., the North German Basin, Upper Rhine Valley and Molasse Basin in Germany (Cacace et al. 2013).

This paper is dealing with modelling of shallow (section 2) and deep geothermal systems (section 3) as well as providing concepts for geothermal modelling workflows (section 4). A brief literature review and research challenges are provided in each section and illustrated by a given example from recent works of the authors.

2 Shallow geothermal systems

2.1 State-of-the-art

To describe the heat transport process in the surrounding soil of the Borehole Heat Exchanger (BHE), classical analytical solutions are available for saturated and homogeneous media. This contains the Infinite Line Source (ILS) model, the Infinite Cylindrical Source (ICS) model, and the Finite Line Source (FLS) model. Philippe et al. (2009) had a review on the validity ranges of these analytical models. When the groundwater flow has to be considered, then the Moving Finite Line Source (MFLS) model can also be adopted (Molina-Giraldo et al. 2011). These analytical solutions are then integrated together with numerical optimisation algorithms, so that the best geometric arrangement and operation mode can be found for maximum energy extraction (Hecht-Mendez et al. 2013; Beck et al. 2013).

If the focus is on the short term temperature evolution in and around the BHE, then the numerical model must be adjusted to include the heat exchange between BHE and the surrounding soil. The conventional approach is to explicitly mesh the pipelines and grout zones in a BHE, such as the code FD3DM, in which the flow and heat transport process in the pipelines can both be simulated. However, the refined mesh grid and small time step size imposed by this approach will lead to very long simulation time. The remediation of this issue was proposed by Al-Khoury et al. (2010), where a dual-continuum approach was adopted. The BHE, separated from the surrounding soil, was simulated as two continua, and the heat flux between them is balanced through numerical iterations. This approach was then adopted by Diersch et al. (2011a; 2011b), and implemented into the software FEFLOW (DHI-WASY 2010). A comparison study shows that the analytical solution of Eskilson and Claesson (1988) cannot be used to simulate the temperature evolution in the starting period of BHE operation (less than 3.5 to 10 hours), when the thermal equilibrium has not been reached with the surrounding soil.

2.2 Challenges

For the shallow geothermal systems, the ultimate challenge for the numerical model is to produce realistic prognoses of the operational status of the entire ground source heat pump system. This imposes two requirements on the model. 1) As the surrounding soil property will have a great impact on the dynamics of heat transport, detailed information such as the groundwater table, groundwater flow direction and velocity, soil matrix porosity and conductivity must be obtained for particular site and be integrated in the model. 2) The numerical model needs to be further extended to include the operation of the heat pump system. Then based on the required heat load information, prognosis can be made on meaningful operational parameters such as the coefficient of performance (COP) and electricity consumption. These parameters can then be optimised for the specific site, which leads to extensive investment and cost savings.

2.3 Example (Taucha)

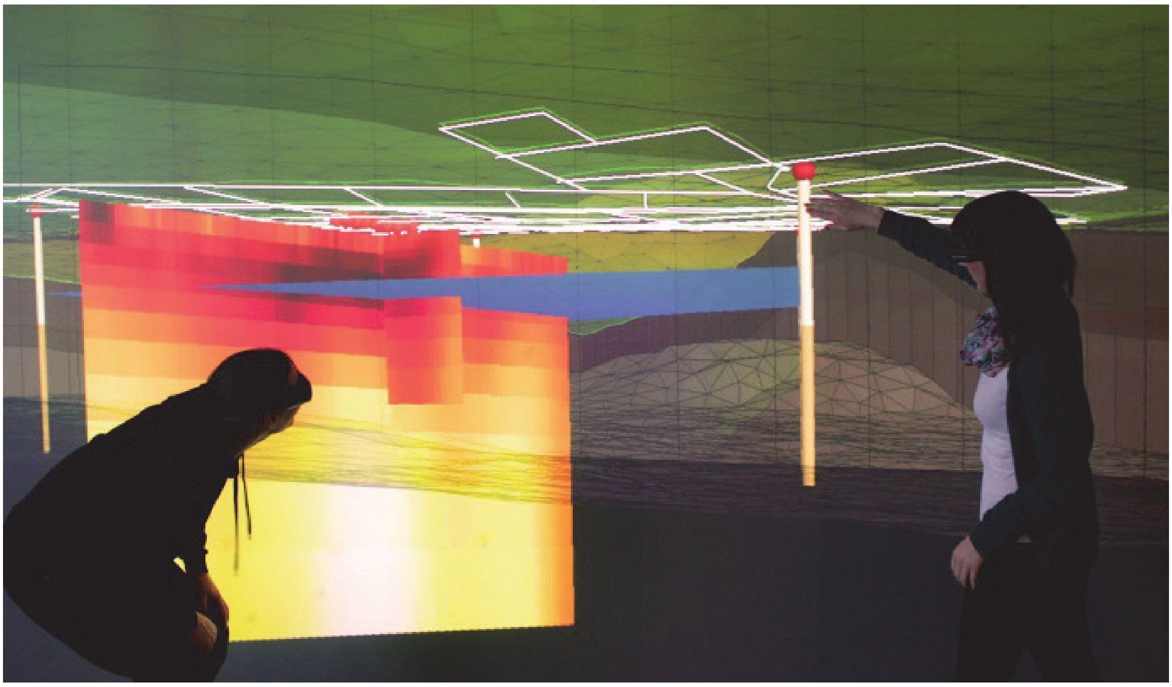

Fig. 2: Visualization of shallow geothermal systems – site study at Taucha (Bilke et al. 2014)

Fig. 2 shows a view to the subsurface of a living quarter which is supposed for using geothermal heat pumps. The borders of private properties (white lines on top) indicate possible positions for geothermal wells (vertical lines) penetrating the groundwater level (blue surface) at about 5 m below surface. Results of geophysical survey are displayed on a vertical surface. The visualisation combines GIS data (infrastructure) with geophysical measurements and modelling results of heat transport in the subsurface. Modelling of the site specific shallow geothermal installations provided a better insight for optimal positioning and number of wellbores taking into account the regional groundwater flow regime.

3 Deep geothermal systems

3.1 State-of-the-art

Predicting evolutions of reservoir permeability is one of the major issues for estimating productivity in deep geothermal systems. Numerical models are desired to simulate the dynamics triggered by interactions of thermo-hydro-mechanical-chemical (THMC) processes. Numerical THM models have been developed and applied to several sites such as Soultz-sous-Foréts in the Rhine Valley (Kohl et al. 1995) and Urach Spa in the Swabian Alb (McDermott et al. 2006). Impacts of mineral dissolution and precipitation have been studied by THC models (Kiryukhin et al. 2004; Kuhn 2004). Mechanical and chemical coupled processes, e.g., stress-induced dissolution, can also affect fracture permeability and its impact on EGS has been first studied with a THMC model (Taron and Elsworth 2010).

3.2 Challenges

Besides the process modelling, accurate representation of fracture networks is a subject of future challenges. Discrete fracture network models are available for the simulation of fluid, solute and heat transport even for realistic geological structures. However, their applicability in the context of THM analysis is still restricted to simplified homogenised approaches using continuum models. The distinct element method (DEM) is one of the promising approaches to overcome the problem if matrix diffusion is negligible (Jing 2003; Min et al. 2004). Alternatively, the extended finite element method (XFEM) also provides attractive features such as no need to represent fractures in meshes and capability of combining both continuum elements for the matrix and discrete elements for the fractures (Belytschko and Black 1999; Moës et al. 1999; Khoei et al. 2012).

3.3 Example

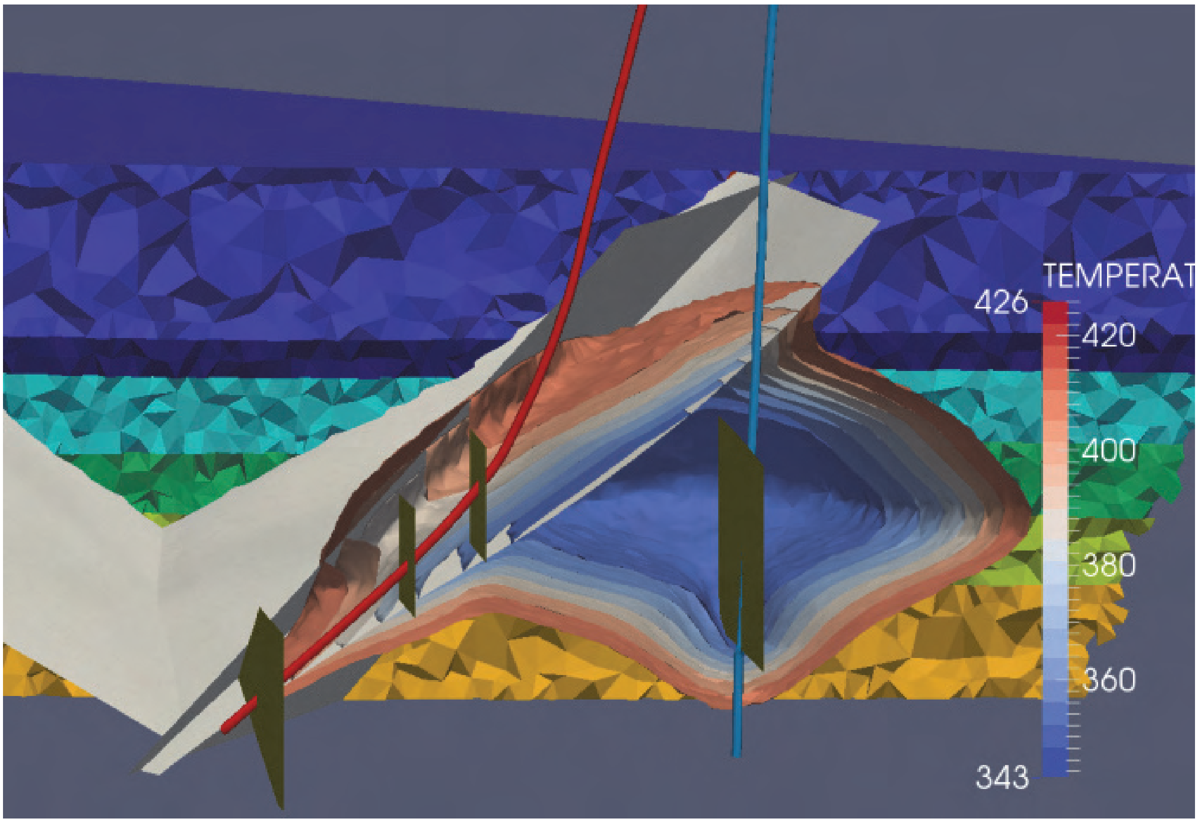

Fig. 3: Numerical simulation of the Groß Schönebeck geothermal reservoir

The Groß Schönebeck research site (50 km north of Berlin, Germany) was established as an in situ laboratory for deep sedimentary geothermal systems by Helmholtz-Centre Potsdam - GFZ German Research Centre for Geosciences. A borehole doublet has been installed there with four induced hydraulic fractures at the depth of around 4 km in sandstones and fractured volcanic rocks of the Lower Permian where formation temperatures are up to 150°C (Zimmermann and Reinicke 2010). N- to NE-striking natural faults are expected to serve as main flow path in the current stress field (Blöcher et al. 2010b). For analysing impacts of the fault zone permeability on reservoir dynamics, hydrothermal simulations have been conducted using OpenGeoSys (Kolditz et al. 2012b). As shown in Figure 3, the complex reservoir structure was modelled in a 3D unstructured grid with multi-dimensional elements representing geological units, faults, hydraulic fractures, and well paths. The simulation assuming a high conductive fault zone showed that computed pressure responses in the wells are in the range of the measured quantities while the influx into the production well from one of the induced fractures in the volcanic rocks was overestimated (Bloecher et al. 2015). More detailed analysis of the fault zone permeability is currently ongoing.

4 Conclusions and outlook

This paper presented an overview on concepts and recent works on modelling both shallow and deep geothermal systems. Numerical modelling of geothermal reservoirs needs to be integrated into workflows for more complete analysis of the whole system (Kolditz et al. 2012a).

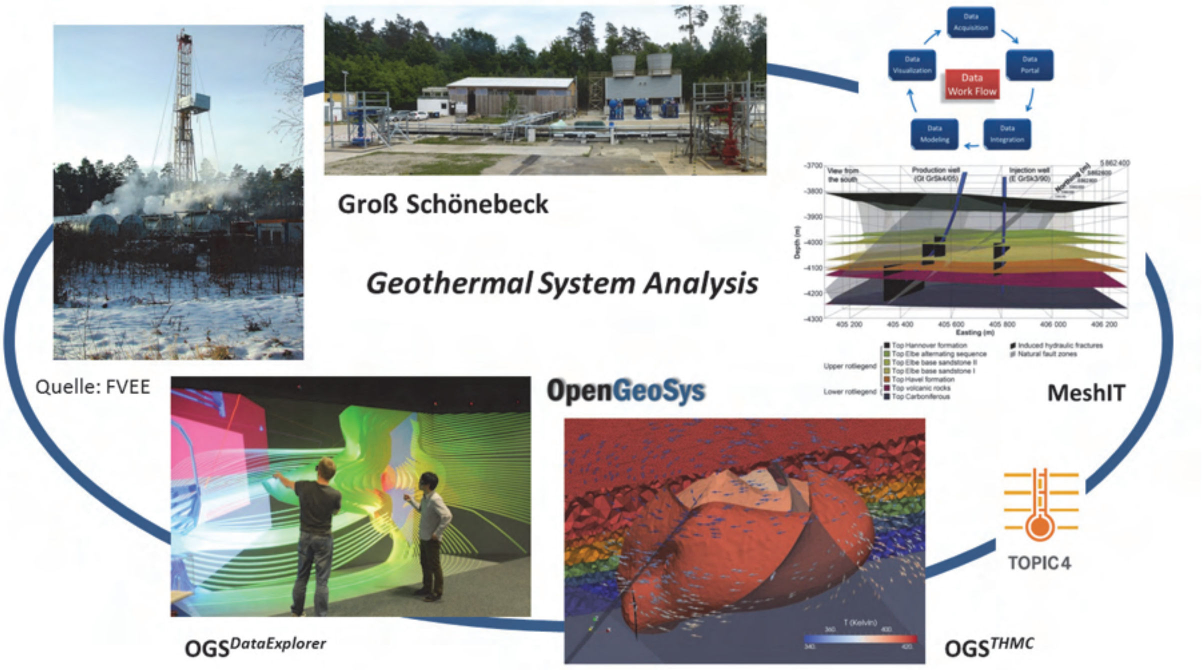

Fig. 4: Workflow definition for geothermal systems analysis (Example Groß Schönebeck)

Figure 4 shows a workflow layout of systems analysis for the geothermal research site Groß Schönebeck (north of Berlin, operated by the GFZ). The modelling workflow includes comprehensive data integration from various sources such as structural geology, drilling trajectories, petrophysical, geophysical data etc. The next step in the workflow is setup of the discretised numerical model for which special software for geometrical modelling and meshing has been developed (MeshIT, Blöcher et al. 2010a). The numerical simulation of thermo-hydro-mechanical-chemical processes in fractured-porous media is conducted with the modelling platform OpenGeoSys (www.opengeosys.org, Kolditz et al. 2012b). Accurate and efficient numerical simulations require the use of high-performance-computing platforms for which code parallelisation is necessary (Wang et al. 2014). In order to display comprehensive data sets together with simulation results we use scientific visualisation (Bilke et al. 2014). Visualisation has proven to be an intuitive tool to discuss complex models among scientists and present scientific results to stakeholders and the public in an understandable way.

Geothermal energy exhibits increasing interest in many countries all over the world. In Germany the efforts in utilisation more and more renewable energy resources are mainly triggered by the new paradigm of the “Energiewende”. Many emerging and newly industrialised countries increase their efforts in using geothermal energy, e.g., substituting coal burning for domestic heating in China and improving air quality in cities (Kong et al. 2014).

Acknowledgements

We acknowledge the support by the Helmholtz Association in the frame of the GEOENERGIES Portfolio and the Renewable Energy Program (POF-3). In particular we are grateful to our colleagues from the German Research Centre for Geosciences (GFZ) and Karlsruhe Institute of Technology (KIT) for fruitful research cooperation. We thank our colleagues from the Department of Monitoring and Exploration Technologies (MET) of the Helmholtz Centre for Environmental Research UFZ and the city of Taucha for cooperation in the “Parteblick” shallow geothermal energy project.

References

Al-Khoury R, Kölbel T, Schramedei R (2010): Efficient numerical modeling of borehole heat exchangers, Computers & Geosciences, 36(10): 1301-1315, DOI: 10.1016/j.cageo.2009.12.010.

Bauer S, Beyer C, Dethlefsen F, Dietrich P, Duttmann R, Ebert M, Feeser V, Görke UJ, Köber R, Kolditz O, Rabbel W, Schanz T, Schäfer D, Würdemann H, Dahmke A (2013): Impacts of the use of the geological subsurface for energy storage – an investigation concept. Environ. Earth Sci., 70(8): pages, DOI: 10.1007/s12665-013-2883-0.

Beck M, Bayer P, de Paly M, Hecht-Méndez J, Zell A (2013): Geometric arrangement and operation mode adjustment in low-enthalpy geothermal borehole fields for heating. Energy, 49: 434-443, DOI: 10.1016/j.energy.2012.10.060.

Belytschko T, Black T (1999): Elastic crack growth in finite elements with minimal remeshing. International Journal for Numerical Methods in Engineering, 45(5): 601–620.

Bilke L, et al. (2014): VISLAB – Laboratory for Scientific Visualization. Environ Earth Sci., submitted.

Blöcher G, Cacace M, Lewerenz B, Zimmermann G (2010a): Three dimensional modelling of fractured and faulted reservoirs: Framework and implementation. Chemie der Erde - Geochemistry, 70, Supplement 3, 145 - 153.

Blöcher G, Zimmermann G, Moeck I, Brandt W, Hassanzadegan A, Magri F (2010b): 3D numerical modeling of hydrothermal processes during the lifetime of a deep geothermal reservoir. Geofluids, 10: 406-421.

Blöcher G, Cacace M, Wong LW, Kastner O, Zimmermann G, Huenges E, Watanabe N, Kolditz O (2015) New approaches of coupled simulation of deep geothermal systems. Proceedings World Geothermal Congress, Melbourne, Australia, 19-25 April 2015.

Cacace M, Blocher G, Watanabe N, Moeck I, Borsing N, Scheck-Wenderoth M, Kolditz O, Huenges E (2013): Modelling of Fractured Geological Reservoirs - Outline of a novel technique via a case study from the Molasse Basin, southern Bavaria (Germany). Environ. Earth Sci., 70(8): 3585-3602, DOI: 10.1007/s12665-013-2402-3.

DHI-WASY (2010): FEFLOW finite element subsurface flow and transport simulation system-User's manu-al/reference manual/white papers. Recent release 6.0, DHI-WASY GmbH, Berlin. http://www.feflow.info.

Diersch HJG, Bauer D, Heidemann W, Rühaak W, Schätzl P (2011a): Finite element modeling of borehole heat exchanger systems: Part 1. Fundamentals, Computers & Geosciences 37(8): 1122-1135, DOI: 10.1016/j.cageo.2010.08.003.

Diersch HJG, Bauer D, Heidemann W, Rühaak W, Schätzl P (2011b): Finite element modeling of borehole heat exchanger systems: Part 2. Numerical simulation, Computers & Geosciences 37(8): 1136-1147, DOI: 10.1016/j.cageo.2010.08.002.

Eskilson P, Claesson J (1988): Simulation model for thermally interacting heat extraction boreholes. Numerical Heat Transfer 13: 149-165.

Hecht-Méndez J, de Paly M, Beck M, Bayer P (2012): Optimization of energy extraction for vertical closed-loop geothermal systems considering groundwater flow. Energy Conversion and Management 66: 1-10, DOI: 10.1016/j.enconman.2012.09.019.

Huenges E, Kohl T, Kolditz O, Bremer J, Scheck-Wenderoth M, Vienken T (2013): Geothermal energy systems: research perspective for domestic energy provision. Environ. Earth Sci., 70(8), DOI: 10.1007/s12665-013-2881-2.

Jing L (2003): A review of techniques, advances and outstanding issues in numerical modelling for rock mechanics and rock engineering. International Journal of Rock Mechanics & Mining Sciences, 40 (2003) 283–353.

Khoei AR, Moallemi S, Haghighat (2012): Thermo-hydro-mechanical modeling of impermeable discontinuity in saturated porous media with X-FEM technique. Engineering Fracture Mechanics, 96: 701-723.

Kiryukhin A, Xu T, Pruess K, Apps J, Slovtsov I (2004): Thermal-hydrodynamic-chemical (THC) modeling based on geothermal field data. Geothermics, 33(3):349–381.

Kohl T, Evans KF, Hopkirk RJ, Rybach L (1995): Coupled hydraulic, thermal and mechanical considerations for the simulation of hot dry rock reservoirs. Geothermics, 24(3):345–359.

Kolditz O, Rink K, Shao HB, Kalbacher T, Zacharias S, Kunkel R, Dietrich P (2012a): Data and modelling platforms in environmental Earth sciences. Environ. Earth Sci., 66: 1279–1284, DOI: 10.1007/s12665-012-1661-8.

Kolditz O, Bauer S, Bilke L, Böttcher N, Delfs JO, Fischer T, Görke UJ, Kalbacher T, Kosakowski G, McDermott CI, Park CH, Radu F, Rink K, Shao H, Shao HB, Sun F, Sun YY, Singh AK, Taron J, Walther M, Wang W, Watanabe N, Wu N, Xie M, Xu W, Zehner B (2012b): OpenGeoSys: an open-source initiative for numerical simulation of thermo-hydro-mechanical/chemical (THM/C) processes in porous media. Environ. Earth Sci., 67(2): 589-599, DOI: 10.1007/s12665-012-1546-x.

Kolditz O, Jakobs LA, Huenges E, Kohl T (2013): Geothermal energy: a glimpse at the state of the field and an introduction to the journal. Geothermal Energy, 1:1, DOI: 10.1186/2195-9706-1-1.

Kong et al. (2014): Geothermal energy resources in China. Geothermal Energy, submitted.

Kuhn M (2004): Reactive flow modeling of hydrothermal systems. Lecture Notes in Earth Sciences. Springer, Berlin 47.

McDermott CI, Randriamanjatosoa AR, Tenzer H, Kolditz O (2006) Simulation of heat extraction from crystalline rocks: The influence of coupled processes on differential reservoir cooling. Geothermics 35(3):321–344

Min KB, Rutqvist J, Tsang CF, Jing L (2004) Stress-dependent permeability of fractured rock masses: a numerical study. International Journal of Rock Mechanics & Mining Sciences, 41: 1191–1210.

Molina-Giraldo N, Blum P, Zhu K, Bayer P, Fang Z (2011): A moving finite line source model to simulate borehole heat exchangers with groundwater advection. International Journal of Thermal Sciences, 50(12): 2506-2513, DOI: 10.1016/j.ijthermalsci.2011.06.012.

Moës N, Dolbow J, Belytschko T (1999): A finite element method for crack growth without remeshing. International Journal for Numerical Methods in Engineering, 46(1): 131–150.

Philippe M., Bernier M., Marchio D. (2009) Validity ranges of three analytical solutions to heat transfer in the vicinity of single boreholes, Geothermics 38(4): 407-413, DOI: 10.1016/j.geothermics.2009.07.002.

Scheck-Wenderoth M, Schmeißer D, Mutti M, Kolditz O, Huenges E, Schultz HM, Liebscher A, Bock M (2013): Geoenergy: new concepts for utilization of geo-reservoirs as potential energy sources. Environ. Earth Sci., 70(8): pages, DOI: 10.1007/s12665-013-2877-y

Taron J and Elsworth D (2010): Coupled mechanical and chemical processes in engineered geothermal reser-voirs with dynamic permeability. Int. J. R. Mechs. 47: 1339 – 1348.

Zimmermann G, Reinicke A (2010): Hydraulic stimulation of a deep sandstone reservoir to develop an Enhanced Geothermal System: Laboratory and field experiments. Geothermics, 39(1): 70-77.

Simulation of hydro-mechanical fracture growth in single- and multi-fracture systems

Simulation hydro-mechanischer Rissausbreitung in Einzel- und Multi-Riss Systemen

C. Zeeb, D. Wolgast, H. Konietzky
Geotechnical Institut, TU Bergakademie Freiberg

Abstract

Hydraulic stimulation is commonly used to engineer the subsurface geothermal heat exchanger (SGHE), which is required for the energy production from geothermal sources. Most projects focus on enhancing preexisting fluid pathways, such as large-scale fractures or fault systems, to create a SGHE with a sufficient volume, surface area and hydraulic conductivity. Drawback of this approach is an induced seismicity with magnitudes close to or even above a tolerable threshold and often unsufficient flowrates. The seismicity can be reduced by stimulating a multitude of small-scale fractures aligned in a row. However, the process of hydraulic stimulation alters the stresses around the stimulated fracture. The presented study investigates the impact of the altered stress field on the propagation of subsequently stimulated fractures. Varying (1) the distance between injection points, (2) the angle between stimulation borehole and the minimum stress component, and (3) the fluid backflow out of finished fractures provided an optimized SGHE design. In this design the hydraulically stimulated fractures align almost perfectly and can be connected by a second borehole.

Zusammenfassung

Hydraulische Stimulation wird oft zur Erzeugung eines geothermischen Untertage Wärmetauschers (SGHE) genutzt, welcher für die Energiegewinnung aus geothermischen Quellen benötigt wird. Viele Projekte setzen ihren Schwerpunkt dabei auf die Erweiterung bereits existierender Fluidwege, wie zum Beispiel großflächige Klüfte oder Störungssysteme, um ein SGHE mit ausreichendem Volumen, sowie ausreichender Oberfläche und Durchflussrate zu erzeugen. Nachteil dieser Vorgehensweise ist eine induzierte Seismizität mit Magnituden nahe an oder sogar über einem vertretbaren Grenzwert und meist unzureichenden Fließraten. Die Seismizität kann durch die Stimulierung einer Vielzahl von in Reihe angeordneter, kleinflächiger Klüfte reduziert werden. Allerdings verändert der Prozess der hydraulischen Stimulation das Spannungsfeld um eine stimulierte Kluft. Die vorgestellte Studie untersucht den Einfluss des veränderten Spannungsfeldes auf die Ausbreitung nachfolgend stimulierter Klüfte. Die Variation (1) des Abstandes zwischen den Injektionspunkten, (2) des Winkels zwischen dem Stimulationsbohrloch und der minimalen Hauptspannung, und (3) des Fluidrückflusses aus fertiggestellten Klüften ermöglichte eine Optimierung des SGHE Designs. Für dieses Design ordnen sich die durch hydraulische Stimulation erzeugten Klüfte beinahe Perfekt an und können mit einer zweiten Bohrung angefahren werden.

1 Introduction

The profitable energy production from geothermal sources depends on many factors. One of the most important is the amount of heat extracted by means of a subsurface geothermal heat exchanger (SGHE). The efficiency of the heat extraction is influenced by the permeability and the surface area of the SGHE. The sustainability of the energy production depends on the rate of heat extraction and thus on the fluid circulation rate and on the volume of the SGHE. Therefore, the design of the SGHE and especially the geometry and the hydraulic conductivity of the fractures have a significant impact on the success of a geothermal installation.

A SGHE design depends on the encountered geological and hydrogeological conditions and varies for each geothermal installation [1] [2] [3]. For example, at Soultz-sous-Forêts [4] the SGHE consists of preexisting fluid pathways, which were reactivated and enhanced by hydraulic stimulation.

The current manuscript investigates a petrothermal system without any major preexisting fractures and negligible porosities. Therefore, the SGHE needs to be engineered by hydraulic stimulation to create a sufficient permeability in the host rock.
Previous projects illustrated the problem of induced seismicity associated with hydraulic stimulation. Especially the reactivation of preexisting large-scale fault systems, like in the case of the Deep Heat Mining Project in Basel [5], might result in seismicities with magnitudes above a tolerable threshold.

An alternative to a SGHE consisting of a few large-scale fractures is the stimulation of a multitude of small-scale fractures aligned in a row [6] [7]. Such a design reduces seismicity induced by hydraulic stimulation and allows the engineering of a SGHE with a large surface area and volume. However, such a multi-fracture approach significantly increases investment costs due to the longer boreholes and the high number of hydraulic stimulations. Moreover, a study by [8] showed that the process of hydraulic stimulation alters the stresses, thereby creating a stress shadow around fractures. This stress shadow might significantly influence the propagation of subsequentially stimulated fractures.

The current study investigates the interaction of fractures in 2D and 3D during the hydraulic stimulation of a multi-fracture SGHE for a potential site of a geothermal installation near Freiberg (Sachsen, Germany) [9]. In a first step the growth of individual fractures is investigated for the targeted geologic formation. Based on the results the models for the multi-fracture simulations were set up to study fracture alignment for different stimulation scenarios and to develop an optimized SGHE design. The simulations were carried out in 2D using the software tool UDEC™ and in 3D using the software tool 3DEC™, both of which are developed by ITASCA™.

2 Methods and materials

2.1 Description of geology

The area of Freiberg (Saxony, Germany) is used as an example location to simulate the creation of a SGHE with a multitude of fractures. The subsurface of Freiberg mainly consists of gneiss with a granite intrusion, which is believed to be situated in a depth below 4000 m and 5000 m. The previously conducted research "Tiefengeothermie Sachsen" [9] included a large-scale stress-field model of the Freiberg region revealing non-uniform stress gradients for the granite intrusion (Fig. 1). Especially the increase of σ_3 at the transitions between granite and gneiss might act as an efficient barrier against undesired fracture propagation beyond the granite.

The rock properties of the gneiss and granite were determined by laboratory measurements analyzing samples from multiple locations in Saxony. Tab. 1 summarizes the rock properties applied to the models of the subsurface below Freiberg.

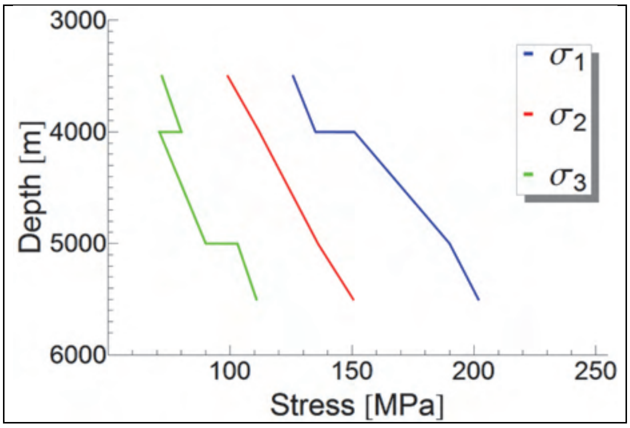

Fig. 1: Stress depth profile for Freiberg.

Tab. 1: Rock properties of granite and gneiss used in this study.

Parameter	Granite	Gneiss
Density ρ [kg m^{-3}]	2660	2700
Young's Modulus E [Pa]	6.5×10^{10}	5.5×10^{10}
Poisson's ratio υ [-]	0.22	0.30
Fracture toughness K_{IC} [Pa m$^{-0.5}$]	1.5×10^{6}	1.0×10^{6}
Tensile strength σ_t [Pa]	9.0×10^{6}	9.0×10^{6}
Cohesion C [Pa]	3.8×10^{7}	3.1×10^{7}
Friction angle φ [°]	40.8	35.5
Dilation angle ψ [°]	20	17

2.2 Model software and model setup

The hydro-mechanically coupled simulations in this study are conducted in 2D using UDEC™ and in 3D using 3DEC™, both of which are commercial software tools based on the discrete element method. Models created by both software tools consist of a variable number of rigid blocks, which become deformable after meshing. Forces are transferred between blocks via their shared contacts. Latter are described by contact-laws, for example by tensile strength, as well as normal and shear stiffness. Meshing blocks will also subdivide contacts into domains (UDEC™) or sub-contacts (3DEC™), with their length/area depending on the mesh size. For convenience we will also use the term sub-contact when referring to the domains in UDEC™. Preexisting discontinuities in a rock mass are modeled by joints, which split existing blocks thereby creating new contacts.

The blocks and contacts in models of both software tools are parameterized using properties equivalent to those of the granite and gneiss (Tab. 1), thus simulating an intact rock mass. In the current study water is used as fracturing fluid, with a density ρ of 1000 kg/m³ and a viscosity υ of 0.001 Pa s. In all models fluid may propagate only along failed sub-contacts.

Fig. 2 and Fig. 3 illustrate the model setups used for the simulation of hydro-mechanical coupled fracture simulation. The single-fracture simulations (Fig. 2a and Fig. 3a) are used to calibrate the models and to investigate the propagation of an individual fracture under the considered geologic conditions. The model setups for the multi-fracture simulations are prepared based on the results of the single-fracture simulations (Fig. 2b and Fig. 3b). Those models are then used to investigate the influence of the stress shadow around existing fractures on the growth of subsequently stimulated fractures.

The model setups for 2D simulations (Fig. 2) represent a horizontal plane in the granite in a depth of approximately 4500 m with the maximum and minimum stress components σ_1 and σ_3 set to 160 MPa and 80 MPa, respectively. The 2D single-fracture model (Fig. 2a) consists of two blocks with a predefined fracture plane in between. Latter is oriented parallel to σ_1 and the fluid is injected in the middle of the plane for 100 s with a rate of 8.3 l/s.

The 2D multi-fracture model (Fig. 2b) is build up by hexagonal blocks with an edge length of 3.5 m. Due to the hexagonal structure angles between the block edges and σ_3 are at 30° and 90°. This block structure and the small block size allow a high freedom of fracture propagation direction. The simulation involves three injection stages with the borehole parallel to σ_3 and a distance between injection points of 100 m. Fluid is injected in each stage for 50 s with a rate of 10 l/s. To reduce the required computation time hydraulic apertures are limited to 5 mm.

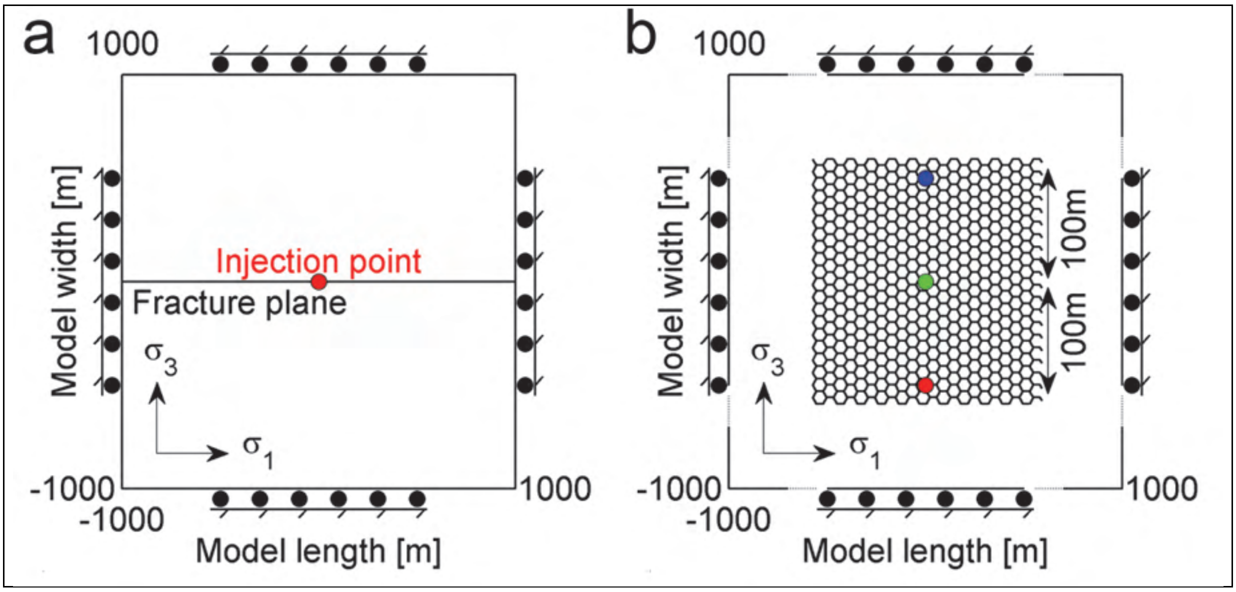

Fig. 2: 2D model setups for the simulation of hydro-mechanical coupled fracture simulation in UDEC™. The models cover a horizontal plane in a potential granite intrusion below Freiberg in a depth of 4500 m. (a) Single-fracture model consisting of two blocks with a potential fracture plane in between. (b) Multi-fracture model consisting of hexagonal blocks with an edge length of 3.5 m. The injection points are marked by the blue, green and red circles.

The model setups for the 3D simulations (Fig. 3) represent the subsurface below Freiberg in a depth between 3500 m and 5500 m. The interfaces between granite and gneiss, as well as the predefined fracture planes with their normal parallel to σ_3 are represented by joints. The stresses for the 3D models are as shown in Fig. 1. A total of 5000 m³ of fluid is injected into the predefined fracture planes in a depth of 4900 m with a rate of 5 m³/min. Assuming mirror symmetry only one half of the fracture is simulated in the 2D single-fracture model (Fig. 3a).

For the 3D multi-fracture simulations (Fig. 3b) five fracture planes are predefined and fractures are stimulated in row. A multitude of simulations were conducted optimizing fracture alignment by (1) varying the distance between the individual fractures, (2) introducing an angle between stimulation borehole and σ_3, thereby shifting injection points horizontally or vertically, and (3) varying the amount of fluid backflow out of finished fractures. The current manuscript presents the results of two simulations. In the first simulation (Sim1) the predefined fracture planes have a distance of 100 m, the stimulation borehole is oriented parallel to σ_3, and at the end of an injection stage the fluid is enclosed in the fracture. In the second simulation (Sim2) the predefined fracture planes have a distance of 200 m, the stimulation borehole is oriented horizontally with an angle between borehole and σ_3 of 45°, and the stimulation of the subsequent fracture is started after the backflow of the previous fracture is less than 0.0001 m³/s.

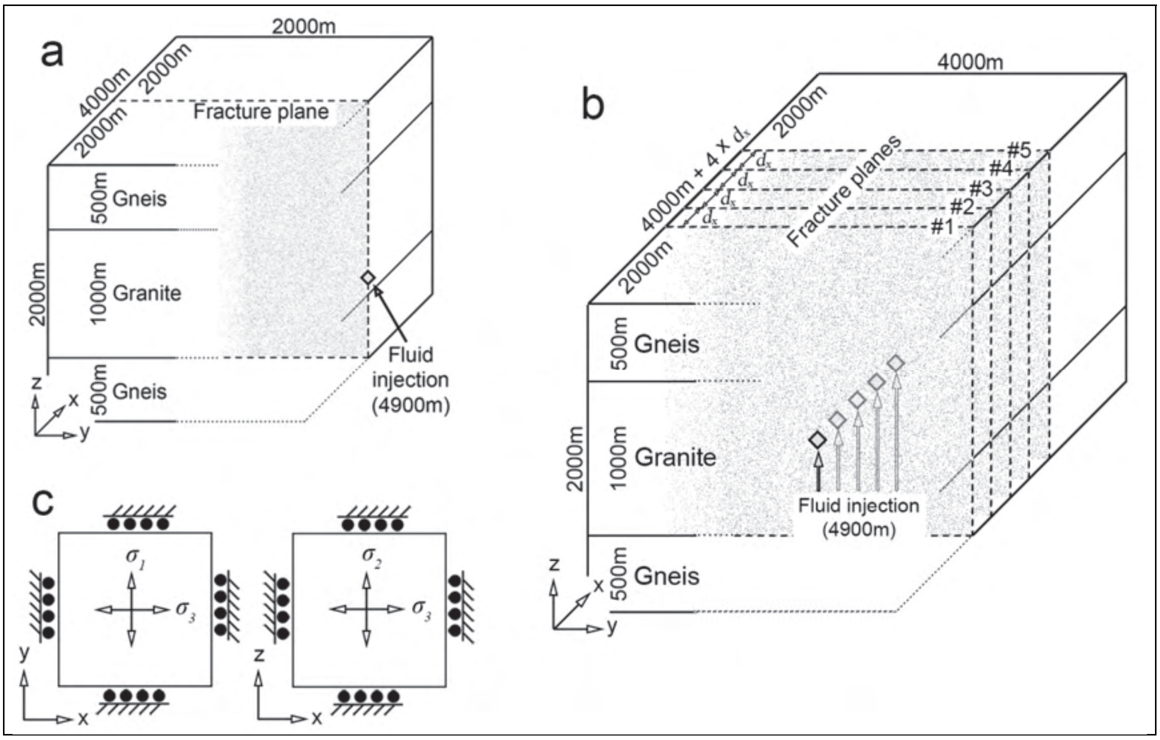

Fig. 3: 3D model setups for the simulation of hydro-mechanical coupled fracture stimulation in 3DEC™. The models cover the subsurface below Freiberg in a depth between 3500 m and 5500 m with a potential granite intrusion between 4000 m and 5000 m. (a) Single-fracture model with one predefined fracture plane and (b) multi-fracture model with five predefined fracture planes. (c) Orientation of the main stress components.

3 Results and discussion

3.1 Single-fracture simulations

Fig. 4 shows the result at the end of the 2D simulation. The fracture has a length of 295 m with an average aperture of 2.6 cm and a maximum aperture of 3.3 cm at the injection point. The stresses are significantly altered by the hydraulic fracture stimulation. In the regions parallel to the fracture an increase of σ_3 (Fig. 4; blue areas) and at the forefront of the fracture a decrease of σ_3 can be observed (Fig. 4; yellow to red areas).

Fig. 5 shows the aperture contours at the end of the 3D simulation. The fracture has a maximum length of 400 m, a height of 660 m, a total fracture area of approximately 195 000 m² and an average aperture of 2.6 cm. Predominant fracture growth direction is upwards towards lower stresses (Fig. 5; injection point as reference) and the maximum apertures of 3.5 cm are located in the upper parts of the fracture. Fig. 6 shows a 3D representation of the fracture. The three cutting planes illustrate the change of σ_3 due to the hydraulic fracture stimulation. Similar to the 2D simulation an increase of σ_3 is observed in the regions parallel to the fracture, with the maximum increase at the fracture tips, and decrease of σ_3 in the regions at the forefront of the fracture.

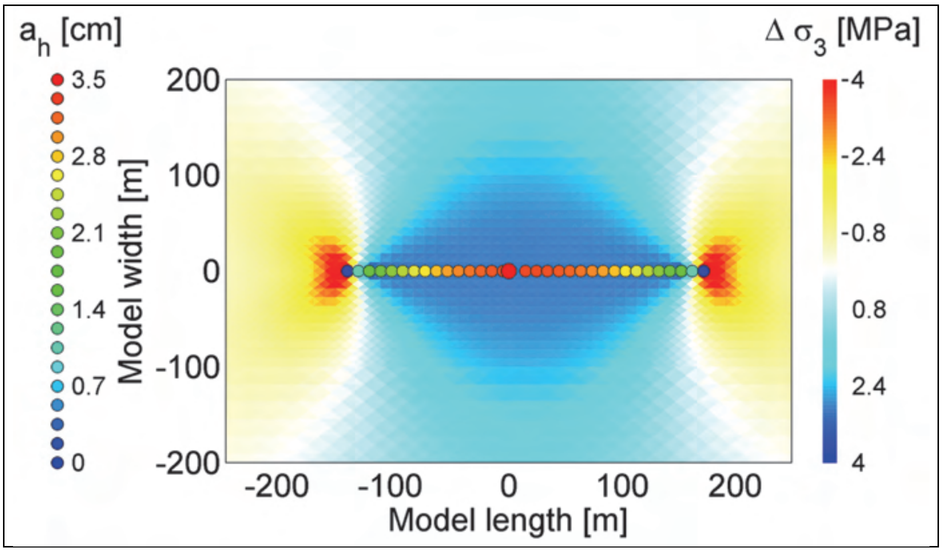

Fig. 4: 2D single fracture at the end of the simulation. Plotted is the change of the minimum stress component $\Delta\sigma_3$ due to the hydraulic stimulation, with blue colored areas marking an increase of σ_3 and red colored areas a decrease of σ_3. The big red circle marks the injection point and the smaller colored circles mark failed sub-contacts with their coloring indicating the hydraulic aperture a_h.

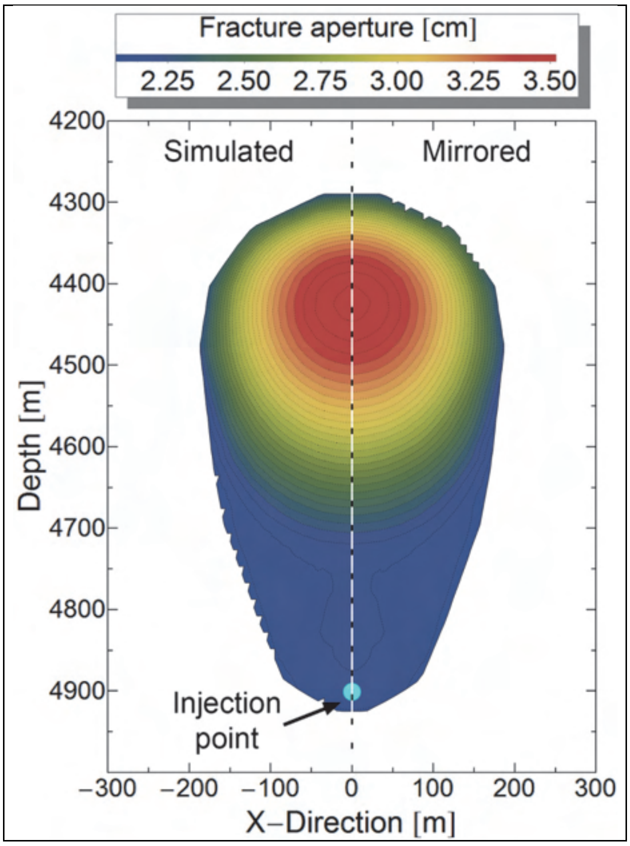

Fig. 5: Contour plot of fracture apertures at the end of the 3D simulation of the single fracture stimulation.

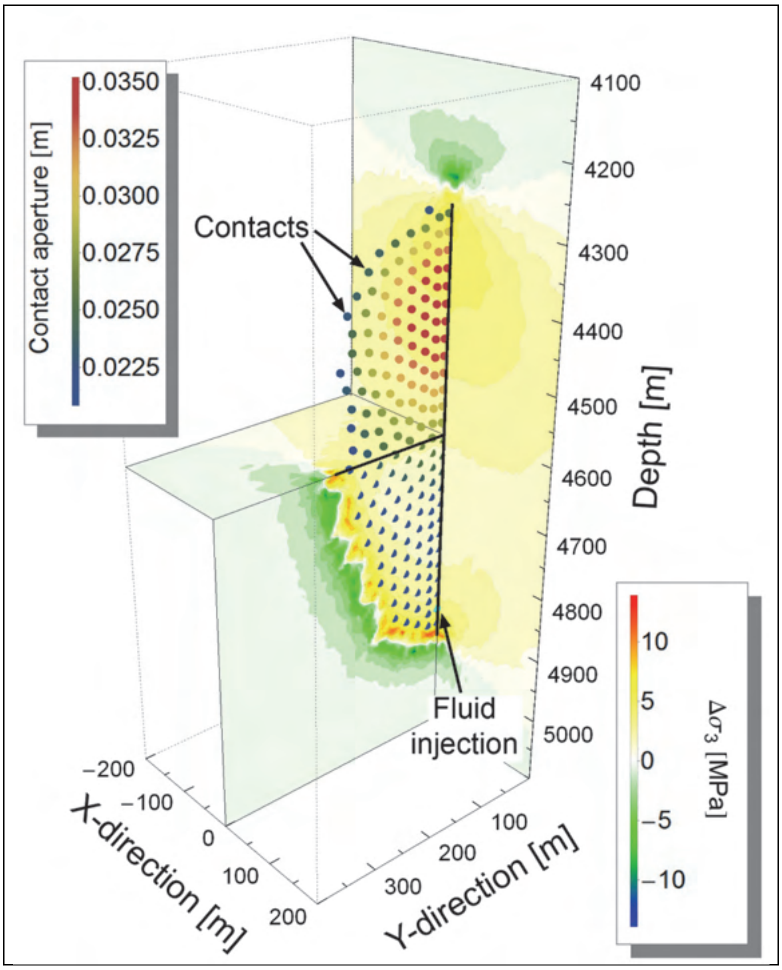

Fig. 6: 3D representation of the single fracture. The colored points represent failed sub-contacts, with the coloring indicating a sub-contacts aperture. The cutting planes indicate the change of the minimum stress component $\Delta\sigma_3$ due to the hydraulic stimulation, with yellow to red colored regions marking an increase of σ_3 and green to blue colored regions marking a decrease of σ_3. The black lines are the intersection of the fracture with the cutting planes.

Both UDEC™ and 3DEC™ provide sophisticated results for the simulation of a hydraulically stimulated fracture. The results of the 2D and the 3D simulations show an alteration of the stresses around the fracture. This stress shadowing, especially the change of σ_3, might influence the propagation of subsequently stimulated fractures.

The 3D simulation indicates a predominant fracture growth towards lower stresses. Moreover, fracture closure occurs due to the higher stresses in the lower fracture part and the fluid is pushed upwards, which leads to a fluid concentration in the upper fracture part. As a result of this process, the fluid pressure in the complete fracture depends more or less on the load (in this case σ_3) acting on the lower part of the fracture. If the fluid overpressure at the upper fracture tip is too high the fracture propagates even without the injection of new fluid. Such a self-sustaining fracture growth emphasizes the necessity of barriers, which limit fractures to the targeted geologic formation.

3.2 2D multi-fracture simulation

The 2D multi-fracture simulations were conducted to investigate the fracture growth in a stress field altered by hydraulic fracture stimulation. The hexagonal block structure provides the possibility for a fracture propagation in any direction. Fig. 7 shows the result of the multi-fracture simulation at the end of each injection stage. The fractures have a length of 74 m, 75 m and 80 m with average apertures of 2.1 cm, 2.2 cm and 2.2 cm. All fractures show some minor branching, but propagation direction is generally parallel to σ_1 and no shortcuts are created between individual fractures. Therefore, predefining fracture planes with their normal parallel to σ_3 for the 3D simulations is valid.

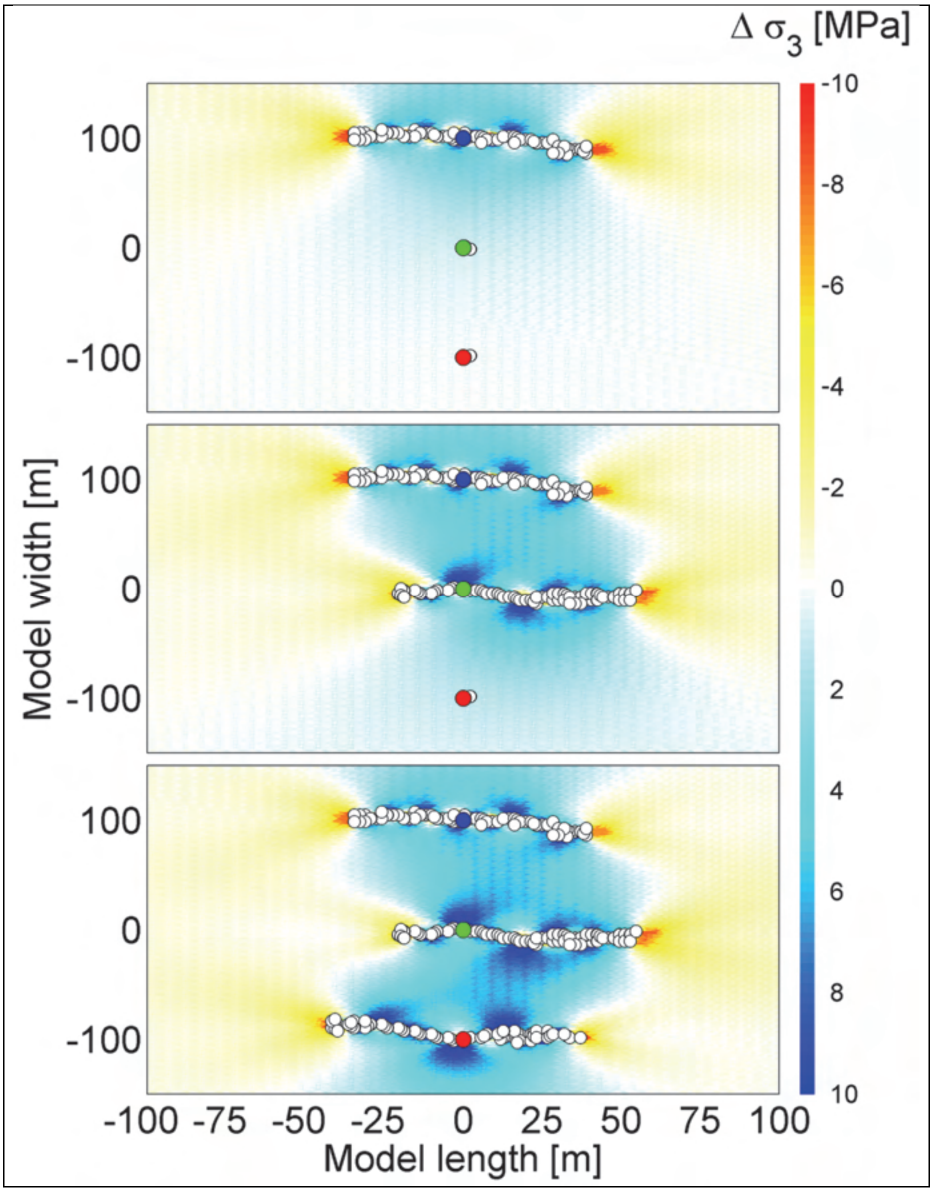

Fig. 7: Result of the 2D multi-fracture simulation at the end of each injection stage. The injection points are marked by the big blue, green and red circles. Shown are the locations of failed sub-contacts (white circles) and the change of the minimum stress component $\Delta\sigma_3$. Blue areas mark an increase and yellow to red areas a decrease of σ_3.

The second fracture grows preferentially towards the right and the third fracture is again parallel to the first fracture. This fracture deflection away from existing fractures is a result of stress shadowing around previously stimulated fractures. Since the fluid pressures required for a fracture to propagate are higher in areas with an increased σ_3 fractures tend to propagate towards lower values of σ_3.

3.3 3D multi-fracture simulation

Fig. 8 shows the change of σ_3 for the 3D multi-fracture simulation Sim1. Like in the 2D simulations the stress shadowing around existing fractures cause a deflection of subsequently stimulated fractures (Fig. 8b) away from regions with an increased σ_3. This fracture deflection results in a complex fracture alignment, which makes it nearly impossible to connect all fractures with a second borehole (Fig. 9).

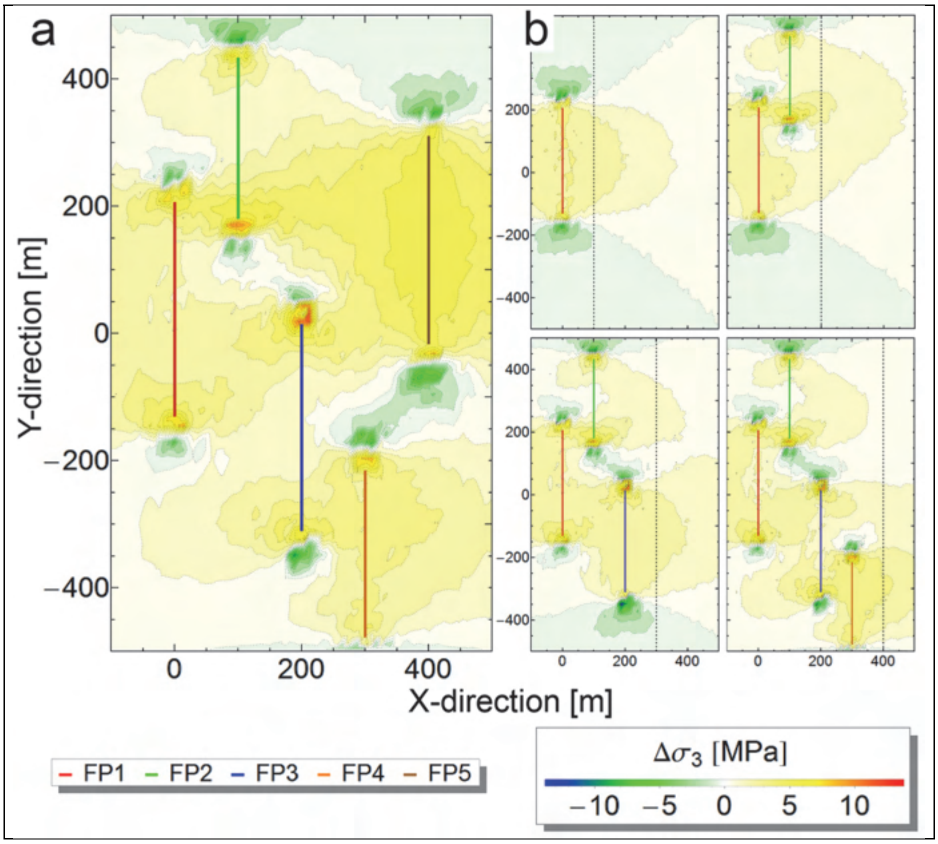

Fig. 8: Difference $\Delta\sigma_3$ between the model state before and after the hydraulic stimulation of the fractures in Sim1. The contour plot shows a horizontal cutting plane in a depth of 4500 m. a) Shows $\Delta\sigma_3$ at the end of the simulation and b) shows $\Delta\sigma_3$ before the stimulation of a subsequent fracture (dotted line) starts.

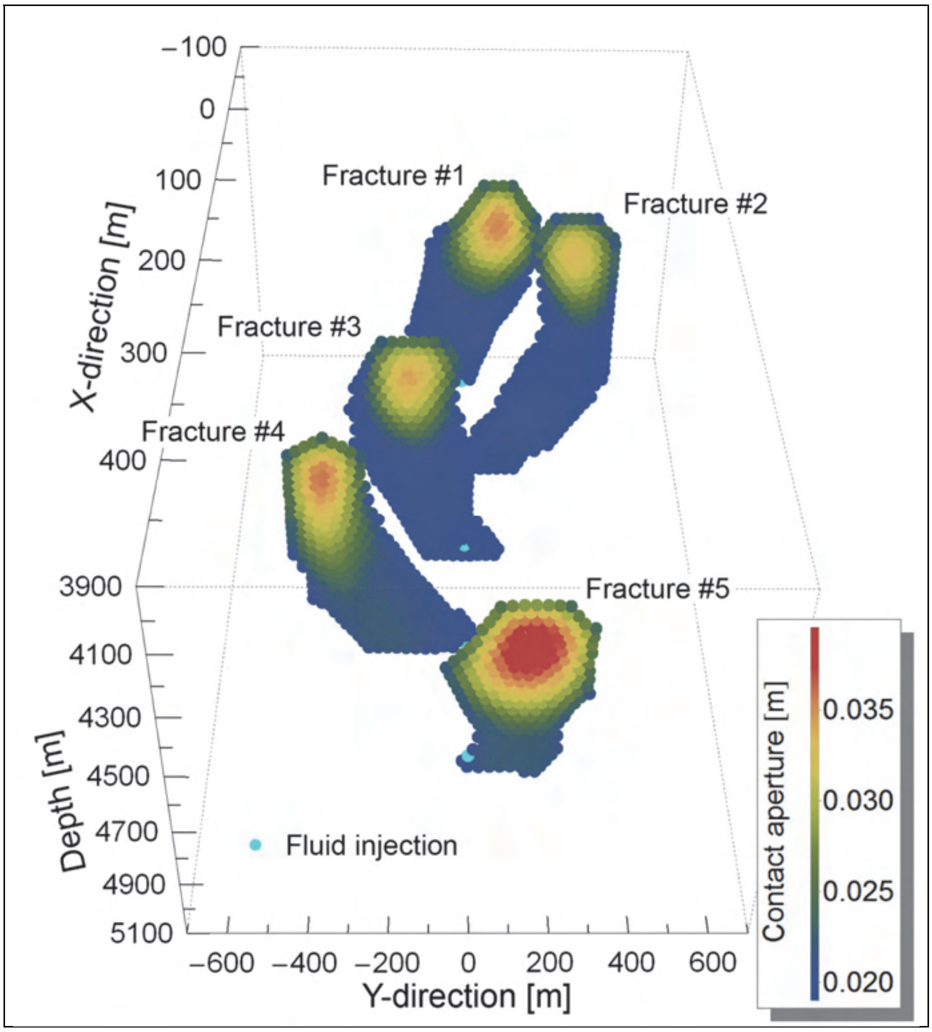

Fig. 9: 3D representation of the fractures in Sim1. The colored points represent failed sub-contacts, with the coloring indicating the sub-contacts apertures.

The results of additional simulations (not shown) revealed that higher distances between fractures and allowing fluid backflow out of finished fractures reduces the deflection of subsequently stimulated fractures. However, deflection could not be avoided completely. For Sim2 the angle between the stimulation borehole and σ_3 is set to a horizontal angle of 45°, thereby supporting a fracture deflection in one direction. Fig. 10 shows the change of σ_3 due to the hydraulic fracture stimulation for Sim2. As expected, all fractures are deflected in the same direction and the values of $\Delta\sigma_3$ are lower than those observed for Sim1 due to the fluid backflow. The 3D representation of the fractures (Fig. 11) illustrates their good alignment, which ensures the connection of all fractures with a second borehole.

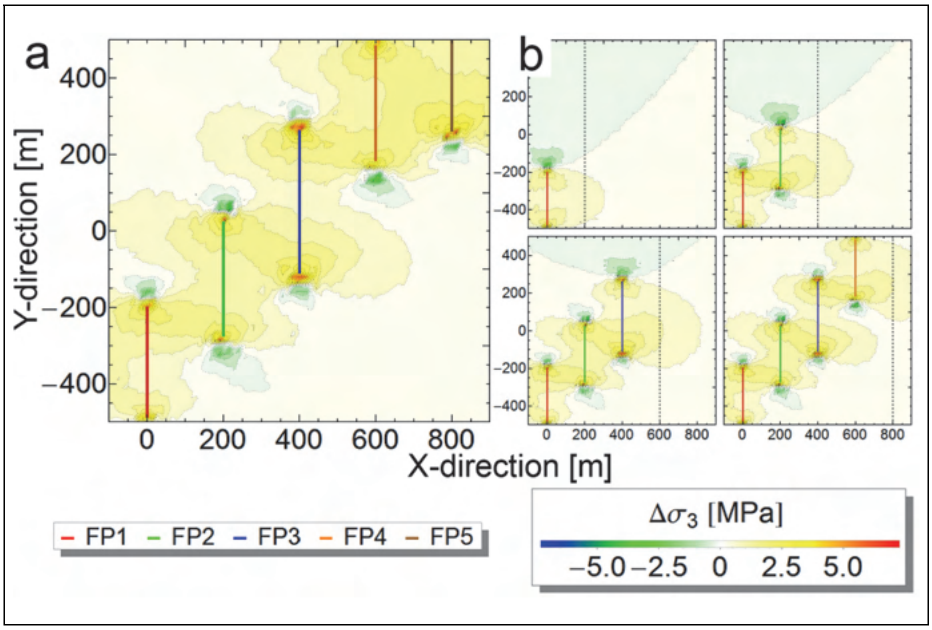

Fig. 10: Difference $\Delta\sigma_3$ between the model state before and after the hydraulic stimulation of the fractures in Sim2. The contour plot shows a horizontal cutting plane in a depth of 4500 m. a) shows $\Delta\sigma_3$ at the end of the simulation and b) shows $\Delta\sigma_3$ before the stimulation of a subsequent fracture (dotted line) starts.

Tab. 2: Fracture geometries for the two 3D multi-fracture simulations Sim1 and Sim2. The lengths and heights are the distance between the leftmost and rightmost, or respectively highest and lowest failed sub-contact in the corresponding fracture plane.

Simulation #			1					2		
Fracture #	1	2	3	4	5	1	2	3	4	*5*[A]
Length [m]	445	474	451	510	388	346	376	395	375	*505*
Height [m]	773	952	811	783	639	842	771	745	712	*825*
Area ($\times 10^3$) [m^2]	203	225	219	209	175	206	192	190	191	*230*
Av. Aperture [cm]	2.4	2.2	2.3	2.4	2.8	1.2	1.2	1.2	1.2	*1.2*
Max. aperture [cm]	3.5	3.3	3.4	3.6	4.0	1.2	1.2	1.2	1.3	*1.3*

[A] Fracture 5 of Sim2 grew into a model region with a rougher mesh and is therefore neglected.

Tab. 2 summarizes the geometries for the fractures generated in the two simulations. For Sim1 fracture lengths vary by 122 m and fracture heights by 313 m. These significant differences in fracture lengths and heights are a result of the strong fracture deflection observed for Sim1. Similar to the results of the single-fracture simulation maximum fracture apertures are located in the upper fracture parts.

Neglecting fracture #5, which grew into a region with a rougher mesh size, in Sim2 fracture lengths vary only by 49 m and heights by 130 m. The lower differences in fracture length and height agree with the good fracture alignment. As a result of the fluid backflow fracture apertures are significantly lower for Sim2.

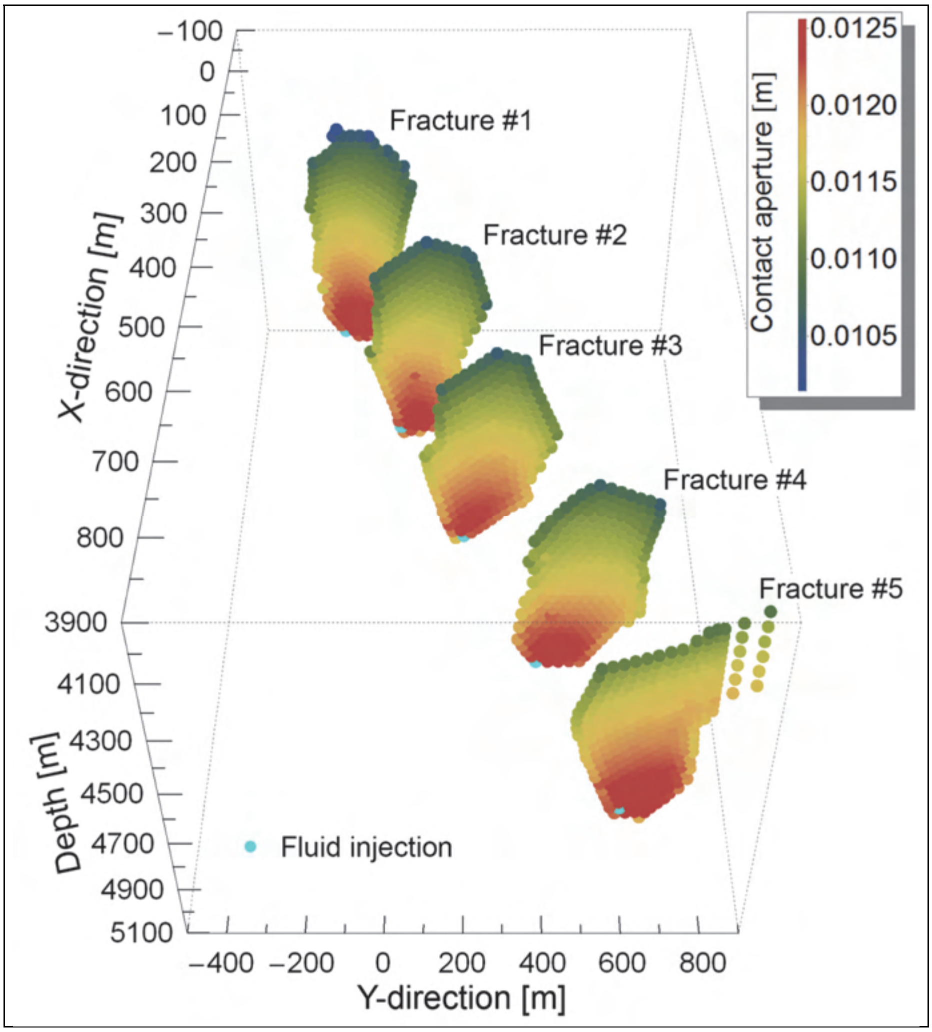

Fig. 11: 3D representation of the fractures in Sim2. The colored points represent broken contacts, with the coloring indicating the sub-contacts apertures. Note, that fracture #5 grew into a model region with a rougher mesh.

4 Conclusions

The current study investigated the alteration of the stress field due to hydraulic fracture stimulation applying 2D and 3D simulations with the aim of optimizing fracture alignment in a subsurface geothermal heat exchangers consisting of a multitude of fractures. The simulations were carried out using the 2D software tool UDEC™ and the 3D software tool 3DEC™, both of which provided sophisticated results.

Simulating the stimulation of a single fracture in 2D and 3D revealed a considerable alteration of the stresses around the stimulated fracture, with a significant increase of σ_3 in regions parallel to the fracture and a decrease of σ_3 at the forefront of the fracture. In addition, the 3D simulation showed that the predominant fracture propagation direction is towards lower stresses.

The 2D multi-fracture simulations investigated the fracture interaction with focus on fracture propagation directions and the potential development of shortcuts between individual fractures. The simulation results illustrate that for the given stresses fractures align parallel to σ_1 and no shortcuts are created.

Both, the 2D and the 3D multi-fracture simulations showed a deflection of fractures away from regions with an increased σ_3 around previously stimulated fractures. Especially the 3D simulation Sim1 illustrates well the problem of connecting the deflected fractures with a second borehole. Additional simulations showed that a fracture deflection cannot be avoided completely. However, a preferable fracture alignment was obtained for Sim2 by orienting the stimulation borehole at a horizontal angle of 45° towards σ_3, thereby supporting a deflection of all fractures in one direction.

Acknowledgement

The presented results are part of the research conducted within the ‘MultiRiss’ and ‘OptiRiss’ projects at the Geotechnical Institute, TU Bergakademie Freiberg. MultiRiss is funded by the „Bundesministerium für Wirtschaft und Energie aufgrund eines Beschlusses des Deutschen Bundestages“. OptiRiss is funded by the „Europäischer Fonds für Regionale Entwicklung“ through the „Sächsiche Aufbaubank“.

References

1 Legarth, B., Huenges, E., Zimmermann, G., 2005. Hydraulic fracturing in a sedimentary geothermal reservoir: Results and implications. International Journal of Rock Mechanics & Mining Sciences, v. 42, p. 1028-1041.

2 Genter, A., Evans, K., Cuenot, N., Fritsch, D., Sanjuan, B., 2010. Contribution of the exploration of deep crystalline fractured reservoir of Soultz to the knowledge of enhanced geothermal systems (EGS). Comptes Rendus Geoscience, v. 342, p. 502-516.

3 Xie, L., Min, K.-B., Song, Y., 2014. Observations of hydraulic stimulations in seven enhanced geothermal system projects. Renewable Energy (in press).

4 Sausse, J., Dezayes, C., Dorbath, L., Genter, A., Place, J., 2010. 3D model of fracture zones at Soultz-sous-Forêts based on geological data, image logs, induced microseismicity and vertical seismic profiles. Comptes Rendus Geoscience, v. 342, p. 531-545.

5 Deichmann, N., Kraft, T., Evans, K. F., 2014. Identification of faults activated during the stimulation of the Basel geothermal project from cluster analysis and focal mechanisms of larger magnitude events. Geothermics, v. 52, p. 84-97.

6 Jung, R., 1986. Erzeugung eines großflächigen künstlichen Risses im Falkenberger Granit durch hydraulisches Spalten und Untersuchung seiner mechanischen und hydraulischen Eigenschaften (Generation of a large-scale artificial fracture in the Falkenberger Granite by means of hydraulic fracturing and investigation of the fractures mechanical and hydraulic properties). Berichte des Institutes für Geophysik, Ruhr-Universität Bochum, Germany.

7 Kappelmeyer, O., Jung, R., 1987. HDR Experiments at Falkenberg/Bavaria. Geothermics, v. 16, p. 375-392.

8 Bunger, A.P., Zhang, X., Jeffrey, R.G., 2012. Parameters Affecting the Interaction Among Closely Spaced Hydraulic Fractures. Society of Petroleum Engineers, SPE 140426.

9 Tiefengeothermie Sachsen. Landesamt für Umwelt, Landwirtschaft und Geologie, Freistaat Sachsen. Schriftenreihe, Heft 9/2011.

More articles

Simulation of heterogeneity and fracturing in loaded Lac du Bonnet granite

Simulation der Heterogenität und Rissbildung im belasteten Lac du Bonnet-Granit

W. Chen, H. Konietzky
TU Bergakademie Freiberg, Geotechnical Institute, Germany

Abstract

A grain-based heterogeneous numerical model originated from the Discrete Element Method is developed and applied for Lac du Bonnet granite. Basing on Voronoi cells, the modelled microstructure considers different mineral components and grain size. Grains are composed of elastic basic elements. Intra- and inter-granular contacts are elasto-plastic. Inter- and intra-granular micro-fracturing and lifetime prediction are based on subcritical crack growth. The procedure is successfully applied to simulate uniaxial compression tests, Brazilian tests, uniaxial creep tests as well as fracture toughness tests for Mode-I and Mode-II. The proposed modelling allows the simulation of time-dependent behaviour in terms of the damage process during primary, secondary and tertiary creeps phase until final failure characterized by macroscopic fracturing (shear band and/or macroscopic tensile fracture). Simulations have shown reasonable agreement with macroscopic observations obtained from lab tests on granite, but have in addition delivered deeper insight into the microscopic damage process and allow time-to-failure predictions. The proposed modelling approach is recommended for brittle rocks.

Zusammenfassung

Mittels der Diskreten Elemente Methode wurde ein heterogenes Modell für den Lac du Bonnet Granit auf der Kornebene entwickelt. Die modellierte Mikrostruktur berücksichtigt die verschiedenen Mineralkomponenten sowie die Korngrößen auf Basis von Voronoi-Zellen. Die Gesteinskörner bestehen aus elastischen Basiselementen. Inter- und intra-granulare Kontakte sind elasto-plastischer Natur. Die Entwicklung von inter- und: intra-granularen Mikrobrüchen sowie die Lebensdauerprognose basieren auf sub-kritischem Risswachstum. Die Methode wurde erfolgreich zur Simulation von einaxialen Druckversuchen, dem Brazilian-Test, einaxialen Kriechversuchen sowie Bruchzähigkeitstests für Mode-I und Mode-II angewandt. Die vorgeschlagene Modellierungsstrategie erlaubt die Simulation des zeitabhängigen Verhaltens in Form des Schädigungsprozesses mit primärer, sekundärer und tertiärer Kriechphase bis hin zum makroskopischen Bruch (Scherband und/oder makroskopischer Zugbruch). Die Simulationen haben gute Übereinstimmung mit den makroskopischen Beobachtungen bei Laborversuchen am Granit gezeigt, liefern aber zusätzlich einen tieferen Einblick in den mikroskopischen

Schädigungsprozess und erlauben Lebensdauerprognosen. Die vorgeschlagene Modellierungsmethodik wird für spröde Gesteine empfohlen.

1 Introduction

Geomaterials and brittle rocks in particular have a complex mechanical behaviour which is related to its internal microstructure (e.g. Hallbauer et al., 1973). This internal microstructure is governed by different mineral grains and microdefects, which produce heterogeneity (e.g. Lan et al., 2010). In addition, the behavior of rocks is often characterized by time dependency, nonlinear failure envelopes and a high ratio of uniaxial compression strength to tensile strength (e.g. Hoek, 1983). It has been documented that sophisticated numerical methods can be used to analyse the damage and fracture behavior of brittle rocks with such characteristics (e.g. Liu et al., 2004; Groh et al., 2011).

In addition to the microdefects the heterogeneity of crystalline rocks at the microscopic scale is primarily governed by the variation in grain size, shape and mineral composition (e.g. Blair and Cook, 1998; Lan et al., 2010, Groh et al., 2011). The Voronoi tessellation technique is suited to build-up grain-based anisotropic models. Models based on Voronoi tessellation could describe not only the micro-mechanical phenomena but also duplicate the macroscopic response (e.g. Espinosa and Zavattieri, 2003; Li et al., 2006; Lan et al., 2010).

Besides the above-mentioned aspects, time-dependent strength and deformation of rocks are important, especially for long-term stability and safety considerations of geotechnical structures such as mines, underground tunnels, nuclear waste repositories or slopes.

Time dependent deformation of brittle rocks is mainly caused by subcritical crack growth which can be explained by the theory of stress corrosion, considering that strained atomic bonds at crack tips may break by the influence of environmental agents and thermal fluctuations (Potyondy, 2007; Rinne, 2008). Subcritical crack growth takes places at extremely low velocities. Whenever the fracture toughness has been reached - either by reaching a critical crack length or a critical load level - the crack growth velocity suddenly approaches values close to the ultrasonic wave speed, which may cause sudden failure. During this process microcracks will interact, connect and form macroscopic fractures or shear bands as a result of damage accumulation. Therefore, the investigation of subcritical crack growth is the key to evaluate the long-term stability of rocks (Lockner and Madden, 1991; Konietzky et al., 2009; Ko and Kemeny, 2013; Li and Konietzky, 2013).

So far the different aspects mentioned above were simulated in an isolated manner by different approaches. The approach presented within this paper combines the explicit consideration of heterogeneity, creep and damage evolution at the grain size level up to final failure including the time-to-failure prediction. The proposed procedure is applied for well investigated Lac du Bonnet (LdB) granite. Lab results obtained from uniaxial compression tests, Brazilian tests and fracture toughness tests are used to calibrate and validate the elasto-plastic model parameters. Creep

tests at different load levels are used to determine the parameters for the subcritical crack growth law.
The numerical simulations were performed with the Discrete Element Code UDEC by extensive usage of the internal programme language in order to implement the constitutive laws.

2 Time independent rock behaviour

In this section, the effect of heterogeneity of the rock at the grain size level on the process of crack initiation, growth and coalescence is investigated. First, the Voronoi based numerical model set-up is explained, followed by a series of simulations to model different lab tests for LdB granite. The constitutive behaviour of the model is governed by two types of constitutive laws: the matrix laws for the grains itself and the contact laws at inner and outer grain boundaries, which control the interaction between the grains and internally inside the grains.

2.1 Grain-based heterogeneous model

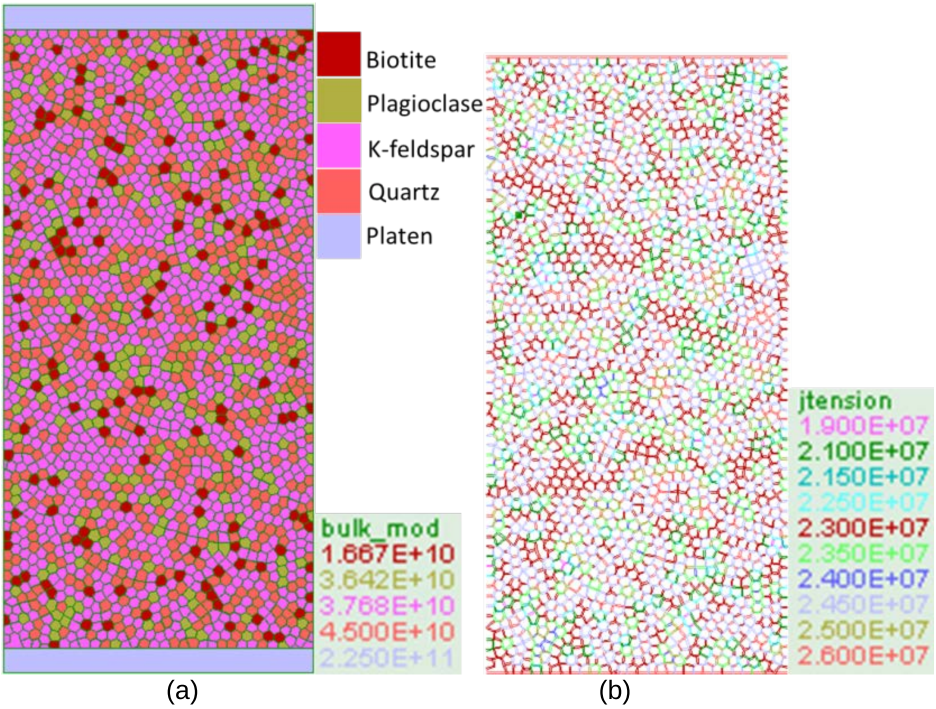

Fig. 1: Model set-up: (a) Voronoi blocks representing different minerals, (b) internal and external grain contacts.

The mineral composition of LdB granite is characterized by 7.1 % biotite, 51.1 % K-feldspar, 31.8 % quartz and 10 % plagioclase. The smallest grains have a diameter of about 1 mm. They are randomly distributed within a piece of rock.

The numerical model was created by Voronoi cells with equivalent diameter of about 1 mm. The percentages of the mineral components were considered and the allocation was performed in a random manner, so that automatically also bigger grains were produced, so that the model also matches the grain size distribution in an approximate manner (Fig. 1). The Voronoi cells themself are unbreakable and behave elastically. The parameters for the mineral components and Voronoi cells, respectively, are given in Table 1.

Tab. 1: Grain parameters (Bass, 1995; Chen et al., 2004; Qinglei et al., 2012)

Mineral	Elastic Modulus [GPa]	Poisson's Ratio
Biotite	35	0.25
K-feldspar	62	0.27
Quartz	91	0.20
Plagioclase	69	0.23

The contact behaviour is elasto-plastic and characterized by a Mohr-Coulomb failure criterion with tension cut-off and softening (Fig. 2). For each mineral component a corresponding set of contact parameters is specified (Table 2). At the contacts between the grains the arithmetic average of the parameters is applied. In the normal and shear direction, the stress-displacement relation below the strength limit at the contacts is assumed to be linear and governed by the normal stiffness k_n and the shear stiffness k_s. If the tensile strength is reached, the contact breaks and the tensile strength is set to zero. If the shear strength is reached, sudden softening takes place and cohesion and friction of the contact are set to residual values. Eqs. (1) and (2) describe the contact behaviour:

$$\begin{cases} \sigma_n = -k_n u_n \\ if\ \sigma_n < -J^T, \sigma_n = J_r^T = 0 \end{cases} \tag{1}$$

$$\begin{cases} \tau_s = k_s u_s \\ \tau_{max} = J^C + \sigma_n \tan\phi \\ if\ |\tau_s| \geq \tau_{max}, \tau_s = sign(\Delta u_s) \cdot \left(J_r^C + \sigma_n \tan\phi_r\right) \end{cases} \tag{2}$$

where σ_n and τ_s are normal stress and shear stress, respectively, u_n and u_s are normal displacement and shear displacement, respectively, J^T and J_r^T are tensile strength and residual tensile strength, respectively, $\tau_{\max}$ is shear strength, J^C and J_r^C are cohesive strength and residual cohesive strength, respectively, φ and φ_r are friction angle and residual friction angle, respectively, and Δu_s is the incremental contact shear displacement.

Within the model the damage and fracture process associated with plastic deformations is controlled by the breakage of contacts and relative movement along or across them.

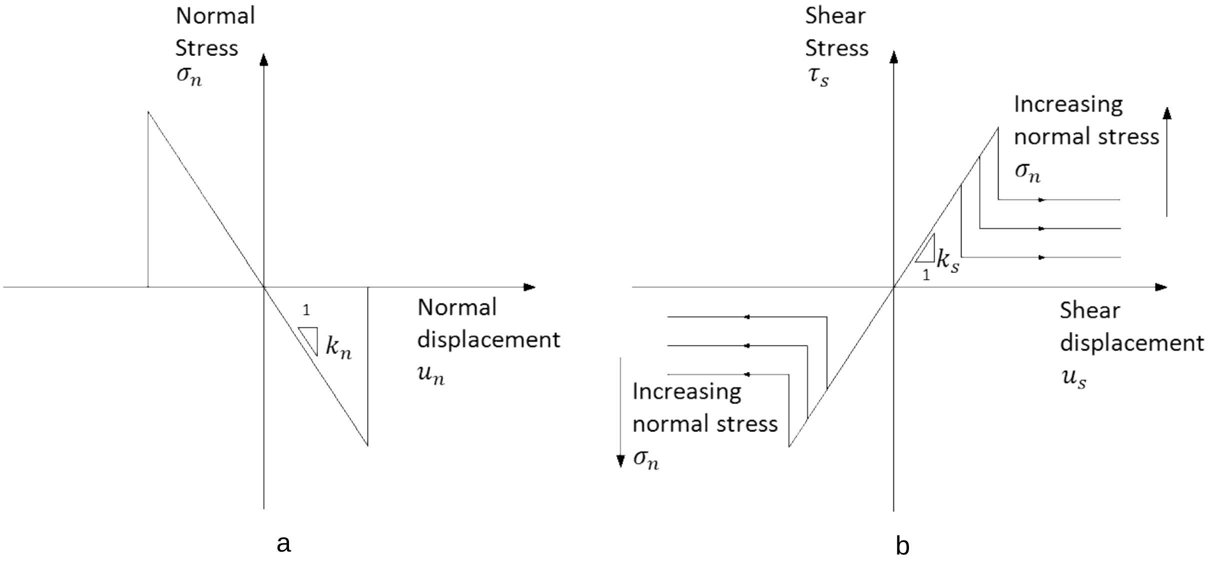

Fig. 2: Elasto-plastic contact behavior with softening: (a) in normal direction, (b) in shear direction.

Tab. 2: Contact parameters (result of own calibration)

Contact	k_n [Pa/m]	$\frac{k_s}{k_n}$ [-]	J^T [MPa]	J_r^T [MPa]	J^C [MPa]	J_r^C [MPa]	φ [°]	$\frac{\varphi_r}{\varphi}$ [-]
Biotite/Biotite	4.20E+14	1	19	0	37	0	48	0.5
K-feldspar/K-feldspar	7.75E+14	1	23	0	52	0	55	0.5
Quartz/Quartz	1.01E+15	1	26	0	62	0	62	0.5
Plagioclase/Plagioclase	8.00E+14	1	24	0	57	0	59	0.5
Biotite/K-feldspar	5.97E+14	1	21	0	44.5	0	51.5	0.5
Biotite/Quartz	7.16E+14	1	22.5	0	49.5	0	55	0.5
Biotite/Plagioclase	6.10E+14	1	21.5	0	47	0	53.5	0.5
K-feldspar/Quartz	8.93E+14	1	24.5	0	57	0	58.5	0.5
K-feldspar/Plagioclase	7.87E+14	1	23.5	0	54.5	0	57	0.5
Quartz/Plagioclase	9.06E+14	1	25	0	59.5	0	60.5	0.5

2.2 Modelling of uniaxial compression tests

Through uniaxial compression tests, not only uniaxial compressive strength (UCS), but also Young's modulus and Poisson's ratio, were obtained. The height and the diameter of numerical model are 63.4 mm and 31.7 mm, respectively (Fig. 1 and 4). Friction angle between loading plates and sample is 25 °. Elastic constants were determined when vertical stress has reached 50% of UCS. Fig. 3 shows the stress strain curve for the Granite model as well as for artificial equivalent homogeneous models, which consist only of Biotite and Plagioclase. The homogeneous models show linear behaviour up to the peak load, whereas the heterogeneous model (Granite) reveals non-linearity already well before the peak load is reached, which clearly documents the influence of heterogeneity on the damage process. This feature is illustrated in Fig. 4 for several load levels according to Fig. 3. Based on the stress strain curve UCS and elastic constants for the modelled Granite were calculated:

$$\begin{cases} \sigma_c = 234.5\,MPa \\ \mu = \varepsilon_b / \varepsilon_a = 0.523/1.646 = 0.32 \\ E_0 = 0.5\sigma_c/\varepsilon_a = 117.25/1.646 = 71.2\,GPa \end{cases} \quad (3)$$

Where σ_c is UCS, E_0 is Young's modulus, ε_a and ε_b are vertical and lateral strains at 50% UCS, respectively, μ is Poisson's ratio.

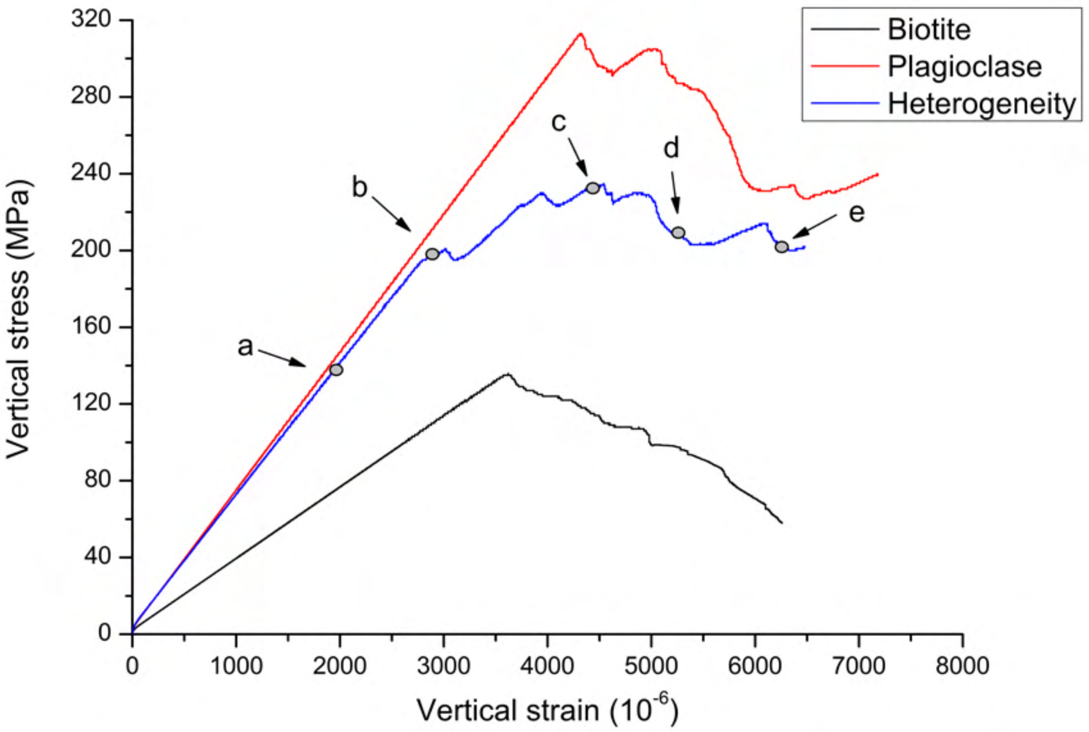

Fig. 3: Stress-strain curves of uniaxial compression tests.

Fig. 4a shows the nearly pure elastic response. As shown in Fig. 4b, at higher load level many cracks emerge first at the grain boundaries between different minerals and only very few cracks occur inside the quartz. However, if the crack tip of formed large cracks reach the high-strength quartz the crack will propagate through the quartz also (Fig. 4b and 4c). With increasing load, cracks propagate, coalesce and form macroscopic tensile fractures (axial splitting) and shear bands (Fig. 4d and 4e). Finally, a macroscopic shear band penetrating the whole sample with inclination of about 60 ° to the vertical is observed.

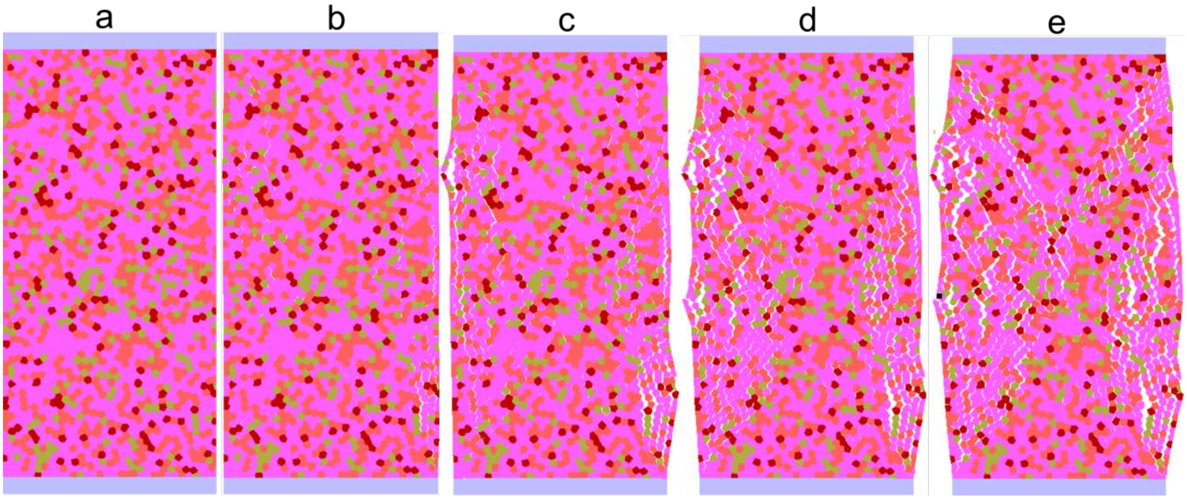

Fig. 4: Uniaxial compression test: damage state at different stress levels according to Fig. 3.

2.3 Modelling of Brazilian tests

According to Jianhong et al. (2009), the elastic solution for the stress field of a 2-dimensional disc under compressive load as shown in Fig. 5 is given by Eqs. (4) to (6):

$$\sigma_x = \frac{2P}{\pi B}\left(\frac{\sin^2\theta_1\cos\theta_1}{r_1}+\frac{\sin^2\theta_2\cos\theta_2}{r_2}\right)-\frac{2P}{\pi dB} \tag{4}$$

$$\sigma_y = \frac{2P}{\pi B}\left(\frac{\cos^3\theta_1}{r_1}+\frac{\cos^3\theta_2}{r_2}\right)-\frac{2P}{\pi dB} \tag{5}$$

$$\tau = \frac{2P}{\pi B}\left(\frac{\cos^2\theta_1\sin\theta_1}{r_1}+\frac{\cos^2\theta_2\sin\theta_2}{r_2}\right) \tag{6}$$

where σ_x and σ_y are stresses in x and y direction, respectively. τ is shear stress, P is applied load, B and d are thickness and diameter of the disc, respectively. θ_1 and θ_2 are angles shown in Fig. 5. When point A is located on the BC line, θ_1 and θ_2 are zero. Then, Eqs. (4) and (5) result in Eqs. (7) and (8).

$$\sigma_x = -\frac{2P}{\pi dB} \tag{7}$$

$$\sigma_y = \frac{2P}{\pi B}\left(\frac{1}{r_1} + \frac{1}{r_2}\right) - \frac{2P}{\pi dB} \tag{8}$$

Hence, a tensile stress σ_x is generated along the loading line. For rock material whose tensile strength is far smaller than compressive strength, this tensile stress will cause tensile failure along the loading line (BC). Consequently, the tensile strength is the absolute value calculated by Eq. (7) with P as maximum force.

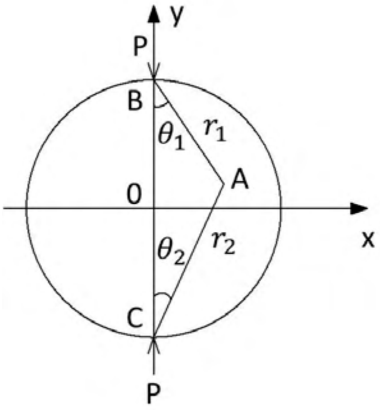

Fig. 5: Sketch of Brazilian disc.

In the numerical model, the diameter of Brazilian disc is 50 mm. All other parameters are the same as for the uniaxial compression tests and are given in Table 1 and 2. Fig. 6 shows the recorded load-strain curves. There is a nearly linear elastic deformation in the region before stage ‘a’ is reached. Post-failure characteristics are recorded after stage ‘c’ is reached. Up to stage ‘a’ the lateral strain increases slowly (only minor crack propagation). After stage ‘b’ has been reached a rapid increase in fracture propagation combined with significant dilation is observed (Fig. 7). According to Eq. (7) the tensile strength was calculated:

$$\sigma_t = |\sigma_x| = \frac{2 \times 863000}{\pi \times 0.05 \times 1} = 11.0\ MPa \tag{9}$$

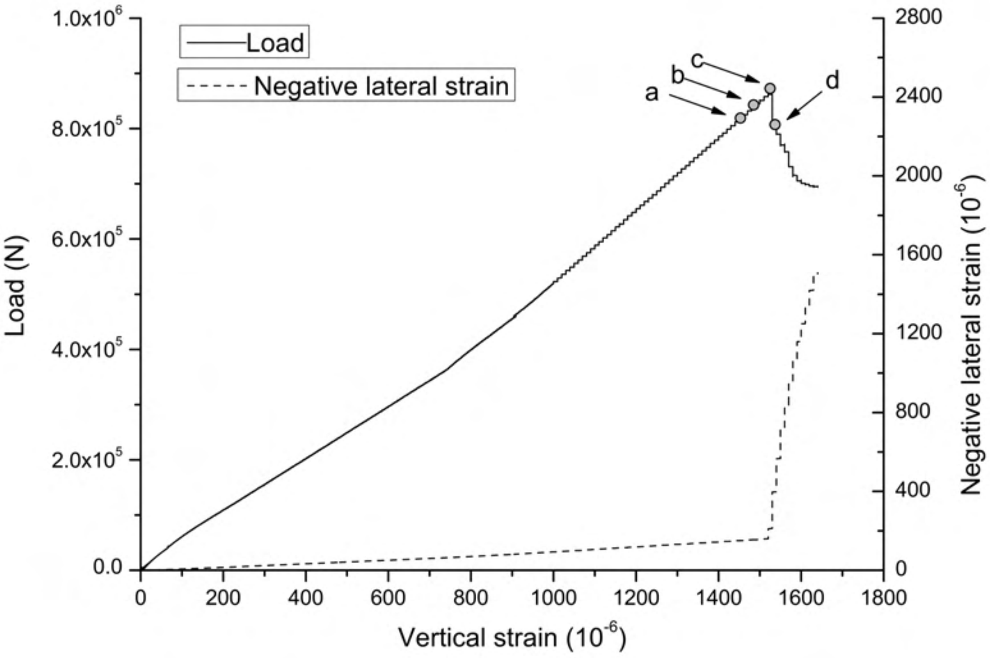

Fig. 6: Brazilian test: Load and strain curves.

The numerical simulations provide a straightforward view on the progressive fracturing process during the Brazilian test as shown in Fig. 7. First, the cracks emerge at both load entry points between the loading plate and disc (Fig. 7a). Later a macroscopic crack extends from the lower end and propagates until the disc is broken (Fig. 7b to 7d). Because of the heterogeneity the fracture pattern slightly deviates from the idealized shape given in Fig. 5, but is in full agreement with the observations in the lab, which show two typical damage pattern: local shear failure close to the load entry points and large tensile fracturing between the two load entry points with some surface irregularities and bifurcation depending on the degree of inhomogeneity. Again, cracks develop preferred as intra-granular cracks and to a lower extent as inter-granular cracks.

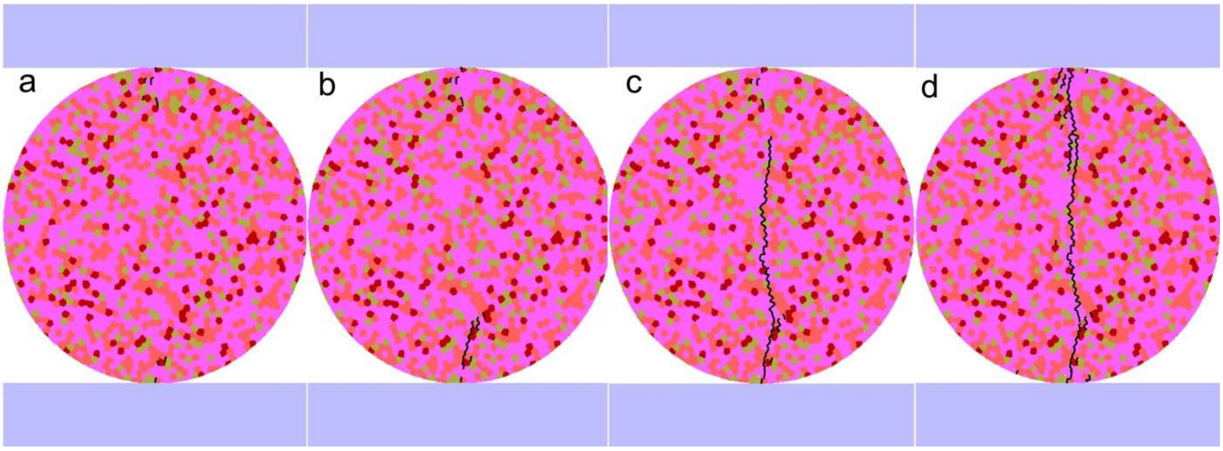

Fig. 7: Brazilian test: damage state at different load levels according to Fig. 6.

2.4 Modelling of Mode-I and Mode-II fracture toughness tests

Since the fracture toughness test using disc specimen was proposed by Awajih & Sato (1978), lab tests, numerical simulations and further theoretical developments were carried out by many researchers (Sanchez, 1979; Atkinson et al., 1982; Chen et al., 1998; Al-Shayea et al., 2000; Liu et al., 2007). Atkinson et al. (1982) have deduced explicit solution for stress intensity factors for the central cracked Brazilian Disc (CCBD) under load (Fig. 8), especially for 'short crack' (crack length to specimen radius less than 0.3):

$$K_{\mathrm{I}} = \frac{P\sqrt{a}}{\sqrt{\pi}RB} N_{\mathrm{I}} \tag{10}$$

$$K_{\mathrm{II}} = \frac{P\sqrt{a}}{\sqrt{\pi}RB} N_{\mathrm{II}} \tag{11}$$

where K_{I} and K_{II} are stress intensity factors for Mode-I and Mode-II, respectively. a is half-crack length, P is load, R is radius of specimen, B is thickness of the specimen, N_{I} and N_{II} are non-dimensional coefficients depending on the specimen and crack dimensions as well as crack orientation.

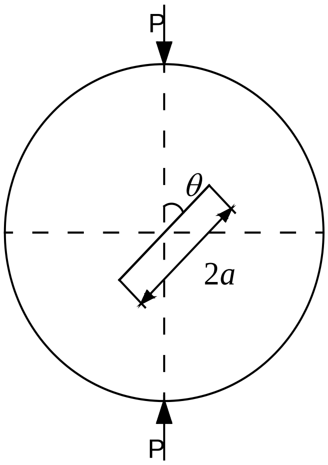

Fig. 8: Sketch for CCBD specimen.

For $a/R = 0.3$, Atkinson et al. (1982) have deduced approximate equations for N_{I} and N_{II}:

$$N_I = 1 - 4\sin^2\theta + 4\sin^2\theta\left(1 - 4\cos^2\theta\right)\left(\frac{a}{R}\right)^2 \tag{12}$$

$$N_{II} = \left[2 + \left(8\cos^2\theta - 5\right)\left(\frac{a}{R}\right)^2\right]\sin 2\theta \tag{13}$$

where θ is the angle between crack orientation and loading direction.

As N_{I} and N_{II} change with θ, for special values of θ the values for N_{I} or N_{II} can be zero. Fig. 9 shows the functions N_{I} and N_{II} for $a/R = 0.3$. When $\theta = 0^\circ$, that means $N_{\mathrm{I}} = 1$ and $N_{\mathrm{II}} = 0$, pure Mode-I conditions exist. When $\theta = 27.2^\circ$, that means $N_{\mathrm{I}} \approx 0$ and $N_{\mathrm{II}} = 1.72342$, pure Mode-II conditions exist.

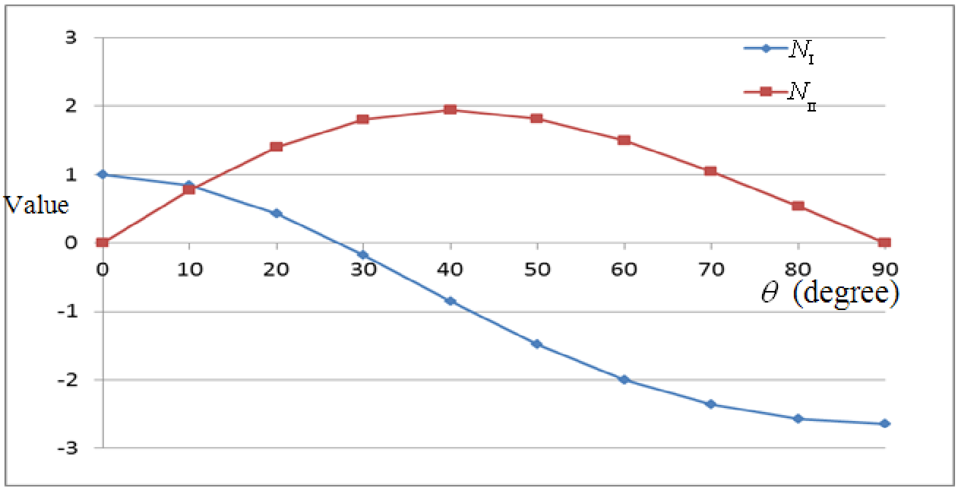

Fig. 9: N_{I} and N_{II} versus θ for $a/R = 0.3$.

According to parameters given in Table 1 and 2, numerical models to simulate CCBD Mode-I and Mode-II fracture toughness tests were built for different θ. The disc diameter is 75 mm and the length of the central crack is 22.5 mm. The corresponding load-strain curves are shown in Fig. 10.

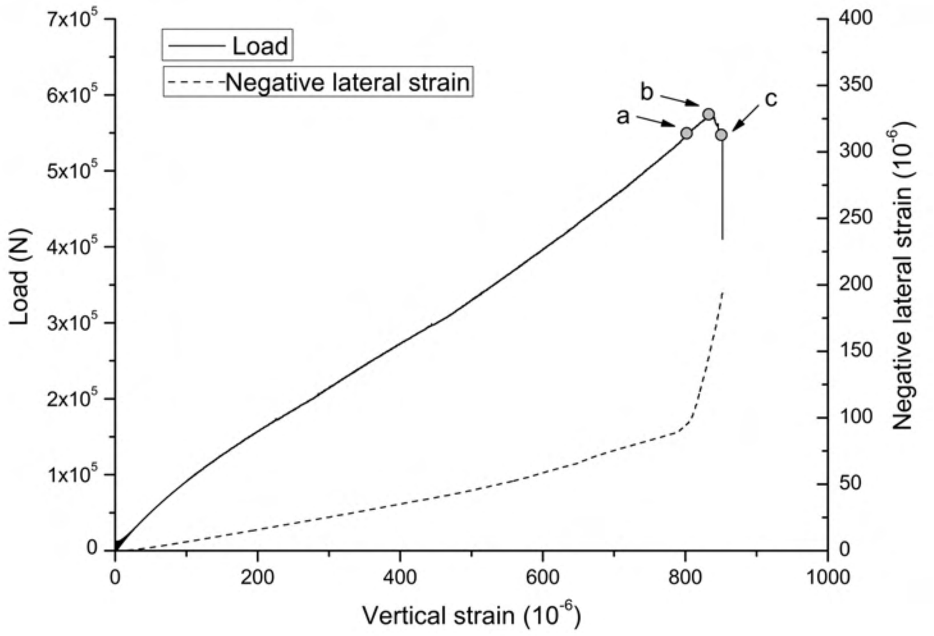

a

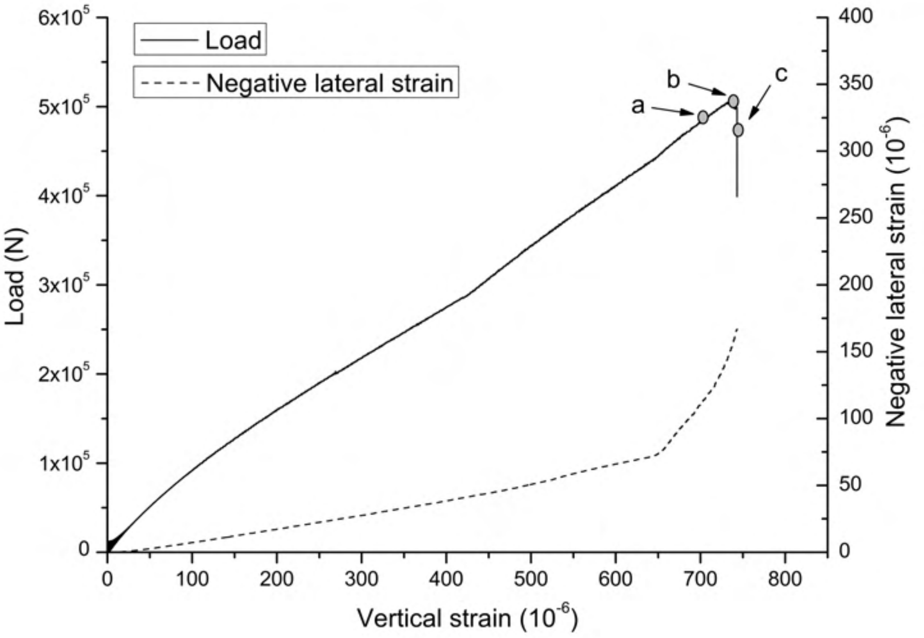

b

Fig. 10: Load strain curves for CCBD tests: (a) Mode-I, (b) Mode-II.

As shown in Fig. 10, both tests reveal brittle failure characteristics. Up to point ‘a’ the behaviour is nearly elastic, only at the load entry points and at the end of the notches minor damage occurs. Between points ‘b’ and ‘c’ crack propagation increases dramatically and leads finally to splitting of the sample (Fig. 11). However, there are some differences between Mode-I and Mode-II conditions. The increase in lateral strain in the post-failure region for Mode-I is larger than that for Mode-II. This is caused by the fact, that the wing-crack type fracturing in Mode-II offers more potential for interlocking and frictional sliding, which limits the dilation.

For $\theta = 0^\circ$ pure tensile cracking occurs, but for $\theta = 27.2^\circ$ the crack propagation starts as a shear crack and develops further as a wing-crack (Fig. 11). The fracture toughness can be calculated as follows:

$$\begin{cases} \theta = 0^\circ \\ N_I = 1 - 4\sin^2 0^\circ + 4\sin^2 0^\circ \times \left(1 - 4\cos^2 0^\circ\right) \times 0.3^2 = 1 \\ N_{II} = \left[2 + \left(8\cos^2 0^\circ - 5\right) \times 0.3^2\right] \times \sin 0^\circ = 0 \\ K_{Ic} = \dfrac{P\sqrt{a}}{\sqrt{\pi}RB} N_I = \dfrac{571800 \times \sqrt{0.01125}}{\sqrt{\pi} \times 0.0375 \times 1} = 0.91\, MPa \cdot m^{1/2} \end{cases} \tag{14}$$

$$\begin{cases} \theta = 27.2^{\circ} \\ N_I = 1 - 4\,sin^2\,27.2^{\circ} + 4\,sin^2\,27.2^{\circ} \times \left(1 - 4\,cos^2\,27.2^{\circ}\right) \times 0.3^2 \approx 0 \\ N_{II} = \left[\,2 + \left(8\,cos^2\,27.2^{\circ} - 5\right) \times 0.3^2\,\right] \times sin\left(2 \times 27.2^{\circ}\right) = 1.72342 \\ K_{IIc} = \dfrac{P\sqrt{a}}{\sqrt{\pi}RB} N_{II} = \dfrac{504700 \times \sqrt{0.01125}}{\sqrt{\pi} \times 0.0375 \times 1} \times 1.72342 = 1.39\ MPa \cdot m^{1/2} \end{cases} \tag{15}$$

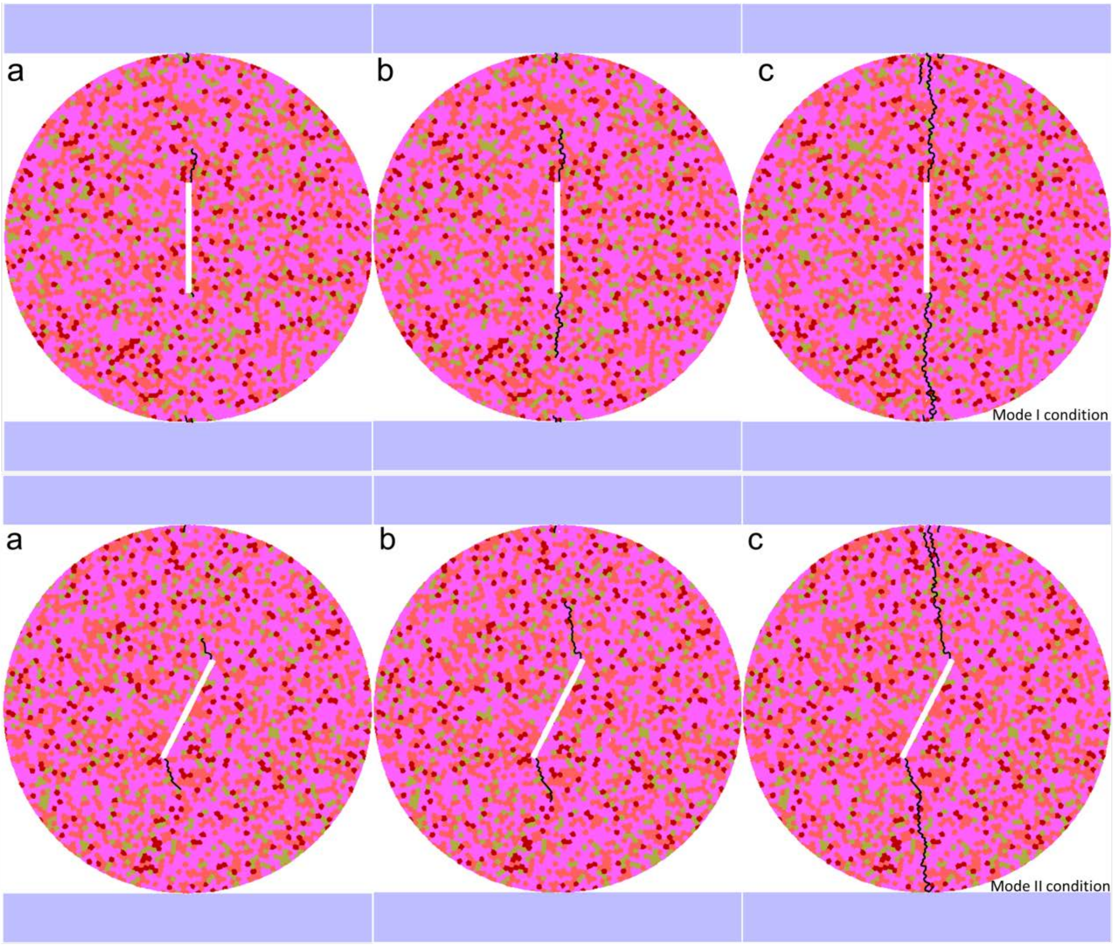

Fig. 11: CCBD tests: damage state at different load levels according to Fig. 10.

2.5 Comparison between lab tests and numerical simulation results

Through a series of simulations (optimization procedure), micromechanical input parameters were obtained, which match the macroscopic lab test results. A comparison between lab test results (Homand-Etienne et al., 1998; Souley et al., 2001; Potyondy and Cundall, 2004; Wang and Tonon, 2009) and our simulation results is listed in table 3.

Tab. 3: Lab test and simulation results

LdB granite parameter	Lab test result	Simulation result
UCS [MPa]	200 ± 22 (n = 81)	234.5
E_0 [GPa]	69 ± 5.8 (n = 81)	71.2
μ [-]	0.26 ± 0.04 (n = 81)	0.32
Tensile strength [MPa]	9.3 ± 1.3 (n = 39)	11.0
K_{Ic} [MPa · m$^{1/2}$]	0.96	0.91
K_{IIc} [MPa · m$^{1/2}$]	/	1.39

3 Time dependent simulation

Rocks subjected to long-term loading suffer microcracking, which is time dependent and sensitive to the applied stress (Lajtai and Bielus; 1986). This process can be explained by the theory of stress corrosion and subcritical crack growth. Therefore, the grain-based heterogeneous model described above is extended by implementing a theory of subcritical crack growth. Uniaxial creep tests of LdB granite were used to calibrate the numerical model.

3.1 Subcritical crack growth

The relationship between subcritical crack growth velocity and stress intensity factor is illustrated in Fig. 12. K_{I0} is the lower limit stress intensity factor, below which the crack is stable. K_{Ic} is the Mode-I fracture toughness, where the velocity of crack growth will suddenly approach large values and cause failure. In region 1, the velocity is controlled by the rate of stress corrosion reactions at the crack tips. In region 2, the velocity is controlled by the rate of transport of reactive species to the crack tips. In region 3, crack growth is mainly ruled by mechanical rupture and relatively insensitive to the chemical environment (Freiman, 1984; Atkinson, 1984; Potyondy, 2007; Rinne, 2008).

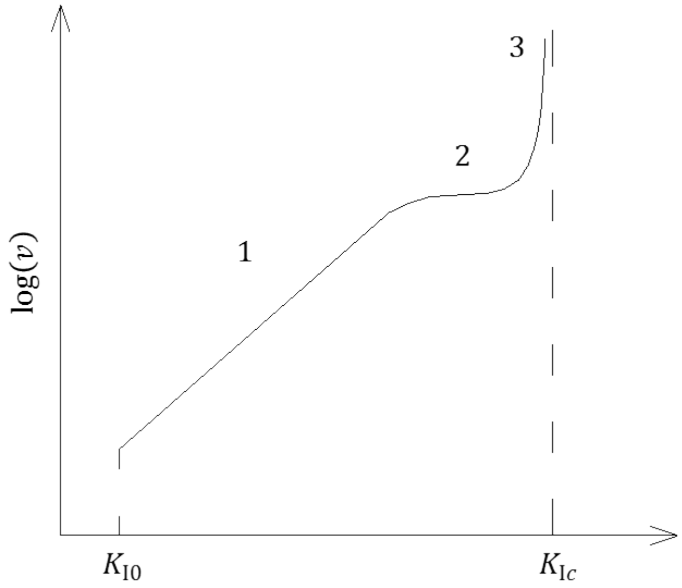

Fig. 12: Schematic representation: crack growth velocity versus stress intensity factor for subcritical tensile crack growth (Atkinson, 1984).

An exponential law is frequently used to describe the subcritical crack growth in region 1 (Fig. 12), where most of the time is spent during the entire crack development process (Amitrano, 2006; Potyondy, 2007). Hillig and Charles (1965) made the hypothesis that the static fatigue in glass follows the rule of chemical reaction between the glass and the environment, but they have also recognized, that the process is stress-sensitive. According to their findings, they proposed a quantitative equation for describing crack velocity:

$$v = v_0 \exp\left[\left(-E + V\sigma - V_m\gamma/\rho\right)/RT\right] \tag{16}$$

where v is the crack growth velocity, v_0 is the initial velocity (constant), E is the stress free activation energy, V is the activation volume, σ is the stress at the crack tip, V_m is the molar volume of the material, γ is the interfacial surface energy between the glass and the reaction products, ρ is the radius of the curvature of the crack tip, R is the gas constant and T is the absolute temperature

Wiederhorn and Bolz (1970) have re-written Eq. (16) by introducing the two-dimensional Griffith crack term $\sigma = 2K_I/\sqrt{\pi\rho}$:

$$\begin{cases} v = v_0 \exp\left[\left(-E_* + 2VK_I/\sqrt{\pi\rho}\right)/RT\right] \\ E_* = E + V_m\gamma/\rho \end{cases} \tag{17}$$

Based on Eq. (17) Wiederhorn et al. (1980) have proposed an empirical relation by fitting lab test data from glass by least square method:

$$v = v_0 \exp\left[\left(-E_* + bK_I\right)/RT\right] \tag{18}$$

where b is empirical constant obtained from curve fitting.
Eq. (18) was successfully used to analyse subcritical crack growth in rocks (e.g. Atkinson, 1984, Amitrano, 2006; Potyondy, 2007).

3.2 Implementation in UDEC

In order to consider subcritical crack growth and to predict lifetime, the exponential law according to Eq. (16) was implemented in UDEC under the following assumptions.

- Stress corrosion only affects contacts and not the rock matrix. Therefore, cracks can only propagate along the edges of the Voronoi cells (inter- and intra-granular fracturing).
- Stress corrosion leads to a time-dependent reduction of tensile and cohesive strengths at the contacts, that means subcritical crack growth in Mode-I and Mode-II follow the same rule.
- The degradation rates at the contacts are stress-dependent.

Taking into account the above-mentioned assumptions, the degradation rates can be described as follows:

$$\begin{cases} \dfrac{dJ_i^T}{dt} = -\lambda_r v_t = -\left(\lambda_r v_0 e^{-(E+V_m\gamma/\rho)/RT}\right) e^{V\bar{\sigma}_i/RT} \\ \dfrac{dJ_i^C}{dt} = -\lambda_r v_c = -\left(\lambda_r v_0 e^{-(E+V_m\gamma/\rho)/RT}\right) e^{V\bar{\tau}_i/RT} \end{cases} \tag{19}$$

where J_i^T and J_i^C are tensile and cohesive strengths at the contact i, respectively, λ_r is a constant describing the proportionality between strength degradation and subcritical crack growth velocity, v_t and v_c are crack growth velocities governed by the level of tensile and shear stress in the contact, respectively. $\bar{\sigma}_i = F_i^n / L_i$ and $\bar{\tau}_i = F_i^s / L_i$ are average tensile and shear stresses at the contact, respectively, F_i^n and F_i^s are normal and shear forces at the contact, respectively, and L_i is the contact length.
Assuming that $\beta_1 = \lambda_r v_0 e^{-(E+V_m\gamma/\rho)/RT}$ and $\beta_2 = V/RT$, and considering the constitutive model of the contacts, Eq. (19) can be re-written into the following simple form:

$$\begin{cases} \dfrac{dJ_i^T}{dt} = \begin{cases} -\beta_1 e^{\beta_2\bar{\sigma}_i}, & \bar{\sigma}_i < J_i^T \\ -\infty, & \bar{\sigma}_i \geq J_i^T \end{cases} \\ \dfrac{dJ_i^C}{dt} = \begin{cases} -\beta_1 e^{\beta_2\bar{\tau}_i}, & \bar{\tau}_i < \tau_{\max(i)} \\ -\infty, & \tau_i \geq \tau_{\max(i)} \end{cases} \end{cases} \tag{20}$$

where $\tau_{\max(i)}$ is the shear strength at the contact i.

The contact strength decrease with time elapsing are ruled by Eq. (20). After a certain period of time, the contact strength degrading velocity approaches infinite, that means that sudden failure at the contact occurs. The stresses around this failed contact will be redistributed and may cause further local stress concentrations, so that strength degrading at neighbouring contacts will accelerate. The calculation scheme is illustrated in the flowchart shown in Fig. 13.

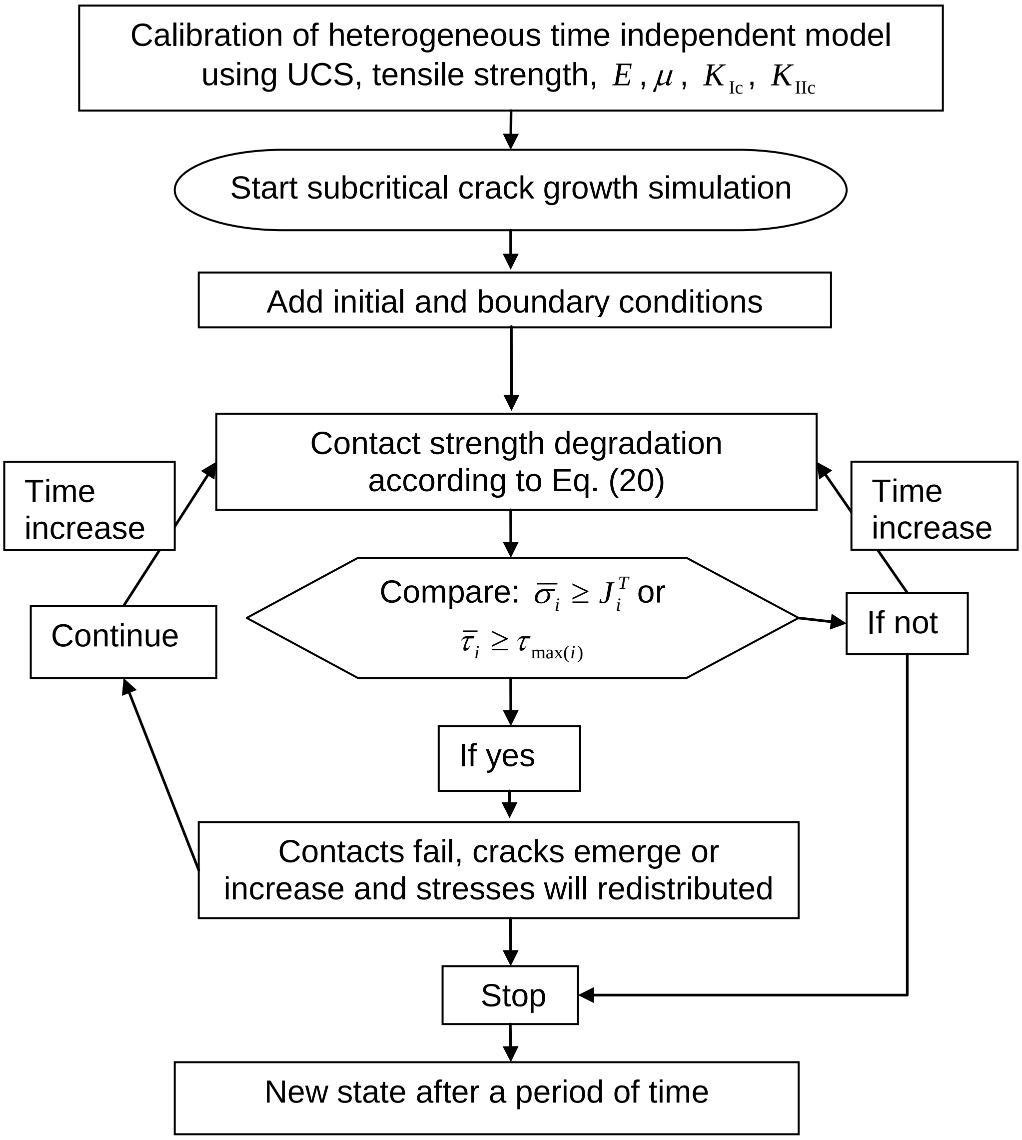

Fig. 13: Flowchart for stress corrosion simulation.

3.3 *Modelling of uniaxial compression creep tests*

Creep or static fatigue of rocks is a phenomenon characterized by increasing deformation and ongoing damage at a load level below the short-term strength and can be investigated by creep tests (e.g. Heap 2009). Schmidtke and Lajtai (1985) have used 126 specimens of LdB granite to perform uniaxial creep tests. The cylindrical specimen with a diameter of 37.1 mm was saturated before testing and kept submerged during testing at a temperature of 25°C. The above-mentioned numerical modelling approach was carried out to compare the simulation results with those obtained by the experiments.

To minimize the CPU time and to guarantee, that the damage process is followed with sufficient precision, a changeable time step scheme is used for the simulations:

$$\begin{cases} \Delta t_{\min} \le \Delta t_n \le \Delta t_{\max} \\ if\ F_u < 100N,\ \Delta t_n = 2 * \Delta t_{n-1} \\ if\ F_u \ge 100N,\ \Delta t_n = \Delta t_{\min} \end{cases} \tag{21}$$

where $\Delta t_{\min}$, Δt_n and $\Delta t_{\max}$ are minimum, actual and maximum time steps, respectively, F_u is unbalanced force, and n is corresponding step number.

The simulation stops whenever the specimen can no longer resist the load and an abrupt increase in strain is observed. The lifetime (time-to-failure) is the total elapsed time during the process until macroscopic failure of the specimen is observed. In this paper, we specify $\beta_1 = 0.001$ Pa/s, $\beta_2 = 1.0 \times 10^{-7}$, $\Delta t_{\min} = 1.0 \times 10^{-5} s$ and $\Delta t_{\max} = 1000 s$. The other parameters are taken from Table 1 and 2.

Results from lab tests (Schmidtke & Lajtai 1985) and numerical simulation with respect to lifetime for LdB granite under different driving-stress ratios are shown in Fig. 14. The driving-stress ratio is defined by σ/σ_c (σ and σ_c are uniaxial actual compression stress and UCS, respectively). The data show, that lifetime of specimens decrease with increasing driving-stress ratio. Variations in lifetime at the same driving-stress ratio are observed due to the heterogeneity of the rock samples.

Fig. 15 shows simulation results of uniaxial compression creep tests, which reveal primary, secondary and tertiary creep phases. The curves in Fig. 15b are smoother than those in Fig. 15a, because time steps change automatically in one case (15a) and are constant, that means it is equal to $\Delta t_{\min}$, in the other case (15b). The introduction of changeable time steps is necessary to get acceptable computer run-times whenever huge lifetime is expected, which is the case for low load levels.

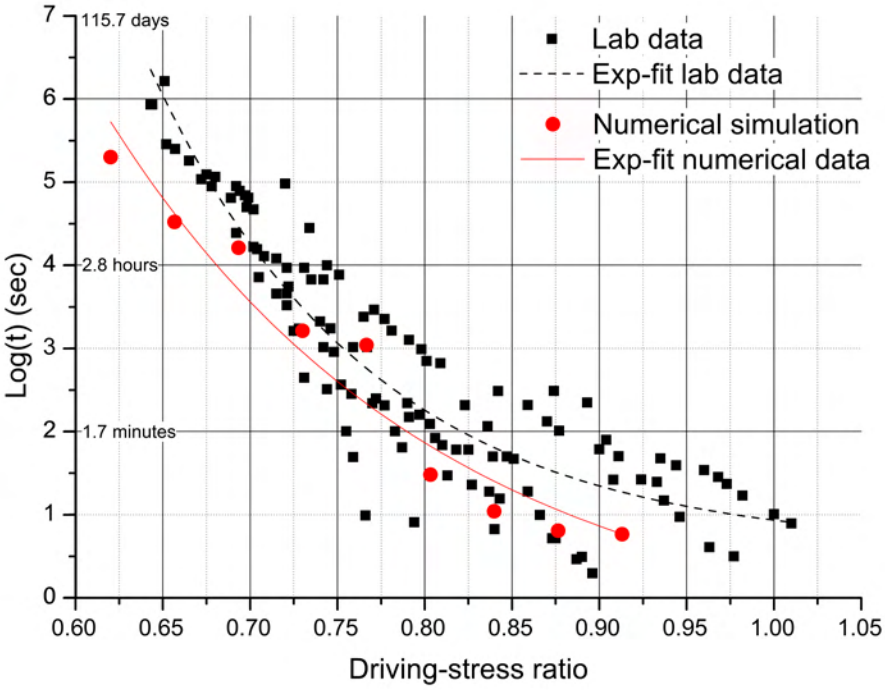

Fig. 14: Lab test (Schmidtke and Lajtai, 1985) and numerical simulation results for lifetime of LdB granite under different driving-stress ratios.

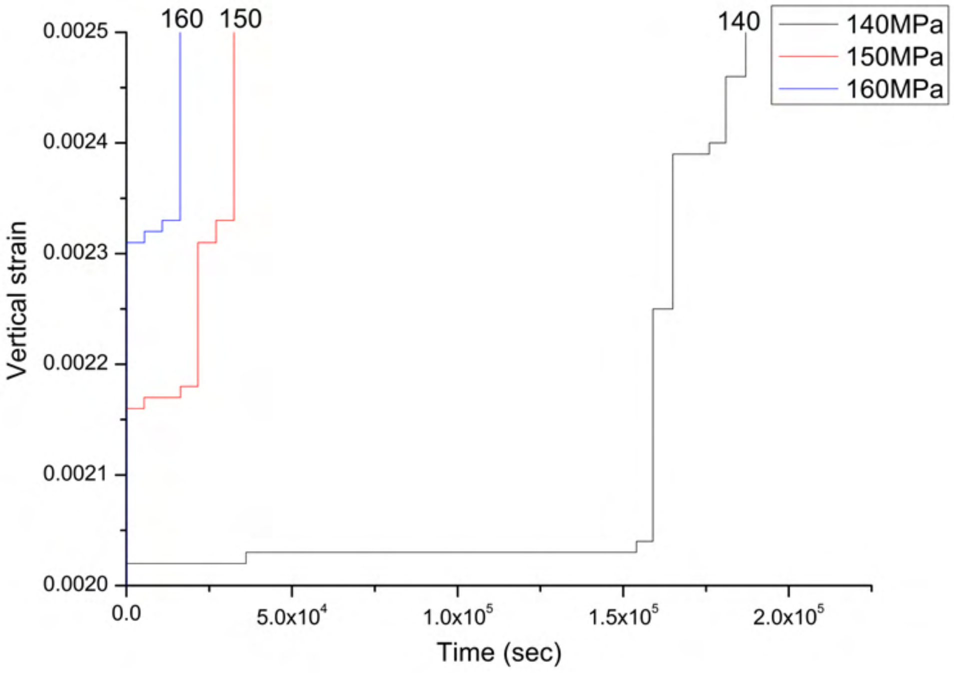

a

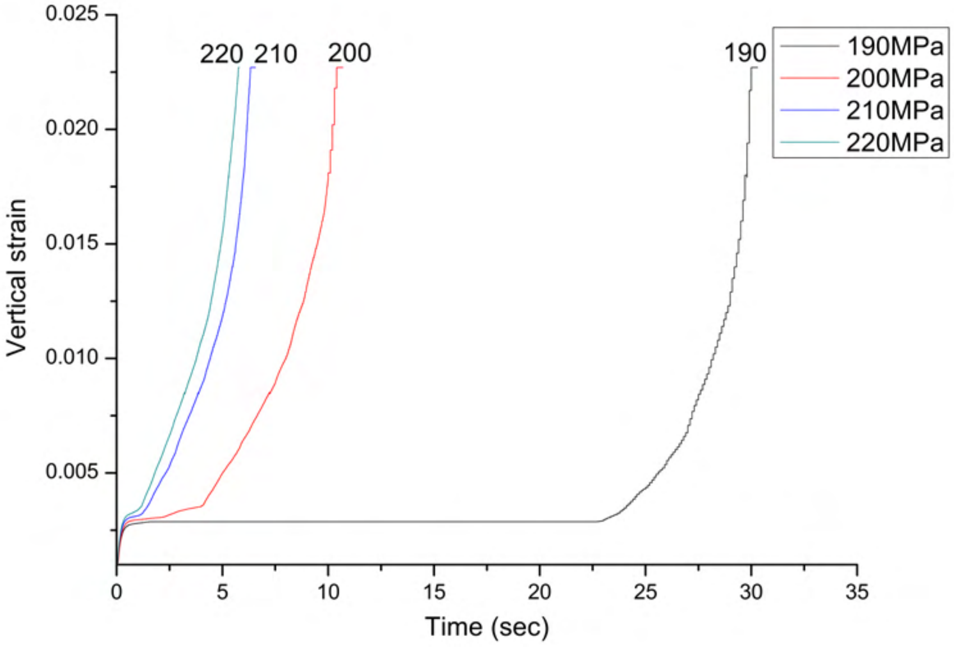

b

Fig. 15: Uniaxial creep tests: strain versus time, (a) load range 140-160 MPa, (b) load range 190-220 MPa.

Fig. 16 shows how contact failure (microcracks) and strain develop with ongoing time under constant load of 160 MPa and 200 MPa, respectively. The rate of contact bond breakage (microcrack development) shows some correlation to the creep phases: the rate is relatively low within the secondary creep phase, but shows stronger values at the primary and tertiary creep phases.

Microcrack distribution inside the specimen for a load level of 160 MPa for different points in time according to Fig. 16a is shown in Fig. 17. During the primary phase microcracks emerge in a more random manner within the specimen (Fig. 17a). Later, within the secondary creep phase, microcracks grow further, interact with each other and form larger cracks mainly parallel to the maximum stress direction (Fig. 17b-c). Finally, within the tertiary creep phase, massive crack interaction is observed and, in addition to large vertical cracks, shear band formation is observed until final macroscopic failure is noticed.

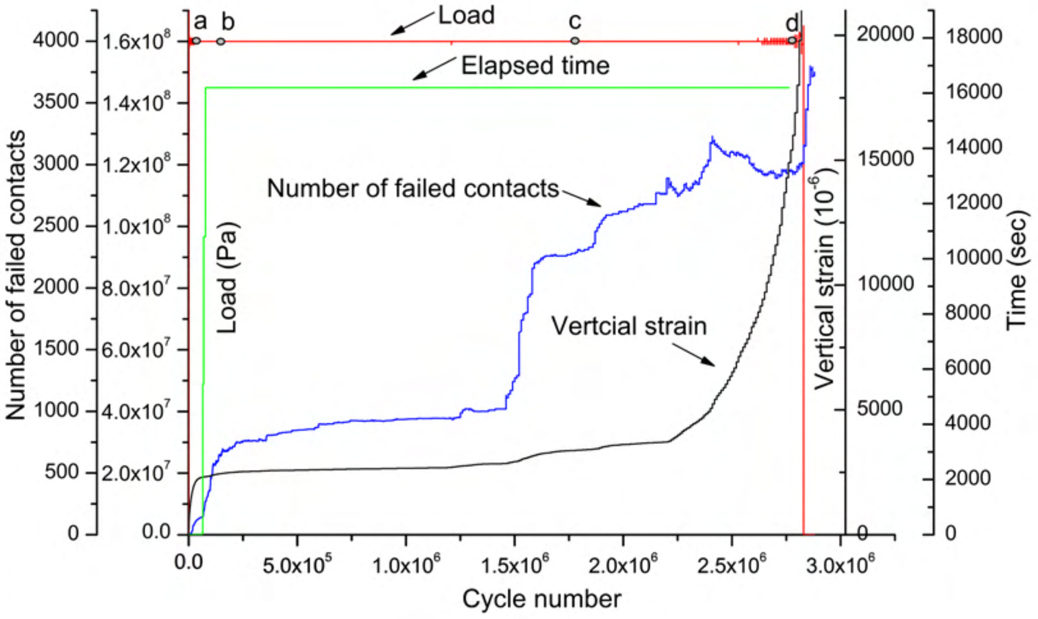

a

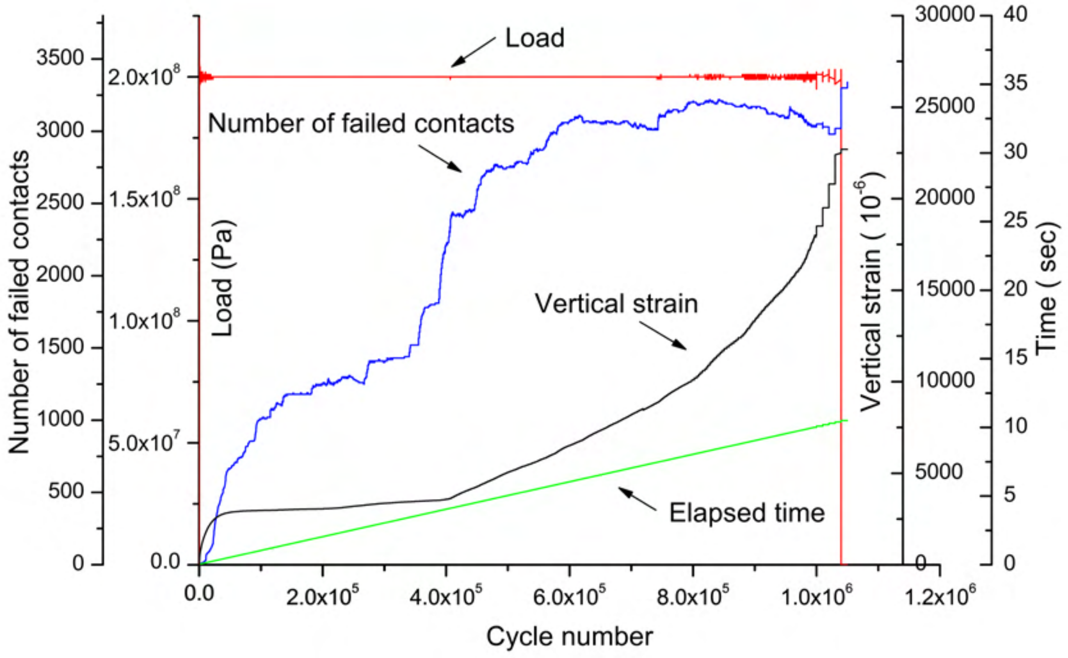

b

Fig. 16: Uniaxial creep test: (a) model behaviour under 160 MPa uniaxial compressive load, (b) model behaviour under 200 MPa uniaxial compressive load.

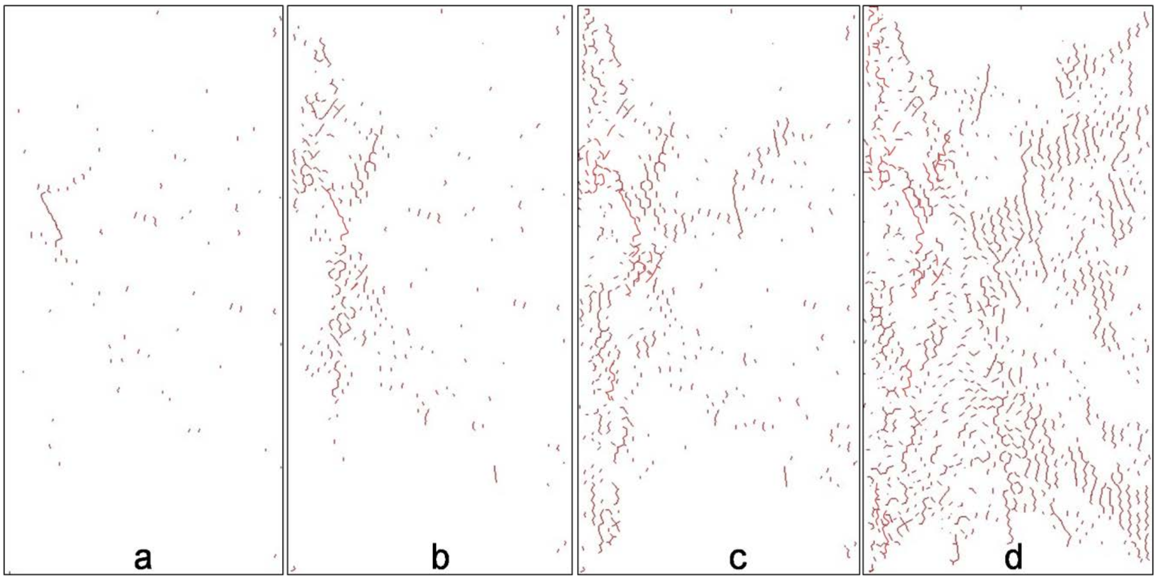

Fig. 17: Microcrack distribution under 160 MPa uniaxial compressive load for different points in time according to Fig. 16a.

4 Conclusions

A micromechanical grain-based model is presented which comprises the following features.

- Consideration of grain size and grain size distribution.
- Explicit consideration or mineral components with their parameters.
- Reproduction of elasto-plastic short-term behaviour based on a Mohr-Coulomb constitutive law with tension cut-off.
- Reproduction of long-term creep and damage behaviour based on an exponential damage evolution law.
- Reproduction of subcritical and critical crack growths.
- Consideration of inter- and intra-granular fracturing.
- Discrimination between shear- and tensile fracturing.
- Formation of meso- and macroscopic wing-cracks and shear bands.
- Determination of damage state and creep deformation (incl. primary, secondary and tertiary creep phases).
- Time-to-failure prediction.

Lab observations and measurements for the well investigated LdB granite were used to demonstrate, that the proposed modelling strategy is able to reproduce the macroscopic short- and long-term behaviours of brittle rocks. The presented procedure allows to get a deeper understanding of the processes at the micro- and mesoscale.

5 References

Al-Shayea N.A., Khan K., Abduljauwad S. N., 2000. Effects of confining pressure and temperature on mixed-mode (I-II) fracture toughness of a limestone rock. Int. J. Rock Mech. Min. Sci., 37: 629-643.

Amitrano David, Helmstetter Agnès, 2006. Brittle creep, damage and time-to-failure in rocks. Journal of Geophysical Research B: Solid Earth 111 (B11201 DOI:10.1029/2005JB004252).

Atkinson C., Smelser R. E., Sanche J., 1982. Combined mode fracture via the cracked brazilian disk. Int J Fracture, 18:279-291.

Atkinson B. K., 1984. Subcritical crack growth in geological materials, J. Geophys. Res., 89: 4077–4114.

Awajih K., Sato S.,1978. Combined mode fracture toughness measure by disk test. J Eng Mater Tech, 100:175-182.

Bass D. J., 1995. Elasticity of minerals, glasses and melts, in: Ahrens, T.J (ed.) Mineral Physics and Crystallography, Ref. Shelf Ser., Vol. 2: 45– 63.

Blair S. C. Cook N. G. W., 1998. Analysis of compressive fracture in rock using statistical techniques: Part I, A non-linear rule-based model, Int. J. Rock Mech. Min. Sci., 35: 837 – 848.

Chen C. S. Pan E., Amadei B., 1998. Fracture mechanics analysis of cracked discs of anisotropic rock using the boundary element method. Int. J. Rock Mech. Min. Sci. 35: 195-218.

Chen S, Yue ZQ., Tham LG., 2004. Digital image-based numerical modeling method for prediction of inhomogeneous rock failure. Int. J. Rock Mech. Min. Sci., 41: 939-957.

Espinosa D. H. Zavattieri D. P., 2003. A grain level model for the study of failure initiation and evolution in polycrystalline brittle materials. Part I: Theory and numerical implementation. J Mechanics of Materials 35: 333-364.

Freiman S.W. 1984. Effect of chemical environments on slow crack growth in glasses and ceramics. J Geophys Res; 89(B6): 4072–6.

Groh U., Konietzky H., Walter K., Herbst M., 2011. Damage simulation of brittle heterogeneous materials at the grain size level, Theoretical and Applied Fracture Mechanics, 55: 31-38.

Hallbauer D. K. Wagner H. Cook N. G. W., 1973. Some observations concerning the microscopic and mechanical behaviour of quartzite specimens in stiff, triaxial compression tests, Int. J. Mech. Min. Sci., Geomech. Abstr.,10: 713–726.

Heap M. J., 2009. Creep: Time-dependent brittle deformation in rocks. PhD dissertation, University College London.

Hillig W. B., Charles R. J., 1965. In: Zackey, V.F. (ed) High-Strength Materials. John Wiley & Sons, Inc., New York, pp. 682-705.

Hoek E., 1983. Strength of jointed rock masses Géotechnique1983; 23(3): 187–223.

Homand-Etienne F., Hoxha D., Shao J.F., 1998. A continuum Damage Constitutive Law for Brittle Rocks. Computes and Geotechnics, Vol.22, No.2, pp.135-151.

Jianhong Ye, Wu F.Q., Sun J.Z., 2009. Estimation of the tensile elastic modulus using Brazilian disc by applying diametrically opposed concentrated loads. International Journal of Rock Mechanics & Mining Sciences 46, 568-576

Konietzky H. Heftenberger A. Feige M., 2009. Life time prediction for rocks under static compressive and tensile loads - a new simulation approach, Acta Geotechnica, 4: 73-78

Ko T.Y. Kemeny J. 2013. Determination of the subcritical crack growth parameters in rocks using the constant stress-rate test. Int. J. Rock Mech. Min. Sci. 59: 166-178.

Lajtai Z.E. Bielus P.L., 1986. Stress corrosion cracking of Lac du Bonnet granite in tension and compression. Rock Mech. Rock Eng., 19: 71-87.

Lan H. Martin C.D. Hu B., 2010. Effect of heterogeneity of brittle rock on micromechanical extensile behavior during compression loading. Journal of Geophysical research Vol.115, DOI:10,1029/2009JB006496

Li H. et al., 2006. Micromechanical modelling of tungsten-based bulk metallic glass matrix composites, Mater. Sci. Eng. A, 429: 115– 123.

Liu H. Y. Kou S. Q. Lindqvist P. A. Tang C. A., 2007. Numerical Modelling of the Heterogeneous Rock Fracture Process Using Various Test Techniques. Rock Mech. Rock Eng. 40: 107-144.

Li X. Konietzky, H., 2013. Time to Failure Prediction Scheme for Rocks, Rock Mech Rock Eng, DOI 10.1007/s00603-013-0447-y

Liu H.Y. Roquete M. Kou S.Q. Lindqvist P.A., 2004. Characterization of rock heterogeneity and numerical verification. Eng. Geology 72: 89-119.

Lockner D.A. Madden T.R. 1991. A multiple-crack model of brittle fracture 2. Time-dependent simulation. J Geophys Res 96(B12): 634-54.

Potyondy D. O., 2007. Simulation stress corrosion with a bonded-particle model for rock. Int. J. Rock Mech. Min. Sci. 44: 677-691.

Potyondy D .O. Cundall P.A., 2004. A bonded-particle model for rock. Int. J. Rock Mech. Min. Sci. 41: 1329-1364.

Qinglei YU, Chao ZHENG, Tianhong YANG, Shibin TANG, Peitao WANG, Chun’an TANG, 2012. Meso-structure characterization based on coupled thermal-mechanical model for rock failure process and applications. Chinese Journal of Rock Mechanics and Engineering, Vol.31 No.1, pp. 42-51 (in Chinese).

Rinne M., 2008. Fracture mechanics and subcritical crack growth approach to model time-dependent failure in brittle rock. PhD thesis, Helsinki University of Technology.

Sanchez J., 1979. Application of the Disk Test to Mode I-II Fracture Analysis. M.S. thesis, Department of Mechanical Engineering, University of Pittsburgh.

Schmidtke R H. Lajtai E Z., 1985. The Long-Term Strength of Lac du Bonnet Granite. Int. J Rock Mech. Min. Sci. & Geomech. Abstr. 22: 461-465.

Souley M. Homand F. Pepa S. Hoxha D., 2001. Damage-induced permeability changes in granite: a case example at the URL in Canada. Int. J. of Rock Mech. Min. Sci. 38: 297-310.

Van de Steen X. Vervoort B. A. Napier J. A. L. Durrheim R. J., 2003. Implementation of a flaw model to the fracturing around a vertical shaft, Rock Mech. Rock Eng., 36, 143– 161.

Wang Y. Tonon F., 2009. Modeling Lac du Bonnet granite using a discrete element model. Int. J. Rock Mech. Min. Sci. 46: 1124-1135.

Wiederhorn S.M. Bolz L.H., 1970. Stress Corrosion and Static Fatigue of Glass. J. Am. Cer. Soc. 53: 544-548.

Wiederhorn S.M. Fuller E.R. Jr. Thomson R. 1980. Micromechanisms of Crack Growth in Ceramics and Glasses in Corrosive Environments, Metal Science, 8-9: 450-458.

Stability and integrity of geotechnical barriers under earthquake loading

Stabilität und Integrität von geotechnischen Barrieren unter Erdbebeneinwirkung

N. Neubert
TU Bergakademie Freiberg, Institut für Geotechnik, Freiberg
DBE TECHNOLOGY GmbH, Peine

Abstract

German regulations define a one million year compliance period for the disposal of nuclear waste in deep geologic repositories. This means that with respect to earthquakes even regions exhibiting relatively low levels of seismicity at present must be assessed in respect to potentially much higher levels of seismic activity that could potentially occur within the period of compliance.

The following paper presents the results of numerical studies on the performance, which includes the safety and integrity, of geotechnical barriers under the expected seismic loads. Results were obtained during the diploma project "Stability and integrity of geotechnical barriers under earthquake loading" [NEU14]. First, an estimate of earthquake loading based on the basic design earthquake is presented as required input for the simulation. Next, the numerical model, constitutive laws and physical parameters used in assessing barrier performance are described. Finally, the results of the numerical simulations are presented. These results demonstrate that the integrity of the barrier is not negatively affected under the considered conditions.

Zusammenfassung

Für radioaktive Endlager in tiefen geologischen Formationen in Deutschland werden Nachweiszeiträume über eine Million Jahre gefordert. In diesem Zeitraum ist es möglich, dass auch in Gebieten mit einer geringen seismischen Aktivität stärkere Erdbeben auftreten.

Im Folgenden werden numerische Untersuchungen zur Standsicherheit von geotechnischen Barrieren unter Erdbebeneinwirkung vorgestellt, die im Rahmen der Diplomarbeit „Standsicherheit und Integrität von geotechnischen Barrieren unter Erdbebeneinwirkung" gewonnen wurden [NEU14]. Die zur Simulation notwendigen Erdbebenlasten werden zunächst anhand eines gegebenen Bemessungserdbebens abgeleitet. Danach wird das Berechnungsmodell, die verwendeten Stoffgesetze und die Kriterien, durch die Aussagen zur Integrität und Standsicherheit abgeleitet werden können näher erklärt. Im Anschluss werden die Ergebnisse der numerischen Berechnung kurz dargelegt und es wird gezeigt, dass die Integrität der geotechnischen Barriere unter den herrschenden Bedingungen nicht negativ beeinflusst wird.

1 Introduction

Earthquakes can result in significant damage to surface structures, while subsurface structures generally suffer significantly less damage. In underground excavations the damage from an earthquake is relatively small; limited to the contours of shafts and drifts. Therefore, little focus has been given to seismic impacts to barrier performance. Earthquake impacts to subsurface excavations, particularly geotechnical barriers, are based primarily on estimations extrapolated from gained experience.

This paper presents the results of a numerical study on the performance of geotechnical barriers in shafts constructed in domal salt formations. The model and proof of concept are based on the conceptual shaft seal design developed for a potential radioactive waste repository in the Gorleben salt dome as described in the Preliminary Safety Assessment Gorleben (Vorläufige Sicherheitsanalyse für den Standort Gorleben VSG) [MUE12a]. The VSG provides numerical verification on the integrity of the shaft sealing system under static loading [MUE12b]. Integrity refers to the continued performance of the system's function as a geotechnical barrier.

The numerical verification of the barrier's performance related to both integrity and stability was conducted using the software code FLAC^{3D} developed by Itasca Consultant Group Inc. [ITA12].

The seismic loads required for the dynamic analysis conducted using FLAC^{3D}, were derived from the design basis earthquake using the software code SeismoArtif developed by Seismosoft Ltd. [SEI13].

2 Earthquake - Database and Generation

Seismic loads including acceleration time-histories, velocity time-histories or stresses are required inputs for conducting numerical simulation of the dynamic processes associated with earthquakes in FLAC^{3D}.

Northern Germany, where the Gorleben site is located, is a region of relatively minor seismic activity. Only nine tectonic earthquakes have been identified in the area over the last 1,200 years. The maximum intensity of these has been estimated as VI on the MSK scale [LEY99]. Time histories are not available for any of these earthquakes. As a result it was necessary to generate artificial time histories to represent likely earthquakes possible for the region. Radioactive waste repositories are classified as nuclear facilities in Germany and their design is based on KTA 2201 [KTA90] and not on Eurocode 8 [CEN10b]. The KTA 2201 defines the seismological criteria for nuclear facilities upon which the basic design earthquakes are derived. The engineering seismic design parameters for a potential earthquake at the Gorleben site are identified in Tab. 2.1 [WOL12]:

Tab. 2.1: Seismic design parameters used for the Gorleben site

Parameter	Symbol	Value
Macroseismic intensity	I_0	7.3 (MSK-scale)
Acceleration, horizontal	a_h	1.4 m/s²
Acceleration, vertical	a_v	0.7 m/s²
Probability of occurrence per year	$W_ü$	$0.5 \cdot 10^{-6} – 1.0 \cdot 10^{-6}$
Subsurface strong ground motion duration	t_{0u}	3.0 s

These parameters coupled with a response spectrum describing the frequency-content of the potential earthquake, are necessary input used to generate the acceleration time-history. The response spectrum (i.e. target spectrum) for the basic design earthquake is given in Fig. 2.1 as dashed line.

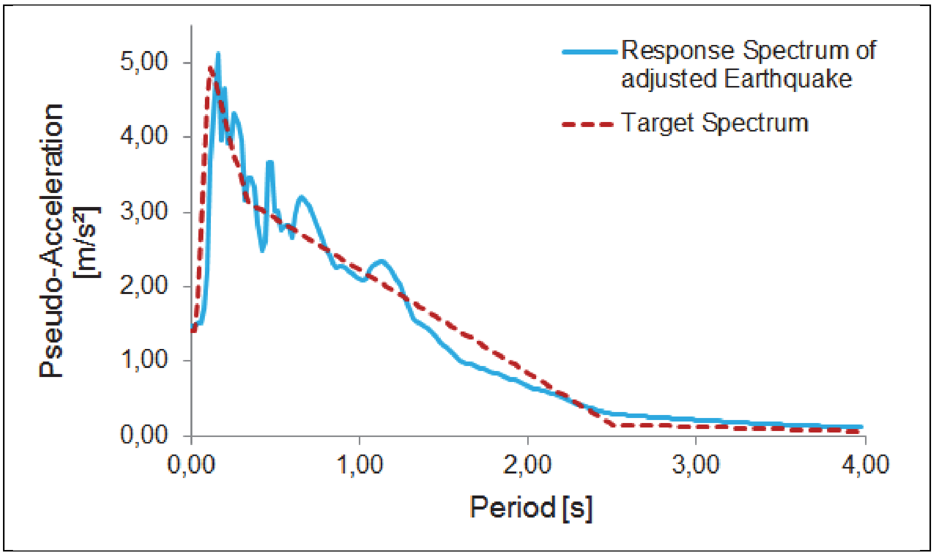

Fig. 2.1: Response spectra for the basic design earthquake (target spectrum) and the generated and adjusted earthquake

The artificial accelerogram (or velocity-history) was generated in SeismoArtif by superposition of sine waves with different frequencies, amplitudes and phase angles. The random time-history was adjusted to the target spectrum and an envelope-shape to describe the rise-phase, the strong-motion-phase and the descending part of the earthquake-history. Fig. 2.2 shows the generated artificial velocity history as a dashed line.

In order to implement the time-histories in FLAC^{3D} it was necessary to adjust the generated time-histories. Baseline correction and filtering were performed using the software code SeismoSignal [SEI12] also developed by Seismosoft Ltd.
Baseline corrections are required to account for physically unrealistic velocities or displacements that may occur at the end of a particular time-history. Velocities unequal to zero can be seen in Fig. 2.2 at the end of the time history (dashed line), i.e., after the end of the earthquake. The velocities in the grey-colored time-history,

where a baseline correction is performed, are equal to zero after the earthquake excitations are finished.

In FLAC^{3D} as with other software codes where continuum discretization is implemented there is a relationship between the highest frequencies in the time-history and the largest zonal dimension. For an input with high frequencies a very fine mesh is necessary to ensure accurate wave propagation through the model. To provide a very fine mesh, which leads to a small time step and thereby significantly increasing calculation time, it is possible to remove the high frequency content by filtering the signal. Frequencies above approximately 9.0 Hz in the signal were removed by the use of a low-pass-filter (Butterworth-filter) with a cutoff frequency of 8.0 Hz. The cutoff frequency was determined by the largest zone size and the associated material parameters.

The grey line in Fig. 2.2 shows in addition to the baseline correction the effects from filtering. The signal is generally smoothed, out of phase and with velocity peaks predominantly somewhat lower. The response spectrum of the generated adjusted earthquake history is shown in Fig. 2.1 by the grey line. Both spectra show good agreement. Key data for the generated earthquake history are identified in Tab. 2.2:

Tab. 2.2: Key parameters derived for the generated earthquake history

Parameter	Symbol	Value
Maximum acceleration	a_{max}	1.486 m/s²
Maximum velocity	v_{max}	0.126 m/s
Maximum displacement	u_{max}	0.029 m
Maximum frequency	f_{max}	9.0 Hz
Duration	t_{Dg}	5.20 s

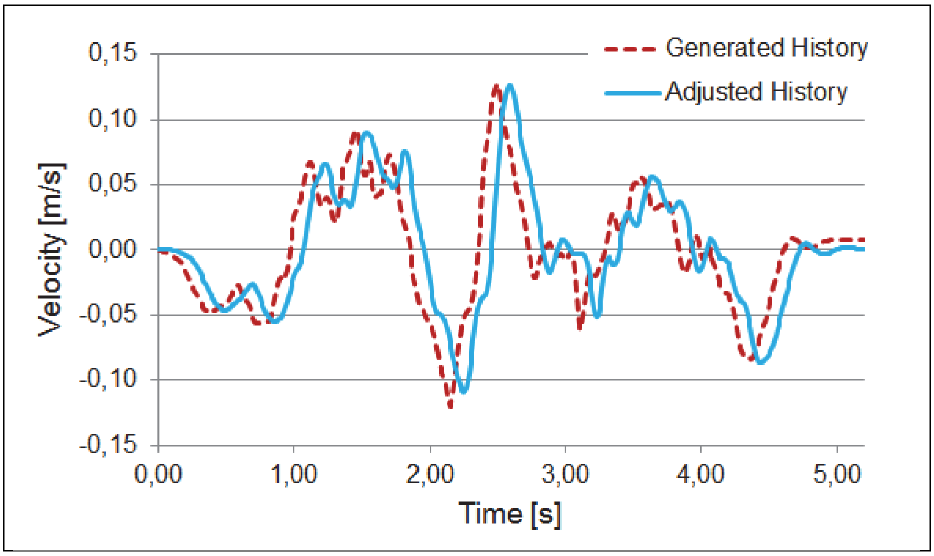

Fig. 2.2: Velocity histories of the generated and the adjusted earthquake

3 Numerical simulation

3.1 Numerical model

The basis for the generic model is provided by the section of the salt-concrete sealing system used in the VSG between depths 650 m and 780 m [MUE12a] and the vertical cross section of the Gorleben 1 and 2 shafts [MUE12a].

The model area is at a depth of 620 m to 810 m and has a horizontal extension of 160 m in each coordinate direction. The surrounding rock is Leine-rock salt with homogeneous areas representing zones susceptible to creeping. The numerical model with the zones of different creep potential is shown in Fig. 3.1.

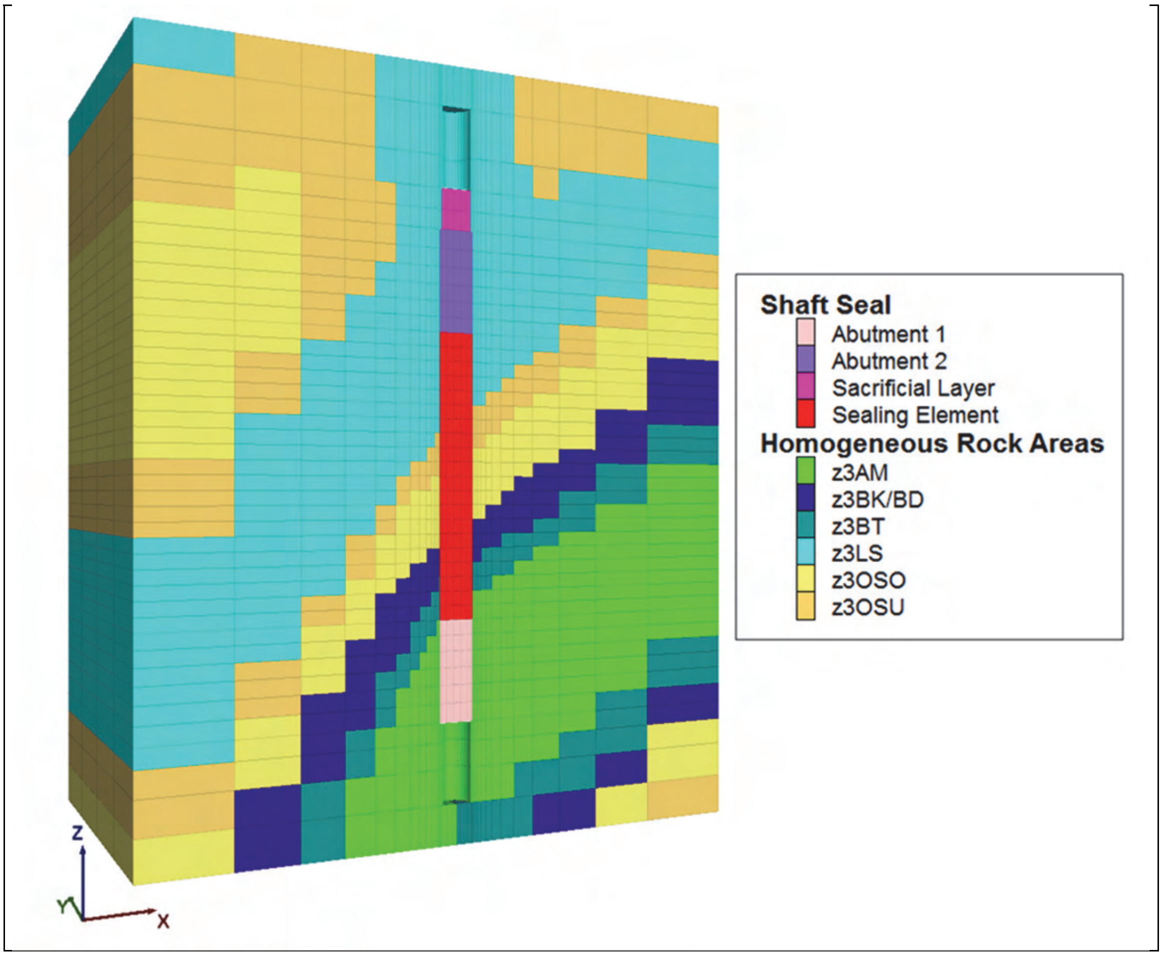

Fig. 3.1: Numerical model with homogeneous rock areas (intersecting plane y = 0)

The portion of the shaft sealing system implemented in the model is constructed from salt-concrete Type Asse and consists of four elements: the sealing element itself, abutments above and below the sealing element, and a sacrificial layer. Fig. 3.1 shows also the numerical model of the shaft sealing system. The shaft above and beneath the sealing system is modelled as air-filled to simplify the model. The blocks at the top and bottom of the model allow a better application of the boundary conditions.

3.2 Calculation procedure

The details of the calculation procedure used in the analysis, such as the schedule of shaft sinking or the installation date of the sealing elements, are adopted from the VSG [MUE12b]. Generally, the numerical simulation can be divided into two major calculation steps: a long-time creep calculation used to establish the initial conditions at the onset of the earthquake event and a short-time dynamic calculation representing the earthquake event itself.

The long-time creep calculation is also used to evaluate the plausibility of the numerical model. The calculation considers the initial stress conditions and changes due to the stress field resulting from the sinking of the shaft, the emplacement of waste packages in the repository, the installation of the shaft sealing and the post-closure period.

Based on the results of the creep calculation two points in time are used as starting point for the earthquake calculation. The most significant effects on barrier performance are expected shortly after completion of the installation of the complete shaft sealing system.

3.3 Constitutive laws and material properties

The mechanical deformation behavior of rock salt consists of two parts: elastic (reversible) deformations and viscoplastic, (irreversible) deformations. The time-independent elastic behavior of salt is described using Hooke's linear-elastic constitutive law. BGRa law is used to characterize the creep behavior (i.e. viscoplastic behavior) of the rock salt by describing the secondary creep. The steady state creep rate $\dot{\varepsilon}_{cr}^{s}$ is described as:

$$\dot{\varepsilon}_{cr}^{s} = V \cdot A \cdot \left(\frac{\sigma_F}{\sigma^*}\right)^n \cdot e^{-\left(\frac{Q}{R \cdot T}\right)} \qquad (1)$$

where V is a factor for the creep potential, A is a structural factor, σ_F is the Von Mises Equivalent Stress, σ^* is a reference stress, n is a stress-exponent, Q is the activation energy, R represents the universal gas constant and T is the temperature.

BGRa law is only used in the creep calculation to describe the viscoplastic part of the deformation behavior in the salt. The mechanical behavior of the rock salt during the earthquake is assumed to be elastic, because of the short loading times, the low velocity-amplitudes of the earthquake, and the associated low stress amplitudes.

The salt-concrete is assumed to be elastic over the entire calculation process but the mechanical properties used to describe Hooke’s law are reduced to consider a creep behavior.

The mechanical properties of the rock salt and the salt-concrete are constant during the entire calculation to simplify the model. The use of dynamic material properties for the earthquake calculation and their influences on the results are discussed below. The material properties used for the elastic calculations are given in Tab. 3.1.

Tab. 3.1: Mechanical properties of the used materials

Property	Leine-rock salt	Salt concrete Type Asse
Density ρ [kg/m³]	2242.6	2074.0
Young's modulus E [GPa]	25.0	2.0
Poisson's ratio ν [-]	0.27	0.13

3.4 Criteria of integrity and history locations

The geotechnical barrier is assumed to consist of the sealing element itself, the contact zone between sealing element and rock and the excavation-damaged-zone in the rock. A limit state to estimate a violation of the integrity is the fracturing of the rock (respectively the concrete) or the growth and opening of existing cracks.

Three criteria are used in the dynamic calculations to obtain information about the integrity of the geotechnical barrier during the earthquake:

- Cristescu/Hunsche dilatation boundary,
- Fluid pressure criteria and
- Drucker-Prager yield criterion.

The dilatation boundary according to Cristescu/Hunsche [CRI98] describes a limit state where an increase of the permeability in the rock salt can be observed. The envelope of the dilatation boundary for Leine-rock salt can be expressed as:

$$F = 0 = -0.01697 \cdot \left(\frac{\sigma_0}{\sigma^*}\right)^2 + 0.8996 \cdot \frac{\sigma_0}{\sigma^*} - \frac{\tau_0}{\sigma^*} \qquad (2)$$

where σ_0 is the average stress and τ_0 is the octahedral shear stress. The results are shown as the utilization factor μ for dilatation.

The dilatation boundary represents an envelope beneath the short time strength limit of the rock salt [HUN94]. If the dilatation criterion is observed the stability of the rock salt is also ensured.

The fluid pressure criterion defines a limit state where a crack opening, or grain boundary migration, under fluid pressure can occur [MUE12b]. The criterion can be described with the following formula:

$$\sigma_3 > p_{fl} \qquad (3)$$

The minimal principal stress σ_3 must be higher than an assumed pore pressure p_{fl}, which can occur when water is present. The criterion is verified by recording σ_3 in the rock salt and salt-concrete during the dynamic calculation and a comparison with an assumed pore water pressure.

The stability and integrity of the salt-concrete is verified using the Drucker-Prager yield criterion [MUE12b]. The envelope of the criterion for salt concrete Type Asse can be described as:

$$F = 0 = \sigma_F - 1.86754 \cdot \sigma_0 - 2.7759 \qquad (4)$$

If the actual load is beneath the envelope described with Formula 4 then the stability of the salt-concrete sealing element is ensured. To obtain conclusions about the integrity (i.e. limitation of cracks) of the concrete the envelope is reduced by a safety factor of 1.25.

The criteria were recorded on several locations during the creep calculation and the dynamic calculation. The right side of Fig. 3.2 shows the general locations for the histories. Horizon 1 is at a depth of 720.0 m, Horizon 2 is at 695.0 m and Horizon 3 is at 685.5 m. Four points on each Horizon are considered. Point P1 is situated in the salt concrete with a distance of 0.3 m from the shaft contour. The other three points are situated in the rock salt at distances of 0.3 m, 0.6 m and 1.0 m from the shaft contour. The right side of Fig. 3.2 shows the grid points and the associated zones (rectangles) where the histories are recorded in detail for Horizon 1.

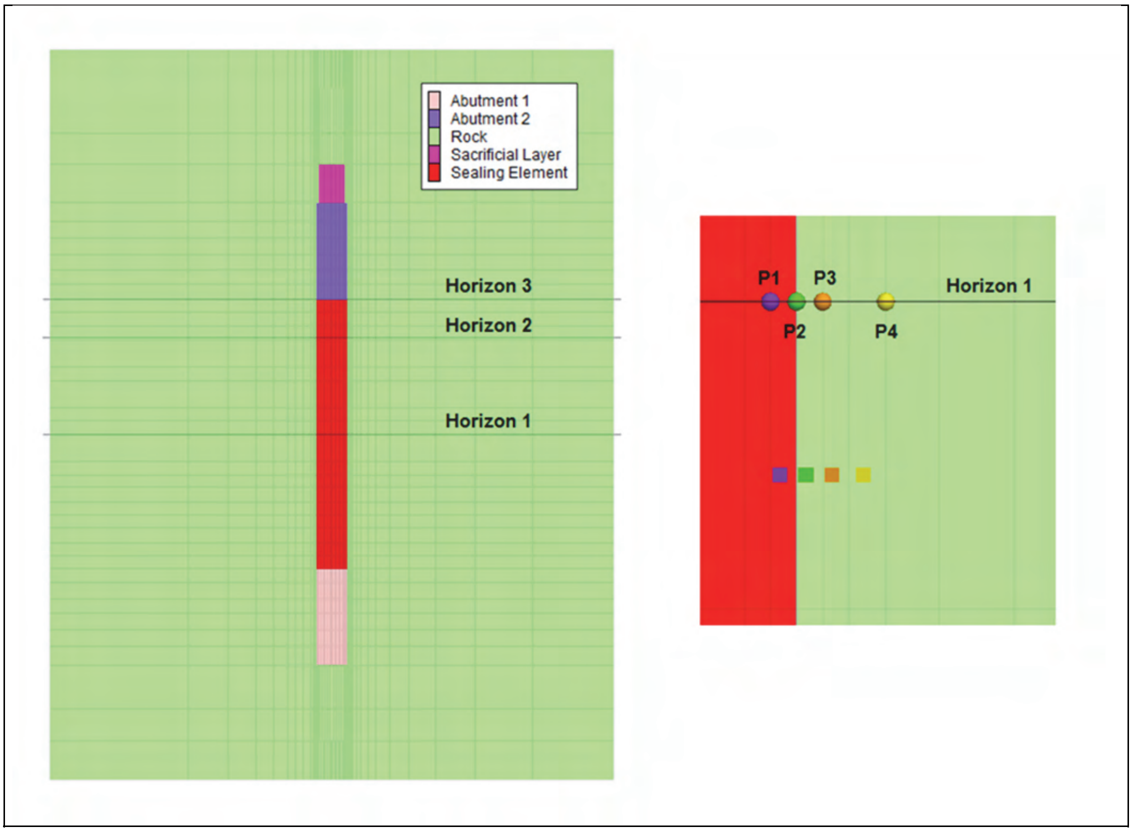

Fig. 3.2: History locations

3.5 Creep Calculation

The creep calculation is necessary to establish the initial conditions for the dynamic calculations and to evaluate the plausibility of the result. Fig. 3.3 shows the history of the utilization factor of dilatation μ during the creep calculation for the history points on Horizon 1. The histories of μ are for all points beneath one, so the dilatation criterion is observed. The dotted line in Fig. 3.3 represents time Point 1 and the chain-dotted line Time Point 2 where the seismic loads were applied. Time Point 1 is two years and Time Point 2 is twenty years after the completion of the shaft sealing.

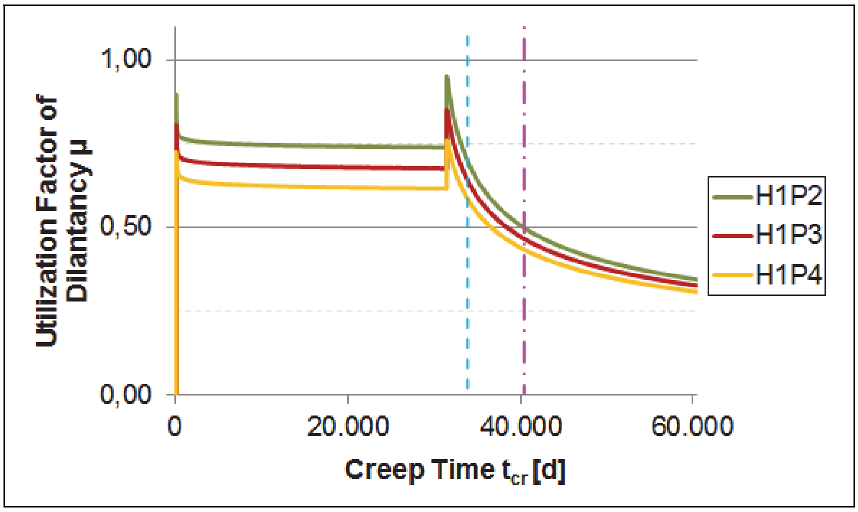

Fig. 3.3: Utilization factor of dilatation μ vs. creep time t_{cr} for the history points on Horizon 1

3.6 Dynamic calculation

The initial conditions for the dynamic calculation are based on the creep calculations performed before. Other initial conditions are not applied.

In dynamic simulations it is possible that the earthquake waves, which propagate through the model, can be reflected at the artificial boundaries. To eliminate this issue special dynamic boundary conditions implemented in FLAC^{3D} are used. On the lateral model boundaries free-field boundaries as defined in FLAC^{3D} are applied. These boundaries are used to simulate the motion of the rock-masses surrounding the model area as forced by the earthquake. Waves induced by structures in the model can propagate straight through the boundaries and are not reflected. On the bottom and top of the model quiet-boundaries are used. These kind of dynamic boundary conditions provide a propagation of the waves through the artificial boundaries by “absorbing” the waves.

The earthquake loads are applied as stress-histories to the bottom of the model. The horizontal shear waves are simulated by applying the history as shear stresses in the x- and y-direction. The compression waves appearing in the vertical direction are applied as a history for the normal stress in the z-direction; reduced by 50 % to account for the maximum vertical acceleration a_v of the basic design earthquake.

Because Hooke’s law is a very simple constitutive law an additional damping is necessary to describe the energy loss of the earthquake waves during the propagation through the model. In the numerical calculation the implemented Rayleigh-Damping is used.

Fig. 3.4 shows the histories of μ during the seismic loading phase for several history locations and the two points in time. The seismic loading primarily results in an increase of μ. The maximum increase of the utility factor of dilatation Δμ, compared to μ at the beginning of the dynamic calculation, is 0.034 at Point P2, Horizon 1 and Time Point 2. Generally, the increases in μ generated by the earthquake are very small and do not impact the integrity of the sealing element.

As shown in Fig. 3.4 the shapes of the time histories of μ differ between the points at each location and between the two points in time. The differences are the result of the diverse stress states in the observed zones.

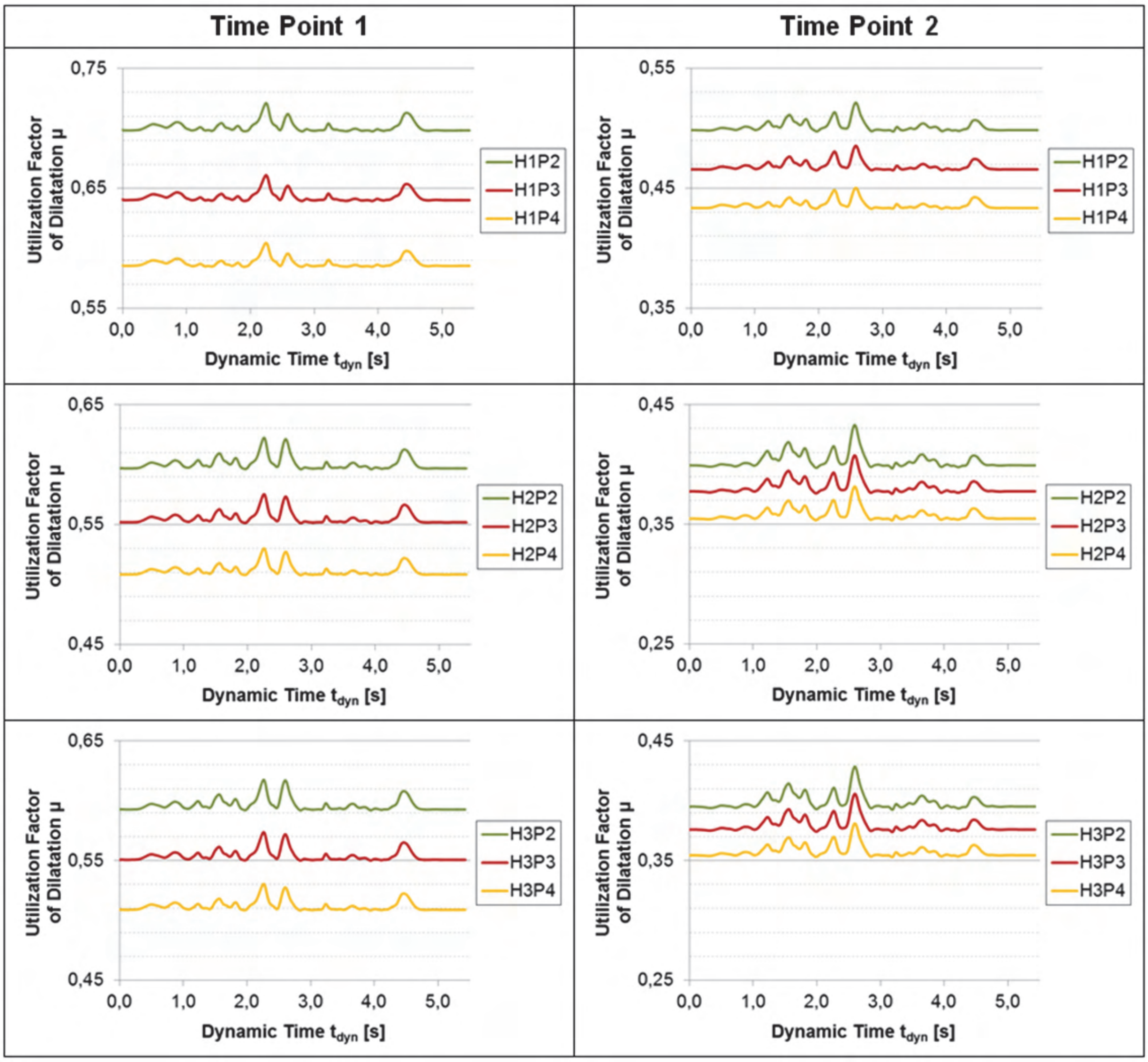

Fig. 3.4: Histories of the utilization factor of dilatation μ during the earthquake loading

The histories for σ_3 are shown in Fig. 3.5. Only small fluctuations of σ_3 are observed resulting from the seismic loads. The maximal decrease $\Delta\sigma_3$, compared to σ_3 at the beginning of the dynamic calculation, is 0.1 MPa at Point P4, Horizon 1 and Time Point 2.

The assumed pore water pressures are adopted from the VSG [MUE12a]. If the shaft sealing is intact there is a maximum p_{fl} of 4.4 MPa at the salt concrete sealing element 1,740 years after the completion. As shown in Figure 8 σ_3 already has values of 1.0 MPa to 5.0 MPa at 20 years after the completion of the shaft sealing and will continue to increase with time. An earthquake at later time will not impact the sealing element's integrity.

For the case where a malfunction in the shaft sealing element occurs a maximum pore water pressure p_{fl} of 1.0 MPa is assumed 55 years after the completion. Under these conditions the sealing elements performance will also not be impacted because σ_3 will increase during this time and $\Delta\sigma_3$ is very small with no significant decreases during an earthquake occurring at later time. It should be noted that the fluid pressure criterion in the form of Formula 3 is only valid for rock salt. For salt-concrete an influence of the tensile strength should be considered.

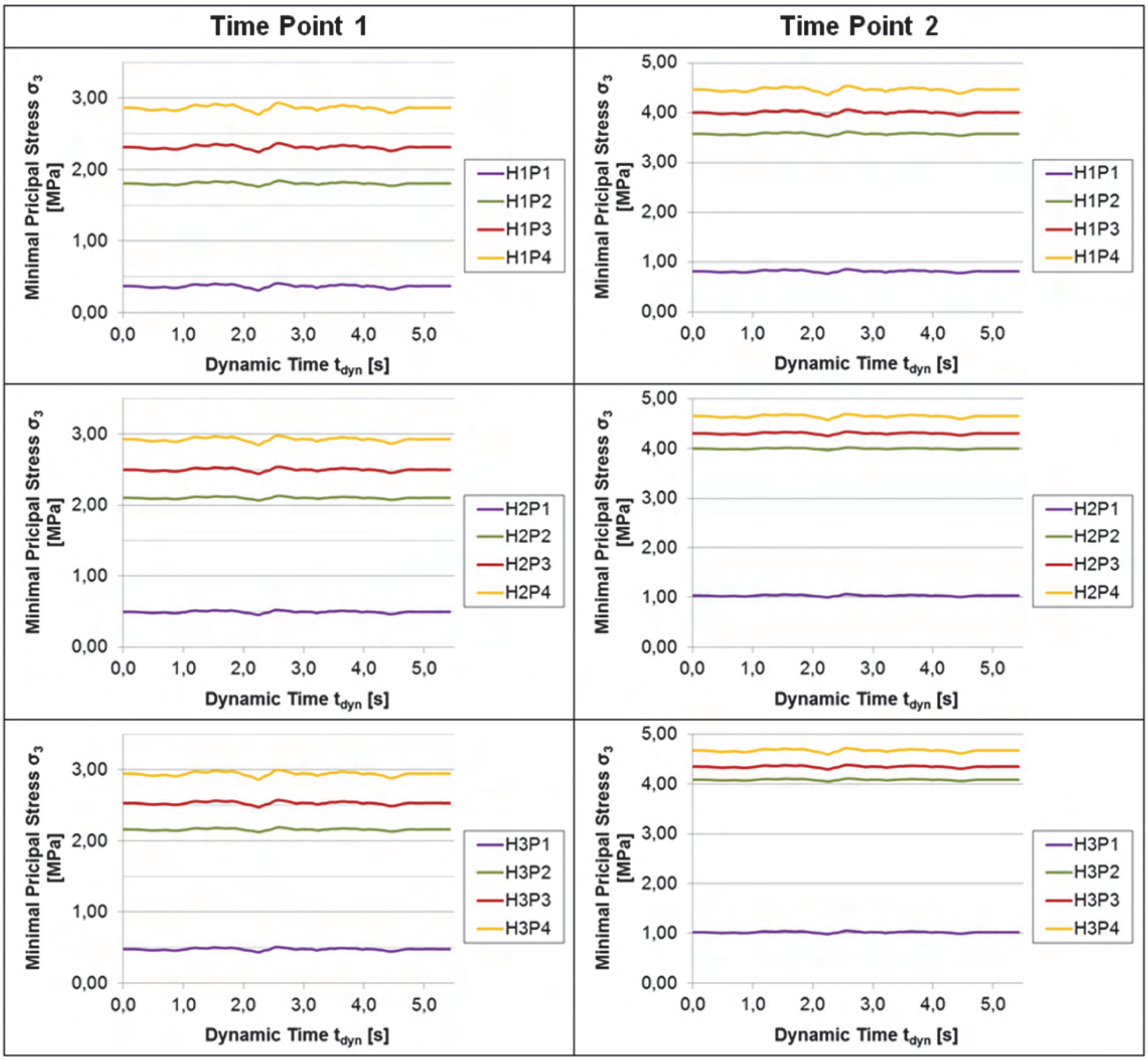

Fig. 3.5: Histories of the minimal principal stress σ_3 during the earthquake loading

Fig. 3.6 shows the loads in the sealing element for the different history locations and different points in time. The chain-dotted line represents the rupture strength boundary and the dotted line is the crack limitation boundary for the concrete. The loads during the earthquake do not change significantly and adequate space remains between the two boundaries and the loads. In this case the performance of the salt concrete sealing element is preserved.

Static material properties were used for the dynamic calculations to simplify the model. If dynamic material properties, which can be up to ten times higher than the static properties, are used during the dynamic calculations the stress amplitudes caused by the earthquake will be higher and therefore the fluctuations in the histories of μ and σ_3 will increase. With respect to the integrity of the surrounding rock salt there will be no major negative influences. With respect to the integrity of the sealing element, especially related to fluid pressure resistance, additional investigations are needed as a result of the major differences between the reduced material properties used in the calculation and the dynamic properties.

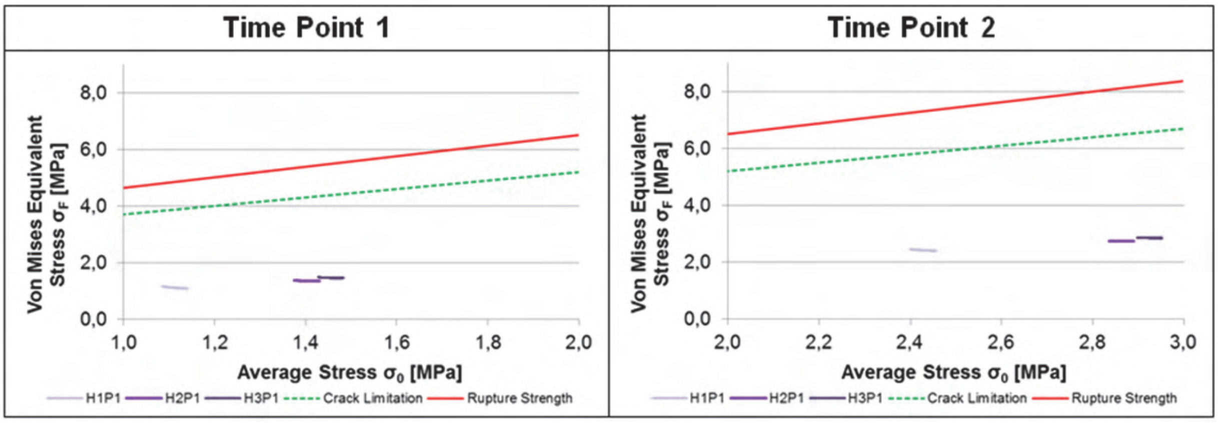

Fig. 3.6: Load in the sealing element during the earthquake loading

4 Conclusion

The results of the numerical simulation confirm the previous assumptions that an earthquake will only have a minor influence on the performance of the sealing element and the integrity will not be negatively impacted. The results are only applicable to the geological and seismological conditions at the Gorleben site or other sites with similar geological and seismological characteristics.

Although the calculation demonstrates that the performance of the sealing element is not negatively impacted during the seismic loading there is still a need for additional investigations. Following topics could be relevant for further investigations:

- Hydro-mechanical-coupled calculation to get further information’s about excessive hydrostatic pressures and their influences
- Discontinuous mechanical calculations to examine effects of the earthquake in the contact zone between sealing element and the rock
- Calculations with representing dynamic material and strength properties

5 References

[CEN10b] Norm DIN EN 1998 -1 (Eurocode 8) Dezember 2010. Auslegung von Bauwerken gegen Erdbeben - Teil 1: Grundlagen, Erdbebeneinwirkungen und Regeln für Hochbauten

[HUN94] Hunsche, U.; Schulze, O.: Das Kriechverhalten von Steinsalz. In: Kali und Steinsalz 11 (1994), Heft 8/9, S. 238-255

[ITA12] ITASCA: FLAC^{3D} - Fast Lagrangian Analysis of Continua in 3 Dimensions. Version 5.0. User's Manual. Minneapolis: ITASCA Consulting Group Inc., 2012

[KTA90] Sicherheitstechnische Regel des KTA: KTA 2201.1 - Auslegung von Kernkraftwerken gegen seismische Einwirkungen, Teil 1: Grundsätze, 1990

[LEY99] Leydecker, G.; Kopera, J.: Seismologisches Gutachten für den Standort des Endlagers für radioaktive Abfälle Morsleben. Salzgitter: Bundesamt für Strahlenschutz, 1999

[MUE12a] Müller-Hoeppe, N.; Buhmann, D.; Czaikowski, O.; Engelhardt, H. J.; Herbert, H. - J.; Lerch, C.; Linkamp, M.; Wieczorek, K.; Xie, M.: Integrität geotechnischer Barrieren - Teil 1: Vorbemessung. Bericht zum Arbeitspaket 9.2, Vorläufige Sicherheitsanalyse für den Standort Gorleben. Köln: Gesellschaft für Anlagen- und Reaktorsicherheit (GRS) mbH., 2012. -ISBN 978-3-939355-63-2

[MUE12b] Müller-Hoeppe, N.; Breustedt, M.; Czaikowski, O.; Wieczorek, K.; Wolf, J. W.: Integrität geotechnischer Barrieren - Teil 2: Vertiefte Nachweisführung. Bericht zum Arbeitspaket 9.2, Vorläufige Sicherheitsanalyse für den Standort Gorleben. Köln: Gesellschaft für Anlagen- und Reaktorsicherheit (GRS) mbH., 2012. -ISBN 978-3-939355-64-9

[NEU14] Neubert, N.: Standsicherheit und Integrität von geotechnischen Barrieren unter Erdbebeneinwirkung. Freiberg, Bergakademie, Diplomarbeit, 2014

[SEI12] Seismosoft: SeismoSignal. Version 5.0. Pavia: Seismosoft Ltd., 2012

[SEI13] Seismosoft: SeismoArtif. Version 2.1. Pavia: Seismosoft Ltd., 2013

[WOL12] Wolf, J.; Behlau, J.; Beuth, T.; Bracke, G.; Bube, C.; Buhmann, D.; Dresbach, C.; Hammer, J.; Keller, S.; Kienzler, B.; Klinge, H.; Krone, J.; Lommerzheim, A.; Metz, V.; Mönig, J.; Mrugalla, S.; Popp, T.; Rübel, A.; Weber, J. R.: FEP-Katalog für die VSG. Dokumentation. Bericht zum Arbeitspaket 7, Vorläufige Sicherheitsanalyse für den Standort Gorleben. Köln: Gesellschaft für Anlagen- und Reaktorsicherheit (GRS) mbH, 2012. -ISBN 978-3-939355-58-8

Numerical stress field modelling for potential EGS sites in Saxony, Germany

Numerische Spannungsfeldmodellierung für einen potentiellen EGS-Standort in Sachsen, Deutschland

K. Otparlik, H. Konietzky
Geotechnical Institut, TU Bergakademie Freiberg

Abstract

The paper describes calibrated 3-dimensional numerical stress field modelling for potential EGS sites in Saxony as part of comprehensive research campaign. The stress field modelling is based on the analysis of existing in situ stress measurement results, rockmechanical data and a detailed geological GIS-based model. The numerical stress field model incorporates several geological units and faults with corresponding elasto-plastic constitutive laws and parameters and considers tectonic stresses as well as pore and joint water pressures.

The model is able to predict the complete stress tensor for any arbitrary point inside the model area. Exemplary, magnitudes and orientations of the principal stresses are shown for selected vertical scan lines. Also, the stress regime at the faults is represented in form of normal stresses and the ratio between shear and normal stress, so that the potential of fault activation due to tensile or shear movement can be assessed.

The in situ stress state at 5 km depth below surface is characterized by a nearly vertical medium principal stress of about 70 to 100 MPa, a major principal stress of about 185 – 230 MPa directed NNW-SSE and a minor principal stress of about 70 - 100 MPa directed EWE-WSW, depending on the chosen parameter constellation, initial and boundary conditions as well as the specific location inside the model.

Zusammenfassung

Die Publikation beschreibt kalibrierte 3-dimensionale numerische Spannungsfeldmodellierungen für potentielle EGS-Standorte in Sachsen als Teil eines größeren Forschungsprojektes. Die Spannungsfeldmodellierung basiert auf der Analyse existierender in-situ Spannungsmessungen, gesteinsmechanischer Parameter und einem geologischen GIS-basierten Modell. Das numerische Spannungsfeldmodell beinhaltet mehrere geologische Formationen und Störungszonen mit entsprechenden elasto-plastischen Materialgesetzen und –parametern und berücksichtigt sowohl tektonische Spannungen als auch Poren- und Kluftwasserdrücke.

Das Modell erlaubt die Prognose des kompletten Spannungstensors für jeden beliebigen Punkt innerhalb des Modellgebiets. Exemplarisch werden Magnituden und Orientierungen der Hauptspannungen für ausgewählte vertikale Profillinien gezeigt. Das Spannungsregime auf den Störungszonen ist in Form der Normalspannungen

und des Verhältnisses von Scher- zu Normalspannungen dargestellt, so dass die Aktivierung von Störungszonen aufgrund von Schub- und Zugbewegungen abgeschätzt werden kann.
Der in-situ Spannungszustand in 5 km Tiefe unter GOK ist charakterisiert durch eine nahezu vertikale mittlere Hauptnormalspannung zwischen 70 und 100 MPa, eine größere Hauptnormalspannung von etwa 185 – 230 MPa NNW-SSE gerichtet und eine kleinere Hauptnormalspannung von etwa 70 – 100 MPa EWE-WSW gerichtet, abhängig von der gewählten Parameterkonstellation, den Anfangs- und Randbedingungen und der gewählten Lokation innerhalb des Modells.

1 Introduction

The mechanical as well as the HTM-coupled behaviour of rock masses is mainly governed by the material characteristics and the stress field. In general, a lot of effort is spent into the determination of material parameters and the choice or development of corresponding constitutive laws to describe the rockmass behaviour. Unfortunately, often less effort is spent for the determination of the in situ stress field, although it has a decisive impact on the general system behaviour. This is mainly because stress measurements are expensive, complicated to conduct and results are difficult to interpret.
To get a more reliable and comprehensive knowledge about the stress field, stress measurements were combined with numerical stress field modelling [e.g. Konietzky 2005]. There are several reasons, why in-situ stress field measurements should be combined with stress field modelling:

- In-situ stress field measurements are always very local 'point measurements' and do not allow to deduce complete stress fields for bigger 3D volumes.
- Evaluation of stress measurements include often several assumptions (e.g. that the vertical is a principal stress axis or material behaviour is isotropic elastic), which have to be confirmed or rejected.
- Stress field modelling in conjunction with measurements allows the separation between different stress components, e.g. tectonic, gravitational, local, regional, thermal ones.
- This procedure allows the determination of complete stress profiles, the determination of stresses outside of the investigated area and the reduction of uncertainty and variation in measurement data.

The in-situ stress is a crucial factor for EGS-systems due to the following reasons:

- The in-situ stress field determines the fracture propagation and/or fault activation during fracturing and stimulation and has therefore important influence on the location and orientation of boreholes as well as the frac design and frac pressure.
- The in-situ stress field is codetermined for the stimulation and operation parameters, including the performance and long-term behaviour of the heat exchanger.
- The in-situ stress field has influence on the occurrence and the magnitude of induced seismicity.

- In combination with the rock strength, the in-situ stress field determines the borehole stability/instability and potential necessary technical countermeasures.

The combination of stress measurements and numerical simulations, also called calibrated numerical stress field modelling, was developed in parallel in applied geology, civil engineering (especially in tunnelling), mining and underground radioactive waste storage [e.g. Konietzky & Blümling 1995, Konietzky & Rummel 2004, Konietzky 2005, Zang & Stephansson 2010]. Most reliable stress field measuring techniques, which can give both magnitudes and orientations of stresses are: hydraulic fracturing, borehole slotter, overcoring techniques and compensation methods on cores. Other techniques, like borehole breakout analysis, induced fracturing, fault plane solutions, moment tensor inversions, core splitting or geological features can act as indicators and provide only restricted, but very valuable information about the in situ stress field.

For EGS or HDR systems at great depth (several km) only hydraulic fracturing or compensation methods on core samples can be used as in-situ stress measurement techniques. In addition analysis of breakouts and induced fractures as well as analysis of natural or induced micro-earthquakes can be used as indicators. The topic ‘in-situ stress field’ in relation to EGS was already the content of several publications, e.g. Baisch et al. 2010, Bommer et al. 2006, Billaux & Konietzky 2005, Bavatzes & Hickman 2006, Faulds 2010, Kato et al. 1998, Islam 2009, Majer et al. 2007, Wong & Munguia 2006, Moeck at al. 2009, Dorbath et al. 2010, Feng & Lees 1998.

To get a general understanding about the stress regime at a more global scale, information from the World Stress Map [WSM 2011] can be used.

2 EGS site investigation program for Saxony (Germany)

The area of Freiberg (Saxony, Germany) is used as an example location to simulate the creation of a SGHE with a multitude of fractures. The subsurface of Freiberg mainly consists of gneiss with a granite intrusion, which is believed to be situated in a depth below 4000 m and 5000 m. The previously conducted research “Tiefengeothermie Sachsen” included a large-scale stress-field model of the Freiberg region revealing non-uniform stress gradients for the granite intrusion. Especially the increase of σ_3 at the transitions between granite and gneiss might act as an efficient barrier against undesired fracture propagation beyond the granite.

The rock properties of the gneiss and granite were determined by laboratory measurements analyzing samples from multiple locations in Saxony. **Fehler! Verweisquelle konnte nicht gefunden werden.** summarizes the rock properties applied to the models of the subsurface below Freiberg.

In 2009 the State of Saxony in Germany has started an initiative to set up a research and development campaign for utilizing its deep geothermal EGS potential [Felix et al. 2010]. The first phase was dedicated to the following aspects:

- Determination of thermal rock parameters
- Development of geothermal models
- Determination of in situ stress field
- Analysis of existing rockmechanical data
- Development of GIS-based geological models

The target areas are located in the 'Erzgebirge', a mountain region in the south of Saxony, which mainly consists of crystalline rocks. A guideline was elaborated to select and quantify sites best suitable for geothermal use and, hence, for baseline exploration (Wolf & Felix 2009). The site screening process resulted in three prime target areas, being close to energy consumers. Areas in Saxony exhibiting elevated natural seismicity with earthquake magnitudes Mw > 2.5 were excluded in the site selection, to minimize the risk for induced seismicity during reservoir stimulation and production/injection.

The geology of the three target areas is well known down to depths between 1000 m and 2500 m, respectively, owing to intensive exploration data available from mining of ore deposits, for which several deep boreholes also were drilled in the past. All areas are rich in tectonic features, such as fracture and fault zones, however of yet poorly known hydraulic properties.

The baseline exploration for geothermal use is targeted to 5 km depth and involves [Felix et al 2010]:

- Generation of 2D-geologic/tectonic cross sections and 3D-geologic/tectonic GIS-based models, using data from deep seismic sounding, boreholes, and underground mining
- Laboratory measurement of thermal properties (thermal conductivity and radiogenic heat production) for representative rock types and calculation of average values for thermally relevant rock complexes/stratigraphic units
- Generation of conductive temperature−depth models (2D, 3D), to identify areas, in which sufficiently high temperatures are to expected at accessible, moderate depths
- Study of the in-situ stress field conditions at the surface and at depth, to predict the local stress field, and to optimize the frac layout and, finally, the design of the underground heat exchanger
- Generation of geomechanical models for the three areas for the tailoring of stimulation techniques.

Representative for the three investigated locations, within this paper only the calibrated numerical stress field modelling for the site 'Freiberg' is presented.

3 Stress field determination

3.1 Stress field measurements and indicators in Saxony

In situ stress field data for the 'Erzgebirge' region were obtained by the following sources:

- In-situ stress measurements (overcoring and hydraulic fracturing) at several mines and construction sites with depths up to about 500 m below surface [e.g. Mjakischew 1987]
- In-situ stress measurements at a deep uranium mine near Aue with depths up to 2000 m below surface [Institut für Bergbausicherheit 1990]
- Evaluation of data from the seismic monitoring system installed at the already mentioned uranium mine (fault plane solutions for determination of principle stress directions) to observe mining induced seismicity up to a depth of about 2500 m [Konietzky & Stoll 1990]
- Evaluation of data from regional seismic network (fault plane solutions for events up to about 10 km deep) [Jakob 2010]
- Interpretation of geological indicators (strain field analysis) [e.g. Knoll et al. 1978]

The available data support the assumption, that the ‘Erzgebirge’ is characterised by a NNW-SSE orientated maximum principal stress component. The most reliable and important data were obtained by intensive stress measurements (hydraulic fracturing and overcoring) inside a uranium mine near Aue at depths up to about 2.000 m below surface as given in Table 1.

Table 1: Principal stress values measured inside the Aue granite massive at about 1.800 m below surface

	Principal stresses [MPa]	**Orientation**
σ_1	**100 – 130**	NNW-SSO
σ_2	**50 – 70**	Vertical
σ_3	**30 – 40**	EWE-WSW

Although the knowledge about the in-situ stress field in the ‘Erzgebirge’ is quite limited in general and especially to a depth of only 2000 m below surface, it seems that it confirms the general trend for Central Europe [WSM 2011] with a NW-SE to NNW-SSE direction of maximum compression.

3.2 Stress field modelling for the region ’Freiberg’ in Saxony

3.2.1 Conceptual model

A conceptual stress field model has to consider the following aspects:

- Choice of suited numerical simulation technique and code
- Incorporation of geological layering and formations (stratigraphy)
- Considering of discontinuities, like faults, fractures, interfaces etc.

- Choice of appropriate constitutive laws and parameters for describing the geological units and discontinuities
- Considering of groundwater
- Considering of topography
- Incorporation of geological history, especially erosion (overconsolidation effect)
- Choice of appropriate boundary conditions, especially tectonic stresses
- Consideration of available measurement results and indicators for calibration
- Determination of appropriate model dimensions and meshing

Because the fracture / fault systems play an important role for the stress state, the Discrete Element Code 3DEC [Itasca 2007] was chosen for the simulations. Different elasto-plastic constitutive laws were applied with parameters based on lab testing results and rock mass classification to take into account the scale effect. The model consist of a dense meshed inner part, which contains the potential heat exchanger and the borehole locations and a surrounding area to guarantee, that boundary effects do not influence the results inside the inner model area. The corresponding appropriate model dimensions were obtained by preceding 2- and 3-dimensional numerical studies. At the outer model boundary tectonic stress components were applied. Available measurements were used for model calibration.

3.2.2 Numerical model set-up

The model region ‘Freiberg’ has a complex joint structure and is divided into two rock materials, namely gneiss and granite. The joint structure was provided by DXF format. The model was prepared using GOCAD (Paradigm 2010), and the final DEM model was generated using the mesh generation software KUBRIX (Simulation Works 2010). The basic model was rotated by 20° and enlarged by adding auxiliary blocks with triangular shaped base to enable the implementation of the maximum horizontal principal stress in the direction of 20° NW. Further enlargement in the horizontal direction was necessary to ensure the generation of a correct stress field inside the inner model area. The whole model has a horizontal extension of 54 by 57 km with a depth of 10 km and encompasses about 7700 blocks meshed into 2.65 million zones. The size of the inner model is 10 by 15 km and the joint structure reaches down to 5 km. Figures 1a-d show the inner model in form of the block structure, the whole model as a numerical block model, the distribution of the material types inside the inner model and the joint structure of the inner model, respectively.

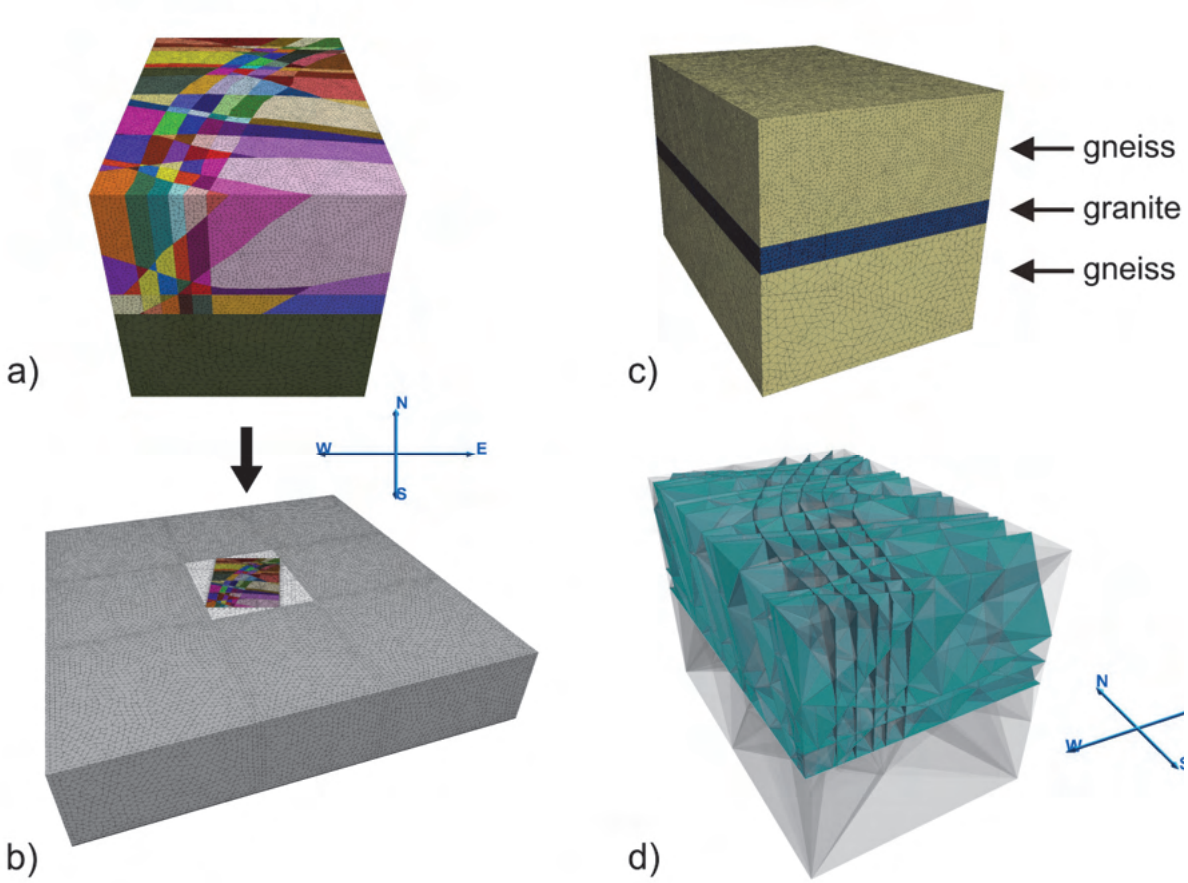

Fig. 1: a) The inner model with block structure. b) The whole model in block structure. c) The location of different materials inside the inner model, d) The joint structure of the inner model.

Due to the limited data base and the need to check the model response, a parameter study was carried out. The initial stress state of the model was set taking into account the material density and gravity and a coefficient of lateral earth pressure of 0.5. The influences of

- the boundary conditions
- the joint parameter set
- the Young’s modulus,
- the pore and joint water pressure
- application of tectonic stresses

were investigated by calculating the model in a multiplicity of combinations of these factors.

Same constitutive models were used for all calculations. The granite matrix was modelled with an elasto-plastic Mohr-Coulomb material model with tension cut-off and the gneiss matrix was modelled with a ubiquitous joint material model [Itasca 2007] taking the foliated rock structure into account. The corresponding material parameters are listed in Table 2. The joints in the model can be divided into four joint classes namely North-East joints, non-North-East joints, joints between granite and lower gneiss blocks and auxiliary joints. The parameters for the faults, characterized by normal and shear stiffness and a Coulomb friction law are given in Table 3.

Tab. 2: Matrix material parameters.

Gneiss (Ubiquitous joint material model)		**Granite (Mohr-Coulomb material model)**	
Density	2700 kg/m³	Density	2660 kg/m³
Young’s modulus	55,000 MPa	Young’s modulus	65,000 MPa
Poisson's ratio	0.30	Poisson's ratio	0.22
Matrix		Cohesion	37.8 MPa
Cohesion	30.5 MPa	Friction angle	40.8 °
Friction angle	35.3 °	Dilatancy angle	20 °
Dilatancy angle	17 °	Tensile strength	1.5 Mpa
Tensile strength	1.0 MPa		
Joints of foliation			
Cohesion	26.5 MPa		
Friction angle	31.9°		
Dilatancy angle	15°		
Tensile strength	0.7 MPa		

The parameter study revealed four calculation cases, which were found to map the stress field satisfactorily. In the following, one of the four cases and its results are presented in more detail.

On all four model sides a stress boundary condition was applied, where the ratio of the maximum horizontal to minimum horizontal to vertical stress equals 1.5 to 0.5 to 1. A thin auxiliary layer at the bottom of the model, of which only a thin belt is fixed, prevents the model from rotation (Fig. 2). A pore and joint water pressure was applied. The Young’s modulus E was inscribed in the model as a quadratic function of the depth z using the following formula.

$$E(z) = \sqrt{\frac{z - z_{max}}{a}} + \frac{1}{10}E_{rock}, \quad a = (z_{min} - z_{max})/(E_{rock} - \frac{1}{10}E_{rock})^2,$$

where z_{min} and z_{max} are the minimum and maximum z-coordinates of the model, and E_{rock} is the Young’s modulus of the respective material gneiss or granite.

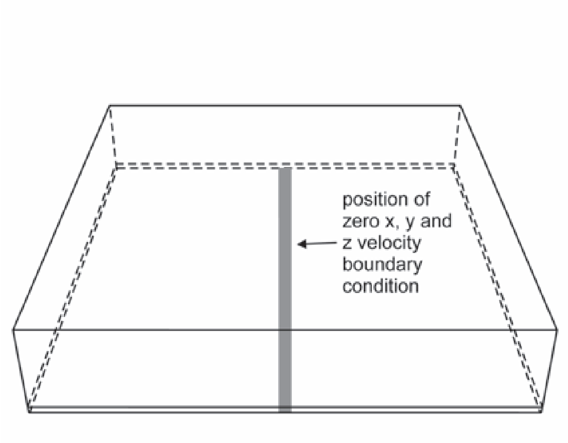

Fig. 2: Model with auxiliary layer at the bottom and corresponding boundary condition to prevent the model from rotation.

Tab. 3: Joint parameter set

Joint parameter	NE-joints	Non-NE-Joints	Joints between granite and lower gneiss	Auxiliary joints
Friction angle (°)	35	40	40	20
Normal and shear joint stiffness (MPa/m)	74.0	74.0	74.0	740.4
Cohesion (MPa)	0	0	0	1e10
Tensile strength (MPa)	0	0	0	1e10

3.2.3 Stress field modelling results

The obtained 3-dimensional stress field was plotted in two ways, as contour plots of planar sections through the model and as diagrams of profile or scan lines in z direction. The latter method was tested for accuracy as it only is possible to obtain the stress values at the position of the respective zone center due to the discretization of the model. Fig. 3 shows an example of a profile line position and the corresponding zone centres next to the profile line. In the lower part of the model the distance between profile line end zone center is up to 150 m long, as the lower part of the model is meshed coarser than the upper part, where this distance is always smaller than 100 m. Exemplary, Fig. 4 shows a principal stress profile line diagram and the corresponding distances of the data points from the profile line position are plotted. It clearly can be seen, that the distance from the profile line position does not influence the stress diagram significantly. Along the scan line shown in Fig. 5 the complete stress profiles in terms of magnitude and orientation of the principal stresses are plotted (Fig. 6 - 8) including the ratio between maximum and minimum principal stress. Dip is measured from vertical, Dip direction is measured clockwise from North. The presented results are based on a calculation case, which assumes hydrostatic pore and joint water pressure.

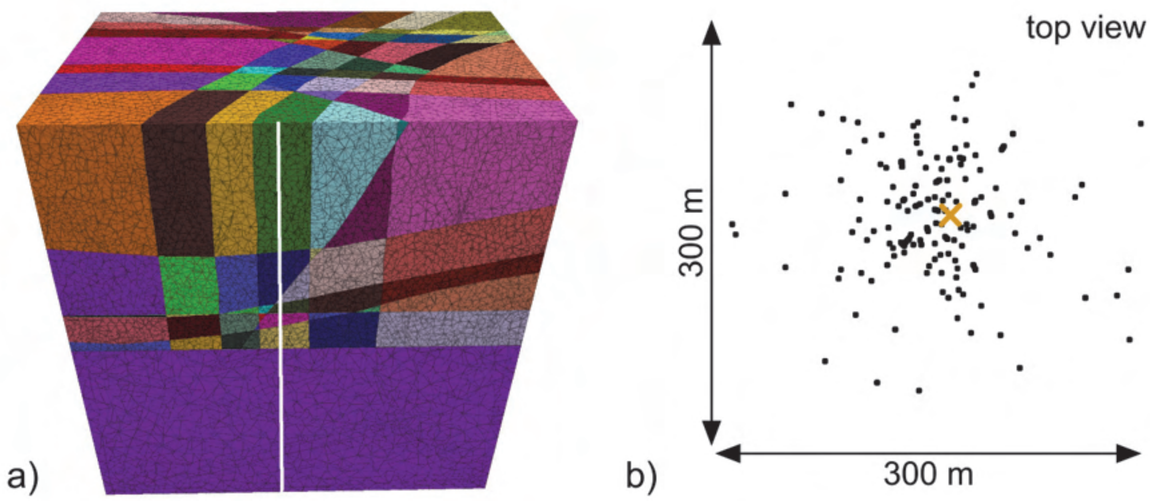

Fig. 3: a) Example of a profile line positioned in the model. b) Top view of the profile line (cross) and corresponding zone centre positions of all zones nearest to the profile line. The zone centre positions far away from the profile line stem from zones in the lower half of the model which is meshed with a bigger zone edge length.

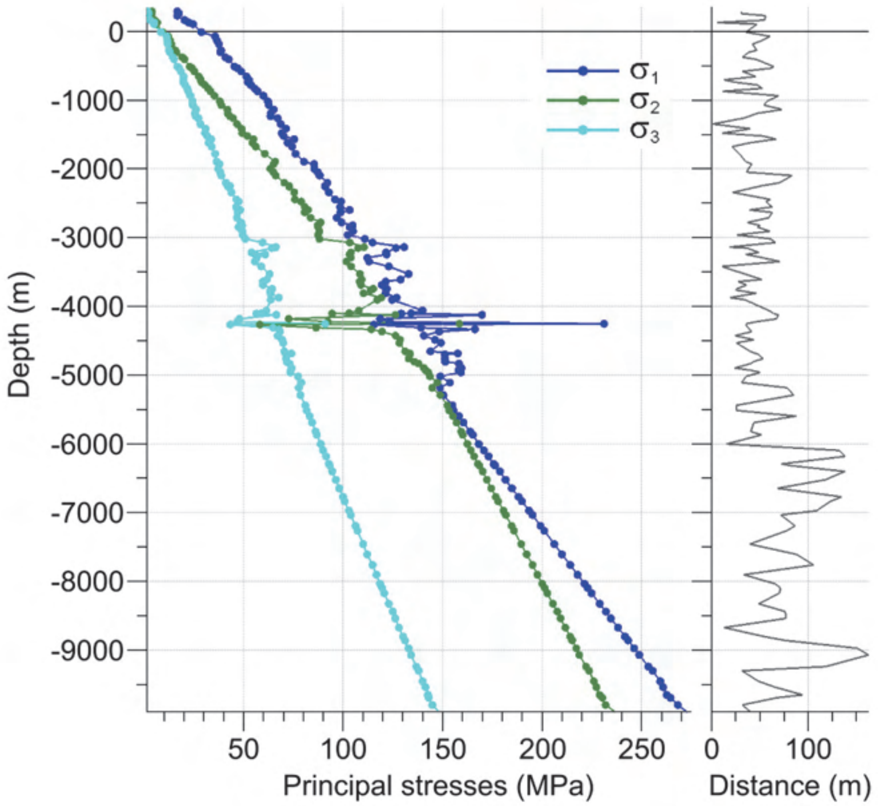

Fig. 4: Example profile line diagram of the principal stress magnitudes (left) and the corresponding absolute data point distances from the profile line position (right). The distances at a depth of 6000 m and more are bigger because the zones are bigger in this region of the model.

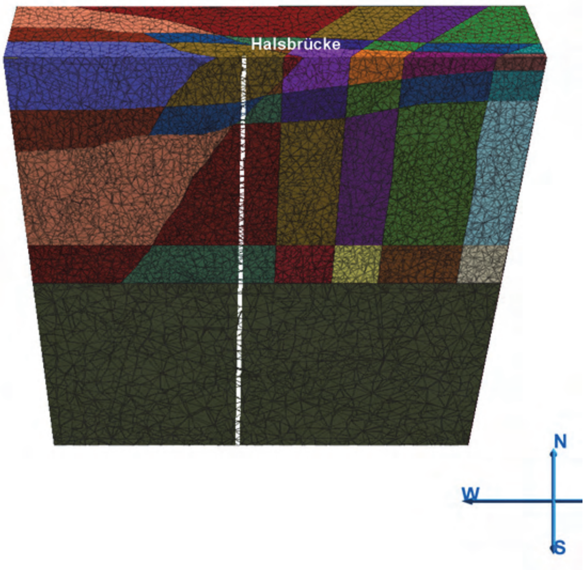

Fig. 5: Positions of the profile lines ‘Halsbruecke’

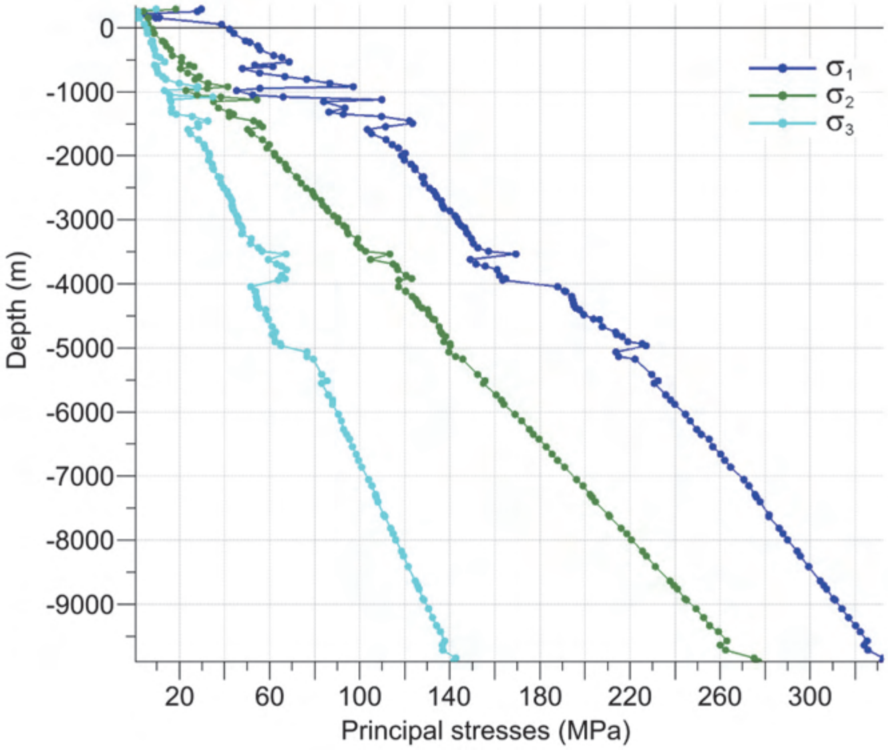

Fig. 6: Profile line diagram of the principal stress magnitudes at the profile point ‘Halsbruecke’

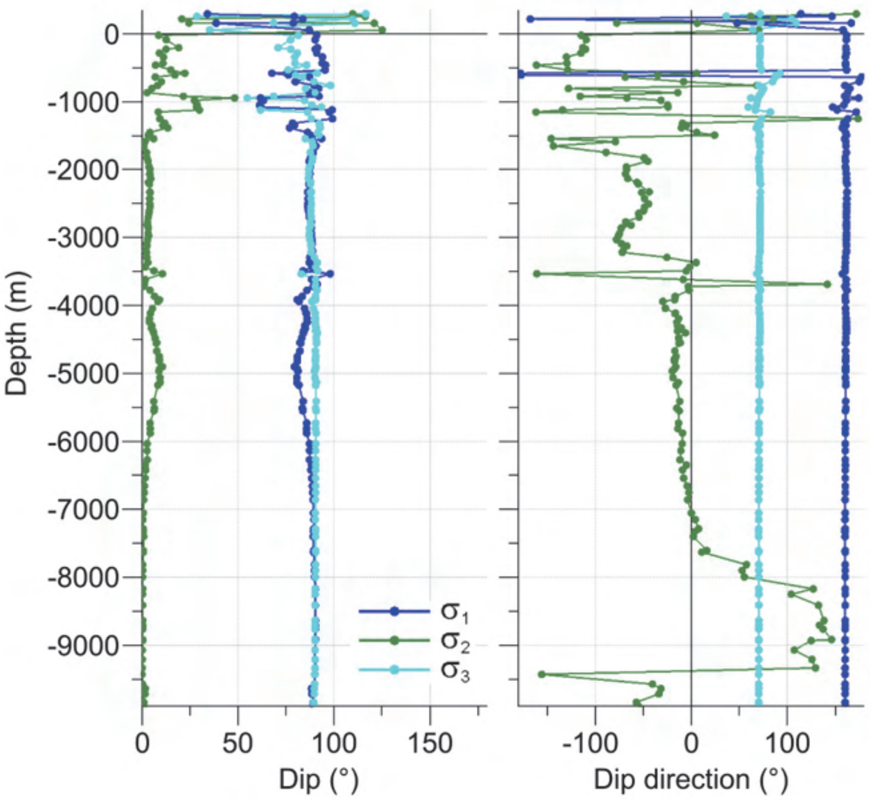

Fig. 7: Profile line diagram of the principal stress directions at the profile point 'Halsbruecke'

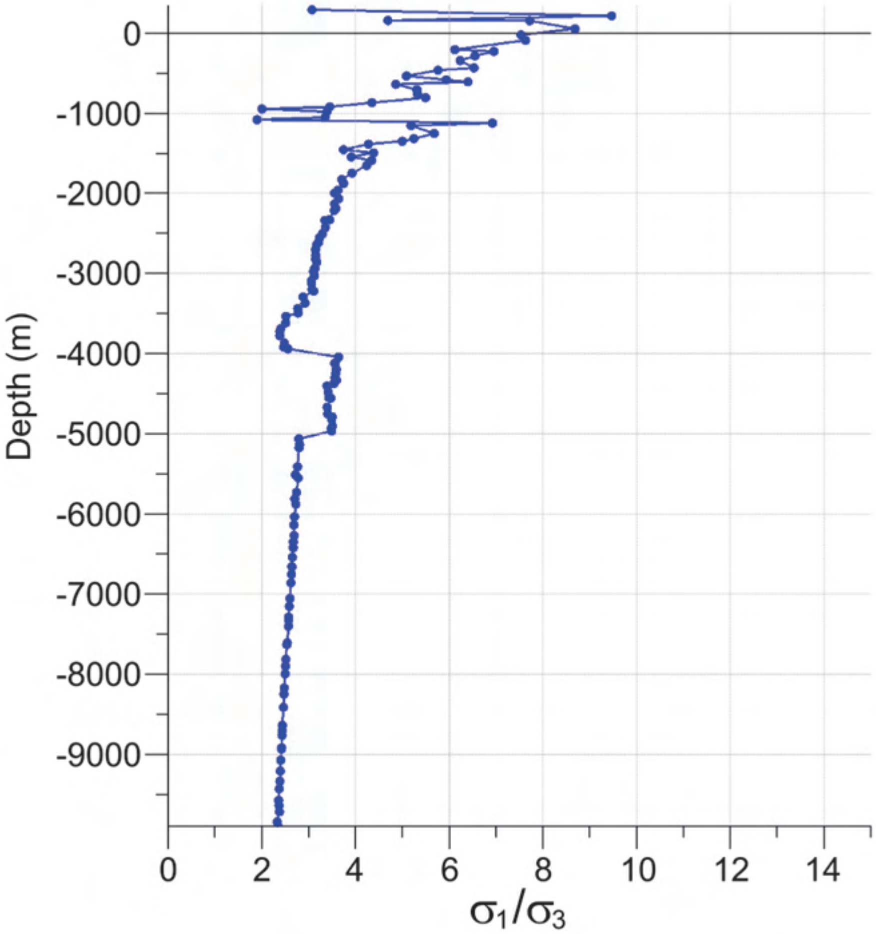

Fig. 8: Profile line diagram of the ratio between maximum and minimum principal stress at the profile point ‘Halsbruecke’

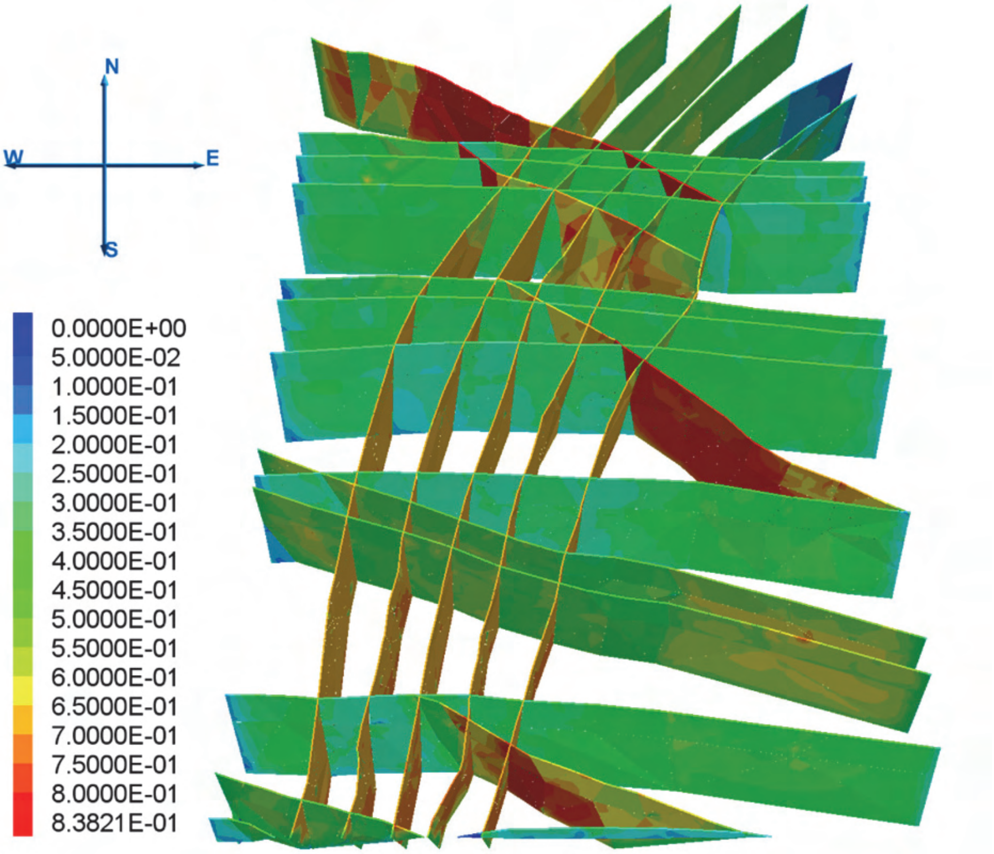

Fig. 9: Contour plot of the ratio of joint shear force to joint normal force ("slip tendency") for the depth range from 3500 m to 5000 m below surface.

3.2.4 Discussion of results

The 3-dimensional numerical stress field model allows to predict the complete stress tensor for any point inside the inner model area. The model was successfully calibrated, in which especially the measurement results from the deep uranium mine were used. The intermediate principal stress component is almost vertical and corresponds to lithostatic pressure. The model shows a predominant NNW-SSE orientation of the maximum principal stress. The ratio between maximum and minimum principal stress, as exemplary shown in Fig. 8 reveals a decreasing ratio, which converges towards about 2 at great depth, but can reach much bigger values close to the surface. Here it should be mentioned that the model results due to the relatively coarse meshing very close to the surface (app. upper 500 m) are not very reliable.

There is significant local increase in stresses between 4 and 5 km depth, which is caused by the assumed granitic intrusion. Local stress field rotations, as shown in Fig. 6 and 7, are generated by the fault systems, which were cut by the scan lines at different depths and positions. The virgin stress state at about 5000 m below surface (potential location of heat exchanger) can be characterized as follows:

σ_1	185 – 230	NNW-SSE
σ_2	130 – 140	Vertical
σ_3	70 – 100	EWE-WSW

The stress state can be characterized as strike-slip. In general, the normal stresses increase with depth and show a strong dependence on the strike as well as local variations due to slip along the faults. To open the existing faults pressures between 90 and 150 MPa, depending on the strike of faults are necessary. Fig. 9 shows the ratio between shear and normal stress. This ratio can be used to characterize the potential of slip along the faults (“slip tendency”). High values indicate bigger potential for slip. Biggest values are observed for the faults with NNE-SSW strike, where the ratio is between 0.7 and 0.8, which corresponds to a friction angle between 35° and 38°.

4 Conclusions

Based on a detailed analysis of existing stress measurement results, additional stress field indicators and comprehensive numerical pre-studies, calibrated 3-dimensional numerical stress field models for three pre-selected sites for a potential EGS were established and evaluated. The models, based on the Discrete Element Method, incorporate the influence of the inhomogeneous isotropic and anisotropic elasto-plastic rockmass behaviour and include in an explicit manner the influence of faults, the effect of pore and joint water pressure as well as the action of tectonic forces. The models allow the prediction of the complete stress tensor for any point of interest inside the modelled region. The predicted stresses can be used for several geomechanical and reservoir-engineering purposes, like the assessment of borehole stability, the optimal orientation of boreholes, the determination of frac pressures, the direction of fracture propagation or the stability / activation potential of fault systems during a potential stimulation process and assessment of potential of induced seismicity.

Acknowlegment

The research was supported by the State of Saxony and was performed within the activities of the research group ‘Forschungsverbund Tiefengeothermie Sachsen’.

References

Baisch, S et al. (2010): A numerical model for fluid injection induced seismicity at Soultz-sous-Forets, Int. J. Rock Mechanics and Mining Sciences 47: 405-413

Baisch, S, Vörör, R. & Weidler, R. (2009): Investigation of fault mechanisms during geothermal reservior stimulation experiments in the Copper Basin, Australia, Bulletin Seismological Society America, 99(1): 148-158

Billaux, D., Konietzky, H. (2005): Key issues in discontinuum modelling of flow in fractured media, Barla G. & Barla, M. (Ed.): Proc. 11th International Conference of the International Association of Computer Methods and Advances in Geomechanics (IACMAG), June 2005, Turin, Patron Editore, 361-371

Bommer, J.J. et al. (2006): Control of hazard due to seismicity induced by a hot fractures rock geothermal project, Engineering Geology 83: 287-306

Davatzes, N.C. & Hickman, S.H. (2006): Stress and faulting in the Coso geothermal field: update and recent results form the esat flank and coso wash, 31. Workshop on Geothermal Reservior Engineering, Standford University, SGP-TR-179

Dorbath, L. et al. (2010): The stress field at Soultz-sous-Forets from focal mechanism of induced seismic events: Case of the wells GPK2 and GPK3, C. R. Geoscience, doi:10.1016/j.crte.2009.12.003

Faulds, J et al. (2010): Structural assessment and 3D geological modelling of the Brady's Geothernal Area, Churchill County (Nevada, USA): a preliminary report, Proc. 35. Workshop on Geothermal Reservior Engineering, Stanford University, SGP-TR-188

Felix, M., Förster, A., Förster, H.-J., Konietzky, H., Wagner, S. (2010): Exploration strategy for a deep EGS development in low-permeable crystalline rocks (Germany), GRC Transactions 34: 335-338

Feng, Q. & Lees, J.M. (1998): Microseismicity, stress and fracture in the Coso geothermal field, California, Tectonophysics 289: 221-238

Institut für Bergbausicherheit Leipzig (1990): Geomechanische Untersuchung zur Gebirgsschlagsgefährdung auf der Lagerstätte Aue-Alberoda

Islam, R. (2009): Origin of the regional stress field along the Liquine-Ofqui Fault Zone (LOFZ), Southern Chilean Andes by means of FE simulation, Journal Material Sciences 6: 1-13

Itasca (2007): 3DEC Manuals; Vers. 4.1, Itasca Consulting Group, Inc. Minneapolis, Minnesota, USA

ITASCA (2010): 3DEC, Vers. 4.1, Itasca Consulting Group, Inc., Minneapolis, Minnesota, USA

Jakob, Ch. (2010): Herparameterbestimmung von erdbeben zur seimotektonischen Analyse in der Schwarmbebenregion Vogtland/NW-Böhmen. Diplomarbeit, TU Bergakademie Freiberg

Kato, O. et al. (1998): Fracture systematics in and around well WD-1, Kakkondo Geothermal Field, Japan, Geothermics 27(5/6): 609-629

Knoll, P. et al. (1978): Spannungsverteilung im Südosten der DDR, abgeleitet aus direkten Untertagemessungen und rezenten Krustenbewegungen, Neue Bergbautechnik 7 S. 366-370

Konietzky, H. & Blümling, P. (1995): In situ stress field in the Wellenberg area Nagra Bulletin Nr.26, 38-47

Konietzky, H. & Rummel, F. (2004): In situ stress field measurements and stress field modelling, 2nd Colloquium Rock Mechanics - Theory and Practice, Mitteilungen für Ingenieurgeologie und Geomechanik der TU Wien, Band 6, 46-54

Konietzky, H. & Stoll, R. (1990): Classification of seismic events in a mining area in the Erzgebirge mountains of the GDR. Gerlands Beitr. Geophysik, 99(2): 169-174

Konietzky, H. (2005): Numerical stress field modelling for underground structures, in: F. Rummel (ed.): Rock mechanics with emphasis on stress, Oxford & IBH Publishing Co. Pvt. Ltd, New Dehli, 55-80

Konietzky, H. et al. (2001): Numerical modelling of in situ stress conditions as an aid in route selection for rail tunnels in complex geological formations in South Germany, Computers and Geotechnics, 28: 495-516

Majer, E.L. et al: (2007): Induced seismicity associated with Enhanced Geothermal Systems, Geothermics 36: 185-222

Mjakischew (1987): Untersuchung des Gebirgsspannungszustandes im Südostteil der DDR, Freiberger Forschungshefte A740, Beiträge zur Gebirgsmechanik, VEB Deutscher Verlag für Grundstoffindustrie, Leipzig

Moeck, I., Kwiatek, G. & Zimmermann, G. (2009): Slip tendency analysis, fault reactivation potential and induced seismicity in a deep geothermal reservior, Journal of Structural Geology 31: 1174-1182

Paradigm (2010): GOCAD Manuals, George Town, Cayman Islands

Simulations Works (2010): Kubrix Manuals, Simulation Works Inc., Saint Paul, Minnesota, USA

Simulations Works (2010): Kubrix, Simulation Works Inc., Saint Paul, Minnesota, USA

Wong, V. & Munguia, L. (2006): Seismicity, focal mechanism, and stress distribution in the Tres Virgenes volcanic and geothermal region, Baja California Sur, Mexico, Geofisica International, 45(1): 23-37

WSM (2011): www.world-stress-map.org, 15.08.2011

Zang, A. & Stephansson, O. (2010): Stress field of the earth's crust, Springer, 322 p.

Progress in underground clean energy: an introduction to 111 project

Fortschrittsbericht zum 111-Projekt: Saubere unterirdische Endergie

Renshu YANG, Jie LIANG, Zhongwen YUE
China University of Mining & Technology, Beijing, China

Abstract

This paper is the basis for a course dedicated to the development of underground clean energy in China, taking into account Underground Coal Gasification environment studied by China University of Mining and Technology (Beijing). A number of correlated questions are discussed in this paper : 1) the significance of the development of underground coal gasification in China; 2) the principle and implementation process of underground coal gasification; 3) the actual research and development of the underground coal gasification technology; 4) mechanical properties of coal and rock and expansion law of combustion space area at high temperatures; 5) the broad development prospects of the underground coal gasification in China.

Zusammenfassung

Diese Publikation betrachtet die Entwicklung von Technologien zur Nutzung von sauberen (‚grünen‘) Energien im untertägigen Bereich, insbesondere die untertägige Kohlevergasung, die seitens der Chinesischen Universität für Bergbau und Technology (Beijing) untersucht wird. Mehrere diesbezügliche Fragen werden diskutiert: 1) die Bedeutung der Entwicklung der untertägigen Kohlevergasung in China; 2) Prinzip und Implementierungsprozess der untertägigen Kohlevergasung; 3) aktuelle Forschungen und Entwicklungen zur Technology der untertägigen Kohlevergasung; 4) mechanische Eigenschaften von Kohle und Nebengestein und Expansionsgesetz im Verbrennungsraum bei hohen Temperaturen; 5) großartige Entwicklungsperspektiven für die untertägig Kohlevergasung in China.

1 Introduction

The Programme of Introducing Talents of Discipline to Universities (Referred to as the "111 Project") aims to advance the process of building Chinese world-class universities. This project is jointly implemented by Ministry of Education and State Administration of Foreign Expert Affairs of the People's Republic of China from 2006. The "111 project" aims at the international forefront of academic development, based on national key disciplines, from advantage multidisciplinary teams in the world's top 100 well-known universities and research institutions more than 1,000 talents are introduced and brought together, so a high-level research team is formed and about 100 world-class talent recruitment bases of discipline innovation are constructed[1].

On October 14, 2013, Ministry of Education and State Administration of Foreign Experts Affairs of the People's Republic of China approved China University of Mining and Technology (Beijing) to establish innovation and talent recruitment base of "the fundamental research on underground clean energy development”. Based on coal and gas extraction (including CBM), coal mine geothermal resource development and coal gasification as engineering background, this base focused on study of common basic scientific issues, such as the multi-physics multiphase coupling. The purpose is the initial formation of the system about production, storage and utilization of underground clean energy development.

The following presents underground coal gasification in China which is one of the project research fields.

2 The significance of the development of underground coal gasification in China

In China coal accounted for about 70% in primary energy is the main energy. Coal occupies an irreplaceable role in China's primary energy structure for a long time in the future because of resource conditions. But the coal resources waste and ecological environmen destruction caused by traditional coal mining, transport, usage can not be ignored. Ground subsidence, a large amount loss of groundwater, smoke and sulfur compounds discharged into the atmosphere, and so on, have given a greater threat to the ecological environment in some areas. Meanwhile, due to limitations of the level of underground mining technology, about 50% of abandoned coal resources in the underground caused a large number of coal waste. Underground coal gasification not only can recycle resources in old abandoned coal mines, but can also be used to mine in difficult underground conditions, poor security thin seams, deep coal seams, coal with high-sulfur and high-ash, high gas coal seams and so on, which greatly improves the utilization of coal resources[2]. Burning ash during underground coal gasification process is left in the ground that greatly reduces the amount of surface subsidence and emissions of no solid matter. Outlet coal gas can be concentrated purification for the removal of tar, sulfur and dust and other harmful substances through underground coal gasification so that clean coal gas can be obtained. The gas not only can be used as fuel for civilian, power generation, industrial boilers burning, but also as a raw material gas for production of synthetic ammonia, methanol, dimethyl ether, gasoline, diesel, or for extracting pure hydrogen. Therefore, underground coal gasification technology that will focus on the source of environmental protection, rather than the treatment of end is an environment-friendly green technology with the sustainable development and has significant economic and social benefits[3-4].

3 Principle and implementation process of underground coal gasification

Underground coal gasification is the process of combustion control in underground coal, combustible gas produced by thermal effects and chemical effects on the coal[5]. This process is mainly done in the gasification passage of underground gasification furnace, as shown in Fig.1.

The gasification agent bubbled through the pores (active ingredients are O_2 and H_2O (g)) ignite seams on the inlet side. Meanwhile, combustion of O_2 and coal can produce CO_2 and release large amounts of reaction heat induced to so hot coal seams in the reducing zone. When the concentration of O_2 in the flow is close to zero, the oxidation zone will end. In reducing zone CO_2 and hot C is reduced to CO and H_2O (g) and hot C is reduced to CO, H_2, and so on. Since the reducing reaction is an endothermic reaction, the temperature of airflow coal seams is gradually reduced. Until the temperature is lower to not be carried out reducing reaction, the reducing zone ends. At this time air temperature is still high and coal seams in the downstream (retorting drying zone) are heated so that pyrolysis gas is released. After three reaction zones, coal gas containing combustible components of H_2, CO and CH_4 is mainly generated and gasification reaction zone is gradually moving to the outlet, thus a continuous reaction process of the gasification is maintained. This shows that the combustible gases are mainly produced from three aspects: decomposition of water vapor, reduction of CO_2 and pyrolysis of coal, and the effect degree of these three aspects is directly proportional to the reaction zone temperature and the specific reaction surface area and also decided the gas composition and calorific value in outlet. The material basis of underground gasification is underground gasification of four elements: inlet passage, outlet passage, gasification passage and airflow passage. Underground gasification can be divided into well type and no well type according to construction methods. Well type means gasification constructions are conducted in the underground, and inlet passage and outlet are wellbores respectively, while gasification passage is coal roadway of artificial excavation. No well type is that all furnaces works are built on the ground, and inlet and outlet passages are drilled from the ground[6].

Underground coal gasification and ground gasification are different that: (1) the material layer (coal seams) of underground gasification does not move, but gasification face moves with time and space; (2) gas-solid phase can even contact and each reaction zone in the bed stably distribute during ground fixed bed gasification, whereas each reaction zone of underground gasification not only extends in the transverse, but also vertically expands in solid coal, so that reaction area are constantly changing; (3) After the anti-zone extends an extent in the underground gasification process, due to the restrictions of seam thickness, gasification structure (hole spacing) and coal seams permeability, gasification zone will generate defects and roof fall which that leads to inert rocks and water into, as shown in Fig.2, and affects temperature and effective gas-solid reactions in the gasification zone.

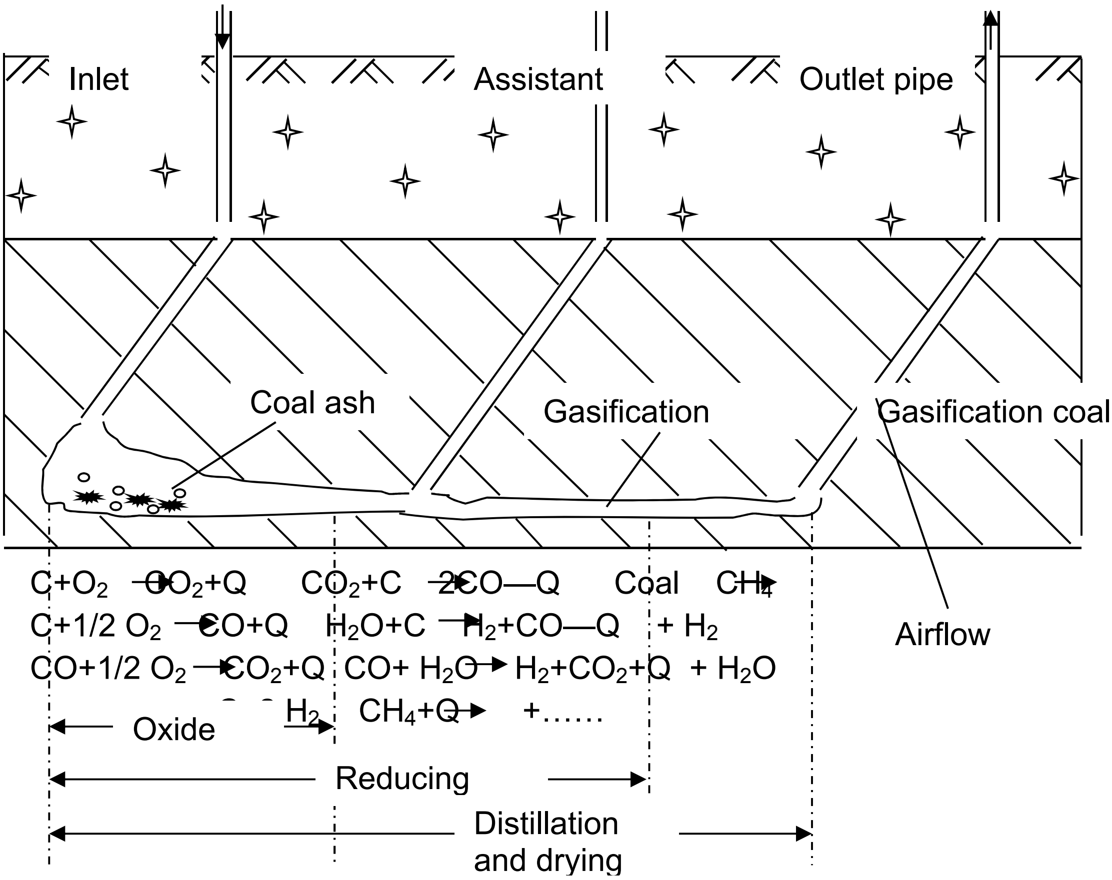

Fig.1 Schematic diagram of Underground Coal Gasification

On the other hand, inorganic and organic contaminants (including tar, polycyclic aromatic hydrocarbons, sulfur, nitrogen, heavy metals) are inevitably generated in the oxidation, reduction and carbonization process of coal seams, that in gas, condensate, and gasification ash are enriched and possibly migrated into the surrounding geologic bodies and at last affect underground environment, as shown in Fig.3. So we must master the law of these contaminants enrichment and migration, then control and governance in order to ensure long-term operation of underground gasification.

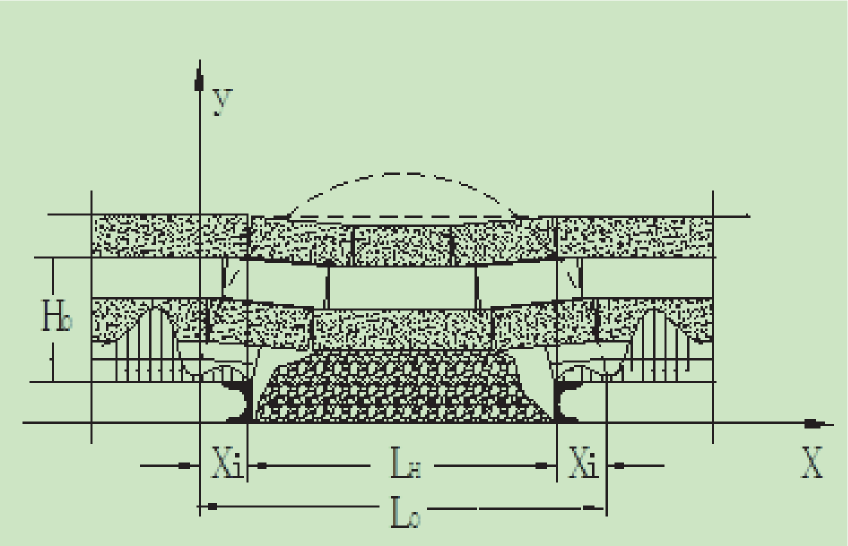

Fig.2 Schematic diagram OF roof falling and water intrusion

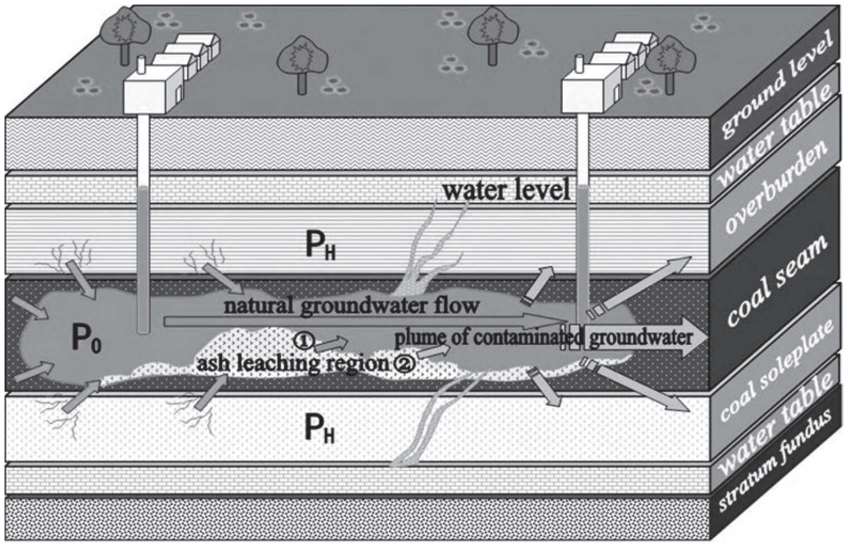

Fig.3 Schematic diagram of contaminant migration

4 The development of underground coal gasification in China

The earliest recorded tests of underground coal gasification in China was in 1958. Between 1958 and 1962, several underground tests were conducted in Chinese mines either by natural burning process (e.g. the mines in the regions of Chinese province Shanxi-Datong city, south of province Anhui, and north of Shenyang city) or by mining gallery (e.g. Yilan mine in the province of Heilongjiang, Hebi’s 3rd mine in Henan province, and Xinmi mines also in Henan).

In 1984, China University of Mining and Technology formed the first and only Chinese research center aiming to study the underground coal gasification test in laboratory conditions. This center was proposed by Prof. Yuli, supported by National High Technology Research and Development Program of China (863 project). The center equipped a world advanced test platform with synthetical and complete measurement system. Numerous tests were performed to study the change of temperature, concentration of gas, the rapidity, ratio of the gasification reaction, the propagation of cavity due to combustion, the stability, the advancement of measurement, and the method to reduce CO_2 during coal gasification, etc. Five in-situ tests with large scale were also performed in parallel to verify the theory acquainted with laboratory tests.

The center in Beijing, submitted to China University of Mining and Technology (Beijing), has also advanced significantly the technology of underground coal gasification. After summarization of worldwide development in the coal gasification, it has principally advanced the technology by three points: i) two-phase-gasification in large section coal gallery of long distance; ii) separate infiltration of air rich oxygen and rich vapor; 3) proposition of the catalysis of underground coal gasification; 4) proposition of industrialization of underground coal gasification. Note, that the catalysis and industrialization of underground coal gasification is a firstly proposed worldwide. This implies the self-confidence for its advanced technologies[7].

4.1 Two-phase-gasification in large section coal gallery of long passage

Gasifier structure concerned about long passages and large section is integrated gasifier mixed together no well type and well type. Inlet passage and outlet passage can be drilled from ground and also by means of existing well and roadway. The workers can construct gasification passages and flow passages in the underground, so gasifier construction of long passages and large section does not require special technology. Gasification passages section can be done about 3 m^2 and the length is more than 100 m in general according to coal seam conditions.

Underground coal gasification process of two stages is a gasification method that circulates the supply air (or pure oxygen, oxygen-enriched air) and water vapor. Each cycle consists of two stages, that is to say, the first stage is a combustion heat storage inlet air (oxygen) and production gas phase, and the second stage is production phase of pyrolysis gas and water gas by vapor[8-9].

Several field tests and application of "long passages, large cross-section and two stages" were carried out, respectively: semi-industrial and industrial tests of underground coal gasification in Xuzhou New River II well in 1994, Lizhuang Coal Mine in 1996, Suncun Coal Mine in 2000.

4.2 Separate infiltration of gas rich oxygen and rich vapor

To further enhance the continuity and controllability of underground coal gasification process, Underground Gasification Engineering Research Center of Coal Industry raised and strengthened the research of new technology - separate control injection gas points enriched oxygen -water vapor. Spontaneous combustion at hole bottom of the air intake tunnel are found in underground gasification test due to contact the gasification agent in the past, so this affects the normal conduct. The method to solve this problem is that gasifying agent is not directly into the roadway, and the oxygen is into the pipe, water vapor is supplied outside the tube. This method is difficult to achieve continuous operation of gasification, and after a period of time of gasification the gas injection point is moved some distance backwards, gasification continues. But the technology of separate control injection gas point can be a good solution to this problem.

4.3 Catalysis processes of underground coal gasification

Underground coal gasification is that during the gasification process a special device is used to add catalyst, through changing the reaction pathway, lowering the activation energy, accelerating the reaction, so that the gas composition, calorific value and gas production rate have been further improved. During underground coal catalytic gasification process the main technical problems are that what catalyst is selected, how pretreatment is conducted before the catalyst is added, how the catalyst is brought into the underground and whether the catalyst sufficiently is mixed with underground coal seams. The calcium salts are chosen as catalyst of underground gasification. In catalytic gasification of the ground catalyst adding methods mixed in advance a certain amount of the coal feed and the catalyst are mainly dry mix, wet impregnation and ion exchange. However, during underground coal gasification the coal directly is gasified under the ground, as is known, the distributions of coal seams are mainly the overall. So adding methods described above are clearly inconsistent with requirements and Research Center designed three new ways of catalyst injection coal seams, liquid atomizing of catalyst and dry powder of catalyst to adding catalytic to solve this problem. Three catalysts also are simultaneously added to obtain the optimum catalytic effect[10].

During underground coal catalytic gasification process the reaction is at lower temperatures and has a higher reaction rate and a higher energy efficiency of the process. For the city gas preparation of enriched hydrogen, good conditions are provided. Therefore, underground coal catalytic gasification to achieve an ideal method of coal replacing oil gives full play to advantages of underground coal gasification and can produce clean energy of high calorific value. This has a very important strategic significance for China's energy adjustment structure and energy security of supply[11].

4.4 Industrialization of underground coal gasification

In 2011, another major 863 project to study the key techniques of underground coal gasification was jointly launched by China University of Mining and Technology (Beijing) and XinAo Group for coal mining and coal gasification (Xin’an group). The total investment of this project is 210 million RMB, 74.43 million RMB of which is financed by Chinese ministry of Science and Technology. Currently, a non-gallery underground coal gasification production and test research system with a gas production capacity of 150 000 Nm^3/d has been firstly founded in China. This is a historical success in this domain. It provides a good platform not only to carry out the related research hence to improve the key techniques, but also to drive greatly on the industrialization process in China.

The continuous research and industrialization are of course essential to assure its advance place in this domain. Several essential innovations have been obtained behind this preliminary success of industrialization: 1. The underground gasifier with the new structure of "L-type back surface extension" is improved and the transition from the "line" gasification to "face" gasification is achieved, so underground gasifier structure is more advanced, reasonable and reliable; 2. Because "technology of penetrating gasification passage", "technology of pneumatic multiphase flow dredge", "technology of high-pressure water control ignition" are developed, the core technology of the gasifier constructed is solved; 3.The "radon detection technology in the combustion zone" is developed, so that the parameter measurement and control system are establish in the gasification process of non-well type and the accurate measurement, remote transmission, data analysis and processing of gasification process parameters are achieved. The research results on underground coal gasification technology have made a historic breakthrough to laid a theoretical and technical foundation for industrial applications of the Chinese underground coal gasification technology[12].

After over 20 years of research by this center in China University of Mining and Technology (Beijing), the related technology of underground coal gasification is getting matured. The previous research indicates that the industrialization of underground coal gasification to recovery the “abandoned mine” and shallow coal resources is technically feasible. However, due to its complexity of the distribution, the complete types, and the diverse storage conditions of the coal mining in china, it allows the continuous research of mechanical properties of coal and the expansion law of combustion space area necessity to advance the industrialization[13].

5 Mechanical properties of coal and rock and expansion law of combustion space area at high temperatures

Research on the combustion space area expansion is crucial for the underground gasification process[14]. With the increasing of gasification space, overlying strata overburdens and fracture generation, which result in the overlying aquifer water coming into the gasification zone. When the moisture content of the coal seam exceeds a certain limit, the temperature of reduction zone and gasification process are strongly destroyed, the heat loss increase, the reaction process is to be not normal, coal gas composition and calorific value become instable, while fractures in overlying strata will exacerbate the spread of pollutants, as shown in Fig.4. Therefore, a topic about rock mechanical is summed up, research on the mechanical properties of coal, rock and regulation of combustion space area expansion under high temperature.

Research on coal, rock mechanical properties and thermal expansion and crushing mechanism under high temperature and pressure focuses on rock mechanical strength, force method and brittle-ductile transition characteristics after the heat, discusses the representation method of thermal- mechanical properties and influence factors of coal and coal-bearing strata under high temperature. In view of underground gasification combustion space area, the regulation of temperature field, stress field, displacement field and the evolution of rock deformation damage, subsidence and fractures of coal in combustion space area and surrounding rock will be studied and thermal-solid coupling model of underground gasification combustion space area will be established, so that expansion law of combustion space area at high are revealed.

Lawrence National Laboratory of America has done work related to numerical simulation on underground gasification combustion space area expansion, but practicality has yet to be tested. China University of Mining and Technology (Beijing) and New Austrian Coal Gasification Company have done these studies. And recently Zhao Limei and Tang Furong[15-16] also carried out study on underground gasification combustion space area. However, due to the short of theory combined rock mechanics and heat transfer, the researches are not comprehensive, not the system, up to now a good model and calculation software are not yet formed.

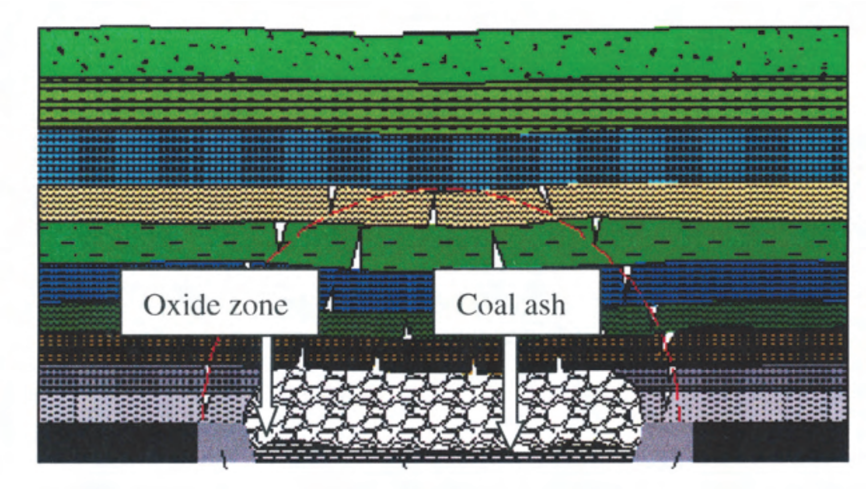

Fig.4 Fracture evolution in combustion space area

6 Broad development prospects of underground coal gasification in China

Currently, the transformation of China's economy is accelerating and the increasing energy efficiency and environmental protection and development of low-carbon economy have become the main tasks of China's economic development in the next stage[3]. This will give development opportunities for underground coal gasification technology. According to statistics, by 2020 China will have more than 500 abandoned mines and abandoned resources reserves of 300 million tons, however underground coal gasification technology can recover these resources. According to incomplete statistics, in China lignite resources of about 370 billion tons are mainly in Inner Mongolia and Xinjiang area, the coal resources of about 219 trillion tons under 1000 m depth include 300 billion tons in Ningxia Autonomous Region. Deep coal resources to be suitable for no well type gasification along the West-East pipeline are about 47.7614 trillion tons, so that coal gas from underground coal gasification can be used for synthetic natural gas. Meanwhile, underground gasification is relatively high safe mining methods and achieves a safe mining of coal resources. This can have a positive effect to change present situation of high accident rates in China's coal enterprises and gain good social benefits.

7 References

1. Management Measures of the Programme of Introducing Talents of Discipline to Universities [EB/OL]. http://www.moe.edu.cn/publicfiles/business/htmlfiles/moe/s3335/201001/82287.html

2. Yang Lanhe. Characteristics of “Three Zones” in Underground Coal Gasification and Its Study of Influence Variables[J]. Journal of Nanjing University of Science and Technology, 2001, 25(5):533-537.
3. Tang Shuyun, Liang Zirong. Safe, efficient, green coal mining technology: Underground Coal Gasification [J]. China Coal,2011,37(1): 12-13.
4. Ma Xiao-fei, Wang Yong-bing. The Development and Application of Underground Coal Gasification[J]. Chemical Equipment, 2013, 2:27-28
5. Yang Zhen,Liang Jie, Li Xiuzhen. STUDY OF BURNING CONTROL SYSTEM OF UNDERGROUND GASIFICATION[J]. COAL CONV ERSION, 2002,25(4):32-33.
6. LIANG Jie, LIU Shuqin, YU Li. Method of stably Controlling the Process of Underground Coal Gasification[J]. Journal of China University of Mining & Technology, 2002, 31(5):358-362.
7. SHEN Fang, LIANG X inxing, MAO Wei zhi, et al. The recent study and development of UCG in China[J]. Energy Engineering, 2008,1:6-9.
8. YANG Lan-he. Method of Multi-point Two-stage Underground Coal Gasification (TSUCG)[J]. Journal of Chongqing University(Natural Science Edition), 2001,24(2):111-115.
9. Liang Jie, Yu Li. STUDY OF TWO - STAGE UNDERGROUND COAL GASIFICATION IN COUNTER DIRECTIONS[J]. JOURNAL OF CHINA COAL SOCIETY, 1996, 21(1):68-71.
10. Liang Xinxing, Liang Jie, Sun Chunbao. STUDY ON THE METHOD OF CATALYSIS ON UNDERGROUND COAL GASIFICATION[J]. COAL CONVERSION, 2013,36(1):34-37.
11. LIANG Xinxing, SHEN Fang, LIANG Jie. New technology of underground coal catalytic gasification[J]. 2008,4:51-54.
12. Liu Shutao Coal green mining technology explored by youth and knowledge[J]. COAL GEOLOGY OF CHINA, 2014,26(1):74-75.
13. LIU Xuejian, XU Jianpei, ZHANG Zaoxiang. Research on the industrialization of underground coal gasification technology[J]. China Coal, 1999,25(7):33-35.
14. Wang Zaiquan, Hua Anzeng. REVIEWON CAVITY GROWTH LAWS AND CONTROL IN UNDERGROUND COAL GASIFICATION[J]. Chinese Journal of Rock Mechanics and Engineering, 2001, 20(3):379-382.
15. ZHAO Limei. Properties of Oil shale In-situ Pyrolysis and Coupling Process of Underground Coal gasification [D]. Beijing, China University of Mining and Technology (Beijing),2013,10.
16. TANG Furong. Fracture Evolution and Breakage of Overlying Strata of Combustion Space Area in Underground Coal Gasification[D]. Xuzhou, China University of Mining and Technology, 2013,6.